

Scalable quantum light sources in silicon photonic circuits

by

Cale Michael Gentry

M.S. (Electrical Engineering), University of Colorado Boulder, 2013

B.S. (Engineering Physics), University of Oklahoma, 2011

A thesis submitted to the

Faculty of the Graduate School of the

University of Colorado in partial fulfillment

of the requirements for the degree of

Doctor of Philosophy

Department of Electrical, Computer, and Energy Engineering

2018

This thesis entitled:
Scalable quantum light sources in silicon photonic circuits
written by Cale Michael Gentry
has been approved for the Department of Electrical, Computer, and Energy Engineering

Prof. Miloš A. Popović

Prof. Juliet Gopinath

Dr. Jeffrey Shainline

Dr. Thomas Gerrits

Prof. Kelvin Wagner

Date _____

The final copy of this thesis has been examined by the signatories, and we find that both the content and the form meet acceptable presentation standards of scholarly work in the above mentioned discipline.

Gentry, Cale Michael (Ph.D., Electrical Engineering)

Scalable quantum light sources in silicon photonic circuits

Thesis directed by Prof. Miloš A. Popović

Chip-scale integrated photonic circuits provide an attractive platform for the implementation of many quantum photonic technologies ranging from precise metrology to secure communication and quantum computation. In particular, silicon photonic platforms support micron-scale nonlinear optical sources of non-classical light which can be mass manufactured using the robust fabrication processes pioneered by the CMOS microelectronics industry. Integration of these quantum photonic sources with high-performance classical photonic devices on the same chip is required for truly scalable quantum information technologies. Integrated nonlinear resonators are investigated as sources of quantum mechanically correlated photon pair sources. An all-order dispersion engineering method is presented as a robust design synthesis for microring sources. In addition, a novel concept of coupled mode dispersion compensation is proposed and demonstrated, providing significantly improved performance characteristics of resonant four-wave mixing sources. Next a photon pair source is demonstrated in a commercial CMOS microelectronics process opening the door to future integration of quantum photonics with electronic logic and control circuits. Classical nonlinear optical measurements of stimulated four-wave mixing are used for the first time to accurately predict the quantum correlations from the same device operating in the photon pair regime. Next the first demonstration of fully on-chip pump rejection is demonstrated with over 95 dB pump extinction improving the figures of merit from previous demonstrations by multiple orders of magnitude, including losses, detected pair rates and size. Finally, proposals for introducing novel degrees of freedom provided by an integrated platform are presented for further improving the performance of both photon pair and classical nonlinear optical sources.

Dedication

To my parents, Mike and Melissa Gentry.

Acknowledgements

I owe much gratitude to the many people who have supported and encouraged me over the course of my graduate studies. The work presented in this thesis is representative of collaboration between many people including fellow group members as well as external collaborators. Xiaoge “Savvy” Zeng, Yangyang Liu, and Jeffrey Shainline, in particular, shared invaluable knowledge and provided me guidance throughout my time as a graduate student. I am also grateful to Mark Wade, who joined the group a few months before myself, for many discussions on integrated photonics and the daily life of a Ph.D. student. Gil Triginer Garces gave me the opportunity to engage in many interesting discussions on quantum optics and the coupled mode formulations of four-wave mixing.

The work presented in this thesis benefited greatly from working with our collaborators at NIST Boulder, who provided me a desk, lab space, and access to arguably the world’s best single photon detectors. My time spent at NIST was enlightening and I was fortunate enough to attend regular group meetings and receive helpful feedback and support on both my experimental and theoretical endeavors. I would like to specifically thank Richard Mirin, Shellee Dyer, Marty Stevens, Thomas Gerrits, Sonia Buckley, Omar S. Magaña-Loaiza, and Sae Woo Nam for their contributions.

My advisor and thesis committee chair Miloš Popović, provided a theoretical foundation in integrated photonics which can not be found elsewhere, and for which I am extremely grateful. I would also like to thank the many post-docs I have worked along side, including Fabio Pavanello, Rajesh Kumar, and Yossi Ehrlichman. My fellow group members – Kareem Nammari, Nathan Dostart, Imbert Wang, Josep Fargas Cabanillas, Hayk Gevorgyan, and Bohan Zhang – provided much support and camaraderie during both tapeouts and coffee breaks. At Berkeley, Sen Lin was instrumental in packaging many of the chips studied in this thesis. I thank my committee members Prof. Juliet Gopinath, Dr. Jeffrey Shainline, Prof. Kelvin Wagner, Dr. Thomas Gerrits, and Prof. Robert Mcleod for their insightful feedback.

Without the support of my family, I would have never been able to pursue this incredible journey. My brothers, Shea and Kade, helped build my character in the way only brothers can. My grandparents, Kenneth and Marie Rotan and “Papa” Jim and “Nana” Karen Gentry, were instrumental in nourishing my scientific aspirations throughout my life. My parents, Mike and Melissa Gentry, went through great lengths to provide me the opportunity to make the choices in life that I have pursued, for which I am eternally grateful. My love, Jennie, has made my life and my graduate pursuits significantly better. I am grateful for all the love and support she and her family have brought into my life.

Contents

Chapter

1	Introduction	1
1.1	Evolution of quantum optics and quantum photonic systems	2
1.2	Photonics for quantum information technology	5
1.3	Silicon photonics	7
1.4	Silicon quantum photonics	8
1.5	Outline of thesis	9
2	Principles of integrated photonics and quantum optics	11
2.1	Maxwell's equations	11
2.2	Dielectric waveguides and their guided modes	14
2.3	Dispersion	20
2.3.1	Material dispersion	21
2.3.2	Dispersion in a single mode waveguide	22
2.4	Directional couplers	25
2.5	Ring resonators	29
2.5.1	Simplification near resonance	30
2.6	Coupling of modes in time	31
2.6.1	Comparison to t-matrix	34
2.6.2	Resonators with gain	35

2.6.3	Quantized coupled mode theory	36
2.7	Summary	40
3	Four-wave mixing and dispersion engineering	41
3.1	Introduction and background	41
3.2	Nonlinear optics	42
3.3	Four-wave mixing in a waveguide	44
3.3.1	Dispersion and phase matching in a waveguide	47
3.4	Four-wave mixing enhancement in a ring resonator: T-matrix	54
3.4.1	Dispersion and phase matching in a ring	56
3.5	Four-wave mixing enhancement in a ring resonator: coupling of modes in time	62
3.6	Discrete resonance dispersion engineering of ring resonators	65
3.7	Tunable coupled-mode dispersion compensation	68
3.7.1	Coupled resonator modes and frequency splitting	68
3.8	Conclusions	77
4	Quantum regime: Photon pair generation and CMOS integration	79
4.1	Introduction and background	79
4.2	Theory	80
4.2.1	Generated photon flux with CW pump	82
4.3	Implementation in advanced CMOS	85
4.3.1	Device design	86
4.3.2	Stimulated four-wave mixing characterization	89
4.3.3	Photon pair generation measurements	91
4.3.4	Noise characterization	96
4.4	Conclusions	97

5	Source purity: characterization, pump filtering, and parasitic noise	99
5.1	Coincidences-to-accidentals ratio	99
5.2	Pump filtering	105
5.2.1	Unintentional light scattering and other modes	108
5.2.2	FSR-doubled ring-based filters	111
5.2.3	Experimental demonstration of on-chip pump rejection	112
5.3	Conclusions	118
6	Resonance linewidth engineering for enhancing quantum and classical sources	119
6.1	Increasing the generation efficiency of a resonant photon pair source	119
6.2	Engineering signal and idler spectral correlations	122
6.3	Imaginary coupling, Q-splitting, and dark state lasers	125
6.4	Conclusions	132
7	Conclusions	133
7.1	Summary of major achievements	133
7.2	Remaining challenges and future work	134
	Bibliography	138

Figures

Figure

1.1	Example of three generations of photon pair sources: (a) Atomic cascade process used in the pioneering Bell tests [38, 5], (b) Spontaneous parametric down-conversion (SPDC) [19, 132, 51, 78], (c) Spontaneous four-wave mixing.	4
1.2	Illustration comparing the interference in a classical Mach-Zehnder interferometer with the relatively higher phase sensitivity interference from a quantum entangled 2-photon N00N state.	6
2.1	Example cross-sectional schematic of an air-cladded strip waveguide fabricated from a silicon-on-insulator wafer. The higher refractive index of the silicon waveguide compared to the air and buried oxide allows the guidance of light on chip through total internal reflection. The buried oxide is typically greater than $1.5\ \mu\text{m}$ thick preventing light from leaking from the silicon waveguide to the support silicon handle wafer.	15
2.2	Mode effective indices at a wavelength of 1550nm versus waveguide width for the waveguide dielectric distributions illustrated in the insets for (a) a vertically symmetric waveguide displaying both quasi-transverse electric (TE) and quasi-transverse magnetic (TM) modes at all widths and a (b) vertically non-symmetric waveguide displaying a cutoff width near 520 nm where only a single TE mode is guided	18

2.3 Schematic comparison of a guided mode in an ideal lossless waveguide and a lossy waveguide illustrated using rough sidewalls and modeled using a complex propagation constant. The loss is greatly exaggerated to illustrate the decay of power amplitude along the propagation direction z . Note that this approximation ignores optical powers after it has left the guided mode and assumes all scattering due to roughness is perfectly uniform. 20

2.4 Illustration of a Gaussian pulse before and after propagation, displaying how a dispersive medium can cause pulse spreading and chirping. 21

2.5 Refractive index of crystalline silicon, n_{si} , measured by various literature sources [54, 66, 111, 39, 127, 119, 147], demonstrating normal dispersion (i.e., $\frac{d}{d\lambda}n_{\text{si}} < 0$) across the entire wavelength range. All refractive indices for silicon in this thesis use the Palik Handbook Fit [111]. 23

2.6 Fundamental mode for a 380 nm wide, 220 nm thick air-cladded waveguide on oxide for the O-band and C-Band. Note how the mode shape changes causing it to “experience” more of the cladding at the longer wavelength resulting in a lower effective index. We refer to the dependence of effective index on wavelength as “modal dispersion.” 25

2.7 (a) Group index of an oxide cladded silicon waveguide of dimensions 220 nm by 420 nm versus wavelength where both modal and material dispersion are used and where only modal dispersion is assumed (using the refractive indices at 1550 nm). (b) Similar plot for the group velocity dispersion (GVD) showing that the zero group velocity dispersion wavelength is significantly affected by the inclusion of material dispersion. 26

2.8	(a) Illustration of a lossless directional coupler allowing the distribution of power from one waveguide to two. (b) Schematic and form of the T-matrix for a 2x2 coupler which is symmetric about the horizontal axis with (c) demonstrating that shift in reference planes can remove the global phase θ_o . (d) represents a generalized lossless coupler with corresponding reference plane shifts (e) allowing it be define equivalently to the symmetric coupler.	27
2.9	Ring resonator constructed from a general 2 by 2 coupler can be modeled as a symmetric (about horizontal axis) point coupler with the additional phases ψ and Δ in a general coupler added to the propagation.	30
3.1	(a) The normalized conversion efficiency in a lossy waveguide for stimulated four-wave mixing (Eq. 3.31) versus waveguide length (scaled by the propagation loss) and phase mismatch (scaled by the waveguide length, L) demonstrates optimal efficiency at zero phase mismatch. (b) Plot of efficiency at zero phase mismatch displaying an optimum waveguide length, where loss becomes dominating the efficiency in waveguides exceeding this length. (c) Conversion efficiency versus scaled phase mismatch at the optimal waveguide length.	48
3.2	(a) Modesolver simulation of the propagation constant versus frequency for a 220 nm thick 370 nm wide silicon strip waveguide on a silica slab. (b) Corresponding group velocity dispersion displaying a zero crossing at 1558.44 nm. (c) Fourth-order derivative of propagation constant with respect to angular frequency which contributes to the phase mismatch as described in Eq. 3.38	51
3.3	Fully simulated, 2nd-order Taylor series expansion, and 4th-order Taylor series expansion of the (a) phase mismatch of 370 nm air cladded waveguide at a pump set to the zero group velocity dispersion (ZGVD) wavelength at 1558.44 nm, (b) corresponding stimulated four-wave mixing efficiency profile	52

3.4	(a) phase mismatch at pump set to 1550 nm with (b) corresponding efficiency profile showing that pumping at the ZGVD wavelength does not necessarily result in the largest bandwidth.	53
3.5	Schematic of the four-wave mixing transfer matrix (T-matrix) model where we investigate the coupling of power amplitudes propagating around the ring and use the vertically symmetric convention for the waveguide to ring point coupler.	55
3.6	Plots demonstrating the resonant enhancement provide by a ring resonator with corresponding power enhancement for the signal, idler, and pump frequencies illustrated by arrows. (a) Dispersionless ring with equal adjacent free spectral ranges allowing all modes to be on peak resonance. (b) Ring resonator modelled with dispersion such that the resonances exhibit a significant difference in free spectral range of $\Delta\nu_{\text{FSR}}$, forcing the idler to be substantially off peak resonance when the signal and idler enhancements are maximized.	58
3.7	Schematic of the four-wave mixing temporal coupled mode theory model where we investigate the coupling of energy amplitudes dynamics in time according to Eqs. 3.68, 3.69, and 3.70.	62
3.8	Sequence for proposed method of dispersion engineering a ring resonator including (a) numerical simulation of mode order versus frequencies, (b) inversion to have frequency versus mode order, (c) calculate frequency \pm one mode order away, and (d) difference of these showing the difference in free spectral range versus wavelength.	66
3.9	Simulation of dispersion induced resonance shift using the proposed discrete resonance dispersion engineering method for a silicon oxide cladded, 220 nm thick silicon ring resonator at a pump wavelength of 1550 nm.	67
3.10	(a) Proposed resonator geometry of two differently sized coupled cavities with corresponding uncoupled resonance frequencies (b) that are not energy matched due to dispersion.	70

- 3.11 (a) Proposed resonator geometry of two differently sized coupled cavities with corresponding uncoupled resonance frequencies (b) that are not energy matched due to dispersion. (c) Coupling results in frequency splitting at a single FSR allowing energy matching between three resonances (d) Supermode of split resonance spans both rings [48]. 71
- 3.12 Optical micrograph of fabricated tunable coupled-mode dispersion compensation device [48] fabricated through ePIXfab Multi-Project Wafer shuttle runs. A resistive gold microheater was fabricated at the Colorado Nanofabrication Laboratory (CNL). 72
- 3.13 Example transmission spectra of the coupled cavities for heater powers of 35 mW, 43 mW, 50 mW, and 57 mW. At a heater power of 57 mW a small transmission dip due to the auxiliary ring is evident at a frequency less than the idler resonance frequency. As the heater power is reduced to 43 mW strong mode coupling at the idler resonance is displayed [48]. 74
- 3.14 (a) Plot of the center frequency for each of the four relevant resonances over the range of heater powers applied. At 44.3 mW, the signal and idler resonances are equally spaced from the pump resonance, thereby demonstrating dispersion compensation. (b) Measured difference in adjacent free spectral range with heater power. The blue line is a fit to the data using temporal coupled mode theory and the dashed red line is the same line shifted up by 6 GHz to represent the combined effect of self- and cross-phase modulation [48]. 75
- 3.15 OSA output spectrum of highest efficiency (-37.9 dB) seeded four-wave mixing measurement. Dashed lines represent the corresponding powers of each mode in the waveguide. The actual values of the spectrum peaks for the pump and signal modes are reduced by the resonance as well as loss due to outcoupling through a grating coupler. Alternatively, the idler mode experiences little loss from the resonance since it is generated within the ring and only experiences loss on transmission through the grating coupler [48]. 76

3.16	Measured converted efficiency versus heater power demonstrating tunable dispersion compensation. The blue line represents the expected efficiency from a model ignoring the effects of phase modulation while the red dashed line takes these effects into account and exhibits a stronger fit [48].	77
4.1	(a) Schematic of a typical transistor composed of a crystalline silicon (c-Si) body and a polysilicon gate. (b) Cross-section illustration of the microring-resonator pair source showing how the sub-100 nm c-Si transistor body layer can be used to confine light after removal of the Si handle wafer. The fundamental resonator mode contours are superimposed in red to illustrate how the majority of the modal field extends into the cladding.	86
4.2	(a) Optical micrograph of the top-side of the CMOS chip showing the various backend metals. (b) The corresponding optical micrograph of the bottom of the CMOS chip, with silicon device layer visible, and zoom-in (c) of the ring-resonator photon pair source and grating couplers [46].	87
4.3	Simulated difference in FSR $\Delta\nu_{\text{FSR}}$ at 1550 nm due to dispersion with chosen design predicted to be a negligible 1.4 GHz [46].	88
4.4	Transmission Spectra	90
4.5	Stimulated FWM	91
4.6	Simplified schematic of the pair generation measurement. The pump light is passed through two C-band (1530-1565 nm) separators and two telecom filters to eliminate noise from the laser. A fiber polarization controller (FPC) is used to optimize coupling efficiency. The signal and idler photons are then filtered individually and sent to high efficiency superconducting nanowire single photon detectors (SNSPDs). A time interval analyzer is then used to count coincidences. The pump power is monitored by a classical photodetector to ensure the pump light is on resonance [46].	92

4.7	Coincidence rate of photon pairs at the detectors with the estimated rate on-chip (b) after subtracting out losses to the detectors. The solid line is the rate expected based on the stimulated four-wave mixing measurements [46].	94
4.8	Coincidences-to-accidentals ratio (CAR) for various pump powers where the coincidence peaks were fit to a Gaussian function (insets) and delay windows selected at the (a) full-width-half-maximum and (b) ± 3 standard deviations [46].	95
5.1	Simplified illustration of coincidence counting and the method coincidence histograms are generated from two arrays of detection events versus time at two detectors. The two arrays are cross-correlated to make a coincidence plot. The number 1 is used as notation for a detection in a given time bin.	100
5.2	Illustration of possible coincidence peaks for (a) a hypothetical source which does not exhibit multi-pair generation and (b) a source which does. Multi-pair photons contribute equally to accidentals as uncorrelated events resulting from photons from different pairs contribute to the out of coincidence measurement background. This mathematical coincidence allows for indirect measurement of the number of accidentals by averaging the number of photons outside the coincidence window.	104
5.3	(a) The amount of pump rejection required found using Eq. 5.19 for the source demonstrated in Chapter 5 to allow for a multi-photon limited CAR of 100. (b) The corresponding ratio of output photon pairs to input pump photons for a range of pump powers.	107
5.4	Comparison of accidental contributions from multi-pairs and leaked pump assuming 110dB pump rejection. The increased slope of the multi-pairs line shows that at higher pump powers more pump rejection is required to maintain a constant CAR.	108
5.5	Measurement of scattered light on a standard SOI photonic chip demonstrating that even 2 mm away, there is still significant background light that will limit the extinction of an on-chip filter.	109

5.6	Illustration of the CMOS process layer stack-up after the substrate has been removed and the chip as been placed upside down such that the silicon device layer is at the top. We hypothesize that the presence of metal fill patterns will aid in the attenuation of scattered light.	110
5.7	Proposed filtering scheme for removing the generated photon pairs from the collinear pump. A serial cascade of four second-order ring resonator filters, each of twice the free-spectral range (FSR), of the source will be used to remove the signal and idler photons simultaneously [44].	112
5.8	Micrograph of the fabricated source and filtering circuit. Thirteen sources of slightly varied radii were used to ensure that at least one would exhibit signal and idler resonances which overlap with the filter passband. Zoomed in micrographs of a (i) grating coupler, (ii) filter, and (iii) microresonator source show the presence of the processes fill pattern in the silicon layers. A similar fill pattern (not visible) is present below in the metallic absorbing layers [44].	113
5.9	(a) Broadband transmission spectrum of the source thru port (blue) exhibiting resonances and the transmission spectrum of the filters (red). (b) The spectrum of photon counts received at the detector from the output of the chip when the pump is placed on resonance. (c) High dynamic range transmission spectra of the filter demonstrating over 95 dB pump rejection. Various colors below -70 dB represent measurements through different telecom filters which eliminate excess spontaneous emission form the swept laser source, thereby increasing the measurements dynamic range [44].	114

- 5.10 (a) Schematic of experimental setup for demonstrating all on-chip pump filtering with a 50%-50% fiber directional coupler probabilistically separating signal and idler photons. (b) Example coincidence histogram with coincidence window of 640 ps for the setup in (a). (c) Detected coincidence rates and CARs for various on-chip pump powers for the setup in (a). (d) Schematic of experimental setup where an off-chip filter was used to remove excess noise photons not contributed by the pump with (e) example coincidence histogram and (f) corresponding measured coincidence rates and CARs [44]. 115
- 5.11 (a) Schematic illustration of the setup of a folded Franson interferometer [149] which was used to measure time-energy entangled photons. (b) The corresponding coincidences demonstrating bi-photon interference and non-classical visibility of $81.4\% \pm 2.3\%$ [44]. 117
- 6.1 Plot of normalized generation efficiencies given by Eq. 6.4 for symmetrically coupled resonators where the signal and idler are coupled equally while the pump is fixed at critical couplings and Eq. 6.5 where all three resonances are equally coupled. At large escape efficiencies the symmetric coupling configuration is much more efficient, including greater than 10 times more efficient at escape efficiencies over 90% [43]. . . 121
- 6.2 (a) Joint spectral intensity of a photon pair generated in a highly mixed bi-photon state. (b) Example normalized joint spectral intensity of an ideal separable bi-photon state. 123
- 6.3 Joint spectral intensities for a resonator with (a) equal couplings ($r_{s,e} = 6r_o$, $r_{p,e} = 6r_o$, and $r_{i,e} = 6r_o$) and a CW pump, (b) symmetric couplings ($r_{s,e} = r_o$, $r_{p,e} = 10r_o$, and $r_{i,e} = r_o$) and a broad pulsed pump (pulse bandwidth of $15r_o$), (c) unequal couplings ($r_{s,e} = 20r_o$, $r_{p,e} = 10r_o$, and $r_{i,e} = r_o$) with a pulsed pump (pulse bandwidth of $40r_o$), and (d) unequal couplings ($r_{s,e} = r_o$, $r_{p,e} = 10r_o$, and $r_{i,e} = 20r_o$) with a pulsed pump (pulse bandwidth of $40r_o$) [43]. 124

6.4	Geometry which displays imaginary coupling coefficient through farfield interference in the waveguide bus [45].	125
6.5	(a) Proposed laser resonator geometry enabling farfield interference at the output coupler resulting in eigenfrequency imaginary splitting at matched resonances to create (b) a broad Vernier-like FSR for ultrawide tuning [45].	128
6.6	Visualization of supermodes with detuning on a Poincaré (Bloch) sphere. For detuning less than the single ring external coupling ($\delta\omega_o < r_e$) the energy is equally distributed across both rings. At greater detuning the supermodes approach the modes of the individual uncoupled rings.	129
6.7	(a)Phase difference between mode-fields of each ring and resulting external coupling of dark state with detuning. (b)Dependence of tuning on output power for fixed r_e (c)Threshold/slope efficiency curves as a function of small-signal gain (pumping), with the operating region of dark-state-only lasing shaded.	130
6.8	An illustration of quasi-continuous tuning of the dark state laser. First (a) both rings are tuned an FSR of the smaller ring (larger FSR). Then the laser can be turned off and reset to the start position Fig 1 (d). (b) An offset can then be introduced to shift the Q-splitting to the previous location where both rings can then be continuously tuned across another FSR. The process can then be repeated across the gain bandwidth.	131

- 7.1 (a) Schematic of fully integrated Hong-Ou-Mandel (HOM) interference experiment for the characterization of heralded single photon sources. Two heralded single photon sources based on Four-Wave Mixing (FWM) consist of counter-propagating pump pulses in the same resonator to generate photon pairs. Each pair of photons then pass through separate high-extinction filters to isolate them from the pump and are then de-multiplexed. The blue arrows represent the trigger photons and the red arrows the heralded single photons. Metallic enclosures isolate the superconducting detectors from stray light, providing access only through the single optical mode of the waveguide. (b) For zero pump pulse offset all four-photon detection events are suppressed due to HOM interference. 135

Chapter 1

Introduction

Research in both quantum optics and on-chip integrated photonics have experienced significant progress over the last few decades. However most of the achievements in each of these fields have, for the most part, been accomplished independently. For example, arguably no quantum optics experiment has been implemented to date, where on-chip integration has enabled performance exceeding results of equivalent experiments utilizing bulk optical components. Yet, there is still much interest in the potential of large scale quantum photonic applications which can benefit from the small footprint, stability, and mass manufacturing provided by integrated photonics. Integrated photonic circuits have the potential to scale to systems containing millions of interconnected optical components on a single centimeter-scale chip, while a comparable system constructed from bulk optical components could fill a building. In addition to footprint, the resources required for manufacturing scale much more reasonably with integrated photonics. While doubling the size of a free space optical system requires approximately twice the time, effort, and cost, it is relatively simple to double the number of components lithographically patterned on a single chip without incorporating additional fabrication equipment to the process.

Development of large photonic systems that can manipulate the quantum properties of light could lead to revolutionary technological advancements with unforeseen capabilities analogous to how controlling the flow of electrons in integrated electronic circuits led to the revolution of the digital microprocessor. This thesis presents work where the fundamental principles of integrated photonics and the implementation of state-of-the-art CMOS photonics are applied to the devel-

opment of quantum photonic sources. By demonstrating low power and small footprint quantum correlated photon sources, the work presented here represents significant progress towards future implementations where thousands of such sources can be built on a single silicon chip. In addition, record performance classical photonic devices such as high extinction filters are developed to demonstrate the scalability of quantum photonic systems.

1.1 Evolution of quantum optics and quantum photonic systems

Investigation of the spectra of light emanating from heated objects led to the first theoretical support, provided by Planck [115], that light is emitted and absorbed in discrete values of energy which we now refer to as photons. Einstein's study of the photoelectric effect [32], the thermodynamics of radiation fluctuations [33], and the processes of spontaneous and stimulated emission [34] (all while concurrently developing the theories of special and general relativity) provided further evidence that the classical Maxwell's equations did not completely describe the observed properties of light. It was not until 1927 that Dirac provided the first true description of the quantized electromagnetic field [29], definitively attributing the process of spontaneous emission to the interaction of the vacuum field with an atom. During the decades following Dirac's theoretical development, the study of quantum electrodynamics regularly utilized the quantized electromagnetic field to describe its interaction with matter (such as relativistic corrections to the optical spectra emitted by atoms), yet the consequences which quantization imposed on the properties of light itself were not significantly investigated until the late 1950's.

Experimentally, one of the first attempts to measure light intensities at which only one photon was under test at any time was Taylor's 1909 measurement of interference fringes from the shadow cast by a needle illuminated by a flame [148]. Taylor expected to observe a diminishing visibility of the interference phenomenon as he added more attenuation through the addition of smoked glass panes. Instead, he found the visibility of the fringes had no dependence on the intensity of light used, even for the weakest of light where the exposure spanned approximately three months. Hardly consisting of more than a single page, Taylor's paper [148] is an illuminating example of the initial

forays into experimenting with faint light. In a similar attempt to disprove the hypothesis that optical energy is comprised of discrete quanta, R. A. Millikan instead provided evidence in favor of Einstein’s photoelectric effect explanation in 1914 [102].

Interestingly, an intensity interferometer for stellar astronomy, developed by R. Hanbury Brown and R. Q. Twiss (HBT) in 1956 [17], became the experiment to spark new theoretical investigations into quantum optics. HBT interference was easily explained by classical Maxwell’s equations [18] but resulted in much controversy over the quantum mechanical description, since it suggested two photons originating from vastly distant locations on a star can be correlated. This led to in-depth theoretical investigation on the coherence properties in quantized light and was first pioneered by Fano [36], Sudarshan [137], and Glauber [52] in the early 1960’s. That same decade, John S. Bell published his groundbreaking paper [10] proposing an experimental procedure for which the predictions of quantum mechanics would disagree with those of any local hidden variable theory. Local hidden variable models permit the formulation of a so-called “Bell inequality,” providing an experimental bound for a measurable parameter, which predictions from a quantum mechanical model can exceed. A measurement of this type is typically referred to as a “Bell test,” whereas a violation of a Bell inequality provides evidence against a local realistic universe.

Construction of the experimental systems for implementing Bell test type experiments led to the first demonstrated entangled photon pair source by Freedman and Clauser in 1972 [38]. The particular source in [38] utilized an atomic cascade process for photon pair generation. We note that photon pairs, correlated in time, had already been produced through similar atomic cascade processes [65]. Photon pairs originating from a parametric nonlinear process were first generated using spontaneous parametric downconversion in 1970 [19], only 10 years after the demonstration of the first functioning laser [92]. After Freedman and Clauser’s initial experiment, entanglement-based tests of local realism set on a 43 year journey removing various so-called “loopholes” which could nefariously expose non-ideal experimental conditions to conceal local realistic mechanisms. Aspect et al’s measurement [5] of each photon of an entangled pair separated by a sufficient distance to require a signal faster than the speed of light (assuming the photons had a mechanism to com-

municate regarding their experimental outcomes) closed the locality loophole in 1981. Experiments continued to remove additional loophole until all reasonable loopholes were removed in 2015 in the three monumental experiments [64], [132], and [51]. The latter two of these experiments benefited greatly from spontaneous parametric down-conversion (SPDC) sources, which since 1995 [78] have become arguably the best sources of photon pairs, due to their ability to support large generation rates at high purity. This spontaneous parametric process is very similar to spontaneous four-wave mixing (FWM), the nonlinear process central to the work of this thesis.

Fig. 1.1 shows a comparison of the three classes of photon pair sources mentioned. While all three techniques necessarily generated photon pairs stochastically, the atomic cascade process suffers from photon pair emission in all directions, making it infeasible to capture all photons. Alternatively SPDC sources are engineered such that photon pair emission occurs in predictable

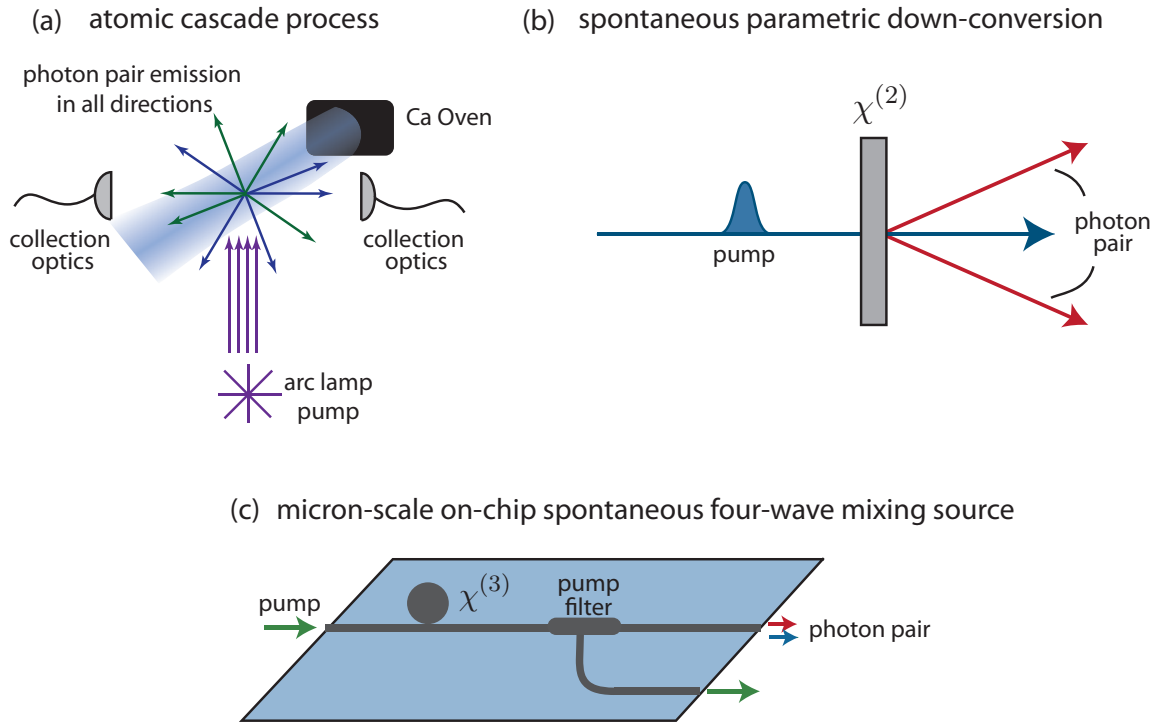


Figure 1.1: Example of three generations of photon pair sources: (a) Atomic cascade process used in the pioneering Bell tests [38, 5], (b) Spontaneous parametric down-conversion (SPDC) [19, 132, 51, 78], (c) Spontaneous four-wave mixing.

beams. On-chip spontaneous FWM sources are comprised of waveguides which along with phase-matching allows for deterministic direction for photon pair emission. One primary challenge with four-wave mixing is that removing the pump from the generated photons is very difficult, not only because they are collinear but because they generated photons wavelengths are much closer to the pump than in the case of atomic cascade or SPDC.

1.2 Photonics for quantum information technology

While the previous section briefly summarized significant demonstrations of fundamental physical properties of quantized light, we now explore the subsequent advancements in the development and implementation of information technologies which leverage these physical principles. A particularly noteworthy example is the ability to create a cryptographic protocol [12] for distributing a key which is completely secure due to the laws of physics. Quantum key distribution (QKD) relies on the destruction of a quantum mechanical state during measurement to safeguard against potential eavesdroppers in the communication channel. The protocol proposed in [12] specifically relied on encoding the states of single photons. The QKD concept was then demonstrated in 1992, using weak coherent light from an attenuated laser in lieu of true single photons [11]. While QKD protocols relying on single photons are inherently limited in distance due to loss [112], entanglement-based protocols have the potential to extend the distance if reliable quantum repeaters can be built. However, demanding specification for effective quantum repeaters such as long photon storage time and high retrieval efficiency have prevented any useful implementation of an entanglement-based protocol to date [165].

Quantum properties of light can also be used for ultra precise measurements using highly entangled states [14] and squeezed states [20]. Fig. 1.2 shows how interference of a so-called “N00N” state (a particular entangled state consisting of N photons), can increase the phase sensitivity of an interference compared to a classical Mach-Zhender interferometer. In addition to metrology and cryptography, quantum photonic states have enormous potential as resources in quantum information processing systems as well. While it had been previously accepted that single photon

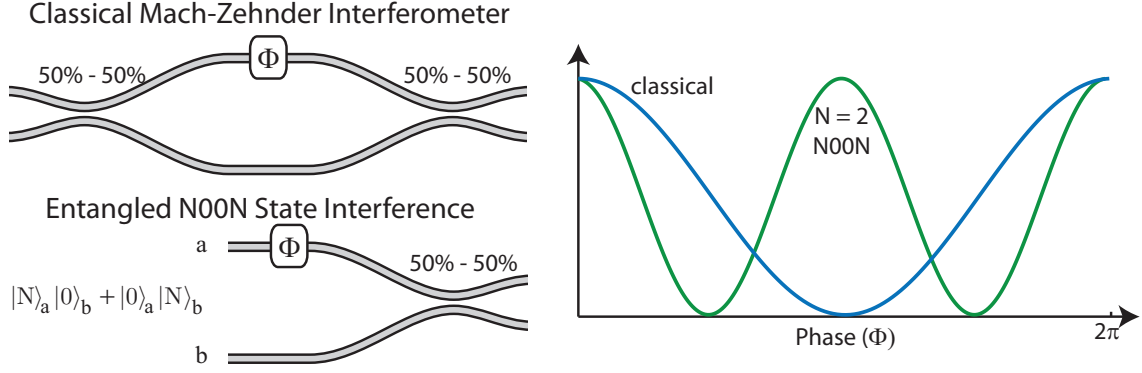


Figure 1.2: Illustration comparing the interference in a classical Mach-Zehnder interferometer with the relatively higher phase sensitivity interference from a quantum entangled 2-photon N00N state.

nonlinearities would be required to build a photonic quantum computer, in setting out to prove this Knill, Laflamme and Milburn demonstrated that it was in principle possible to build a quantum computer using only linear optics, single photon sources, and single photon detectors [76]. Soon after, basic demonstrations of photonic quantum computing gates were achieved [108, 107, 106]. There have been additional advancements in linear optical quantum computing architecture through the use of cluster states and measurement based quantum computing, thereby greatly reducing the necessary overhead for number of physical components [122, 50]. In addition, there has been work towards building a photonic system which could sample a distribution which is classically hard to solve on a computer [1], and is commonly referred to as “Boson Sampling”. While such system would not be a general purpose (universal) quantum computer, it could provide the first evidence of “quantum supremacy” over classical computing and demonstrate a violation of the extended Church-Turing thesis [2], a central tenet in theoretical computer science.

Quantum photonic technology has also benefited greatly from recent advancements in single photon detectors. While the detection of single photons has been possible since the 1930’s due to the availability of photomultiplier tubes [99], advancements in avalanche photodiodes and eventually superconducting detectors such as transition edge sensors (TESs) with near unity detection efficiencies [85] and superconducting (SNSPDs) with up to 93% detection efficiencies [94],

have contributed greatly to both fundamental experiments and new quantum photonic information technologies.

1.3 Silicon photonics

While dielectric waveguides had been greatly studied in the field of fiber optics, the first rectangular dielectric waveguides based on total internal reflection were proposed and demonstrated in the mid-1960's, primarily through the use of liquids and air as a dielectric materials [72, 73, 128]. These were motivated by attempts to provide a guide with less attenuation than fibers, which at the time were quite lossy. Of course, today optical fibers have become ubiquitous with long range and high-bandwidth information transfer due to their excellent transmittances with attenuation of the order of 0.2 dB/km. Meanwhile integrated optical systems built from on-chip lithographically patterned waveguides likely began with Miller's paper [100] proposing many of the integrated photonic devices available today, evening coining the term "Integrated optics" only a decade after Kilby and Noyce had patented the first integrated electronic circuits [75, 105]. Miller was well ahead of his time and his motivations for proposing such a revolutionary technology are still integral to the motivations behind the work comprising this thesis. In his own words Miller championed that integrated photonics would "facilitate isolating the laser circuit assembly from thermal, mechanical, and acoustic ambient changes through small overall size" [100]. He also recognized its application to nonlinear optics due to the strong confinement of microphotonic waveguides "giving relatively high fields and low absolute power levels... [and] it would be feasible to have long interaction lengths not feasible in unguided beams"[101]. If we include the additional benefits of low-cost and high-yield to Miller's stability and strong confinement, we now have the motivations behind essentially all integrated photonic devices today.

Silicon photonics became a mainstream technology at the beginning of the 21st century when corporations began taking interest, with the noteworthy demonstration by Intel of the first GHz speed silicon modulator [87]. Silicon photonics processes support high-performance classical devices such as filters [117, 161, 109], switches [156, 79], and delay lines [97, 74, 80]. Recently, monolithic

integration of classical photonics in commercial CMOS processes has been pursued in the context of enabling energy efficient optical interconnects between processors and memory [9] resulting in the demonstration of a chip-to-chip optical link [139] and the first single chip microprocessor to communicate directly using light [141].

1.4 Silicon quantum photonics

Quantum photonics experiments tend to involve large numbers of optical components and can easily span multiple optical tables. Linear optical quantum computing specifically entails the use of millions of photonic components necessitating the implementation of such a system in an integrated platform [126]. Less ambitious, but still useful, applications such as the construction of an “on-demand” single photon source which multiplexes many photon pair sources [98] could benefit from the scalability of on-chip photonics.

The prospect of building many photon pair sources led to Lin and Agrawal’s 2006 proposal of using spontaneous four-wave mixing in a high-index contrast silicon waveguide [83] to generate photon pairs on-chip. Within that same year, Sharping *et al.* demonstrated the first silicon waveguide photon pair source [134]. After many more demonstrations of photon pairs from silicon waveguides [144, 56, 162, 95], sources were made even smaller and more efficient through the use of coupled resonator optical waveguides [27, 96] and microresonators [23, 8, 35]. Recently, time-energy [144, 56, 143, 53, 142, 159, 124] and polarization entanglement [95, 142] have both been shown between photon pairs generated in silicon sources. Systems have continued to scale to include on-chip interference between multiple integrated photon sources [135, 136], demultiplexing of signal and idler photons [77, 25], and multi-chip high-extinction pump rejection [57, 114].

While size and scalability are attractive features of the silicon photonic platform, the stability provided by a monolithic solid state material also provides many advantages to quantum photonic systems. To maintain stability, having a source is necessary but not sufficient. On-chip detectors are also required such that the photons are generated and detected without ever leaving the chip and are then not subject to air currents in free space propagation or temperature and strain fluctuations

in optical fiber. Superconducting nanowire single photon detectors have been implemented in both silicon [113, 103] and silicon nitride waveguides [129]. An added advantage of having an all on-chip quantum photonic circuit is that the entire chip would be placed at cryogenic temperatures (to ensure operation of the superconducting nanowire detectors) and therefore would be shielded from room temperature blackbody radiation which is typically the dominant background source when using superconducting detectors to measure single photons [94].

1.5 Outline of thesis

In this thesis we explore the theoretical development and experimental investigation of small footprint and low-power quantum nonlinear sources of light which can be fabricated using standard microelectronics processing techniques enabling ultra-large scale quantum photonic systems able to support the rapid growth of quantum information technologies such as quantum computing and quantum communication.

In Chapter 2, the theoretical background of integrated photonics and the important concepts in the design of photonic devices are presented. The physical concepts of electromagnetic propagation and dispersion are presented. We also introduce the tool box of components available in the silicon photonic platform, including waveguides, directional couplers, and ring resonators. We then introduce the coupling of modes in time formalism which most of the resonant analysis of sources is described by in this thesis.

In Chapter 3, we introduce nonlinear optics and specifically the four-wave mixing process. We discuss the intrinsic challenges which dispersion presents by looking at the simple case of classical four-wave mixing in a waveguide geometry. Following the methods established in Chapter 1, we build the waveguides into resonator devices demonstrating the improved efficiency and footprint provided by these devices while analyzing the additional design constraints they introduce. We describe the resonant four-wave mixing process using both transfer matrix and coupling in modes in time analysis and compare and contrast the results. We next present a discrete resonance dispersion engineering technique for designing efficient four-wave mixing resonators. We next propose and

demonstrate four-wave mixing in dual coupled cavity configuration where dispersion can be actively tuned to phase match the nonlinear process.

In Chapter 4, we theoretically explore the production of photon pairs through the spontaneous four-wave mixing process using a quantized coupling of modes in time model. We then experimentally demonstrate the first photon pair source fabricated within a commercial CMOS process on the same wafer as billions of electronic transistors. Here we show that classical four-wave mixing experiments can be used to accurately predict the efficiency of the spontaneous four-wave mixing process.

In Chapter 5, we study the noise properties present in on-chip silicon photon pair sources and specifically discuss the contribution of excess pump accompanying the pairs to the single photon detectors. We demonstrate the first single chip system of photon pair source with monolithic pump rejection and measure a pump extinction of over 95 dB. In addition to a coincidences-to-accidentals ratio, we measure the time-energy entanglement of the photons to establish the sufficient enough of pump filtering for multiple applications.

Chapter 6 investigates the application and implementation of engineering the resonance linewidths of photon pair sources. Methods for increasing efficiency, reducing losses, and engineering photon frequency correlations are shown. In addition, the concept is extended to the classical regime in the proposal of a novel “dark state” laser configuration.

Chapter 7 concludes the thesis and summarizes the results found through the research comprising it. We establish potential future work than can be built off of the work presented here and give a general overview of the current state of the field.

Chapter 2

Principles of integrated photonics and quantum optics

This chapter will provide the theoretical background as well as establish the conventions and notation used in the thesis. I debated whether this information was necessary for a chapter of its own as I have made it here or whether it should be a series of appendices referred to throughout the thesis. In the end, the consideration of who the likely audience to be reading this thesis convinced me to include this theoretical background as its own chapter. Since the work of this thesis refers both to optoelectronic engineering principles likely to have been studied by photonics engineers and also quantum optical concepts likely only to have been thoroughly studied by physicists, this chapter, while far from comprehensive, is intended to provide the needed background to readers from one of these communities.

2.1 Maxwell's equations

Maxwell's equations are the backbone describing of all the physics of electromagnetic radiation. In integrated photonics, and specifically using high-index contrast waveguides, rigorous simulation of Maxwell's equations is essential to the design and characterization of high-performance devices. These equations describe how time varying magnetic fields $\vec{B}(\vec{r}, t)$ generate electric fields

$\vec{E}(\vec{r}, t)$ and vice versa. In isotropic media, the macroscopic equations can be written as

Faraday's Law:

$$\nabla \times \vec{E}(\vec{r}, t) = -\frac{\partial}{\partial t} \vec{B}(\vec{r}, t) \quad (2.1)$$

Ampere's Law:

$$\nabla \times \vec{H}(\vec{r}, t) = \frac{\partial}{\partial t} \vec{D}(\vec{r}, t) \quad (2.2)$$

Gauss's Law for the Electric Field:

$$\nabla \cdot \vec{D}(\vec{r}, t) = 0 \quad (2.3)$$

Gauss's Law for the Magnetic Field:

$$\nabla \cdot \vec{B}(\vec{r}, t) = 0 \quad (2.4)$$

where the electric displacement field $\vec{D}(\vec{r}, t)$ is related to the dielectric polarization density $\vec{P}(\vec{r}, t)$ and the electric field by

$$\vec{D}(\vec{r}, t) = \epsilon_0 \vec{E}(\vec{r}, t) + \vec{P}(\vec{r}, t). \quad (2.5)$$

Here, ϵ_0 is the permittivity of free space related to the permeability of free space μ_0 , defined (in SI units) as

$$\mu_0 = 4\pi \times 10^{-7} \text{ V} \cdot \text{s}/(\text{A} \cdot \text{m}) \quad (2.6)$$

and the speed of light in a vacuum $c = 299\,792\,458 \text{ m/s}$ by the equation

$$\epsilon_0 = 1/(\mu_0 c^2) \approx 8.854 \times 10^{-12} \text{ A} \cdot \text{s}/(\text{V} \cdot \text{m}). \quad (2.7)$$

In general, $\vec{B}(\vec{r}, t) = \mu_0 \vec{H}(\vec{r}, t) + \vec{M}(\vec{r}, t)$, however in the scope of this thesis we will work strictly with nonmagnetic media allowing us to take the magnetization density $\vec{M}(\vec{r}, t) \rightarrow 0$ and $\vec{B}(\vec{r}, t) = \mu_0 \vec{H}(\vec{r}, t)$.

Since optical frequencies cycle at much faster time scales than typically experienced in everyday life, we are often interested in the so-called “steady state” behavior of many optical processes. In addition, there is a large availability of high performance lasers providing nearly single frequency light sources, making it convenient to work in the frequency domain in many situations.

The frequency domain fields are related to the time domain fields by a Fourier transform

$$\vec{\mathbf{E}}(\vec{r}, \omega) = \frac{1}{\sqrt{2\pi}} \int_{-\infty}^{\infty} \vec{E}(\vec{r}, t) e^{i\omega t} dt \quad (2.8)$$

with corresponding inverse Fourier transform

$$\vec{E}(\vec{r}, t) = \frac{1}{\sqrt{2\pi}} \int_{-\infty}^{\infty} \vec{\mathbf{E}}(\vec{r}, \omega) e^{-i\omega t} d\omega, \quad (2.9)$$

where we use a bold vector for the frequency domain representation to emphasize that the fields are, in general, complex numbers. The unitary form of the Fourier and inverse Fourier transform are used for aesthetic reasons to maintain a unitary transformation on L^2 and to preserve the symmetry between the two transformations. At relatively low optical intensities we can make the assumption that the polarizability in the frequency domain $\vec{\mathbf{P}}(\omega, t)$ is linear with respect to electric field such that

$$\vec{\mathbf{P}}(\vec{r}, \omega) = \epsilon_0 \chi^{(1)}(\vec{r}, \omega) \vec{\mathbf{E}}(\vec{r}, \omega), \quad (2.10)$$

where $\chi^{(1)}$ is the linear electric susceptibility. In the next chapter we will see that this is not always the case and specifically engineering structures and applying high enough optical powers where this assumption does not hold is essential to the work presented in this thesis. For monochromatic light at a specific vacuum wavelength λ_0 with radial frequency $\omega = 2\pi c/\lambda_0$, Maxwell's equations in a linear isotropic medium can now be written as

Faraday's Law:

$$\nabla \times \vec{\mathbf{E}}(\vec{r}, \omega) = i\omega\mu_0 \vec{\mathbf{H}}(\vec{r}, \omega) \quad (2.11)$$

Ampere's Law:

$$\nabla \times \vec{\mathbf{H}}(\vec{r}, \omega) = -i\omega\epsilon(\vec{r}, \omega) \vec{\mathbf{E}}(\vec{r}, \omega) \quad (2.12)$$

Gauss's Law for the Electric Field:

$$\nabla \cdot \epsilon(\vec{r}, \omega) \vec{\mathbf{E}}(\vec{r}, \omega) = 0 \quad (2.13)$$

Gauss's Law for the Magnetic Field:

$$\nabla \cdot \mu_0 \vec{\mathbf{H}}(\vec{r}, \omega) = 0 \quad (2.14)$$

We chose to represent the magnetic field using the “H-Field” rather than the “B-Field” out of aesthetic preference for the symmetry seen between equations above. The spatial dependence of $\epsilon(\vec{r}, \omega)$ describes a distribution of optical materials which we can characterize by their refractive indices $n(\vec{r}, \omega)$, a measure of the speed of a light wave within a large homogeneous sample of that material, defined such that $\epsilon(\vec{r}, \omega) = n^2(\vec{r}, \omega)\epsilon_0$. In general, a propagating light wave will span more than two materials often requiring a rigorous solution of Maxwell’s equation to find the corresponding wave velocity.

2.2 Dielectric waveguides and their guided modes

A particularly advantageous distribution of refractive indices occurs when we surround a higher index material, referred to as the “core”, by materials of lower index, referred to as “cladding.” This allows light to be guided in the structure through total internal reflection, thereby resulting in a device referred to as a “dielectric waveguide”. A strip waveguide, illustrated in Fig. 2.1, can be readily fabricated on-chip through standard CMOS fabrication techniques. Such a waveguide relies on a higher index of refraction core of silicon ($n_{\text{si}} \approx 3.48$ at 1550 nm) on top of a slab of lower index thermal silicon oxide ($n_{\text{si}} \approx 1.45$ at 1550 nm), which along with air acts as the cladding. Often an upper cladding is deposited to isolate the waveguide from the air and protect the structure from water vapor, dust, or other contaminants which could alter the waveguide’s designed properties.

Consider a dielectric distribution which only varies in two cartesian directions (we will refer to as the x - y plane) but is invariant in one direction which we want to transmit light and will refer to, by convention, as z . Since, the z -direction is special in the case we are considering, we can reformulate the Maxwell curl equations (Eq. 2.1 and Eq. 2.2) to have all the z operations on one side of the equation as so:

$$\frac{\partial}{\partial z} \begin{pmatrix} 0 & -\hat{z} \times \\ \hat{z} \times & 0 \end{pmatrix} \begin{pmatrix} \vec{E} \\ \vec{H} \end{pmatrix} = \begin{pmatrix} 0 & \nabla_t \times \\ -\nabla_t \times & 0 \end{pmatrix} \begin{pmatrix} \vec{E} \\ \vec{H} \end{pmatrix} - \frac{\partial}{\partial t} \left[\begin{pmatrix} \epsilon_0 & 0 \\ 0 & \mu_0 \end{pmatrix} \begin{pmatrix} \vec{E} \\ \vec{H} \end{pmatrix} + \begin{pmatrix} \vec{P} \\ 0 \end{pmatrix} \right]. \quad (2.15)$$

Here, we define a transverse differential vector operator ∇_t such that it is related to the familiar

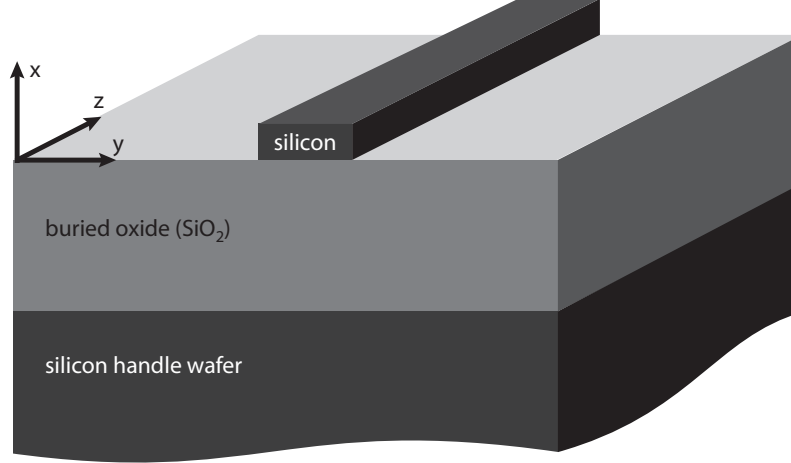


Figure 2.1: Example cross-sectional schematic of an air-cladded strip waveguide fabricated from a silicon-on-insulator wafer. The higher refractive index of the silicon waveguide compared to the air and buried oxide allows the guidance of light on chip through total internal reflection. The buried oxide is typically greater than $1.5 \mu\text{m}$ thick preventing light from leaking from the silicon waveguide to the support silicon handle wafer.

nabla operator by $\nabla = \nabla_{\text{t}} + \frac{\partial}{\partial z} \hat{z}$. The transverse curl can be written in cartesian coordinates as

$$\nabla_{\text{t}} \times \equiv \begin{pmatrix} 0 & 0 & \frac{\partial}{\partial y} \\ 0 & 0 & -\frac{\partial}{\partial x} \\ -\frac{\partial}{\partial y} & \frac{\partial}{\partial x} & 0 \end{pmatrix}. \quad (2.16)$$

In Eq. 2.15, we have explicitly included the polarizability \vec{P} to allow for the inclusion of nonlinear optical effects in subsequent chapters. For now we can assume the dielectric materials comprising the waveguide are isotropic and linear (see Eq. 2.10), so that moving to the frequency domain and multiplying by $-i$ gives

$$-i \frac{\partial}{\partial z} \begin{pmatrix} 0 & -\hat{z} \times \\ \hat{z} \times & 0 \end{pmatrix} \begin{pmatrix} \vec{\mathbf{E}} \\ \vec{\mathbf{H}} \end{pmatrix} = \begin{pmatrix} \omega \epsilon(\vec{r}, \omega) & -i \nabla_{\text{t}} \times \\ i \nabla_{\text{t}} \times & \omega \mu_{\text{o}} \end{pmatrix} \begin{pmatrix} \vec{\mathbf{E}} \\ \vec{\mathbf{H}} \end{pmatrix}. \quad (2.17)$$

We can expand the total guided electric field into a summation of normal modes with each mode having a dependence in z by a complex exponential, such that

$$\vec{\mathbf{E}}(\vec{r}, \omega) = \sum_j a_j \vec{\mathbf{e}}_j(x, y; \omega) e^{i\beta_j z}. \quad (2.18)$$

β_j is referred to as a propagation constant for the j -th mode and describes the spatial frequency at which the mode acquires phase in the guided direction. Inserting Eq. 2.18 into Eq. 2.17, we obtain the generalized eigenvalue equation

$$\begin{pmatrix} \omega\epsilon(\vec{r}, \omega) & -i\nabla_t \times \\ i\nabla_t \times & \omega\mu_o \end{pmatrix} \begin{pmatrix} \vec{\mathbf{e}}_j \\ \vec{\mathbf{h}}_j \end{pmatrix} = \beta_j \begin{pmatrix} 0 & -\hat{z} \times \\ \hat{z} \times & 0 \end{pmatrix} \begin{pmatrix} \vec{\mathbf{e}}_j \\ \vec{\mathbf{h}}_j \end{pmatrix}. \quad (2.19)$$

While it is possible to formulate Maxwell's equations in a z -invariant medium as a standard eigenvalue problem, we have intentionally set up the generalized eigenvalue problem in Eq. 2.19 such that the two operators are self-adjoint (Hermitian) under the assumption that $\epsilon(\vec{r}, \omega)$ is real over the infinite cross-section A_∞ (i.e., all dielectrics comprising the waveguide are lossless). Using the properties of an eigenvalue problem constructed with self-adjoint operators [71], we can readily find the orthogonality condition

$$\begin{aligned} 4P_j \delta_{jk} &= \int_{A_\infty} \begin{pmatrix} \vec{\mathbf{e}}_k \\ \vec{\mathbf{h}}_k \end{pmatrix}^\dagger \begin{pmatrix} 0 & -\hat{z} \times \\ \hat{z} \times & 0 \end{pmatrix} \begin{pmatrix} \vec{\mathbf{e}}_j \\ \vec{\mathbf{h}}_j \end{pmatrix} da \\ &= \int_{A_\infty} (\vec{\mathbf{e}}_j \times \vec{\mathbf{h}}_k^* + \vec{\mathbf{e}}_k^* \times \vec{\mathbf{h}}_j) \cdot \hat{z} da \end{aligned} \quad (2.20)$$

where δ_{jk} is the Kronecker delta and P_j is a scalar constant representing the power flowing in mode j with fields $\{\vec{\mathbf{e}}_j, \vec{\mathbf{h}}_j\}$ in the \hat{z} direction. Note that if this were a homogeneous medium invariant in all directions, we could assign corresponding ‘‘propagation constants’’ in all three orthogonal directions and build up eigenmodes which are the familiar plane waves. Here, we only have the convenience of this simplification in the z -direction.

The formulation of the eigenvalue problem in Eq. 2.19 can help illuminate many features of guided waves including aiding the derivation of the strength of four-wave mixing-based frequency conversion in Chapter 3. However, when a numerical mode solver is implemented, one typically uses a simplified formulation where Eq. 2.19 can be reduced to only two polarization components of a single field (here we choose the electric) using Maxwell's divergence equations (Gauss's laws). Therefore, we expand out the modal field into a transverse component $\vec{\mathbf{e}}_t(x, y; \omega) = e_x(x, y; \omega)\hat{x} + e_y(x, y; \omega)\hat{y}$ and a longitudinal component $e_z(x, y; \omega)\hat{z}$ such that $\vec{\mathbf{e}}(x, y; \omega) = \vec{\mathbf{e}}_t(x, y; \omega) + e_z(x, y; \omega)\hat{z}$.

Meanwhile, the magnetic components are recoverable from Faraday's law. Here, we demonstrate that all the necessary information describing a mode can be determined by the transverse electric field and the propagation constant β (assuming we have already defined that the mode is propagating in the z -direction, as an equivalent mode travelling in the $-z$ -direction would have the same $\vec{\mathbf{e}}_t(x, y; \omega)$ profile with a negative corresponding transverse h -field). Eq. 2.19 can then be reduced to a standard eigenvalue equation with only two of the total field components [22]

$$\left[\nabla_t \frac{1}{\epsilon(x, y; \omega)} \nabla_t \cdot \epsilon(x, y; \omega) - \nabla_t \times \nabla_t \times + \omega^2 \mu_o \epsilon(x, y; \omega) \right] \vec{\mathbf{e}}_t(x, y; \omega) = \beta^2(\omega) \vec{\mathbf{e}}_t(x, y; \omega) \quad (2.21)$$

where $\vec{\mathbf{e}}_t(x, y; \omega)$ is explicitly written to include a null z -component as

$$\vec{\mathbf{e}}_t(x, y; \omega) \equiv \begin{pmatrix} e_x \\ e_y \\ 0 \end{pmatrix}. \quad (2.22)$$

The transverse gradient and divergence can be explicitly written as

$$\nabla_t \equiv \begin{pmatrix} \frac{\partial}{\partial x} \\ \frac{\partial}{\partial y} \\ 0 \end{pmatrix}, \quad \nabla_t \cdot \equiv \begin{pmatrix} \frac{\partial}{\partial x} & \frac{\partial}{\partial y} & 0 \end{pmatrix}. \quad (2.23)$$

In general, a rectangular dielectric waveguide, such as that shown in Fig. 2.1, will support a number of guided propagating modes. It is often convenient to describe the modes using an effective refractive index defined such that

$$n_{j,\text{eff}} = \beta_j \frac{c}{\omega} \quad (2.24)$$

where $v_{j,\text{phase}} = \frac{c}{n_{j,\text{eff}}}$ is the phase velocity of the particular mode, j . As an example, in Fig. 2.2 (a) we consider a standard 220 nm thick silicon strip buried within a silicon dioxide cladding and plot the effective indices of all guided modes over a range of waveguide widths using a finite-difference numerical mode solver [116]. In this geometry, we can classify the modes into two categories, quasi-transverse electric (TE) where the majority of the electric field is parallel to the surface of the chip and quasi-transverse magnetic (TM) where the majority of the magnetic field is parallel to the

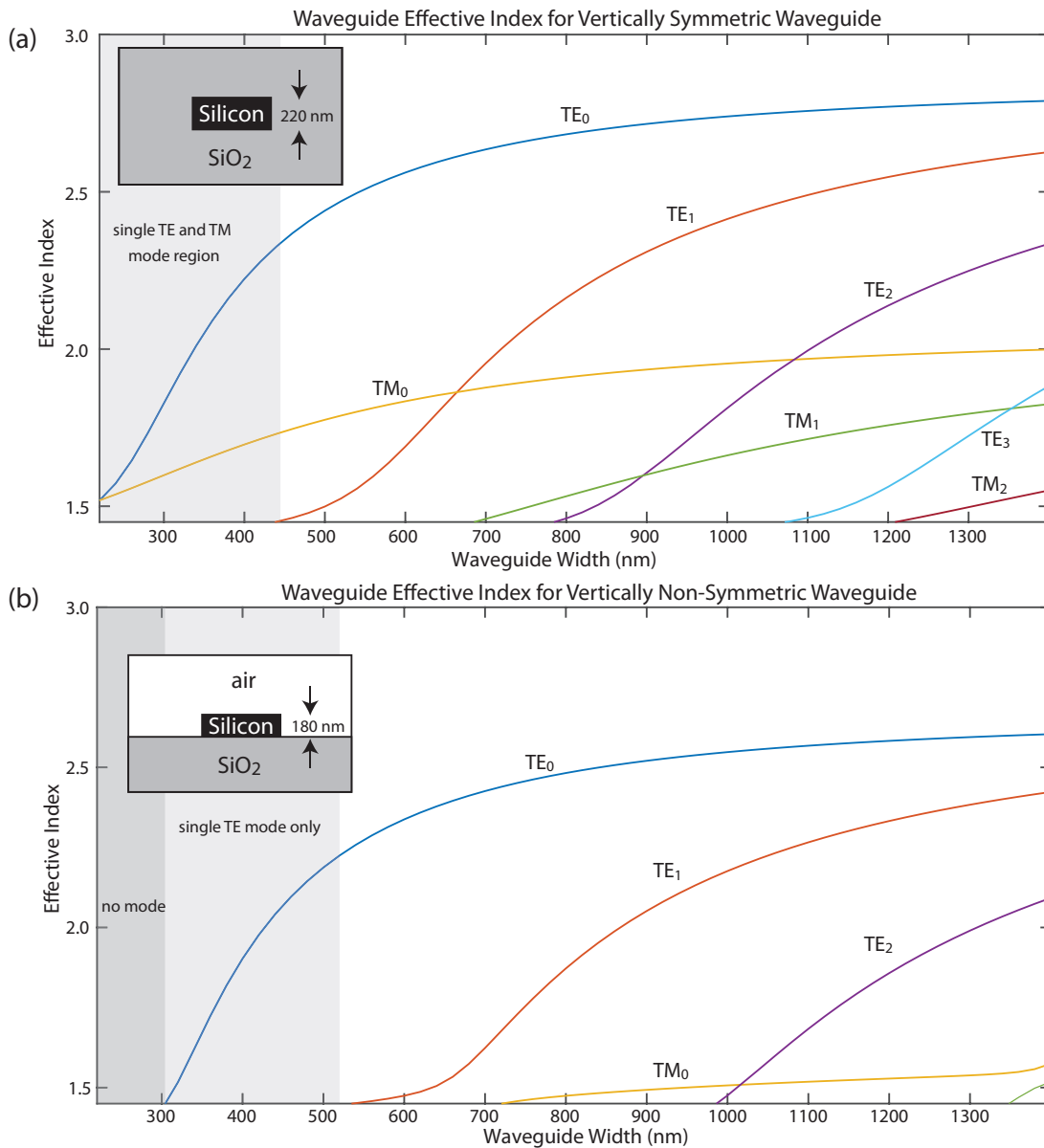


Figure 2.2: Mode effective indices at a wavelength of 1550nm versus waveguide width for the waveguide dielectric distributions illustrated in the insets for (a) a vertically symmetric waveguide displaying both quasi-transverse electric (TE) and quasi-transverse magnetic (TM) modes at all widths and a (b) vertically non-symmetric waveguide displaying a cutoff width near 520 nm where only a single TE mode is guided

surface of the chip. If the thickness (dimension out of the plane of the structure) is smaller than the width of the waveguide, the boundary conditions of Maxwell's equations necessarily require a TM mode to have a lower effective index than the corresponding TE mode of the same order. Below

a certain waveguide width [≈ 450 nm in the example considered in Fig. 2.2 (a)], the waveguide can support only a single TE and single TM mode. We refer to this width as the single-mode cutoff width. It is important to note that since the waveguide is symmetric across a horizontal axis and vertical axis, it will always support these two modes [93]. If instead we want to ensure there is truly only a single optical mode at a given frequency, we can break the symmetry across the horizontal axis, for instance by using air-cladding on the top section of the waveguide, as shown in Fig. 2.2 (b), where the waveguide is now only 180 nm thick. As we can see in the figure, below a cutoff width around 530 nm, there is only a single TE mode. In Chapter 5, we will find that using a geometry similar to this, where there are no guided TM modes, will be advantageous for ultra-high extinction wavelength filtering.

By simply restricting the geometry to widths below the single mode cutoff we can permit the waveguide to a single mode which we can then use to route light around a chip while only acquiring phase $e^{i\beta z}$ along the way. If the geometry of the waveguide varies slowly along z we can approximate the total effect as only a phase progression given by $e^{i \int_0^z \beta(z') dz'}$. In reality waveguides are not perfectly invariant in the z direction and will often have small fluctuations in width due to imperfections in fabrication referred. Typically, the largest perturbations to a the waveguide's geometry are on the sidewalls which are defined by lithography, giving the structure a "sidewall roughness." The top and bottom surfaces are usually much smoother in comparison, as they are often planarized using chemical mechanical polishing during wafer fabrication. Sidewall roughness can scatter power from the fundamental mode to non-guided (radiation) modes resulting in loss as light propagates down the waveguide. Assuming that this loss per unit length is approximately uniform and also consistent across the chip, as it typically is in practice (at least for a given waveguide width), we can model this scattering loss as an imaginary part of the propagation constant $\beta_{\text{complex}} = \beta + i\alpha$. This way we can keep track of only a single amplitude $A(z)$, normalized such that $|A(z)|^2$ is the optical power for a single mode as it propagate through a waveguide. When exploring effects intrinsically sensitive to phase such as the interference between two or more optical modes, we will implicitly include the phase progression in the amplitude and will

notationally distinguish this amplitude by using a lowercase letter such that $a(z) = A(z)e^{i\beta z}$.

Fig. 2.3 illustrates how we model a mode in an ideal lossless waveguide propagates compared to

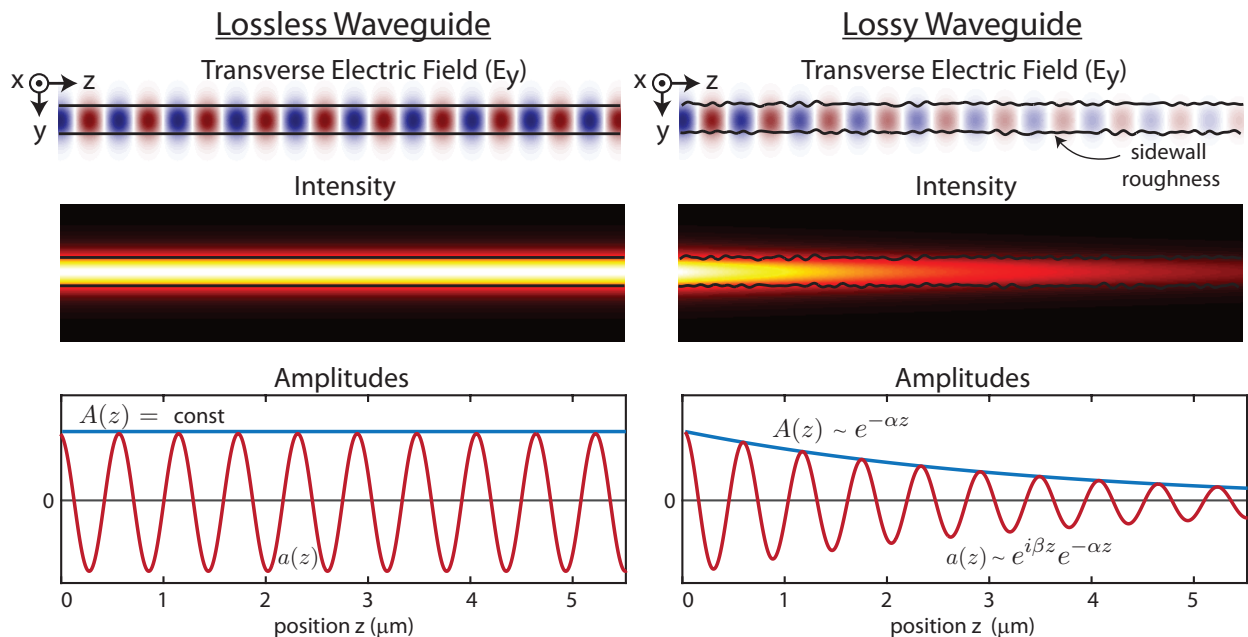


Figure 2.3: Schematic comparison of a guided mode in an ideal lossless waveguide and a lossy waveguide illustrated using rough sidewalls and modeled using a complex propagation constant. The loss is greatly exaggerated to illustrate the decay of power amplitude along the propagation direction z . Note that this approximation ignores optical powers after it has left the guided mode and assumes all scattering due to roughness is perfectly uniform.

that of a fairly lossy waveguide. In practice, the loss in a waveguide mode is negligible over the handful of optical periods illustrated in the figure and will typically be experienced after thousands of optical cycles using standard silicon processing techniques today. Note that in Fig. 2.3, after the attenuation of the guided mode is considered, the power scattered into radiation modes is ignored when using a complex propagation constant. This model is necessarily **not** power conserving and is phenomenologically equivalent to a waveguide with absorption.

2.3 Dispersion

In free space, light of all frequencies travels at 299 792 458 m/s. However, when propagating through a dielectric medium, electromagnetic waves of different frequencies can travel at different

velocities. If we consider a pulse centered around a particular frequency as shown in Fig. 2.4, the longer wavelengths of light often propagate faster resulting in the pulse width widening and the instantaneous frequency becoming chirped. We refer to this effect as dispersion, since the pulse becomes dispersed as it propagates. The particular case in which the longer wavelengths travel faster is often referred to as “normal” dispersion, while a situation where longer wavelengths travel slower is referred to as “anomalous dispersion.” Since nonlinear optical sources generally involve the interaction of multiple frequencies of light, dispersion becomes an important property to consider in their design and implementation.

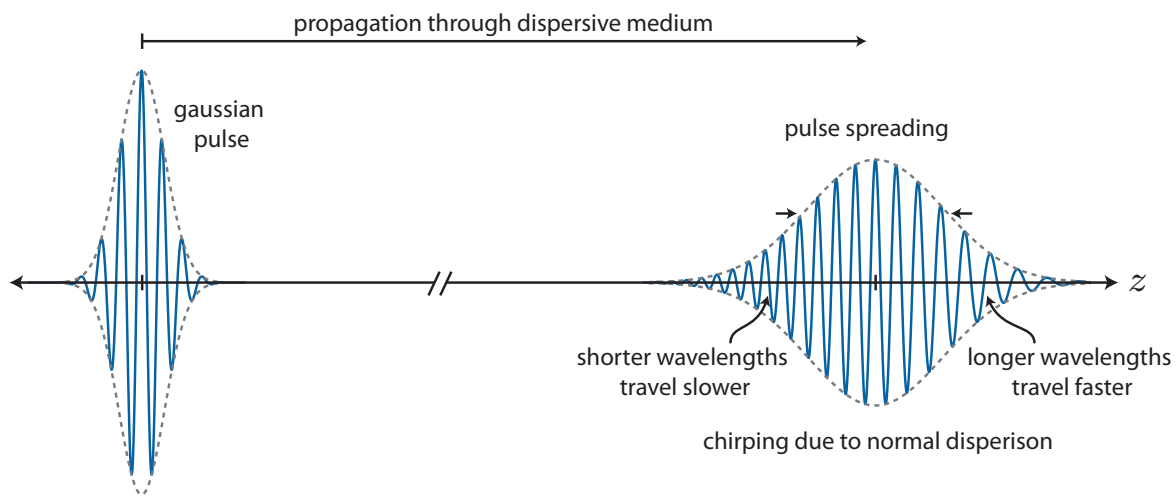


Figure 2.4: Illustration of a Gaussian pulse before and after propagation, displaying how a dispersive medium can cause pulse spreading and chirping.

2.3.1 Material dispersion

In a homogeneous medium, dispersion is a direct result of the frequency dependence of the electric permittivity $\epsilon(\vec{r}, \omega)$. In the time domain, this manifests as a non-instantaneous response of the electric polarizability of a medium to an applied electric field. In a linear isotropic material, this can be described by the convolution of an electric susceptibility $\chi^{(1)}(\vec{r}, t)$ with the electric field

at prior times, i.e.

$$\vec{P}(\vec{r}, t) = \epsilon_0 \int_{-\infty}^t \chi^{(1)}(\vec{r}, t - t') \vec{E}(\vec{r}, t') dt'. \quad (2.25)$$

From the convolution theorem, the polarizability in the frequency domain is

$$\vec{P}(\vec{r}, \omega) = \epsilon_0 \chi^{(1)}(\vec{r}, \omega) \vec{E}(\vec{r}, \omega). \quad (2.26)$$

As a result, the refractive index is also a function of frequency $n(\omega) = \sqrt{\epsilon(\omega)/\epsilon_0}$. In Fig. 2.5 we plot the measured refractive index of crystalline silicon from a sample of sources from the literature [54, 66, 111, 39, 127, 119, 147] over wavelengths ranging from $1.2 \mu\text{m}$ to $1.9 \mu\text{m}$. Due to the advanced performance requirements of modern microelectronic devices, crystalline silicon is produced at extremely high purity, resulting in reasonably consistent refractive index and dispersion properties between separate samples. For example, Fig. 2.5 shows that there is an uncertainty in refractive index of approximately 0.0025, which at a refractive index of ≈ 3.48 at $1.55 \mu\text{m}$ is less than 0.1%, which is typically much lower than the uncertainty in the parameters of a waveguide's geometry. For all other optical materials considered in this thesis, this degree of certainty in refractive index will not be available as there are many different types and methods of production of amorphous material such as silica (SiO_2) and silicon nitride (SiN).

2.3.2 Dispersion in a single mode waveguide

As we have seen in the case of a dielectric waveguide, in general, the refractive index “experienced” by an optical mode in an integrated photonic device will not be homogeneous, but will be a distribution across various positions \vec{r} such that $n(\vec{r}, \omega) = \sqrt{\epsilon(\vec{r}, \omega)/\epsilon_0}$. While the dispersion of each individual dielectric material contributes to the overall dispersion of an optical mode, there is an additional contribution resulting from a waveguide mode's tendency to change shape with frequency. Guided modes in integrated optics rely on the principle of total internal reflection, where light within a material with higher refractive index completely reflects off a boundary with a lower index. Due to the boundary conditions defined by Maxwell's equations there is an evanescent (exponentially decaying) field extending into the lower index material (cladding). Since the photonic

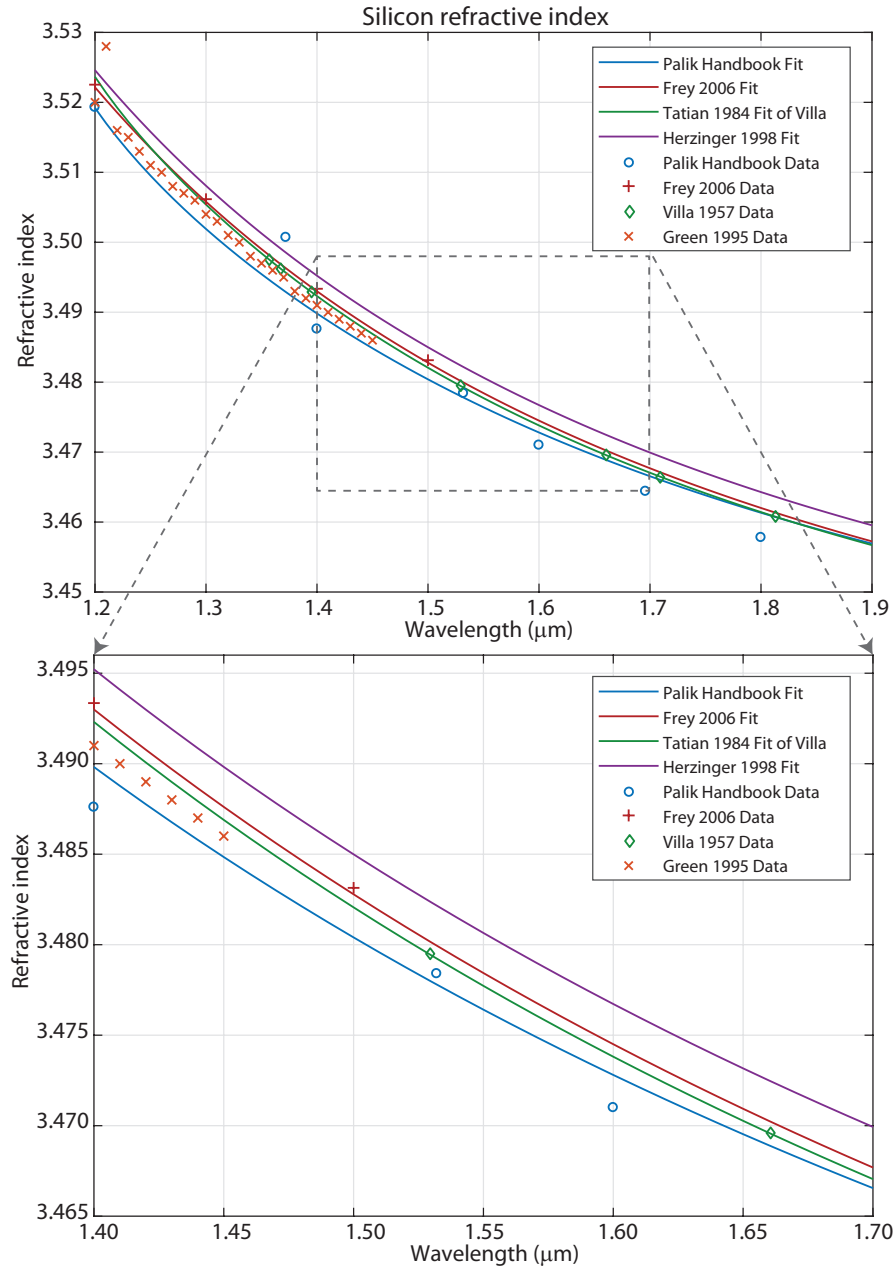


Figure 2.5: Refractive index of crystalline silicon, n_{si} , measured by various literature sources [54, 66, 111, 39, 127, 119, 147], demonstrating normal dispersion (i.e., $\frac{d}{d\lambda}n_{\text{si}} < 0$) across the entire wavelength range. All refractive indices for silicon in this thesis use the Palik Handbook Fit [111].

devices of interest are often fabricated to a scale much smaller than the wavelength, a significant portion of a mode experiences both the core material and the cladding material. For instance, a shorter wavelength mode could be more confined within the core compared to a longer wavelength

mode, resulting in an effective dispersion.

The dispersion in a straight waveguide can be characterized by a mode's propagation constant dependence on angular frequency ω . It is common to Taylor series expand β with respect to a frequency we will call ω_p (where 'p' will represent the 'pump' in future chapters) to the second order:

$$\begin{aligned}\beta(\omega) &= \sum_{n=0}^{\infty} \frac{1}{n!} \left. \frac{\partial^n \beta}{\partial \omega^n} \right|_{\omega_p} (\omega - \omega_p)^n \\ &\approx \beta \Big|_{\omega_p} + \left. \frac{\partial \beta}{\partial \omega} \right|_{\omega_p} (\omega - \omega_p) + \frac{1}{2} \left. \frac{\partial^2 \beta}{\partial \omega^2} \right|_{\omega_p} (\omega - \omega_p)^2.\end{aligned}\quad (2.27)$$

The term $\frac{\partial^2 \beta}{\partial \omega^2}$ is often called the group velocity dispersion (GVD) as it is the first derivative of the inverse of the group velocity, i.e, $\text{GVD} \equiv \frac{\partial}{\partial \omega} \left(\frac{1}{v_g} \right)$. The wavelength at which it is zero is therefore referred to as the zero group velocity dispersion (ZGVD) wavelength. It is important to note that this is not necessarily a wavelength where the group velocity does not depend on frequency, since there could potentially be non-zero higher order dispersion terms. In optical fiber, this effect is sometimes instead described by a dispersion parameter, D , which is related to the GVD as $D = -\frac{2\pi c}{\lambda^2} \text{GVD}$ [4]. The dispersion parameter is often expressed in units of ps/(nm km) to signify how separated in time (in picoseconds) pulses at wavelengths differing by 1 nm will be after propagating 1 km.

It is interesting to note that modal dispersion will be present even if the individual materials used were not dispersive. As an example, we show the dielectric cross-section for a single mode air-cladded waveguide on a buried oxide in Fig. 2.6. Included is the mode profile for the fundamental mode at the center of the O-band (1310 nm) and center of the C-band (1550 nm). Of course this wavelength range is much larger than what is typically explored for a particular device, but it accurately illustrates how a waveguide mode can "experience" a different proportion of the cladding material at different wavelengths. This effect allows a waveguide mode to have an effective modal dispersion even if all the dielectrics have zero dispersion.

We have noted that there are two contributors to waveguide dispersion: modal and material. It is interesting to explore which, if either, of these effects dominates the other. In Fig. 2.7 we have

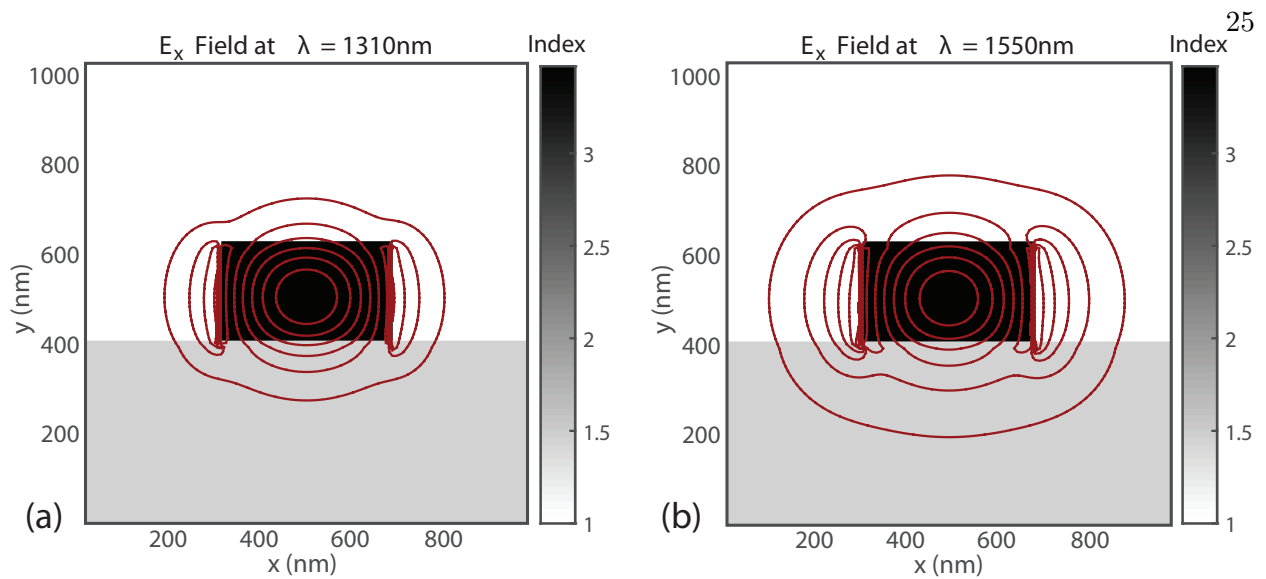


Figure 2.6: Fundamental mode for a 380 nm wide, 220 nm thick air-cladded waveguide on oxide for the O-band and C-Band. Note how the mode shape changes causing it to “experience” more of the cladding at the longer wavelength resulting in a lower effective index. We refer to the dependence of effective index on wavelength as “modal dispersion.”

plotted both the group index and the group velocity dispersion versus wavelength for the same waveguide geometry used in in Fig. 2.6 but with and without including material dispersion. When material dispersion is included, the ZGVD wavelength shifts over 75 nm in wavelength, making it evident that both contributing factors to dispersion in a single-mode waveguide are imperative to consider when designing a device.

2.4 Directional couplers

Waveguides are convenient for transporting light around a chip and for maintaining a small modal shape and thereby permitting higher intensities over larger distances compared to bulk optical systems. In order to “distribute” light from one waveguide to additional waveguides we need multi-port couplers. A fairly simple method for coupling a fraction of light from one waveguide to another operates based on “dragging” the evanescent field from the mode of one waveguide through the other. Fig. 2.8 shows how this can be done to create a 4-port device. We can often make these 4-port devices in a manner in which the ports have negligible amounts of reflection, reducing them

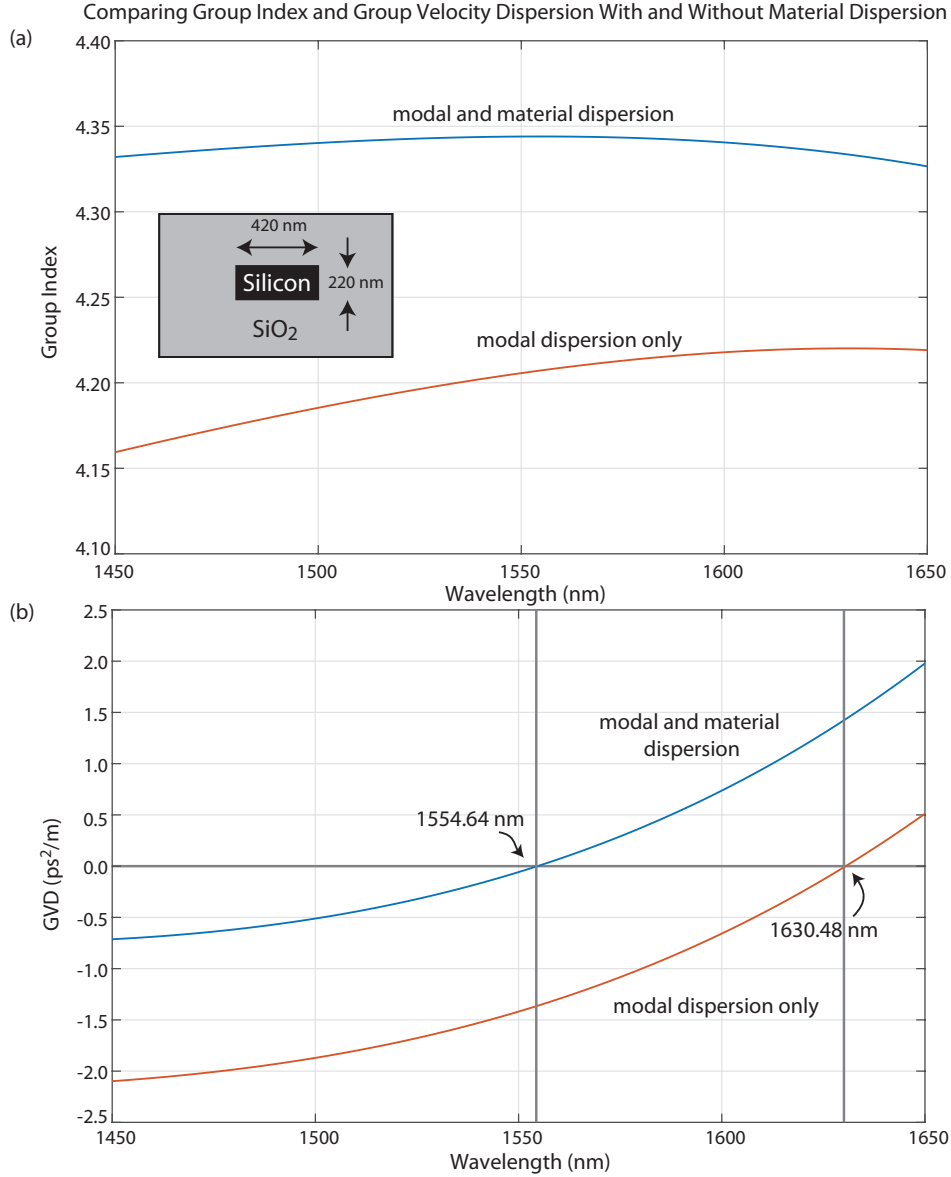


Figure 2.7: (a) Group index of an oxide cladded silicon waveguide of dimensions 220 nm by 420 nm versus wavelength where both modal and material dispersion are used and where only modal dispersion is assumed (using the refractive indices at 1550 nm). (b) Similar plot for the group velocity dispersion (GVD) showing that the zero group velocity dispersion wavelength is significantly affected by the inclusion of material dispersion.

to an equivalent 2-port device [118].

We can describe the transmission matrix (T-matrix) of this device by a matrix transformation $\bar{\bar{\mathbf{T}}}$, of the input field amplitudes a_1 and a_2 and corresponding output amplitudes b_1 and b_2 such

that

$$\vec{b} = \bar{\mathbf{T}}\vec{a}$$

$$\begin{bmatrix} b_1 \\ b_2 \end{bmatrix} = \begin{bmatrix} t_{11} & t_{12} \\ t_{21} & t_{22} \end{bmatrix} \begin{bmatrix} a_1 \\ a_2 \end{bmatrix}. \quad (2.28)$$

If the directional coupler is symmetric about a horizontal axis, like the one depicted in Fig. 2.8 and also power conserving (i.e., light only leaves through the defined output ports) we can reduce

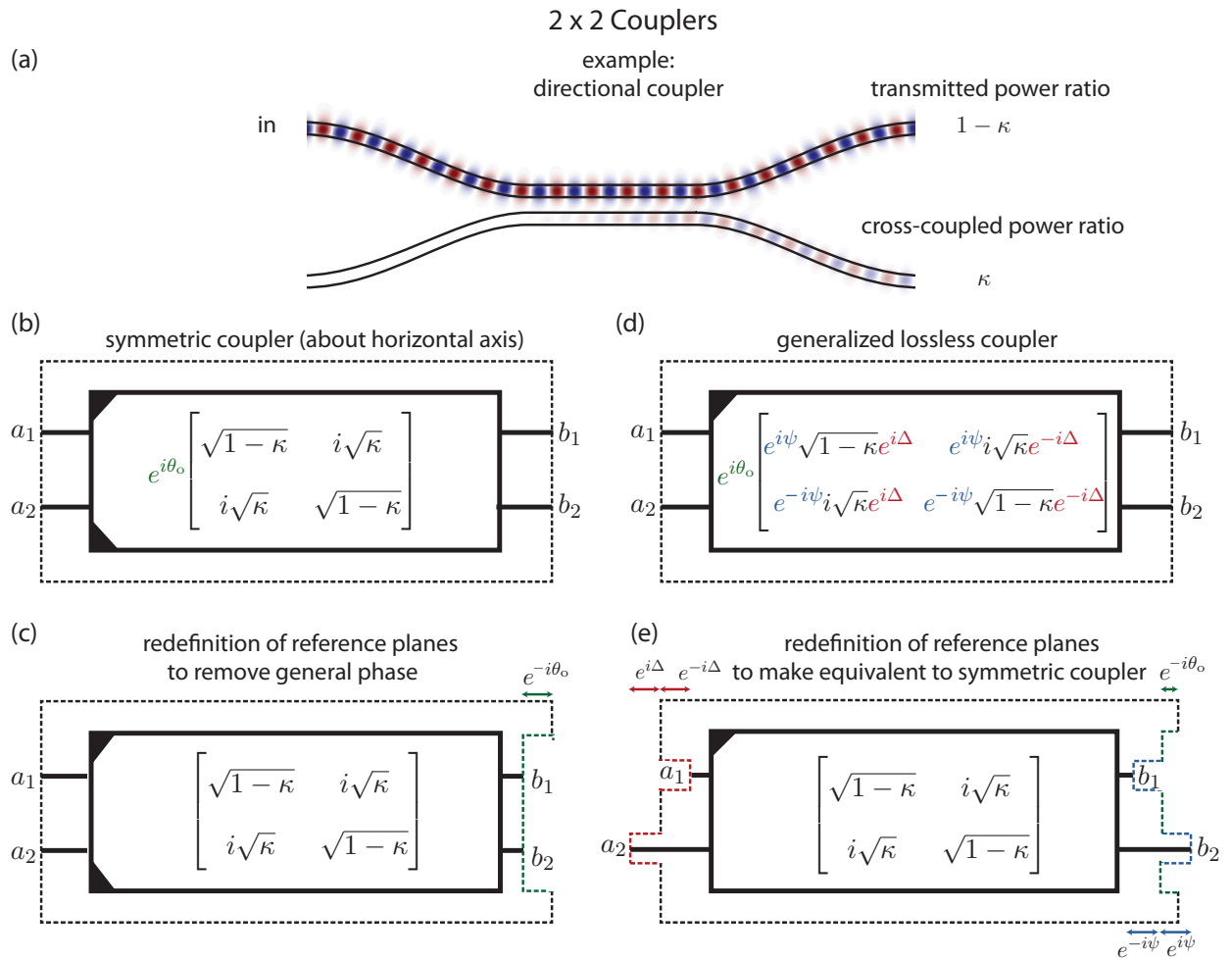


Figure 2.8: (a) Illustration of a lossless directional coupler allowing the distribution of power from one waveguide to two. (b) Schematic and form of the T-matrix for a 2x2 coupler which is symmetric about the horizontal axis with (c) demonstrating that shift in reference planes can remove the global phase θ_0 . (d) represents a generalized lossless coupler with corresponding reference plane shifts (e) allowing it be define equivalently to the symmetric coupler.

the matrix down to the form [118]

$$\vec{b} = \bar{\bar{\mathbf{T}}}_{\text{sym}} \vec{a}$$

$$\begin{bmatrix} b_1 \\ b_2 \end{bmatrix} = e^{i\theta_o} \begin{bmatrix} \sqrt{1-\kappa} & i\sqrt{\kappa} \\ i\sqrt{\kappa} & \sqrt{1-\kappa} \end{bmatrix} \begin{bmatrix} a_1 \\ a_2 \end{bmatrix}, \quad (2.29)$$

where κ is the power cross-coupling ratio from input port 1 to output port 2 (due to symmetry, also the ratio from input port 2 to output port 1) and θ_o is a global phase. A convenient result of formulating a coupler in this manner is that a $\pi/2$ phase shift for the light cross-coupled is explicitly revealed in the off diagonal components of the matrix (i.e., $i = e^{i\pi/2}$).

While Eq. 2.29 specifically describes a lossless coupler with symmetry across a horizontal axis, it can also be used as a convention for any lossless 2-by-2 coupler with properly chosen reference planes. For instance, consider a generalized coupler where we only assume power conservation, reducing the degrees of freedom in the transmission matrix from 8 real numbers (4 complex numbers) down to 5. We can now reformulate the matrix, $\bar{\bar{\mathbf{T}}}_{\text{gen}}$, in a way that explicitly depicts additional phases described by ψ and Δ , which distinguish it from the matrix of the symmetric coupler in Eq. 2.29.

$$\bar{\bar{\mathbf{T}}}_{\text{gen}} = e^{i\theta_o} \begin{bmatrix} e^{i\psi} \sqrt{1-\kappa} e^{i\Delta} & e^{i\psi} i\sqrt{\kappa} e^{-i\Delta} \\ e^{-i\psi} i\sqrt{\kappa} e^{i\Delta} & e^{-i\psi} \sqrt{1-\kappa} e^{-i\Delta} \end{bmatrix} \quad (2.30)$$

Since the propagation through a waveguide provides only a phase shift (assuming negligible losses), we can simply redefine the reference frames which we are considering for our general coupler to compensate for these phases and recover exactly the T-matrix of the symmetric coupler as shown in Fig. 2.8. Therefore, for the remainder of this thesis, we will describe lossless 2-by-2 couplers using the convention of the symmetric coupler (Eq. 2.29 with $\theta_o = 0$), even in the cases of non-symmetric couplers with the understanding that a simple shift in reference planes makes this assumption rigorously correct.

2.5 Ring resonators

By looping one of the outputs from a directional coupler back into an input, say b_2 to a_2 as shown in Fig. 2.9, we can create a feedback which will allow the light to constructively interfere at specific wavelengths in order to create a large field enhancement (and therefore power enhancement). This allows light to effectively propagate long distances while using only a small area of a chip. By implementing the transfer matrix for a symmetric coupler and the propagation of light through a waveguide we can reduce the relevant physics of this process down to the three equations:

$$b_1 = \sqrt{1 - \kappa}a_1 + i\sqrt{\kappa}a_2 \quad (2.31)$$

$$b_2 = i\sqrt{\kappa}a_1 + \sqrt{1 - \kappa}a_2 \quad (2.32)$$

$$a_2 = b_2e^{(i\beta - \alpha)L}, \quad (2.33)$$

where L is the length of the loop. Solving for ratio of the field amplitudes in the ring compared to the input waveguide (i.e., b_2/a_1) we can find the field enhancement provided by the ring resonator

$$\frac{b_2}{a_1} = \frac{i\sqrt{\kappa}}{1 - \sqrt{1 - \kappa}e^{(i\beta - \alpha)L}}. \quad (2.34)$$

The power enhancement would then be

$$\left| \frac{b_2}{a_1} \right|^2 = \frac{\kappa}{1 + (1 - \kappa)e^{-2\alpha L} - 2\sqrt{1 - \kappa}e^{-\alpha L} \cos(\beta L)}. \quad (2.35)$$

The maximum power will occur at frequencies which would provide an integer number of wavelengths around the ring, (i.e., where $\beta L = 2\pi m$, where m is the corresponding mode order). This is the resonance condition and only at frequencies near this condition will the field be significantly enhanced. The power enhancement on resonance [i.e., where $\cos(\beta L) = 1$] then becomes

$$\left| \frac{b_2}{a_1} \right|_{\text{resonant}}^2 = \frac{\kappa}{(1 - \sqrt{1 - \kappa}e^{-\alpha L})^2}. \quad (2.36)$$

To find the coupling condition for maximum power enhancement, we can perform a first derivative test with respect to κ and find that to couple to a ring resonator with a given waveguide loss α , a power coupling ratio equal to the round trip loss is required (i.e., $\kappa = 1 - e^{-2\alpha L}$) to

maximize power enhancement. Here, α is related to the loss in dB/cm by $\alpha = \ln(10)/0.2 \times L_{\text{dB/cm}}$ with units of inverse meters [m^{-1}]. This condition is known as the “critical coupling” condition.

2.5.1 Simplification near resonance

Often the physical phenomena under study are of interest only near the resonance condition, where fields are significantly enhanced. We can approximate the cosine function near a particular resonance frequency as a quadratic function of frequency. The resonant frequency we are interested in exploring is $\omega_o = \beta_o c/n_{\text{eff}}(\omega_o)$ where the resonant propagation constant is $\beta_o = 2\pi m/L$, for the m -th order resonance. Initially assuming there is no group velocity dispersion over the range of frequencies we are exploring, we can expand the propagation constant such that

$$\beta \approx \beta_o + \left. \frac{\partial \beta}{\partial \omega} \right|_{\omega_o} (\omega - \omega_o) = \beta_o + \frac{1}{v_g(\omega_o)} (\omega - \omega_o). \quad (2.37)$$

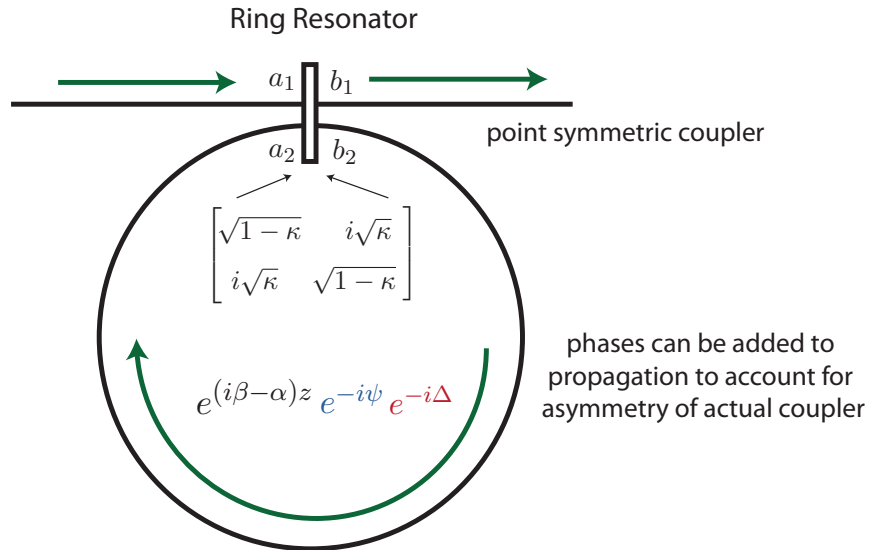


Figure 2.9: Ring resonator constructed from a general 2 by 2 coupler can be modeled as a symmetric (about horizontal axis) point coupler with the additional phases ψ and Δ in a general coupler added to the propagation.

Here $\frac{\partial\beta}{\partial\omega}\big|_{\omega_0}$ is the inverse of the group velocity $v_g(\omega)$ evaluated at ω_0 . We can now Taylor series expand the cosine function in Eq. 2.35 around the resonance frequency ω_0 as

$$\cos(\beta L) \approx 1 - \frac{L^2}{2v_g^2}(\omega - \omega_0)^2 = 1 - \frac{1}{2\nu_{\text{FSR}}^2}(\omega - \omega_0)^2, \quad (2.38)$$

where the free spectral range in frequency is $\nu_{\text{FSR}} = v_g/L$ and is the inverse of the round trip time τ_{rt} , in the absence of dispersion. The power enhancement relation of Eq. 2.35 becomes a Lorentzian function of detuning $\Delta\omega$ from the resonance frequency such that $\Delta\omega \equiv \omega - \omega_0$ and

$$\left|\frac{b_2}{a_1}\right|^2 = \frac{\kappa}{(1 - \sqrt{1 - \kappa}e^{-\alpha L})^2 + \sqrt{1 - \kappa}e^{-\alpha L}\Delta\omega^2/\nu_{\text{FSR}}^2}. \quad (2.39)$$

Now as we will find later, it will often be useful to characterize the total energy in a resonator W_{energy} . As such, we can convert the power distributed throughout the resonator to energy by multiplying it by the round trip time $\tau_{\text{rt}} = L/v_g$ (i.e., $W_{\text{energy}} = \tau_{\text{rt}}P_{\text{avg}}$). P_{avg} is the average power around the entire ring and can be calculated by

$$P_{\text{avg}} = \frac{1}{L} \int_0^L P(z) dz = \frac{1}{2\alpha L} \left(1 - e^{-2\alpha L}\right) P(0), \quad (2.40)$$

where $P(0)$ (equivalent to $|B_2|^2$ in the Fig. 2.9) is the power in the ring just after it has been coupled in from the bus and before it has propagated far enough to experience intrinsic loss. The full equation for the ratio of the energy in the ring to the power input becomes

$$\frac{W_{\text{energy}}}{P_{\text{in}}} = \frac{\nu_{\text{FSR}} \frac{\kappa}{\sqrt{1-\kappa}} \frac{1}{\alpha L} \sinh(\alpha L)}{[2 \sinh(\alpha L/2) + \frac{\kappa}{2} \cosh(\alpha L/2)]^2 \nu_{\text{FSR}}^2 + \Delta\omega^2} \quad (2.41)$$

and is of Lorentzian shape with respect to the frequency detuning $\Delta\omega$.

2.6 Coupling of modes in time

There is another approach to treating the properties of resonators which, although requiring more assumptions (namely high-Q), can often be much more general and powerful, as long as we are working within the a region of parameters where the assumptions are justified. Previously we had assumed some fairly general properties of waveguides and couplers and pieced them together to form a resonator. Here, we will consider a resonator as its own component and then piece it together

with an input waveguide. Maxwell's equations can be arranged, with no regard for symmetry in any particular direction to obtain

$$i \frac{\partial}{\partial t} \left[\begin{pmatrix} \epsilon_o & 0 \\ 0 & \mu_o \end{pmatrix} \begin{pmatrix} \vec{E}(\vec{r}, t) \\ \vec{H}(\vec{r}, t) \end{pmatrix} + \begin{pmatrix} \vec{P}(\vec{r}, t) \\ 0 \end{pmatrix} \right] = \begin{pmatrix} 0 & i\nabla \times \\ -i\nabla \times & 0 \end{pmatrix} \begin{pmatrix} \vec{E}(\vec{r}, t) \\ \vec{H}(\vec{r}, t) \end{pmatrix} \quad (2.42)$$

which in the linear regime is

$$i \frac{\partial}{\partial t} \begin{pmatrix} \epsilon(\vec{r}) & 0 \\ 0 & \mu_o \end{pmatrix} \begin{pmatrix} \vec{E}(\vec{r}, t) \\ \vec{H}(\vec{r}, t) \end{pmatrix} = \begin{pmatrix} 0 & i\nabla \times \\ -i\nabla \times & 0 \end{pmatrix} \begin{pmatrix} \vec{E}(\vec{r}, t) \\ \vec{H}(\vec{r}, t) \end{pmatrix}. \quad (2.43)$$

Using the expansion into frequency modes

$$\begin{pmatrix} \vec{E}(\vec{r}, t) \\ \vec{H}(\vec{r}, t) \end{pmatrix} = \sum_j a_j(t) \begin{pmatrix} \vec{e}_j(\vec{r}) \\ \vec{h}_j(\vec{r}) \end{pmatrix} \quad (2.44)$$

where $a_j(t) = A_j e^{-i\omega_j t}$ leads to the generalized eigenvalue problem

$$\begin{pmatrix} 0 & i\nabla \times \\ -i\nabla \times & 0 \end{pmatrix} \begin{pmatrix} \vec{e}_j(\vec{r}) \\ \vec{h}_j(\vec{r}) \end{pmatrix} = \omega_j \begin{pmatrix} \epsilon(\vec{r}) & 0 \\ 0 & \mu_o \end{pmatrix} \begin{pmatrix} \vec{e}_j(\vec{r}) \\ \vec{h}_j(\vec{r}) \end{pmatrix}. \quad (2.45)$$

If the dielectric permittivity is completely real, then the eigenvalue equation contains two self-adjoint (Hermitian) operators and therefore all the frequencies are real. Though, in general, the frequency modes (eigenfunctions) will span all real space. However, it is possible to construct specialized dielectric distributions which can create bound modes spanning a finite mode volume. For instance, a waveguide with perfect electric conductors at each end would support standing wave modes which are finite and oscillate at a real resonance frequencies indefinitely. Of course, this example is somewhat artificial as perfect electrical conductors are unphysical, but we can often describe the properties of “leaky” quasi-modes by referring to their fictitious lossless cousins. Another example would be a ring resonator. In reality, any curvature of a waveguide is a perturbation which introduces loss by coupling the guided mode and radiation modes. Typically, the radii of ring resonators are chosen large enough that this loss is far less than the roughness loss intrinsic to a particular fabrication process. The precise radii for which this approximation is valid depends on the resonators geometry and the refractive index contrast of the materials comprising it.

We consider modes with a modal amplitude a_j , normalized such that $|a_j|^2$ is the energy in the resonator mode. First, we consider a lossless mode which would simply oscillate in time at its resonant frequency ω_o such that

$$\frac{d}{dt}a = -i\omega_o a. \quad (2.46)$$

The effect of a bus waveguide, where power can evanescently couple out of the resonator and to the bus, can be modelled by an exponential decay of the energy in the resonator. The resulting loss rate due to this external coupling is denoted by r_e .

$$\frac{d}{dt}a = (-i\omega_o - r_e)a \quad (2.47)$$

The power amplitude in the output of the resonator, s_{out} , will be related to energy amplitude of the resonator mode by a constant factor, we will refer to as D , such that

$$s_{\text{out}} = Da. \quad (2.48)$$

From basic power conservation (i.e., making sure that the same amount of power leaving the resonator is equal to the power gained by the output bus $d|a|^2/dt = |s_{\text{out}}|^2$), we find

$$2r_e = |D|^2. \quad (2.49)$$

Similarly, we can consider a power amplitude from the input of the waveguide, s_{in} , that has the potential to add energy to the resonator at a constant rate K and to the output waveguide at fraction C such that

$$\frac{d}{dt}a = (-i\omega_o - r_e)a + Ks_{\text{in}} \quad (2.50)$$

$$s_{\text{out}} = Cs_{\text{in}} + Da. \quad (2.51)$$

Time reversal symmetry constrains $K = D$ and $CD^* = -D$ [138]. In a process similar to our treatment of directional couplers, we simplify notation by defining reference frames such that C is both real and unity (i.e., $C = 1$) necessarily making $D = \pm i\sqrt{2r_e}$, for which we choose the positive relation, $D = i\sqrt{2r_e}$, for the remainder of this thesis. We have chosen this convention

out of symmetry to our convention for 2-by-2 couplers, where reference planes are set such that the cross-coupled field is $\pi/2$ behind the input field for the resonance condition. Inserting these conventions for K , D , and C , along with an included intrinsic loss rate r_o due to factors such as roughness loss, radiation loss, and material absorption, into Eq. 2.50 and Eq. 2.51 we find the simple equations for the dynamics of a single mode resonator [59]

$$\frac{d}{dt}a = (-i\omega_o - r_e - r_o)a + i\sqrt{2r_e}s_{\text{in}} \quad (2.52)$$

$$s_{\text{out}} = s_{\text{in}} + i\sqrt{2r_e}a. \quad (2.53)$$

2.6.1 Comparison to t-matrix

We can now compare the coupling of modes in time (CMT) model to the transfer matrix model. Solving the equations above in the steady state (i.e., $d/dt \rightarrow -i\omega$) we find the ratio between the energy in the resonant mode and the input waveguide power as

$$\left| \frac{a}{s_{\text{in}}} \right|^2 = \frac{2r_e}{(r_e + r_o)^2 + \Delta\omega^2}, \quad (2.54)$$

where $\Delta\omega = \omega - \omega_o$ is the detuning from resonance. While also a Lorentzian function, there are significant differences between this equation and Eq. 2.41. The numerator of Eq. 2.54 only depends on the coupling to the waveguide and not on any intrinsic loss. Secondly, the factors relating coupling and loss on the left hand side of the denominator are separable by addition, in contrast to the denominator in Eq. 2.41. Despite these seemingly significant differences, a very interesting case occurs at small coupling and low waveguide loss. By Taylor series expanding to first-order in α and κ , we find we can approximate

$$\sinh(\alpha L) \approx \alpha L \quad (2.55)$$

$$\sinh(\alpha L/2) \approx \alpha L/2 \quad (2.56)$$

$$\cosh(\alpha L/2) \approx 1 \quad (2.57)$$

$$\frac{\kappa}{\sqrt{1 - \kappa}} \approx \kappa, \quad (2.58)$$

and reduce Eq. 2.41 to

$$\frac{W_{\text{energy}}}{P_{\text{in}}} = \frac{\nu_{\text{FSR}}\kappa}{[(\alpha L + \kappa/2)\nu_{\text{FSR}}]^2 + \Delta\omega^2}, \quad (2.59)$$

leaving us with exactly the relationship we found from the coupling of modes in time model (Eq. 2.54) under the variable substitutions:

$$\kappa = \frac{2r_e}{\nu_{\text{FSR}}} \quad (2.60)$$

$$\alpha L = \frac{2r_o}{\nu_{\text{FSR}}}. \quad (2.61)$$

While this is a specific example relating these two formulations, it is helpful in understanding the additional assumptions required for describing a resonant system using CMT, namely that the loss in a single round trip is small enough that Eqs. 2.55 to 2.57 are valid and that we are working relatively near resonance (i.e., the detuning $\Delta\omega/2\pi$ is much smaller than the free spectral range ν_{FSR}).

2.6.2 Resonators with gain

While all resonators have intrinsic losses resulting from various mechanisms, some resonators can generate light through a property we refer to as “gain.” We can phenomenologically include a gain rate r_g to the coupled mode equations

$$\frac{d}{dt}a = (-i\omega_o - r_e - r_o + r_g)a + i\sqrt{2r_e}s_{\text{in}} \quad (2.62)$$

$$s_{\text{out}} = s_{\text{in}} + i\sqrt{2r_e}a. \quad (2.63)$$

If the gain is fixed and larger than the losses of the resonator, i.e. $r_g > r_o + r_e$, as is the necessary condition for a laser, then our model will experience exponential growth of energy amplitude in the resonator tending towards infinity, which is obviously unphysical. To more accurately model a real world situation like a laser, we will add in gain saturation which reduces the gain as the modal energy increases, described by a small signal gain r_{ssg} which is the initial gain rate before saturation becomes significant. We define a saturation energy $|a_{\text{sat}}|^2$ as the cavity energy where

the gain becomes half of the small signal gain such that

$$r_g = \frac{r_{\text{ssg}}}{1 + \left| \frac{a}{a_{\text{sat}}} \right|^2}. \quad (2.64)$$

In maximizing the output power $|s_{\text{out}}|^2$, there exists an optimal coupling rate $r_{\text{e,opt}}$, where

$$r_{\text{e,opt}} = \sqrt{r_{\text{ssg}} r_o} - r_o. \quad (2.65)$$

2.6.3 Quantized coupled mode theory

Classical formulations of the electromagnetic field fall short in accurately predicting the correlations and photon pair generation efficiencies we plan to describe and measure in the following chapters. For this reason, we will require a quantum description of light in waveguides and resonators. When moving to the quantum domain, we can describe the dynamics of photons in a resonant cavity using coupled mode equations which are very closely related to their classical counterparts (Eq. 2.52 and Eq. 2.53). The primary difference is that we must promote the complex energy amplitudes, a and its complex conjugate a^* , to their corresponding quantum operators $\hat{a}(t)$ and $\hat{a}^\dagger(t)$ which instead will be normalized such that $\hat{a}(t)^\dagger \hat{a}(t) = \hat{N}$ is the photon number operator. Here we explicitly write the time dependence to emphasize that we are working in the so-called “Heisenberg Picture” where operators rather than states carry the time dependence [133]. The expectation value $\langle \hat{N} \rangle$ is the “expected” number of photons in the corresponding mode. Since $\hat{a}(t)$ and $\hat{a}^\dagger(t)$ are conjugate operators, they do not commute and we can postulate the commutation relations

$$[\hat{a}(t), \hat{a}^\dagger(t)] \equiv \hat{a}(t) \hat{a}^\dagger(t) - \hat{a}^\dagger(t) \hat{a}(t) = 1. \quad (2.66)$$

This approach is heuristic and unfortunately many interesting details beyond the scope of this thesis are seemingly “swept under the rug.” The more formal and enlightening (but also laborious) method of formulating these equations is often called “canonical quantization” and relies on considering Maxwell’s equations as being derived variationally from a more fundamental Lagrangian [24]. This approach allows for a deeper understanding for why a and a^* are conjugate variables which are

promoted to operators that satisfy Eq. 2.66 and provides a general method for quantizing any classical field (with gravitational field theory being the only exception).

The relation of a resonant optical mode to a harmonic oscillator can be found by inspecting the dynamics of a lossless resonator mode Eq. 2.46. This becomes apparent by simply using the Hamiltonian of the harmonic oscillator,

$$\hat{H} = \frac{\hbar\omega}{2}[\hat{a}^\dagger(t)\hat{a}(t) + \hat{a}(t)\hat{a}^\dagger(t)] = \hbar\omega\hat{a}^\dagger(t)\hat{a}(t) + \frac{1}{2} \quad (2.67)$$

and the commutation relation from Eq. 2.66 in Heisenberg's dynamical equation

$$\frac{d}{dt}\hat{a}(t) = -\frac{i}{\hbar}[\hat{a}(t), \hat{H}], \quad (2.68)$$

to find

$$\frac{d}{dt}\hat{a}(t) = -i\omega_o\hat{a}(t). \quad (2.69)$$

This is exactly Eq. 2.46, with the classical mode amplitudes replaced with quantum operators. In fact, quantization of a classical field simply relies on quantizing the frequency eigenmodes of the given field (in our case described by Eq. 2.45) as a collection of harmonic oscillators [166]. In a resonator for which we want to describe multiple modes the Hamiltonian becomes a summation of all the individual modes' corresponding Hamiltonians such that

$$\hat{H} = \sum_j (\hbar\omega_j\hat{a}_j^\dagger(t)\hat{a}_j(t) + \frac{1}{2}). \quad (2.70)$$

It is often convention to omit the scalar $\frac{1}{2}$ from the Hamiltonian since it does not contribute to the dynamical equations when applied to the equation of motion Eq. 2.68. This omission is valid since the difference in energy, rather than the total energy itself, is more fundamental in describing physical phenomena. Similarly, we can extend the optical cavity (such as a ring resonator) to infinite size to describe a waveguide. In this case, what were formerly referred to as resonance frequencies transition from being discrete to continuous and Eq. 2.70 becomes an integral equation rather than a summation. Dropping the scalar $\frac{1}{2}$ terms, the Hamiltonian for a waveguide becomes

$$\hat{H} = \hbar \int \omega \hat{s}^\dagger(\omega) \hat{s}(\omega) d\omega, \quad (2.71)$$

where we have used $\hat{s}(\omega)$ to describe the modes of a waveguide in an attempt both to provide symmetry to the classical equations in Section 2.6 and to emphasize that the units of $\langle \hat{a}(t)^\dagger \hat{a}(t) \rangle$ are number of photons and $\langle \hat{s}^\dagger(t) \hat{s}(t) \rangle$ are number of photons per second, where $\hat{s}(t)$ is the Fourier transform of $\hat{s}(\omega)$

$$\hat{s}(t) = \frac{1}{\sqrt{2\pi}} \int \hat{s}(\omega) e^{-i\omega t} d\omega \quad (2.72)$$

such that we can now refer to the “photon flux operator” in the waveguide as

$$\begin{aligned} \text{photon flux operator} &\equiv \frac{1}{2\pi} \int \int \hat{s}(\omega)^\dagger \hat{s}(\omega') d\omega d\omega' \\ &\equiv \hat{s}^\dagger(t) \hat{s}(t). \end{aligned} \quad (2.73)$$

At first glance, one might attempt to perform a direct conversion of the classical coupled mode dynamics (Eq. 2.47 and Eq. 2.48) to quantum dynamics of an undriven cavity by only the promotion of mode energy amplitudes to operators like so:

$$\frac{d}{dt} \hat{a}(t) = (-i\omega_o - r_o) \hat{a}(t) \quad (2.74)$$

$$\hat{s}_{\text{out}}(t) = i\sqrt{2r_e} \hat{a}(t). \quad (2.75)$$

Unfortunately, this does not accurately model the physical situation since the commutation relation for the mode creation and annihilation operators would not be conserved in time, as they must to obey the Heisenberg uncertainty principle [60]. For instance, if we simply solve for the time derivative of the commutation relation using Eq. 2.74 we find

$$\begin{aligned} \frac{d}{dt} [\hat{a}(t), \hat{a}^\dagger(t)] &= \left[\frac{d}{dt} \hat{a}(t), \hat{a}^\dagger(t) \right] + [\hat{a}(t), \frac{d}{dt} \hat{a}^\dagger(t)] \\ &= -2r_o [\hat{a}(t), \hat{a}^\dagger(t)], \end{aligned} \quad (2.76)$$

which would result in an exponentially decaying value of the commutator (i.e., $[\hat{a}(t), \hat{a}^\dagger(t)] \propto e^{-2r_o t}$) and the two conjugate operators commuting as time approached infinity. Of course this is not the case, and we need to include additional terms to conserve the commutator.

Since the cavity modes are lossy, they are coupled to external radiation modes which have vacuum fluctuations that can couple into the resonator. These Langevin noise terms can be added

to the coupled mode equations to conserve the commutators (defined in Eqs. 2.79–2.82) and in fact, for the purposes of this thesis, behave equivalently to an additional external port such as an evanescently coupled bus waveguide, as shown in [155]. Our linear resonator dynamics become

$$\frac{d}{dt}\hat{a}(t) = (-i\omega_o - r_o - r_e)\hat{a}(t) + i\sqrt{2r_e}\hat{s}_{\text{in}}(t) + i\sqrt{2r_o}\hat{n}_{\text{in}}(t) \quad (2.77)$$

$$\hat{s}_{\text{out}}(t) = \hat{s}_{\text{in}}(t) + i\sqrt{2r_e}\hat{a}(t). \quad (2.78)$$

where \hat{n}_{in} is the before mentioned Langevin noise source. The operators obey the commutation relations

$$[\hat{a}(t), \hat{a}^\dagger(t')] = \delta(t - t') \quad (2.79)$$

$$[\hat{s}_{\text{in}}(t), \hat{s}_{\text{in}}^\dagger(t')] = \delta(t - t') \quad (2.80)$$

$$[\hat{n}_{\text{in}}(t), \hat{n}_{\text{in}}^\dagger(t')] = \delta(t - t') \quad (2.81)$$

$$[\hat{s}_{\text{out}}(t), \hat{s}_{\text{out}}^\dagger(t')] = \delta(t - t'). \quad (2.82)$$

These same dynamics can be alternatively found from a phenomenological Hamiltonian [40]

$$\begin{aligned} \hat{H}_{\text{linear}} &= \hbar\omega\hat{a}^\dagger(t)\hat{a}(t) + \hbar \int \omega\hat{s}^\dagger(\omega)\hat{s}(\omega)d\omega \\ &+ i\frac{\hbar}{\sqrt{2\pi}} \int [\kappa_e\hat{s}(\omega)\hat{a}^\dagger(t) - \kappa_e^*\hat{a}(t)\hat{s}^\dagger(\omega)]d\omega \\ &+ i\frac{\hbar}{\sqrt{2\pi}} \int [\kappa_o\hat{n}(\omega)\hat{a}^\dagger(t) - \kappa_o^*\hat{a}(t)\hat{n}^\dagger(\omega)]d\omega. \end{aligned} \quad (2.83)$$

The input field $\hat{s}_{\text{in}}(t)$ and output field $\hat{s}_{\text{k,out}}(t)$ are related to the bus and reservoir modes as following

$$\hat{s}_{\text{in}}(t) = \frac{1}{\sqrt{2\pi}} \int \hat{s}(\omega) \Big|_{t=t_{\text{in}}} e^{-i\omega(t-t_{\text{in}})} d\omega \quad (2.84)$$

$$\hat{s}_{\text{out}}(t) = \frac{1}{\sqrt{2\pi}} \int \hat{s}(\omega) \Big|_{t=t_{\text{out}}} e^{-i\omega(t-t_{\text{out}})} d\omega, \quad (2.85)$$

where $t_{\text{in}} < t < t_{\text{out}}$. At first sight, it might seem strange to evaluate a frequency distribution at a particular time as we have done for $\hat{s}(\omega)$ in Eqs. 2.84–2.85. However, it is clear that at a time long before the quantized electromagnetic field in the waveguide has interacted with the resonator

that it can be described by a Fourier superposition of waveguide modes as in Eq. 2.84. Similarly after this field has interacted with the resonance and possibly some has coupled to the reservoir \hat{n} , we may have a different frequency distribution which is described by Eq. 2.85. After solving the Heisenberg dynamical equation for the modal annihilation operator $\hat{a}(t)$ given by Eq. 2.68 we recover the coupled mode equations above under the substitution of $\kappa_o = i\sqrt{2r_o}$ and $\kappa_e = i\sqrt{2r_e}$.

2.7 Summary

Within this chapter, we have summarized the theoretical background to which derivations in the proceeding chapters will rely upon. We presented Maxwell's equations and how they permit guided modes within z -invariant structures. Dispersion, an important property in the design of devices relying on nonlinear parametric processes, was also introduced. We briefly investigated directional couplers so that we could combine their properties with waveguides to describe compound structures such as ring resonators.

Ring resonators have proved to be promising structures for enhancing optical fields on-chip and increasing the efficiency of nonlinear processes. In addition, ring resonators provide a frequency response which will allow for the creation of photonic filters. The coupling of modes in time model was introduced and will act as the backbone of most the theoretical analysis we investigate in the remaining chapters. A quantum analogue of this model was also presented, which will be pivotal in understanding how the spontaneous generation of photon pairs are a result of amplified vacuum fluctuations.

It was the intention of this chapter to cover material which while important for understanding derivations would otherwise be distracting if included in proceeding chapters. With any introduction of theoretical background, much analysis was necessarily left out for the sake of brevity and we direct the reader to the references for more in-depth discussions of any specific topic. In addition, to providing theoretical background, this chapter is intended to serve as a reference for the particular notation and conventions used within the thesis.

Chapter 3

Four-wave mixing and dispersion engineering

3.1 Introduction and background

At low intensities it is often safe to assume that the polarizability of a material depends linearly on an applied electric field as we did when we introduced Maxwell's equations in the previous chapter. In these cases, the light at a specific frequency can scatter into many spatial modes but will consistently stay at the same optical frequency. With the invention of the laser it became much easier to work in a regime where the polarizability of a material responds to higher powers of the electric field thus allowing the transfer of energy between different frequencies of light. In this thesis we are interested in the production of photon pairs from such a nonlinear process. Before diving fully into the quantum mechanical treatment of the nonlinear optical process, it will be helpful to understand, at the classical level, practical design considerations for supporting an efficient nonlinear interaction.

Historically, the most common nonlinear conversion process used for photon pair generation is spontaneous parametric down-conversion (SPDC). SPDC results in the annihilation of a photon from an input pump beam and the subsequent creation of two photons (the photon pair). The corresponding classical nonlinear optical process is difference frequency generation, where the pump light “mixes” with an input “signal” light to produce an output “idler” field at the difference frequency of the pump and signal. SPDC occurs when the signal input is removed and quantum vacuum fluctuations “seed” the process, thereby spontaneously generating photon pairs. This process relies on specific 2nd-order nonlinear crystals, which although are quite successful at

efficiently supporting these processes, are expensive and not readily available at mass production in way similar to the mass manufacturing of silicon microelectronic circuits. Despite these challenges, second-order nonlinear materials in chip-based quantum optical circuits are readily being explored [145, 21, 55]. The work in this thesis will focus on silicon as a nonlinear optical medium due to the maturity of fabrication processes and the ease of integration with classical electronic logic and control circuits. Silicon, as all transparent materials, supports the third-order nonlinear optical process of four-wave mixing, where instead of one pump photon, two pump photons annihilate to generate a photon pair.

In this chapter, we investigate the four-wave mixing process in on-chip integrated waveguides and resonators, while also quantifying the effect dispersion plays in each of these devices. In addition, we introduce a novel dispersion engineering method for single-ring resonators and also propose and demonstrate a tunable method of compensating for dispersion in ring resonators through the coupling of additional resonator modes.

3.2 Nonlinear optics

Many of the characteristic features of nonlinear optics can be described by a power series expansion of the polarizability with respect to electric field

$$\vec{P}(\vec{r}, t) = \epsilon_o[\chi^{(1)}(\vec{r})\vec{E}(\vec{r}, t) + \chi^{(2)}(\vec{r})\vec{E}^2(\vec{r}, t) + \chi^{(3)}(\vec{r})\vec{E}^3(\vec{r}, t) + \dots] \quad (3.1)$$

In general all order of the susceptibilities $\chi^{(k)}$ are tensoral in nature and can represent anisotropic characteristics of their respective materials. In general, if a material has inversion symmetry at near the atomic scale it will have vanishing second order nonlinearity $\chi^{(2)}$. This includes all amorphous materials and crystals which are centrosymmetric such as silicon [84]. For the purpose of this thesis we can describe the polarizability as

$$\begin{aligned} \vec{P}(\vec{r}, t) &= \epsilon_o[\chi^{(1)}(\vec{r})\vec{E}(\vec{r}, t) + \chi^{(3)}(\vec{r})\vec{E}^3(\vec{r}, t)] \\ \vec{P}(\vec{r}, t) &= \vec{P}_{\text{lin}}(\vec{r}, t) + \vec{P}_{\text{nl}}(\vec{r}, t). \end{aligned} \quad (3.2)$$

We note that it is possible to obtain a quasi-second order nonlinearity in silicon [150] which could potentially be used for spontaneous parametric down-conversion, but this requires large a DC field near the breakdown of many materials and its support of SPDC has not been tested at this time.

Let's consider the situation where all relevant frequencies will be near the primary input frequency which we will henceforth refer to as the pump at radial frequency ω_p . We will also consider light at two other frequencies ω_s and ω_i though at much lower optical powers. We can now see how the polarizability responds to an electric field comprised of these three modes, by expanding the electric field into its complex frequency components

$$\vec{E}(\vec{r}, t) = \frac{1}{2}(\vec{\mathbf{E}}_p e^{-i\omega_p t} + \vec{\mathbf{E}}_s e^{-i\omega_s t} + \vec{\mathbf{E}}_i e^{-i\omega_i t}) + \text{c.c.} \quad (3.3)$$

where c.c. is shorthand for the complex conjugate. The corresponding polarizability contains 22 different frequency components [15]. Considering only frequencies near the input pump frequency ω_p , results in three distinct frequencies: ω_p , ω_s , and ω_i , where we have assumed that $2\omega_p = \omega_i + \omega_s$. Despite containing only three distinction frequencies the nonlinear polarizability $\vec{P}_{\text{nl}}(\vec{r}, t)$ contains contributions from multiple different nonlinear optical processes:

$$\begin{aligned} \vec{P}_{\text{nl}}(\vec{r}, t) = & \frac{1}{8}\epsilon_0\chi^{(3)}[(3\vec{\mathbf{E}}_p|\vec{\mathbf{E}}_p|^2 + 6\vec{\mathbf{E}}_p|\vec{\mathbf{E}}_i|^2 + 6\vec{\mathbf{E}}_p|\vec{\mathbf{E}}_s|^2)e^{-i\omega_p t} + \\ & (6\vec{\mathbf{E}}_s|\vec{\mathbf{E}}_p|^2 + 6\vec{\mathbf{E}}_s|\vec{\mathbf{E}}_i|^2 + 3\vec{\mathbf{E}}_s|\vec{\mathbf{E}}_s|^2)e^{-i\omega_s t} + \\ & (6\vec{\mathbf{E}}_i|\vec{\mathbf{E}}_p|^2 + 3\vec{\mathbf{E}}_i|\vec{\mathbf{E}}_i|^2 + 6\vec{\mathbf{E}}_i|\vec{\mathbf{E}}_s|^2)e^{-i\omega_i t} + \\ & 6\vec{\mathbf{E}}_s\vec{\mathbf{E}}_i\vec{\mathbf{E}}_p^* e^{-i\omega_p t} + 3\vec{\mathbf{E}}_p^2\vec{\mathbf{E}}_i^* e^{-i\omega_s t} + 3\vec{\mathbf{E}}_p^2\vec{\mathbf{E}}_s^* e^{-i\omega_i t}] + \text{c.c.} \end{aligned} \quad (3.4)$$

where the first three terms are due to phase modulation and the last three result from the four-wave mixing process with a degenerate pump. Here, a degenerate pump refers to the fact that two identical pump photons are converted to a signal and idler photon pair. Since photon pairs are generated at power levels **much** lower than typical laser powers, we can ignore the phase modulation terms where there is more than one non-pump field term. For example, the phase modulation terms at the signal frequency ω_s can be well approximated as

$$\frac{1}{8}\epsilon_0\chi^{(3)}(6\vec{\mathbf{E}}_s|\vec{\mathbf{E}}_p|^2 + 6\vec{\mathbf{E}}_s|\vec{\mathbf{E}}_i|^2 + 3\vec{\mathbf{E}}_s|\vec{\mathbf{E}}_s|^2)e^{-i\omega_s t} \approx \frac{3}{4}\epsilon_0\chi^{(3)}\vec{\mathbf{E}}_s|\vec{\mathbf{E}}_p|^2 e^{-i\omega_s t} \quad (3.5)$$

since

$$\vec{\mathbf{E}}_s |\vec{\mathbf{E}}_p|^2 \gg \vec{\mathbf{E}}_s |\vec{\mathbf{E}}_i|^2 \quad (3.6)$$

$$\gg \vec{\mathbf{E}}_s |\vec{\mathbf{E}}_s|^2. \quad (3.7)$$

Therefore, the resulting nonlinear polarizability becomes

$$\begin{aligned} \vec{P}_{\text{nl}}(\vec{r}, t) = & \frac{1}{8} \epsilon_0 \chi^{(3)} [3 \vec{\mathbf{E}}_p |\vec{\mathbf{E}}_p|^2 e^{-i\omega_p t} + 6 \vec{\mathbf{E}}_s |\vec{\mathbf{E}}_p|^2 e^{-i\omega_s t} + 6 \vec{\mathbf{E}}_i |\vec{\mathbf{E}}_p|^2 e^{-i\omega_i t} + \\ & 6 \vec{\mathbf{E}}_s \vec{\mathbf{E}}_i \vec{\mathbf{E}}_p^* e^{-i\omega_p t} + 3 \vec{\mathbf{E}}_p^2 \vec{\mathbf{E}}_i^* e^{-i\omega_s t} + 3 \vec{\mathbf{E}}_p^2 \vec{\mathbf{E}}_s^* e^{-i\omega_i t}] + \text{c.c.} \end{aligned} \quad (3.8)$$

Through a Fourier transform we can represent the nonlinear polarization in the frequency domain

$\vec{\mathbf{P}}_{\text{nl}}(\vec{r}, \omega)$ such that

$$\vec{P}_{\text{nl}}(\vec{r}, t) = \frac{1}{2} [\vec{\mathbf{P}}_{\text{nl}}(\vec{r}, \omega) + \vec{\mathbf{P}}_{\text{nl}}^*(\vec{r}, \omega)] \quad (3.9)$$

and

$$\vec{\mathbf{P}}_{\text{nl}}(\vec{r}, \omega) = \vec{\mathbf{P}}_{\text{nl,p}}(\vec{r}) + \vec{\mathbf{P}}_{\text{nl,s}}(\vec{r}) + \vec{\mathbf{P}}_{\text{nl,i}}(\vec{r}) \quad (3.10)$$

where

$$\vec{\mathbf{P}}_{\text{nl,p}}(\vec{r}) = \frac{1}{4} \epsilon_0 \chi^{(3)} [3 \vec{\mathbf{E}}_p |\vec{\mathbf{E}}_p|^2 + 6 \vec{\mathbf{E}}_s \vec{\mathbf{E}}_i \vec{\mathbf{E}}_p^*] \quad (3.11)$$

$$\vec{\mathbf{P}}_{\text{nl,s}}(\vec{r}) = \frac{1}{4} \epsilon_0 \chi^{(3)} [6 \vec{\mathbf{E}}_s |\vec{\mathbf{E}}_p|^2 + 3 \vec{\mathbf{E}}_p^2 \vec{\mathbf{E}}_i^*] \quad (3.12)$$

$$\vec{\mathbf{P}}_{\text{nl,i}}(\vec{r}) = \frac{1}{4} \epsilon_0 \chi^{(3)} [6 \vec{\mathbf{E}}_i |\vec{\mathbf{E}}_p|^2 + 3 \vec{\mathbf{E}}_p^2 \vec{\mathbf{E}}_s^*]. \quad (3.13)$$

3.3 Four-wave mixing in a waveguide

In general, we can describe the four-wave mixing process in a waveguide by expanding the electric field into a basis of linear guided modes. Explicitly adding the nonlinear polarizability to Eq. 2.15, we find

$$\frac{\partial}{\partial z} \begin{pmatrix} 0 & -\hat{z} \times \\ \hat{z} \times & 0 \end{pmatrix} \begin{pmatrix} \vec{E} \\ \vec{H} \end{pmatrix} = \begin{pmatrix} 0 & \nabla_t \times \\ -\nabla_t \times & 0 \end{pmatrix} \begin{pmatrix} \vec{E} \\ \vec{H} \end{pmatrix} - \frac{\partial}{\partial t} \left[\begin{pmatrix} \epsilon(x, y) & 0 \\ 0 & \mu_0 \end{pmatrix} \begin{pmatrix} \vec{E} \\ \vec{H} \end{pmatrix} + \begin{pmatrix} \vec{P}_{\text{nl}} \\ 0 \end{pmatrix} \right]. \quad (3.14)$$

which in the frequency domain is

$$-i \frac{\partial}{\partial z} \begin{pmatrix} 0 & -\hat{z} \times \\ \hat{z} \times & 0 \end{pmatrix} \sum_{k=p,s,i} \begin{pmatrix} \vec{\mathbf{E}}_k \\ \vec{\mathbf{H}}_k \end{pmatrix} = \sum_{k=p,s,i} \left[\begin{pmatrix} \omega_k \epsilon(\vec{r}, \omega_k) & -i \nabla_t \times \\ i \nabla_t \times & \omega_k \mu_o \end{pmatrix} \begin{pmatrix} \vec{\mathbf{E}}_k \\ \vec{\mathbf{H}}_k \end{pmatrix} + \omega_k \begin{pmatrix} \vec{\mathbf{P}}_{\text{nl},k} \\ 0 \end{pmatrix} \right]. \quad (3.15)$$

We now represent the waveguide mode at each frequency as

$$\begin{pmatrix} \vec{\mathbf{E}}_k \\ \vec{\mathbf{H}}_k \end{pmatrix} = a_k(z) \begin{pmatrix} \vec{\mathbf{e}}_k(x, y) \\ \vec{\mathbf{h}}_k(x, y) \end{pmatrix} = A_k(z) \begin{pmatrix} \vec{\mathbf{e}}_k(x, y) \\ \vec{\mathbf{h}}_k(x, y) \end{pmatrix} e^{i\beta_k z} \quad (3.16)$$

where $|a_k(z)|^2 = |A_k(z)|^2$ is the power of each mode k at position z along the waveguide. Note that in the nonlinear regime we are investigating, the amplitudes $A_k(z)$ have an explicit dependence on z , whereas in the lossless linear regime of Chapter 2, they were constant. Since the nonlinear polarizability couples different frequencies, this is no longer the case. Applying the orthogonality relation given by Eq. 2.20 to Eq. 3.15 we find the spatial coupled mode equations

$$\frac{d}{dz} a_p(z) = i\beta_p a_p(z) + i\gamma |a_p(z)|^2 a_p(z) + 2i\gamma a_p^*(z) a_i(z) a_s(z) \quad (3.17)$$

$$\frac{d}{dz} a_s(z) = i\beta_s a_s(z) + 2i\gamma |a_p(z)|^2 a_s(z) + i\gamma a_p^2(z) a_i^*(z) \quad (3.18)$$

$$\frac{d}{dz} a_i(z) = i\beta_i a_i(z) + 2i\gamma |a_p(z)|^2 a_i(z) + i\gamma a_p^2(z) a_s^*(z), \quad (3.19)$$

with

$$\gamma \equiv \frac{\frac{3}{16} \epsilon_o \omega \chi^{(3)} \int_{A_\infty} |\vec{\mathbf{e}}_p|^4 da}{[\frac{1}{4} \int_{A_\infty} (\vec{\mathbf{e}}_p \times \vec{\mathbf{h}}_p^* + \vec{\mathbf{e}}_p^* \times \vec{\mathbf{h}}_p) \cdot \hat{z} da]^2}. \quad (3.20)$$

We have assumed that all three frequencies are near each other such that $\omega = \omega_p \approx \omega_s \approx \omega_i$ and that the transverse mode shapes are not significantly different between the three modes. We can phenomenologically include losses by substituting β_k with its complex value $\beta_k + i\alpha_k$. In the approximation that self- and cross-phase modulation is not significant, the coupled mode equations

become

$$\frac{d}{dz}a_p(z) = (i\beta_p - \alpha_p)a_p(z) + 2i\gamma a_p^*(z)a_i(z)a_s(z) \quad (3.21)$$

$$\frac{d}{dz}a_s(z) = (i\beta_s - \alpha_s)a_s(z) + i\gamma a_p^2(z)a_i^*(z) \quad (3.22)$$

$$\frac{d}{dz}a_i(z) = (i\beta_i - \alpha_i)a_i(z) + i\gamma a_p^2(z)a_s^*(z). \quad (3.23)$$

When working with low conversion rates, such that the pump power, throughout the entire length of the waveguide, is much larger than the signal and idler mode powers, we can implement the undepleted pump approximation. In this approximation, a negligible fraction of the pump power is converted to the signal and idler modes, making it sufficient to model the pump mode's spatial dependence in a linear fashion and the pump modal equation becomes

$$\frac{d}{dz}a_p(z) = (i\beta_p - \alpha_p)a_p(z). \quad (3.24)$$

The validity of the undepleted pump approximation can usually be checked by plugging in the actual parameters in the device under test. For instance, if the resulting analysis determines that the output power of the idler is a significant fraction of the pump, then the undepleted pump approximation was likely not valid.

In addition to simplifying to an undepleted pump, we can also consider a sufficiently small idler, where the idler powers being generated are much smaller than the input signal light, throughout the length of the waveguide. Therefore, the signal equation, similar to the pump, can be approximated as linear such that

$$\frac{d}{dz}a_s(z) = (i\beta_s - \alpha_s)a_s(z). \quad (3.25)$$

Since Eq. 3.24 and Eq. 3.25 model the propagation of the pump and signal modes, respectively, as a simple linear waveguide mode with loss, their modal amplitudes as a function of propagation distance, z , are readily found to be

$$a_p(z) = a_p(0)e^{(i\beta_p - \alpha_p)z} \quad (3.26)$$

$$a_s(z) = a_s(0)e^{(i\beta_s - \alpha_s)z}. \quad (3.27)$$

The solution to Equation 3.23 can be found by direct integration to be

$$a_i(L) = e^{(i\beta_i - \alpha_i)L} \left[a_i(0) + i\gamma a_p^2(0) a_s^*(0) \int_0^L e^{(\alpha_i - \alpha_s - 2\alpha_p)z} e^{i\Delta\beta z} dz \right], \quad (3.28)$$

where we have defined a phase mismatch parameter $\Delta\beta$ as

$$\Delta\beta \equiv 2\beta_p - \beta_s - \beta_i. \quad (3.29)$$

In this situation we are assuming the initial condition that we have no input idler light such that $a_i(0) \rightarrow 0$ and we find that the small-signal conversion efficiency $\eta_{\text{st-fwm, wg}}$ for stimulated four-wave mixing to be

$$\begin{aligned} \eta_{\text{st-fwm, wg}} &\equiv \frac{P_{i, \text{out}}}{P_{s, \text{in}}} \equiv \frac{|a_i(L)|^2}{|a_s(0)|^2} \\ &= (\gamma P_p L)^2 e^{-(2\alpha_p + \alpha_s + \alpha_i)L} \left[\frac{\sin^2(\Delta\beta L/2) + \sinh^2[(2\alpha_p + \alpha_s - \alpha_i)L/2]}{(\Delta\beta L/2)^2 + [(2\alpha_p + \alpha_s - \alpha_i)L/2]^2} \right]. \end{aligned} \quad (3.30)$$

In many situations, the pump, signal, and idler frequencies are very near to each other, such that their propagation losses are nearly identical. Assuming that the propagation losses are all equal (i.e., $\alpha \equiv \alpha_p = \alpha_s = \alpha_i$) the conversion efficiency becomes

$$\begin{aligned} \eta_{\text{st-fwm, wg}} &\equiv \frac{P_{i, \text{out}}}{P_{s, \text{in}}} \equiv \frac{|a_i(L)|^2}{|a_s(0)|^2} \\ &= (\gamma P_p L)^2 e^{-4\alpha L} \left[\frac{\sin^2(\Delta\beta L/2) + \sinh^2(\alpha L)}{(\Delta\beta L/2)^2 + (\alpha L)^2} \right]. \end{aligned} \quad (3.31)$$

In Fig. 3.1 we plot the normalized FWM efficiency, $(\frac{\alpha}{\gamma P_p})^2 \eta_{\text{st-fwm, wg}}$, versus $\Delta\beta L/2$ and αL to demonstrate the dependence on both phase mismatch and loss. At zero phase mismatch, the normalized conversion efficiency is optimized at a length corresponding $\alpha L = \frac{\ln(3)}{2}$. We see that the efficiency in Fig. 3.1(a) and (b) is greatest as the phase mismatch $\Delta\beta \rightarrow 0$ and tends to zero as the phase mismatch gets large.

3.3.1 Dispersion and phase matching in a waveguide

Until now, we have modelled the four-wave mixing process in a waveguide and have found that the efficiency depends strongly on the phase mismatch parameter $\Delta\beta$, defined in Eq. 3.29. We

now investigate the physical origin of this deleterious effect. Reformulating Eq. 3.29 with respect to the effective index of each mode rather than propagation constants provides the first clue that

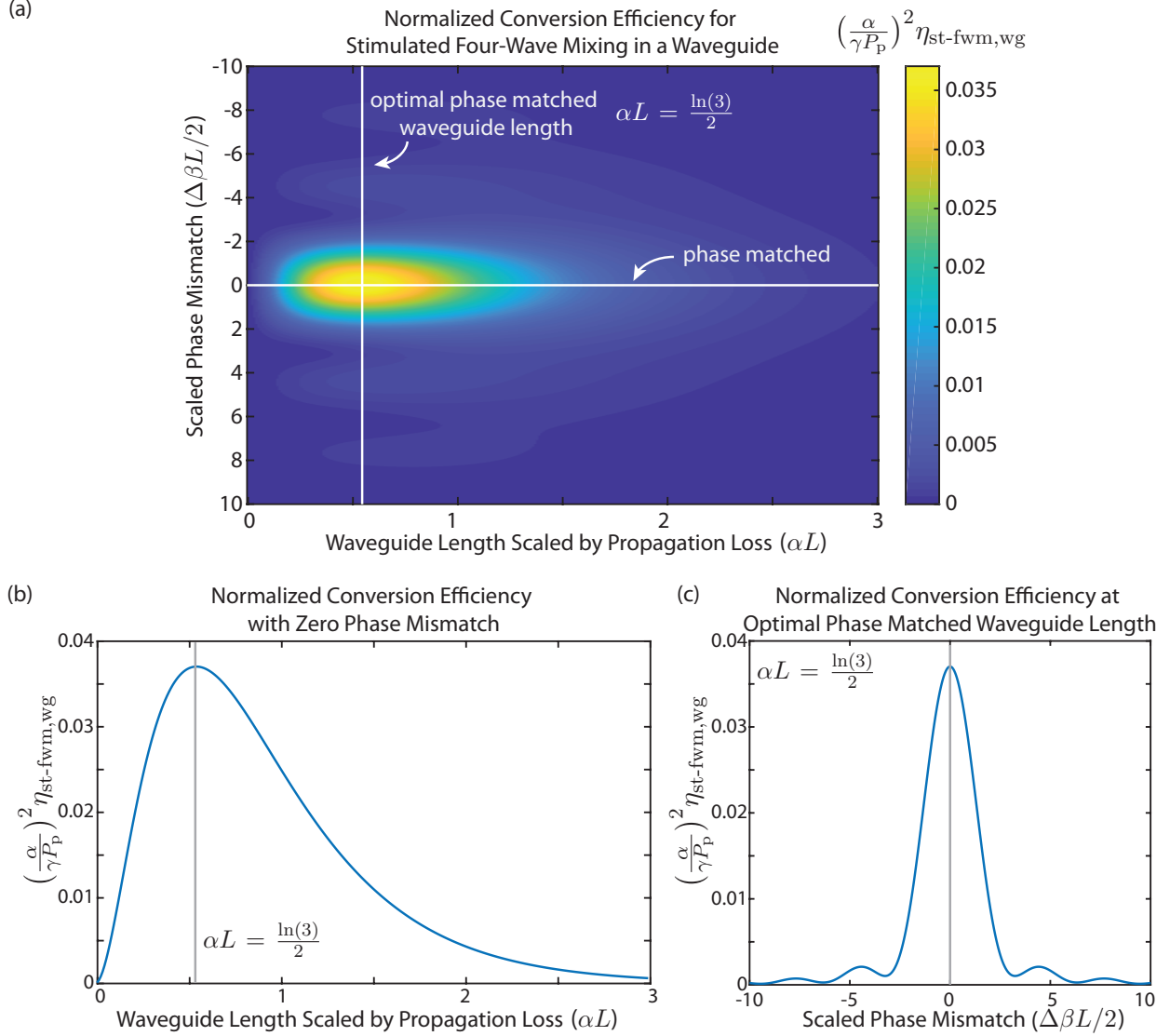


Figure 3.1: (a) The normalized conversion efficiency in a lossy waveguide for stimulated four-wave mixing (Eq. 3.31) versus waveguide length (scaled by the propagation loss) and phase mismatch (scaled by the waveguide length, L) demonstrates optimal efficiency at zero phase mismatch. (b) Plot of efficiency at zero phase mismatch displaying an optimum waveguide length, where loss becomes dominating the efficiency in waveguides exceeding this length. (c) Conversion efficiency versus scaled phase mismatch at the optimal waveguide length.

dispersion is the culprit contributing to the phase mismatch.

$$\Delta\beta \equiv 2\beta_p - \beta_s - \beta_i = \frac{1}{c} \left[2\omega_p n_{\text{eff}}(\omega_p) - \omega_s n_{\text{eff}}(\omega_s) - \omega_i n_{\text{eff}}(\omega_i) \right] \quad (3.32)$$

Through inspection of Eq. 3.32, it is evident that when the effective indices of the three modes are equal [i.e., $n_{\text{eff}}(\omega_p) = n_{\text{eff}}(\omega_s) = n_{\text{eff}}(\omega_i)$], the phase matching condition $\Delta\beta = 0$ is equivalent to energy conservation (i.e., $2\omega_p - \omega_s - \omega_i = 0$).

If we Taylor series expand the propagation constant β to the 2nd-order in detuning around the pump frequency ω_p we find

$$\beta(\omega) \approx \beta_p + \left. \frac{\partial\beta}{\partial\omega} \right|_{\omega_p} (\omega - \omega_p) + \frac{1}{2} \left. \frac{\partial^2\beta}{\partial\omega^2} \right|_{\omega_p} (\omega - \omega_p)^2 \quad (3.33)$$

and therefore the phase mismatch becomes

$$\Delta\beta \approx - \left. \frac{\partial\beta}{\partial\omega} \right|_{\omega_p} (\omega_s + \omega_i - 2\omega_p) - \frac{1}{2} \left. \frac{\partial^2\beta}{\partial\omega^2} \right|_{\omega_p} [(\omega_i - \omega_p)^2 + (\omega_s - \omega_p)^2]. \quad (3.34)$$

Energy conservation sets the signal detuning from the pump, which we will call $\Delta\omega$, to be equivalent to the negative of the idler detuning from the pump such that $\Delta\omega \equiv \omega_s - \omega_p = -(\omega_i - \omega_p)$, reducing Eq. 3.34 to

$$\Delta\beta \approx - \left. \frac{\partial^2\beta}{\partial\omega^2} \right|_{\omega_p} \Delta\omega^2. \quad (3.35)$$

Since Eq. 3.35 gives the relationship between phase mismatch and signal detuning, we can investigate the frequency bandwidth of the stimulated four-wave mixing process in a waveguide for a particular pump frequency with group velocity dispersion $\left. \frac{\partial^2\beta}{\partial\omega^2} \right|_{\omega_p}$. Assuming no losses (i.e., $\alpha = 0$) and substituting the approximate phase mismatch from Eq. 3.35 into the efficiency relation given by Eq. 3.31, we arrive at

$$\eta_{\text{st-fwm, wg}} = (\gamma P_p L)^2 \text{sinc}^2 \left(- \frac{1}{2} \left. \frac{\partial^2\beta}{\partial\omega^2} \right|_{\omega_p} \Delta\omega^2 L \right), \quad (3.36)$$

where we have used the non-normalized convention for the sinc function [specifically, $\text{sinc}(x) \equiv \frac{\sin(x)}{x}$]. The non-normalized $\text{sinc}(x)$ function falls to 3 dB of its peak value when $x \approx \pm 1.39$.

Therefore, we find that to the second order in detuning, the 3 dB angular frequency bandwidth $\Delta\omega_{3\text{ dB}}$ is

$$\Delta\omega_{3\text{ dB}} \approx \sqrt{\frac{2.78}{L} \left(\frac{\partial^2 \beta}{\partial \omega^2} \Big|_{\omega_p} \right)^{-1}}. \quad (3.37)$$

From Eq. 3.37, it is evident that to increase the bandwidth of the four-wave mixing process, we can either decrease the length of the waveguide (though reducing the overall efficiency) or minimize the group velocity dispersion at the pump frequency.

While it is, in principle, possible to simulate the propagation constant $\beta(\omega)$ in a modesolver for all frequencies, it is also computationally intensive to do so over the large parameter space of waveguide geometries. The process of Taylor series expansion of $\beta(\omega)$ around the pump frequency simplifies the dispersion design process since only the group velocity dispersion at a single frequency (the pump) is required. Although a very good approximation when the signal detuning $\Delta\omega$ is fairly small, analysis following Eq. 3.36 can often lead to misleading results when investigating frequencies significantly detuned from the pump, for which the expansion approximation is no longer valid. To increase the model's accuracy at larger signal detunings we expand the propagation constants for the signal an idler out to all orders of detuning and find the full formula for the phase mismatch

$$\begin{aligned} \Delta\beta &= - \sum_{n=2,4,6,\dots}^{\infty} \frac{2}{n!} \frac{\partial^n \beta}{\partial \omega^n} \Big|_{\omega_p} \Delta\omega^n \\ &= - \frac{\partial^2 \beta}{\partial \omega^2} \Big|_{\omega_p} \Delta\omega^2 - \frac{1}{12} \frac{\partial^4 \beta}{\partial \omega^4} \Big|_{\omega_p} \Delta\omega^4 + \mathcal{O}(\Delta\omega^6). \end{aligned} \quad (3.38)$$

Since the signal and idler detuning differ in sign, only the even order derivatives of the propagation constant are relevant to phase matching as explicitly shown in Eq. 3.38. The odd orders derivatives are still important for finding the exact propagation constants at the detuned frequencies but have no effect on the phase matching condition.

It is helpful to consider an example to investigate the level of contribution from the different orders of dispersion. Consider a silicon strip waveguide on a silica slab that is 220 nm thick and 370 nm wide as shown in the inset of Fig. 3.2(a). Fig. 3.2(b) shows the group velocity dispersion (i.e., $\frac{\partial^2 \beta}{\partial \omega^2}$) with a zero crossing at a wavelength of 1558.44 nm. Fig. 3.2(c) shows that there is a

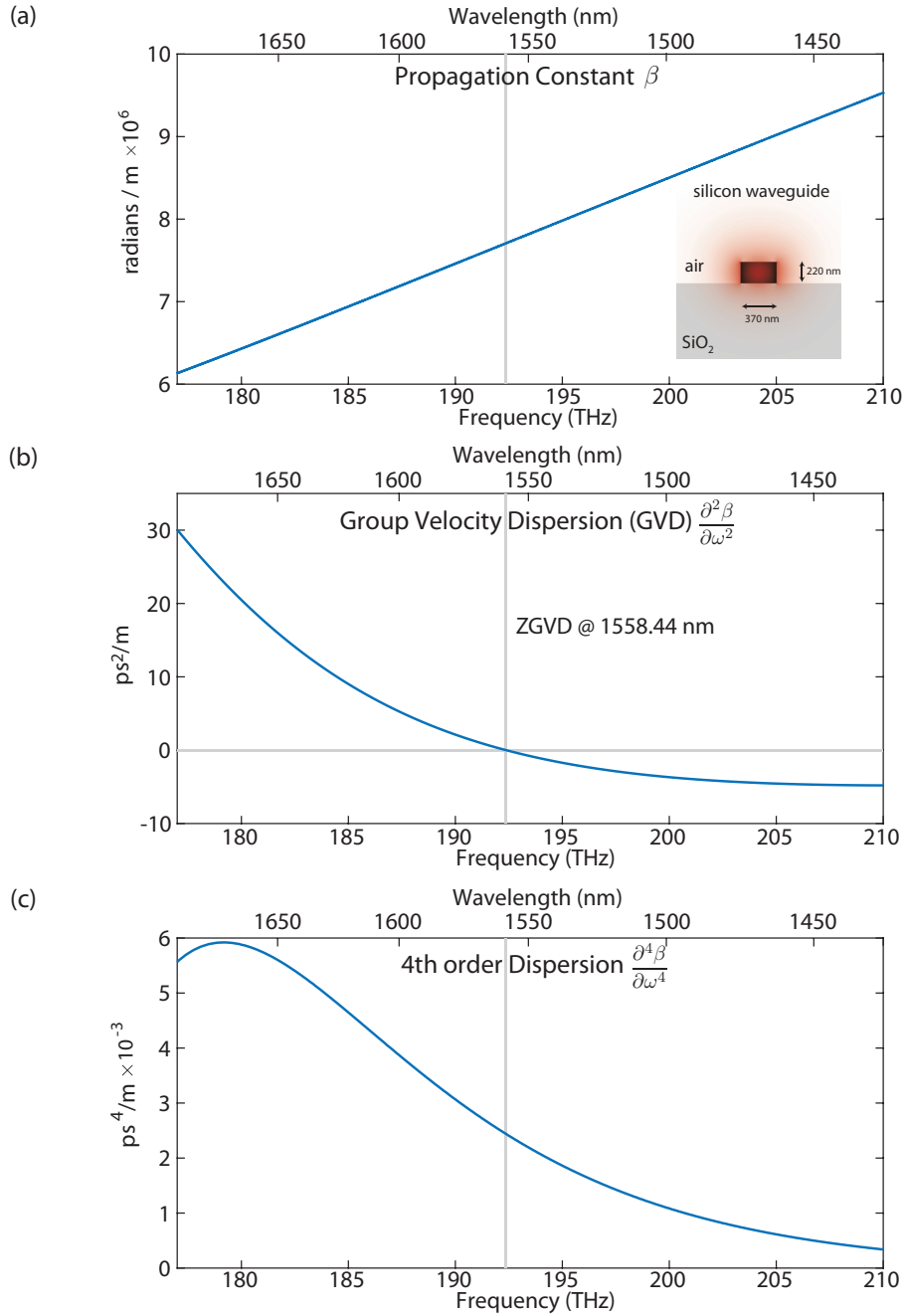


Figure 3.2: (a) Modesolver simulation of the propagation constant versus frequency for a 220 nm thick 370 nm wide silicon strip waveguide on a silica slab. (b) Corresponding group velocity dispersion displaying a zero crossing at 1558.44 nm. (c) Fourth-order derivative of propagation constant with respect to angular frequency which contributes to the phase mismatch as described in Eq. 3.38

still a finite fourth-order dispersion term at that zero group velocity dispersion (ZGVD) wavelength which will contribute to a phase mismatch. Purposely evaluating the approximation in Eq. 3.37

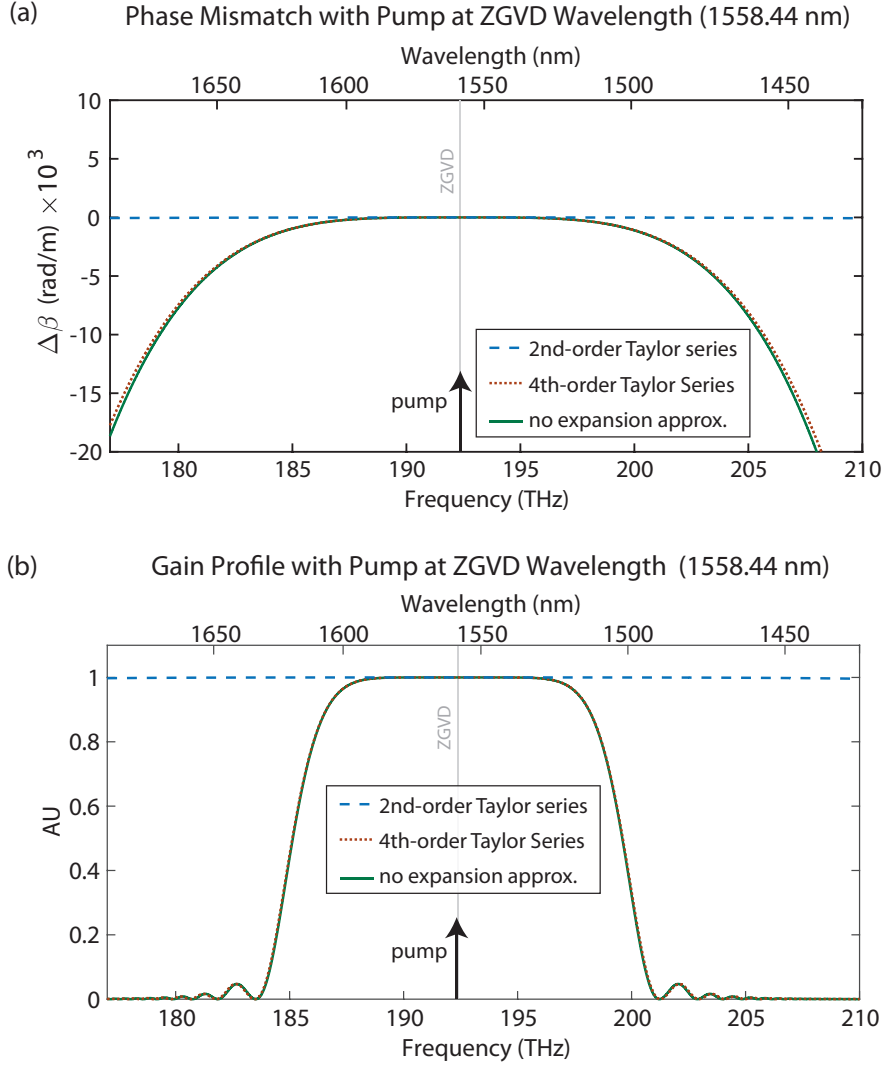


Figure 3.3: Fully simulated, 2nd-order Taylor series expansion, and 4th-order Taylor series expansion of the (a) phase mismatch of 370 nm air cladded waveguide at a pump set to the zero group velocity dispersion (ZGVD) wavelength at 1558.44 nm, (b) corresponding stimulated four-wave mixing efficiency profile

outside the bounds for which it is valid, we find that pumping at the ZGVD wavelength would permit an infinite bandwidth, allowing conversion at an arbitrarily large signal detuning as shown in Fig. 3.3(a). Obviously, this is unphysical and a more precise formulation of the phase mismatch (i.e., using higher order terms from Eq. 3.38) is required to quantify the four-wave mixing bandwidth when pumping at the ZGVD wavelength of this structure.

In Fig. 3.3(a), we assume a pump at the ZGVD wavelength of 1558.44 nm and calculate

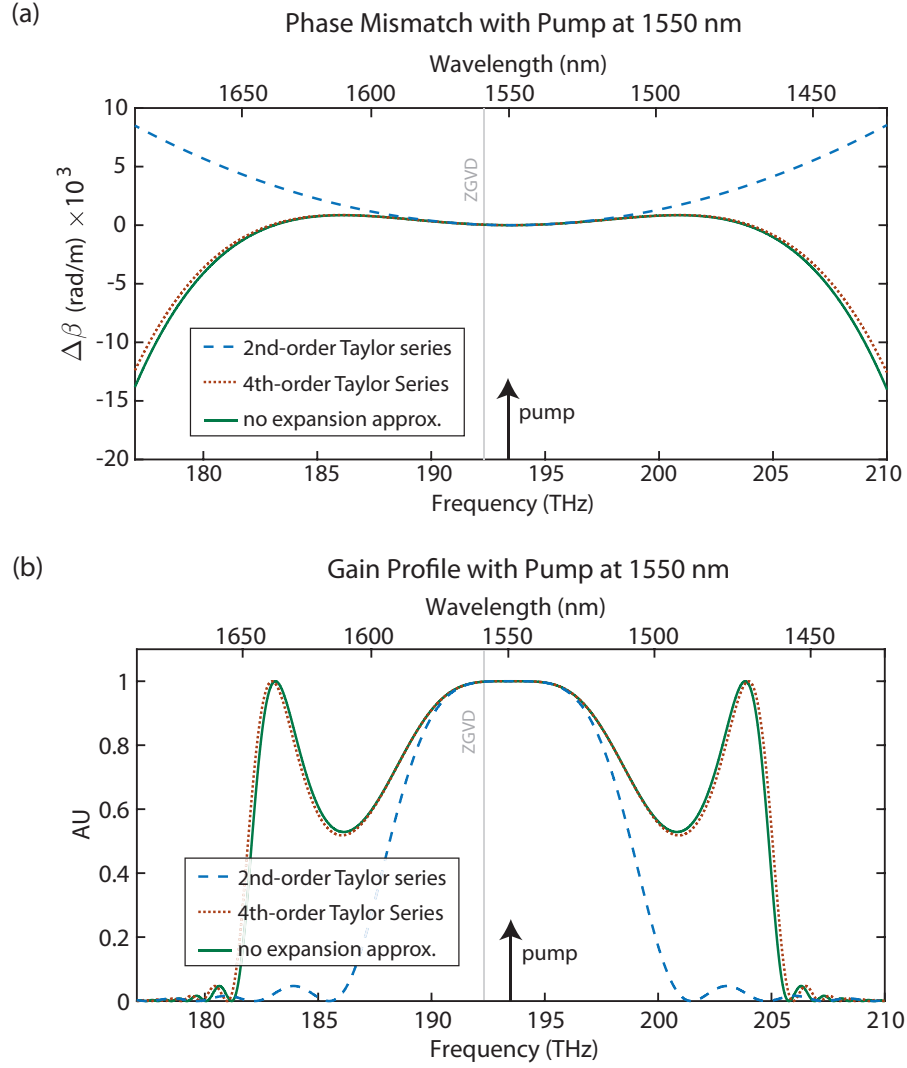


Figure 3.4: (a) phase mismatch at pump set to 1550 nm with (b) corresponding efficiency profile showing that pumping at the ZGVD wavelength does not necessarily result in the largest bandwidth.

the frequency dependence of the phase mismatch approximated by truncating the Taylor series in Eq. 3.38 to both the 2nd-order and 4th-order in detuning. We also compare the approximations to the rigorously calculated phase mismatch, found by numerical modesolver simulations of $\beta(\omega)$ over frequencies from 175 THz to 210 THz. Fig. 3.4(a) presents the same comparison with the exception of having the pump wavelength set to the center of the C-Band (1550 nm). For both pumping scenarios, it is evident that the 4th-order expansion in detuning is nearly equivalent to the rigorous calculation, while the 2nd-order expansion becomes significantly inaccurate at large

detunings. We compare the corresponding normalized four-wave mixing efficiency versus frequency plots (i.e., gain profiles) in Fig. 3.3(b) and Fig. 3.4(b). We see that for this particular waveguide, pumping away from the ZGVD wavelength actually **increases** the gain bandwidth of the four-wave mixing process. The increase in bandwidth from pumping at a wavelength with non-zero group velocity dispersion is a consequence we would not have expected using the 2nd-order expansion relation found in Eq. 3.37. By blue-shifting the pump a mere 8.44 nm from the ZGVD wavelength to 1550 nm, the bandwidth is significantly expanded due to the zero crossings of the phase mismatch at frequencies nearly 10 THz away [Fig. 3.4 (a)], a region of signal detuning where the 2nd-order expansion could lead one to believe had negligible gain [Fig. 3.3 (b)].

The phase mismatch analysis presented in this section demonstrates the need for careful consideration of dispersion properties at signal and idler wavelengths significantly detuned from the pump. When making photon pair sources based on four-wave mixing, it is imperative to have the photon pairs generated far enough away from the pump in wavelength to facilitate pump rejection filters with sufficient extinction to detect the photon pairs.

3.4 Four-wave mixing enhancement in a ring resonator: T-matrix

The analysis used for waveguides in the previous section can be extended to model the corresponding process in a ring resonator [3, 82]. We treat the ring as a section of waveguide with length L and assume that each mode has the same loss (i.e., $\alpha \equiv \alpha_i = \alpha_p = \alpha_s$). After applying the undepleted pump and small-idler approximations, the pump and signal mode propagation are described by

$$a_p(z) = a_p(0)e^{(i\beta_p - \alpha)z} \quad (3.39)$$

$$a_s(z) = a_s(0)e^{(i\beta_s - \alpha)z}. \quad (3.40)$$

with corresponding idler equation found from Eq. 3.28 to be

$$a_i(L) = e^{(i\beta_i - \alpha)L} \left(a_i(0) + i\gamma a_p^2(0) a_s^*(0) \frac{1}{i\Delta\beta - 2\alpha} [e^{(i\Delta\beta - 2\alpha)L} - 1] \right). \quad (3.41)$$

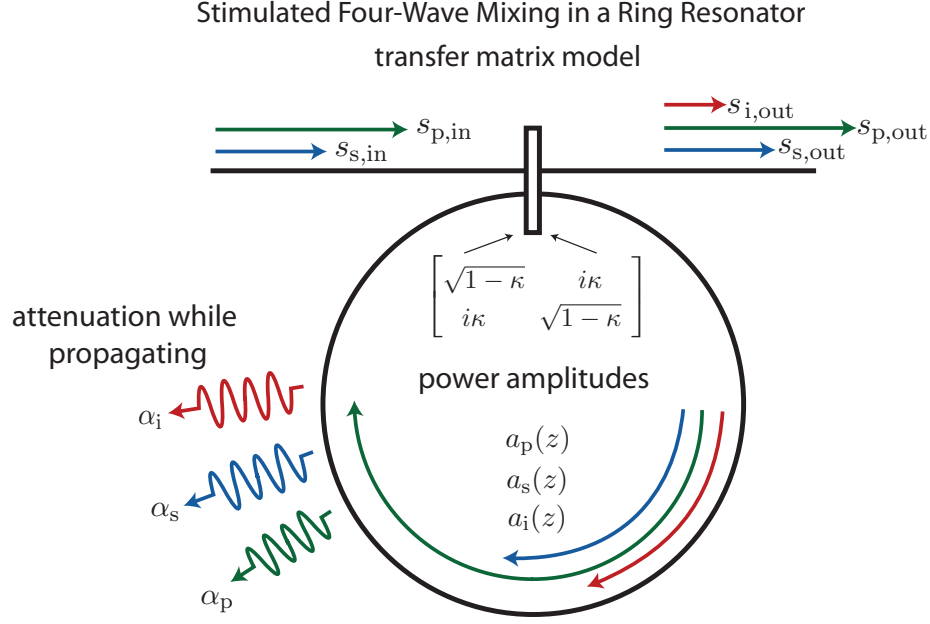


Figure 3.5: Schematic of the four-wave mixing transfer matrix (T-matrix) model where we investigate the coupling of power amplitudes propagating around the ring and use the vertically symmetric convention for the waveguide to ring point coupler.

A characteristic difference between the analysis of resonant and non-resonant four-wave mixing arises in the boundary condition for the idler amplitude at $z = 0$. In a straight waveguide, we assumed the idler amplitude was null at the beginning of the waveguide. The idler light was then generated along the waveguide's propagation length. Alternatively, for the steady-state four-wave mixing condition in a ring resonator, there will be finite idler light present at $z = 0$ from the previous round-trips. We use the T-matrix formulation of the directional coupler (Eq. 2.31 and Eq. 2.32) with cross-coupling power coefficient κ to relate the intra-ring modal amplitudes to the waveguide bus amplitudes ($s_{k,in}$ and $s_{k,out}$ at the input and output, respectively) by

$$s_{k,out} = \sqrt{1-\kappa}s_{k,in} + i\sqrt{\kappa}a_k(L) \quad (3.42)$$

$$a_k(0) = i\sqrt{\kappa}s_{k,in} + \sqrt{1-\kappa}a_k(L), \quad (3.43)$$

where $k \in \{p, s, i\}$. The analysis is illustrated schematically in Fig. 3.5. Solving for the resonantly enhanced four-wave mixing efficiency we find

$$\begin{aligned} \eta_{st-fwm,ring} &= \frac{P_{i,out}}{P_{s,out}} \equiv \left| \frac{s_{i,out}}{s_{s,out}} \right|^2 \\ &= (\gamma P_p L)^2 e^{-4\alpha L} \left[\frac{\sin^2(\Delta\beta L/2) + \sinh^2(\alpha L)}{(\Delta\beta L/2)^2 + (\alpha L)^2} \right] |FE_p|^4 |FE_s|^2 |FE_i|^2, \end{aligned} \quad (3.44)$$

where $|FE_k|$ is the field enhancement (ie., $|FE_k|^2$ is the power enhancement given by Eq. 2.35) for each mode such that

$$|FE_k|^2 = \frac{\kappa}{1 + (1 - \kappa)e^{-2\alpha L} - 2\sqrt{1 - \kappa}e^{-\alpha L} \cos(\beta_k L)}. \quad (3.45)$$

Comparing Eq. 3.44 and Eq. 3.31, we find that the stimulated four-wave mixing efficiency in a ring resonator with circumference L is equivalent to the efficiency in a waveguide of length L scaled by a factor, $|FE_p|^4 |FE_s|^2 |FE_i|^2$, comprised of the product of the power enhancements of the three optical modes, such that

$$\eta_{st-fwm,ring} = \eta_{st-fwm,wg} |FE_p|^4 |FE_s|^2 |FE_i|^2. \quad (3.46)$$

Note, that the factor includes the power enhancement of the pump twice to account for the fact that the pump is degenerate. As a consequence of Eq. 3.44, we find that the maximum four-wave mixing efficiency is achieved at the critical coupling condition for each resonance, where the power enhancements are maximized for a given propagation loss α .

3.4.1 Dispersion and phase matching in a ring

Previously, we investigated the effect dispersion has on the phase matching condition for four-wave mixing in a waveguide. The formula for stimulated four-wave mixing in a ring resonator (Eq. 3.44) suggests that dispersion has the additional effect of influencing the power enhancement of the three interacting modes. When working in the regime where the Q is high enough that negligible power is lost after a single round trip, we can simplify Eq. 3.44 to

$$\eta_{st-fwm,ring} = (\gamma P_p L)^2 |FE_p|^4 |FE_s|^2 |FE_i|^2 \text{sinc}^2(\Delta\beta L/2). \quad (3.47)$$

Note that in this approximation, we only set $\alpha L \rightarrow 0$ in the phase matching component of Eq. 3.44. Attempting to do so in the power enhancement factors would allow for an unphysical infinite efficiency, since it would be possible to reduce the coupling κ arbitrarily towards zero and thereby support an infinite quality factor.

The pump and signal power enhancements are maximized by placing the two laser inputs at the center of their corresponding resonances. In order to mitigate the effects of dispersion, it is often convenient to utilize two resonances separated by a single free spectral range (FSR) for the pump and signal modes. The frequency at which the idler is generated will then be determined by energy conservation in addition to the the pump and signal input frequencies (ω_p and ω_s , respectively), such that $\omega_i = 2\omega_p - \omega_s$. Therefore, if the two free spectral ranges adjacent to the pump resonance are equal, the idler will be generated at the peak of its corresponding resonance as shown in Fig. 3.6(a). However, dispersion (in addition to inducing a phase mismatch) can result in the FSR's on either side of a resonance to differ as shown in 3.6(b). We define the “adjacent FSR mismatch” (in Hz) as

$$\begin{aligned}\Delta\nu_{\text{FSR}} &\equiv \frac{1}{2\pi} [(\omega_{p,o} - \omega_{s,o}) - (\omega_{i,o} - \omega_{p,o})] \\ &\equiv \frac{1}{2\pi} (2\omega_{p,o} - \omega_{s,o} - \omega_{i,o}),\end{aligned}\tag{3.48}$$

where the pump, signal, and idler angular resonance frequencies are $\omega_{p,o}$, $\omega_{s,o}$, and $\omega_{i,o}$, respectively. In the case we are considering, where the pump and signal are on resonance, the energy matching condition sets the frequency ω_i of the generated idler detuned from its corresponding resonance by $\omega_i - \omega_{i,o} = 2\pi\Delta\nu_{\text{FSR}}$. Therefore, the power enhancement of the idler mode contributes an approximately Lorentzian dependence on $\Delta\nu_{\text{FSR}}$ to the four-wave mixing efficiency given by Eq. 3.47.

To quantify the degree to which dispersion affects the spacing of adjacent free spectral ranges, we expand the resonance mode order m around the pump resonance frequency $\omega_{p,o}$ such that we

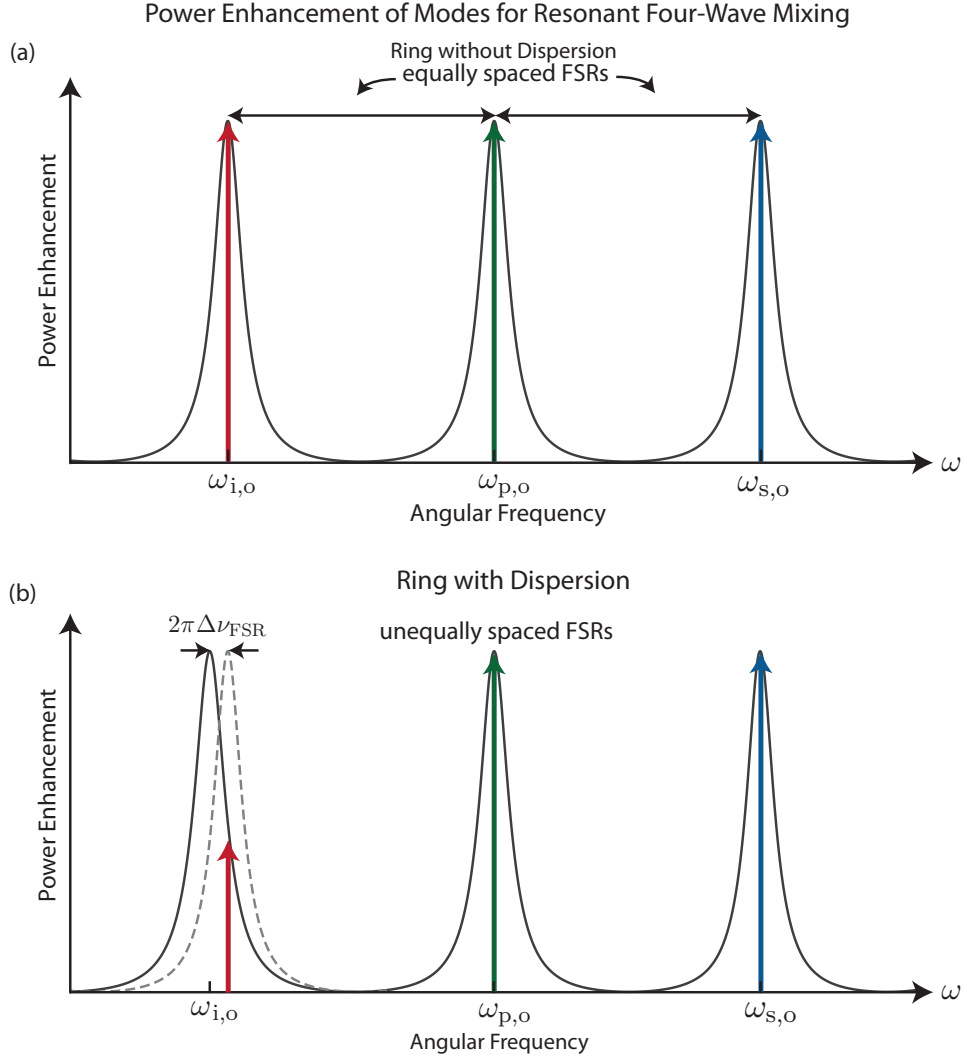


Figure 3.6: Plots demonstrating the resonant enhancement provide by a ring resonator with corresponding power enhancement for the signal, idler, and pump frequencies illustrated by arrows. (a) Dispersionless ring with equal adjacent free spectral ranges allowing all modes to be on peak resonance. (b) Ring resonator modelled with dispersion such that the resonances exhibit a significant difference in free spectral range of $\Delta\nu_{\text{FSR}}$, forcing the idler to be substantially off peak resonance when the signal and idler enhancements are maximized.

can approximate

$$m(\omega) \approx m(\omega_{p,o}) + \left. \frac{\partial m}{\partial \omega} \right|_{\omega_{p,o}} (\omega - \omega_{p,o}) + \left. \frac{1}{2} \frac{\partial^2 m}{\partial \omega^2} \right|_{\omega_{p,o}} (\omega - \omega_{p,o})^2. \quad (3.49)$$

Since the pump mode order is related to the propagation constant β and the ring radius R by

$$m(\omega_{p,o}) = \beta(\omega_{p,o})R, \quad (3.50)$$

we can readily find

$$\left. \frac{\partial m}{\partial \omega} \right|_{\omega_{p,o}} = R \left. \frac{\partial \beta}{\partial \omega} \right|_{\omega_{p,o}} = \frac{R}{v_g(\omega_{p,o})} \quad (3.51)$$

and

$$\left. \frac{\partial^2 m}{\partial \omega^2} \right|_{\omega_{p,o}} = R \left. \frac{\partial^2 \beta}{\partial \omega^2} \right|_{\omega_{p,o}}. \quad (3.52)$$

Defining the signal resonance such that $\omega_{s,o} > \omega_{p,o} > \omega_{i,o}$, the difference in signal and pump mode order is unity (when pump resonance and signal resonance are separated by a single FSR), such that

$$\begin{aligned} m(\omega_{s,o}) - m(\omega_{p,o}) &= 1 \\ &\approx \frac{R}{v_g(\omega_{p,o})}(\omega_{s,o} - \omega_{p,o}) + \frac{1}{2} R \left. \frac{\partial^2 \beta}{\partial \omega^2} \right|_{\omega_{p,o}} (\omega_{s,o} - \omega_{p,o})^2. \end{aligned} \quad (3.53)$$

Similarly, the difference in idler mode order and pump mode order becomes

$$\begin{aligned} m(\omega_{i,o}) - m(\omega_{p,o}) &= -1 \\ &\approx \frac{R}{v_g(\omega_{p,o})}(\omega_{i,o} - \omega_{p,o}) + \frac{1}{2} R \left. \frac{\partial^2 \beta}{\partial \omega^2} \right|_{\omega_{p,o}} (\omega_{i,o} - \omega_{p,o})^2. \end{aligned} \quad (3.54)$$

Defining the average of the two adjacent free-spectral ranges $\nu_{\text{FSR,avg}}$ such that

$$\begin{aligned} \nu_{\text{FSR,avg}} &\equiv \frac{1}{2\pi}(\omega_{p,o} - \omega_{i,o}) - \Delta\nu_{\text{FSR}}/2 \\ &\equiv \frac{1}{2\pi}(\omega_{s,o} - \omega_{p,o}) + \Delta\nu_{\text{FSR}}/2 \end{aligned} \quad (3.55)$$

which can be approximated by the FSR in absence of dispersion

$$\nu_{\text{FSR,avg}} \approx \frac{v_g(\omega_{p,o})}{2\pi R}. \quad (3.56)$$

We evaluate the sum of Eq. 3.54 and Eq. 3.53 and drop all quadratic $\Delta\nu_{\text{FSR}}$ terms to give the approximation of the FSR mismatch [6, 70]

$$\Delta\nu_{\text{FSR}} \equiv 2\omega_{p,o} - \omega_{i,o} - \omega_{s,o} \approx 2\pi v_g(\omega_{p,o}) \left. \frac{\partial^2 \beta}{\partial \omega^2} \right|_{\omega_{p,o}} \nu_{\text{FSR,avg}}^2. \quad (3.57)$$

From Eq. 3.57 we find that, to the second order in frequency, the condition for having equal adjacent free spectral ranges is equivalent to the condition for phase matching (i.e., $\frac{\partial^2 \beta}{\partial \omega^2} = 0$).

To further simplify Eq. 3.47, we investigate how strongly the four-wave mixing efficiency in a ring depends on the two different contributions from dispersion (i.e., the effects of phase matching and FSR matching). Recall that we can approximate the power enhancement near resonance as a Lorentzian (Eq. 2.59). Assuming the pump and signal are both on resonance our efficiency becomes proportional to the product of a Lorentzian term (a characteristic property of resonance) and a $\text{sinc}^2(\Delta\beta L/2)$ term (a characteristic property of phase matching) such that Eq. 3.47 gives

$$\eta_{\text{st-fwm,ring}} \propto \text{sinc}^2(\Delta\beta L/2) \frac{\kappa}{[(\alpha L + \kappa/2)\nu_{\text{FSR}}]^2 + (2\pi\Delta\nu_{\text{FSR}})^2}. \quad (3.58)$$

We can also assume that the resonator is near the critical coupling condition (i.e., $\alpha L \approx \kappa/2$) to optimize the power enhancements for each mode and further simplifying Eq. 3.58 to

$$\eta_{\text{st-fwm,ring}} \propto \text{sinc}^2(\Delta\beta L/2) \frac{\kappa}{(2\alpha L\nu_{\text{FSR}})^2 + (2\pi\Delta\nu_{\text{FSR}})^2}. \quad (3.59)$$

To quantify the individual contribution of the two factors in four-wave mixing bandwidth, we can investigate the 3 dB bandwidth of each of the components. First, we consider the Lorentzian component

$$f_{\text{FSR matching}} \equiv \frac{\kappa}{(2\alpha L\nu_{\text{FSR}})^2 + (2\pi\Delta\nu_{\text{FSR}})^2}, \quad (3.60)$$

where we find that the FSR mismatch $\Delta\nu_{\text{FSR}}$ must be

$$\Delta\nu_{\text{FSR}} < 2\alpha R\nu_{\text{FSR}} \quad (3.61)$$

for $f_{\text{FSR matching}}$ to be within 3 dB of its dispersionless peak. We relate this condition to the GVD in Eq. 3.57 to find that the group velocity dispersion must be

$$\left. \frac{\partial^2 \beta}{\partial \omega^2} \right|_{\omega_p} < \frac{2}{(2\pi\nu_{\text{FSR}})^2} \alpha. \quad (3.62)$$

Similarly, we investigate the phase matching term of Eq. 3.59

$$f_{\text{phase matching}} \equiv \text{sinc}^2(\Delta\beta L/2). \quad (3.63)$$

Since $\text{sinc}^2(1.39) \approx 1/2$, we can approximate $\Delta\beta$ at a free spectral range ν_{FSR} using Eq. 3.35 to find

$$\frac{\Delta\beta L}{2} \approx \frac{1}{2} \left. \frac{\partial^2 \beta}{\partial \omega^2} \right|_{\omega_p} (2\pi\nu_{\text{FSR}})^2 2\pi R < 1.39, \quad (3.64)$$

which rearranged in terms of group velocity dispersion becomes

$$\left. \frac{\partial^2 \beta}{\partial \omega^2} \right|_{\omega_p} < \frac{2}{(2\pi\nu_{\text{FSR}})^2} \frac{1.39}{2\pi R}. \quad (3.65)$$

Comparing the bandwidth given by the FSR mismatch term and the bandwidth given by the phase matching term (Eq. 3.65 and Eq. 3.62, respectively), we find that if

$$\alpha \ll \frac{1.39}{2\pi R} \quad (3.66)$$

the bandwidth of the total four-wave mixing efficiency is dominated by the FSR matching condition. Or in other words, $f_{\text{FSR matching}}$ varies with frequency much faster than $f_{\text{phase matching}}$. In terms of waveguide loss in dB/cm, $L_{\text{dB/cm}}$, the relation in Eq. 3.66 becomes

$$L_{\text{dB/cm}} \ll \frac{0.019}{R}, \quad (3.67)$$

with R in units of meters and $L_{\text{dB/cm}} = 0.2\alpha/(\ln 10)$ [118].

As an example, we can consider a ring radius of $100 \mu\text{m}$ (much larger than the resonators we will investigate in this work, which have a radius on the order of $\sim 10 \mu\text{m}$) and find that the waveguide loss must approach 200 dB/cm for the phase matching bandwidth condition to become significant compared to the FSR matching condition. Silicon photonic waveguides typically exhibit < 10 dB/cm waveguide propagation loss, confirming that the devices investigated within this work are well within the regime defined by Eq. 3.67. This simple analysis demonstrates that the design of dispersion engineered ring resonators is reduced to matching adjacent FSRs, which in turn, guarantees that the process is adequately phase matched.

3.5 Four-wave mixing enhancement in a ring resonator: coupling of modes in time

In the previous section, we determined that the propagation along the waveguide in the ring introduces little loss on a single round trip and that the phase matching condition over such a short distance is negligible with respect to the field enhancement reduction caused by dispersion. Since these assumptions are within the approximations allowed by temporal coupled mode theory which we found in Section 2.6.1, we now build a simplified model of seeded four-wave mixing. The full

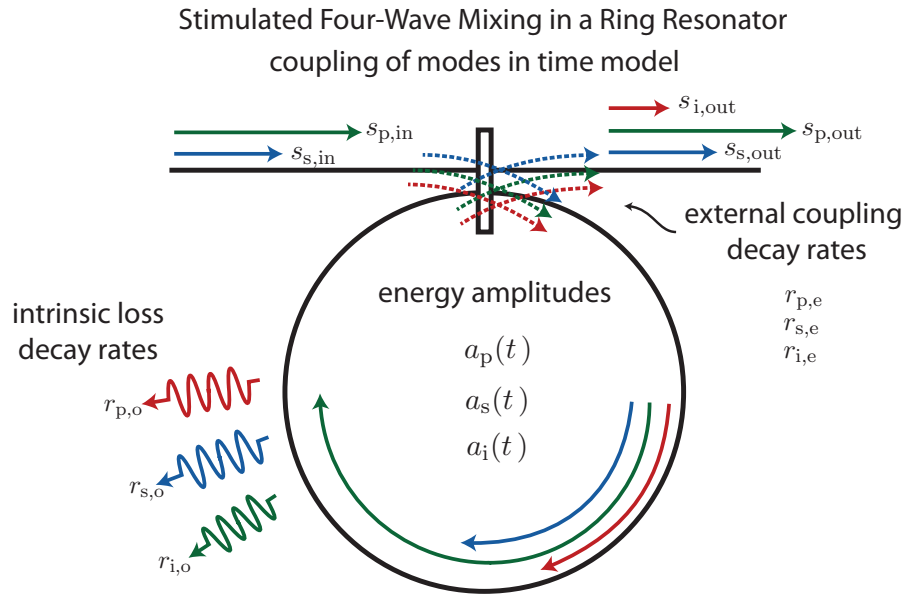


Figure 3.7: Schematic of the four-wave mixing temporal coupled mode theory model where we investigate the coupling of energy amplitudes dynamics in time according to Eqs. 3.68, 3.69, and 3.70.

four-wave mixing temporal coupled mode equations are given by [121, 168]

$$\frac{d}{dt}a_p = (-i\omega_{p,o} - r_{p,e} - r_{p,o})a_p + 2i\omega\beta_{fwm,p}a_s a_i a_p^* + i\sqrt{2r_{p,e}}s_{p,in} \quad (3.68)$$

$$\frac{d}{dt}a_s = (-i\omega_{s,o} - r_{s,e} - r_{s,o})a_s + i\omega\beta_{fwm,s}a_p^2 a_i^* + i\sqrt{2r_{s,e}}s_{s,in} \quad (3.69)$$

$$\frac{d}{dt}a_i = (-i\omega_{i,o} - r_{i,e} - r_{i,o})a_i + i\omega\beta_{fwm,i}a_p^2 a_s^* + i\sqrt{2r_{i,e}}s_{i,in} \quad (3.70)$$

and can be readily found using a similar analysis to that which we used to find the coupling of modes in space equations in Section 3.3, where use of the temporal form of Maxwell's equations

found in Eq. 2.42 is utilized rather than spatial form of Eq. 2.15. We can assume

$$\begin{aligned}\beta_{\text{fwm}} &\equiv \beta_{\text{fwm,p}} \approx \beta_{\text{fwm,s}} \approx \beta_{\text{fwm,i}} \\ &\equiv \frac{n_2 c}{n_{\text{Si}}^2 V_{\text{eff}}}\end{aligned}\quad (3.71)$$

where n_{Si} is the linear index of refraction of the nonlinear material (silicon in our case) and V_{eff} is an effective mode volume.

In the steady state we can take $\frac{d}{dt}a_i \rightarrow -i\omega_i$, $\frac{d}{dt}a_s \rightarrow -i\omega_s$, and $\frac{d}{dt}a_p \rightarrow -i\omega_p$ where ω_k is the frequency of the light in each mode detuned from their corresponding resonance frequency by $\Delta\omega_k = \omega_k - \omega_{k,o}$, with $k \in \{p, s, i\}$. To get an idea of the powers involved for different processes we can see what the energy of pump light $|a_p|^2$ in the resonator will be when we have reached powers above the optical parametric oscillation threshold. To do so we assume that there is no input for the signal and idler modes, i.e. that $s_{i,\text{in}} = s_{s,\text{in}} = 0$. Now simply using equations (3.69) and (3.70) we find that either the device is below threshold (i.e. that $a_s = a_i = 0$) or that it is above threshold and the pump energy in the ring is

$$|a_p|_{\text{oscil}}^2 = \frac{1}{\omega\beta_{\text{fwm}}} \sqrt{(r_{s,\text{tot}} - i\Delta\omega_s)(r_{i,\text{tot}} + i\Delta\omega_i)}. \quad (3.72)$$

It is interesting to note that since the left hand side of Eq. 3.72 is real, when above oscillation threshold the detunings of the signal and idler must obey

$$\frac{\Delta\omega_s}{r_{s,\text{tot}}} = \frac{\Delta\omega_i}{r_{i,\text{tot}}}. \quad (3.73)$$

As a consequence, an above threshold optical parametric oscillator with different signal and idler decay rates can be utilized to asymmetrically distribute the frequency noise of a pump laser [42].

We can now investigate how resonant enhancement improves the efficiency of the four-wave mixing process. As an example we first consider stimulated four-wave mixing where a seed is injected into the resonator along with a strong pump beam such that they mix to generate light at the idler wavelength. As we have seen, dispersion results in adjacent free-spectral ranges differing by a value we have denoted by $\Delta\omega_{\text{FSR}} = 2\omega_{p,o} - \omega_{s,o} - \omega_{i,o}$. If we are far below the threshold for

oscillation we can once again assume that most of the pump light is not converted into the signal and idler frequency modes, by using the before mentioned undepleted pump approximation. Since, we are inputting only a seed at ω_s and a pump at ω_p , we take $s_{i,\text{in}} = 0$. The steady-state nonlinear coupled mode equations then become

$$\frac{d}{dt}a_p = (-i\omega_{p,o} - r_{p,e} - r_{p,o})a_p + i\sqrt{2r_{p,e}}s_{p,\text{in}} \quad (3.74)$$

$$\frac{d}{dt}a_s = (-i\omega_{s,o} - r_{s,e} - r_{s,o})a_s + i\omega\beta_{\text{fwm},s}a_p^2a_i^* + i\sqrt{2r_{s,e}}s_{s,\text{in}} \quad (3.75)$$

$$\frac{d}{dt}a_i = (-i\omega_{i,o} - r_{i,e} - r_{i,o})a_i + i\omega\beta_{\text{fwm},i}a_p^2a_s^* \quad (3.76)$$

$$s_{i,\text{out}} = i\sqrt{2r_{i,e}}a_i. \quad (3.77)$$

Here we have intentionally treated the dynamics of the signal and idler modes symmetrically (with the exception of null idler input power) to include coupling from the pump mode and have not taken the small idler approximation as done previously in Eq. 3.40. We take this small step now, because later in the next chapter when investigating spontaneous four-wave mixing, there is no designated signal input and the two modes must be treated identically.

In the steady state the modal equations become

$$a_p = \frac{i\sqrt{2r_{p,e}}}{-i\Delta\omega_p + r_{p,\text{tot}}}s_{p,\text{in}} \quad (3.78)$$

$$a_s^* = \frac{-i\omega\beta_{\text{fwm}}(a_p^*)^2a_i}{i\Delta\omega_s + r_{s,\text{tot}}} + \frac{-i\sqrt{2r_{s,e}}}{i\Delta\omega_s + r_{s,\text{tot}}}s_{s,\text{in}}^* \quad (3.79)$$

$$a_i = \frac{i\omega\beta_{\text{fwm}}a_p^2a_s^*}{-i\Delta\omega_i + r_{i,\text{tot}}}. \quad (3.80)$$

We can combine the signal and idler equations to find

$$|a_i|^2 = |C_{\text{thresh}}|^{-2} \frac{2r_{s,e}\omega^2\beta_{\text{fwm}}^2|a_p|^4}{(\Delta\omega_i^2 + r_{i,\text{tot}}^2)(\Delta\omega_s^2 + r_{s,\text{tot}}^2)} |s_{s,\text{in}}|^2 \quad (3.81)$$

where

$$\begin{aligned} C_{\text{thresh}} &\equiv 1 - \frac{\omega^2\beta_{\text{fwm}}^2|a_p|^4}{(-i\Delta\omega_i + r_{i,\text{tot}})(i\Delta\omega_s + r_{s,\text{tot}})} \\ &= 1 - \frac{|a_p|^4}{|a_p|_{\text{oscil}}^4}. \end{aligned} \quad (3.82)$$

Here the limitations of the undepleted pump approximation become evident. Specifically, if the pump is strong enough to induce optical parametric oscillation $|a_p|^2 \rightarrow |a_p|_{\text{oscil}}^2$, $C_{\text{thresh}} \rightarrow 0$, and $|a_i|^2 \rightarrow \infty$. But as specified before, we are working in the approximation far below threshold, resulting in $C_{\text{thresh}} \rightarrow 1$ and

$$\begin{aligned} |s_{i,\text{out}}|^2 &= 2r_{i,e}|a_i|^2 \\ &= P_p^2 \omega^2 \beta_{\text{fwm}}^2 \left(\frac{2r_{p,e}}{\Delta\omega_p^2 + r_{p,\text{tot}}^2} \right)^2 \frac{2r_{s,e}}{\Delta\omega_s^2 + r_{s,\text{tot}}^2} \frac{2r_{i,e}}{\Delta\omega_i^2 + r_{i,\text{tot}}^2} |s_{s,\text{in}}|^2. \end{aligned} \quad (3.83)$$

Including dispersion and assuming that the pump and signal are placed on their corresponding resonances the efficiency of the stimulated four-wave mixing process can be written as

$$\eta_{\text{st,fwm}} \equiv \left| \frac{s_{i,\text{out}}}{s_{s,\text{in}}} \right|^2 = P_p^2 \omega^2 |\beta_{\text{fwm}}|^2 \left(\frac{2r_{p,e}}{r_{p,\text{tot}}^2} \right)^2 \frac{2r_{s,e}}{r_{s,\text{tot}}^2} \frac{2r_{i,e}}{(2\pi\Delta\nu_{\text{FSR}})^2 + r_{i,\text{tot}}^2}, \quad (3.84)$$

showing that the efficiency has a Lorentzian dependence with respect to the difference in adjacent free spectral ranges due to dispersion, $\Delta\nu_{\text{FSR}}$.

3.6 Discrete resonance dispersion engineering of ring resonators

In the previous section we found that to dispersion engineer a ring resonator for efficient four-wave mixing, the difference between two adjacent FSRs in frequency, $\Delta\nu_{\text{FSR}}$, must be minimized. Previously, we had simply used a second order Taylor expansion of the propagation constant and found that minimizing the group velocity dispersion is one way of engineering a dispersionless cavity. In Fig. 3.3 we also observed that the second order expansion was increasingly inaccurate as the signal and idler are detuned from the pump frequency. Here we present an all-order dispersion engineering method which takes advantage of the discrete nature of resonance frequencies [47].

Since a waveguide supports a continuum of frequency modes, dispersion engineering entails minimizing the phase mismatching term $\Delta\beta(\Delta\omega)$

$$\Delta\beta = 2\beta(\omega_p) - \beta(\omega_p + \Delta\omega) - \beta(\omega_p - \Delta\omega) \quad (3.85)$$

over some continuous range of frequency detuning $\Delta\omega$. However, a resonant cavity has discrete frequency modes thereby permitting dispersion engineering over the much smaller bandwidth of a

resonance linewidth. Instead of performing a Taylor series expansion of the propagation constant β with respect to frequency, this discrete property of the modes can be used as an advantage in design. For instance, we can solve numerically for the mode number $m(\nu) = R\beta(\nu)$ versus frequency for a given waveguide geometry using a bent waveguide mode solver. This is a monotonic function provided that we are working in the common case where the group velocity maintains sign. We can now invert the function to get $\nu(m)$ as shown in Fig. 3.8 (b). The mode number here is the eigenvalue for a mode in a bent waveguide [116] and is only truly a mode number of a resonance if it is an integer value. To find the difference between adjacent free-spectral ranges versus mode number, we must only calculate $\Delta\nu_{\text{FSR}} = 2\nu(m_p) - \nu(m_p + 1) - \nu(m_p - 1)$. Similarly, we can extend this analysis to N_{FSRs} free spectral ranges away from the pump resonance and inspect how

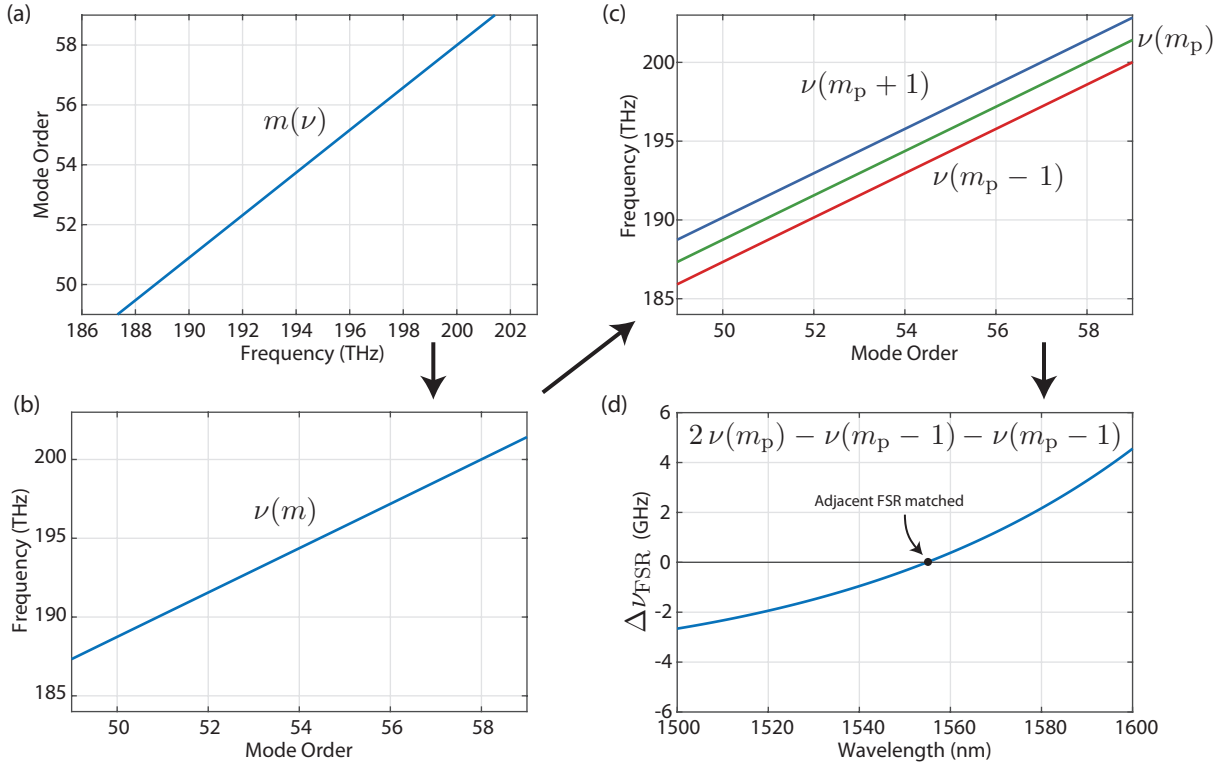


Figure 3.8: Sequence for proposed method of dispersion engineering a ring resonator including (a) numerical simulation of mode order versus frequencies, (b) inversion to have frequency versus mode order, (c) calculate frequency \pm one mode order away, and (d) difference of these showing the difference in free spectral range versus wavelength.

the efficiency changes at these farther detuned resonances by taking the generalization of “FSR mismatching” to $\Delta\nu_{N\text{-FSRs}} = 2\nu(m_p) - \nu(m_p + N_{\text{FSRs}}) - \nu(m_p - N_{\text{FSRs}})$. Now we can pick a pump frequency which is appropriate for the particular application under consideration and then calculate this parameter for various ring geometries to find a dispersionless design.

We note that even if we find a geometry with our calculated $\Delta\nu_{\text{FSR}} = 0$ for a given pump frequency, we have not guaranteed that that particular pump frequency is actually on resonance with a mode of the cavity. In fact, absolute knowledge of the resonance frequency of a ring resonator is almost never possible due to the sensitivity of fabrication imperfections. In this case, a tunable ring via a thermo-optic heater may be helpful to ensure pumping at exactly the pump frequency intended with minimal effect on the dispersion properties of the device.

As an example, we simulate using this procedure the single FSR resonance frequency mismatch $\Delta\nu_{\text{FSR}}$ for an oxide-cladded silicon ring of thickness 220 nm at a pump wavelength of 1550 nm. We simulate this parameter for widths from 380 nm to 600 nm and ring radii from 3 to 12 microns

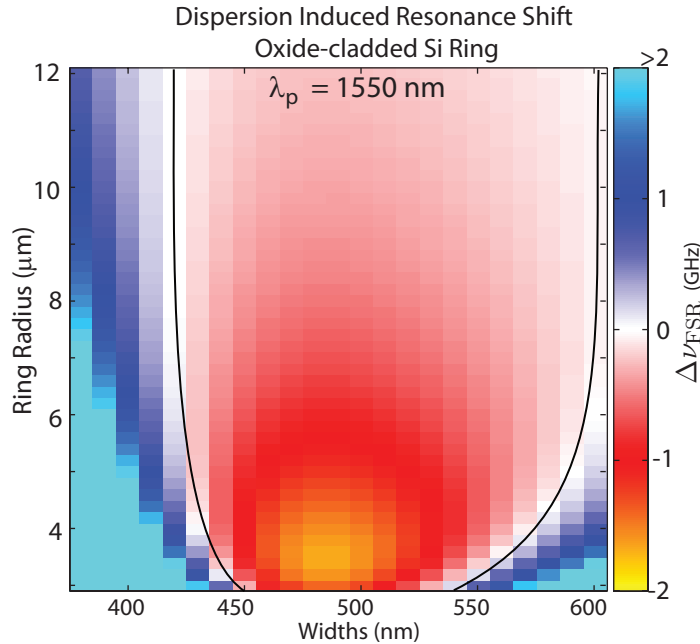


Figure 3.9: Simulation of dispersion induced resonance shift using the proposed discrete resonance dispersion engineering method for a silicon oxide cladded, 220 nm thick silicon ring resonator at a pump wavelength of 1550 nm.

as shown in Fig. 3.9. At large radii the waveguide width for a dispersionless design stays fairly constant at 420 nm and 600 nm. However, at radii shorter than $\approx 6 \mu\text{m}$, the dispersion induced by the mode shape deformation from the sharp bending begins to dominate and the zero dispersion width becomes much more sensitive to ring radius.

3.7 Tunable coupled-mode dispersion compensation

We have looked at simulating a parameter space of a ring resonator geometry to find the dimensions which are most supportive of phase matching and the four-wave mixing process. However, there is also no guarantee that the process used to fabricate the photonic devices supports a ring resonator geometry that has a dispersionless design. Alternatively, a process may support a dispersionless design but at a free spectral range which is not suitable to a certain application. For instance, this type of design can impose severe restrictions on the wavelength and mode volume. Furthermore, once a dispersionless design is set by a particular geometry, it is fixed. There are many applications which benefit from the ability to tune the amount of dispersion within the ring resonator. For instance, although we had not included the effects of phase modulation in the analysis of the devices we have been investigating due to the low powers involved, other applications such as wavelength conversion, optical parametric oscillation, and optical frequency combs require higher powers where it is necessary to account for these effects. The different strength of self-phase modulation (SPM) and cross-phase modulation result in an intensity dependent phase matching condition (or equivalently an intensity dependent effective dispersion). Therefore if we would like one of these higher power devices to operate over a wide range of input powers, it would be beneficial to actively tune the dispersion properties to account for different applications. In this section we investigate a method for achieving tunable dispersion compensation.

3.7.1 Coupled resonator modes and frequency splitting

In Section 3.4.1 we found that satisfying the phase matching condition in a ring resonator reduces to constructing a resonator with equal (in frequency) adjacent free spectral ranges. Rather

than exclusively tailoring a ring's geometry based on its dispersive properties, here we investigate the possibility of designing a ring resonator without any regard for dispersion or phase matching until the very end of the design process. Instead, the initial steps in designing the four-wave mixing device can be concerned with optimizing other parameters and then compensating for dispersion as a last step. For instance, a particular FSR or pump wavelength may be restricted by a specific application. To optimize efficiency it would also be advantageous to maximize the tradeoff between high quality (Q) factor and small mode volume found in Eq. 3.84. Then after these parameters have all been set, we would like to determine the “FSR mismatch” and simply apply a physical process to compensate for this effect.

Such a mechanism is available through the coupling of resonator modes [48]. Consider two resonant modes represented by the amplitudes a_1 and a_2 , with uncoupled resonant frequencies denoted by $\omega_o + \delta\omega_o$ and $\omega_o - \delta\omega_o$, respectively, with identical decay rates r_o . We can formulate the dynamics of such a structure by the coupled mode equations [58, 138]

$$\frac{d}{dt}\vec{a} = -i\bar{\omega} \cdot \vec{a} + i\bar{\mu} \cdot \vec{a} \quad (3.86)$$

where

$$\bar{\omega} = \begin{pmatrix} \omega_o + \delta\omega_o - ir_o & 0 \\ 0 & \omega_o - \delta\omega_o - ir_o \end{pmatrix} \quad (3.87)$$

and

$$\bar{\mu} = \begin{pmatrix} 0 & \mu_{12} \\ \mu_{21} & 0 \end{pmatrix}. \quad (3.88)$$

The coefficients μ_{12} and μ_{21} represent the strength at which energy couples between the modes and are constrained by energy conservation to obey $\mu_{12} = \mu_{21}^*$. In the lossless case where μ_{12} is real, we can define the parameter μ such that $\mu \equiv \mu_{12} = \mu_{21}$.

Steady state solutions of Eq. 3.86 can be found where the eigenmodes of the system are

$$\vec{a}_+ = \frac{1}{C} \begin{pmatrix} 1 \\ \frac{\sqrt{\mu^2 + \delta\omega_o^2} - \delta\omega_o}{\mu} \end{pmatrix} \quad (3.89)$$

$$\vec{a}_- = \frac{1}{C} \begin{pmatrix} -\frac{\sqrt{\mu^2 + \delta\omega_o^2} - \delta\omega_o}{\mu} \\ 1 \end{pmatrix} \quad (3.90)$$

where C is a normalization constant. The corresponding eigenfrequencies are

$$\omega_+ = \omega_o - ir_o + \sqrt{\mu^2 + \delta\omega_o} \quad (3.91)$$

$$\omega_- = \omega_o - ir_o - \sqrt{\mu^2 + \delta\omega_o}. \quad (3.92)$$

It is convenient to evaluate Equations 3.89 to 3.92 in the limits of degenerate resonances ($\delta\omega_o = 0$). In this situation, the supermodes contain equal energy in each resonance with a symmetric supermode $\vec{a}_+ = (1, 1)^T/\sqrt{2}$ and an antisymmetric supermode $\vec{a}_- = (1, -1)^T/\sqrt{2}$, separated in frequency by 2μ . This frequency splitting is a defining characteristic of mode coupling and when weak can be used to create a 2nd-order filter response [86], while stronger splitting can create two distinct Lorentzian shaped resonances. Note that in the regime where the two resonances differ greatly in frequency (i.e., $\delta\omega_o \gg \mu$), the resonances behave as though they are not coupled, such

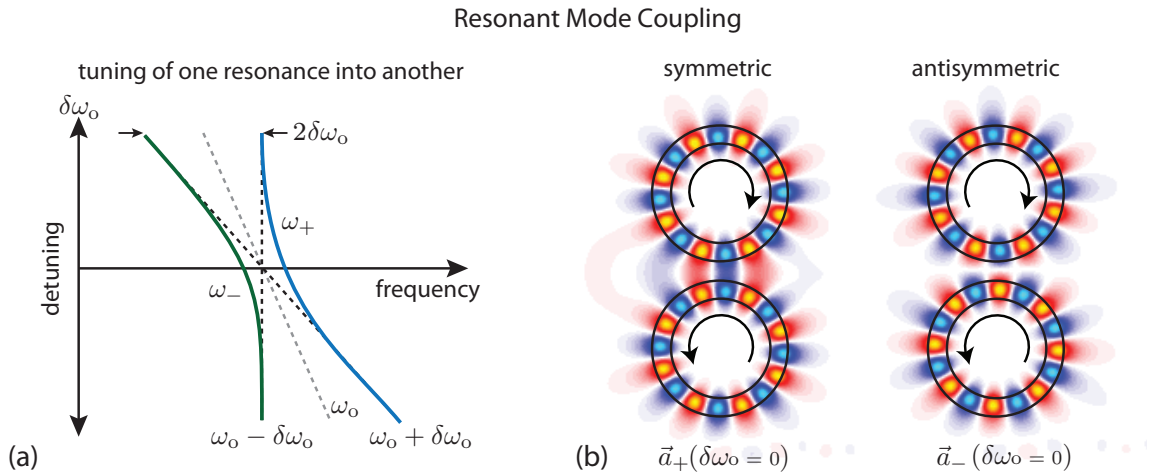


Figure 3.10: (a) Proposed resonator geometry of two differently sized coupled cavities with corresponding uncoupled resonance frequencies (b) that are not energy matched due to dispersion.

that the eigenfrequencies approach their uncoupled resonance frequencies ($\omega_{\pm} \rightarrow \omega_o + \delta\omega_o - ir_o$) and the energy in the supermodes becomes primarily concentrated in a single ring [$\vec{a}_+ = (1, 0)^T$ and $\vec{a}_- = (0, 1)^T$]. In Fig. 3.10(a) we illustrate the coupling of two resonances where the resonance frequency of one is tuned across the other.

Since mode coupling can shift a resonance frequency, we now consider the possibility of strategically translating (in frequency) one of the three modes present in four-wave mixing for compensating dispersion and thereby enabling phase matching. We first consider which resonance modes and what underlying physical process for mode coupling is best suited to fit this application. Within a single-ring resonator there are at least two relatively simple ways of creating degenerate (in frequency) resonant modes that can then be coupled. First, counter propagating modes in an ideal ring resonator are degenerate and therefore can be strongly coupled by introducing scatterers such as a bragg grating within the ring [91]. Another option, is engineering a degeneracy between two resonant modes of different polarizations such as a TE and TM mode [120]. These modes can similarly be coupled by perturbations to the ring. Unfortunately both of these options leave little control over each individual mode as any perturbation to one of the modes will unintentionally

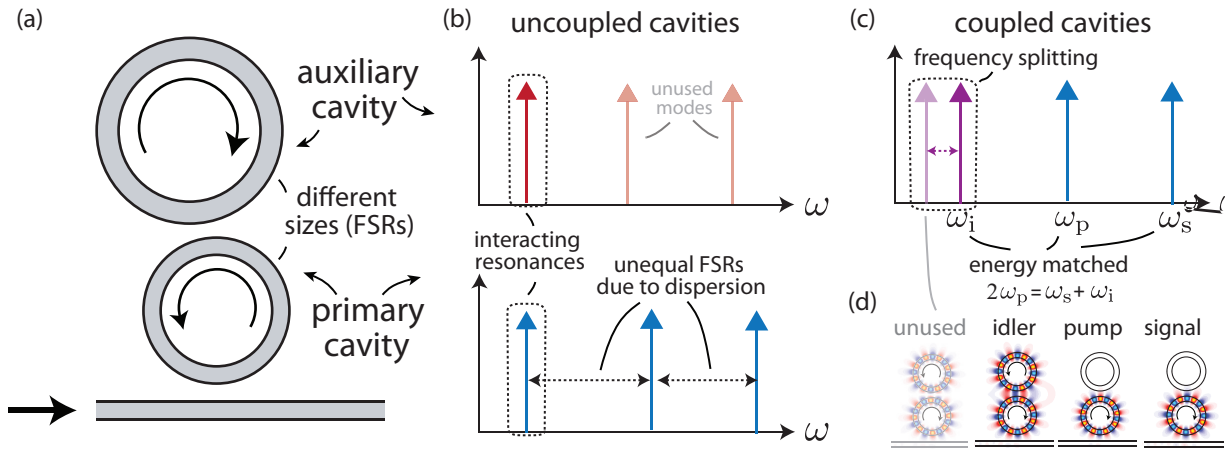


Figure 3.11: (a) Proposed resonator geometry of two differently sized coupled cavities with corresponding uncoupled resonance frequencies (b) that are not energy matched due to dispersion. (c) Coupling results in frequency splitting at a single FSR allowing energy matching between three resonances (d) Supermode of split resonance spans both rings [48].

affect its degenerate counterpart. This makes it nearly impossible to reliably control the strength of frequency splitting, an important factor for creating a tunable dispersion compensating mechanism.

Here, we propose and demonstrate mode coupling between two distinct side-coupled ring resonators [48]. Since the degenerate uncoupled modes in this situation are spatially separated in two different resonators, we can actively tune one with respect to the other with low cross-talk to the other mode. If the two resonators are identical as illustrated in Fig. 3.10(b), they would have identical free spectral ranges, and therefore the mode coupling would occur at all resonances. To localize the mode coupling to the single mode order which we wish to split, we use ring resonators with slightly different radii, resulting in mismatch FSRs. A schematic of the proposed method of operation is illustrated in Fig. 3.11. The four-wave mixing occurs in a “primary cavity” which is the smaller ring to maximize efficiency. A slightly larger ring resonator, which we refer to as the “auxiliary cavity”, can then be tuned to interact with the idler mode and split the resonance just enough to compensate for the “FSR mismatch” caused by dispersion.

The concept was experimentally demonstrated in a silicon microring system fabricated in a silicon-on-insulator platform with a 220 nm thick silicon device layer, a 2 μm buried oxide, and a

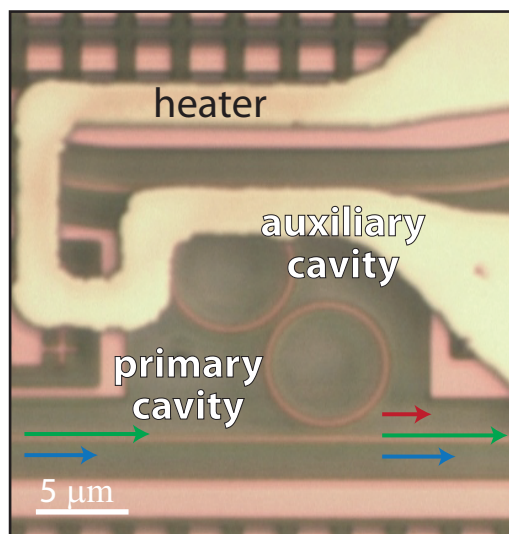


Figure 3.12: Optical micrograph of fabricated tunable coupled-mode dispersion compensation device [48] fabricated through ePIXfab Multi-Project Wafer shuttle runs. A resistive gold microheater was fabricated at the Colorado Nanofabrication Laboratory (CNL).

1 μm thick silica overladding. The fabricated device consists of a primary and auxiliary ring with 3.5 μm and 3.61 μm radius respectively [Fig. 3.12]. The primary ring has a measured 27 GHz “FSR mismatch” due to dispersion ($\Delta\nu_{\text{FSR}}$). The device includes an additional auxiliary waveguide bus which is very weakly coupled for device characterization. A resistive heater for thermal tuning was fabricated above the auxiliary cavity on the silica overladding using contact photolithography. Fig. 3.13 shows the passive (low power) spectral responses of the through port of the primary ring for a range of heater powers. In Fig. 3.14 we plot the center of the four relevant resonances over a range of heater powers. As the heater power on the auxiliary ring is reduced the unused mode begins to overlap with idler mode where they couple and frequency splitting occurs.

Maximum mode splitting occurs at a heater power of 43 mW. The heater power at which optimum dispersion compensation ($\Delta\nu_{\text{FSR}} = 0$) occurs was found to be 44.3 mW as shown in Fig. 3.14(a). The auxiliary resonance (labeled as the “unused” mode in Fig. 3.14(a) at high heater powers and the idler mode at low heater powers) shows a strong dependence on heater power. A linear fit provides a thermal tuning efficiency of approximately 0.11 nm/mW. The pump and signal resonance frequencies also vary slightly over the range of heater power due to thermal crosstalk, which is fit to be about five times less efficient at 0.02 nm/mW. Fig. 3.14(b) shows the difference in free-spectral range over the same range of heater powers. This is then fitted to the coupling of modes in time model (Eq. 3.86) and shows strong agreement with the model.

Seeded FWM was then demonstrated at a range of heater powers spanning from 30 to 70 mW as shown in Fig. 3.16. At each heater power, the pump and signal wavelengths were subsequently tuned to optimize conversion efficiency to account for slight changes in the absolute resonance frequency of each mode due to thermal crosstalk and temperature variations. To achieve high pump power, a tunable telecom single frequency laser was amplified by an erbium-doped fiber amplifier (EDFA) followed by two cascaded 5 nm wide band-pass filters to remove most of the EDFA’s amplified spontaneous emission noise.

Each measurement was performed with an estimated on-chip pump power of 8.7 dBm and signal power of -14.9 dBm in the waveguide bus. A peak FWM efficiency of -37.9 dB, correspond-

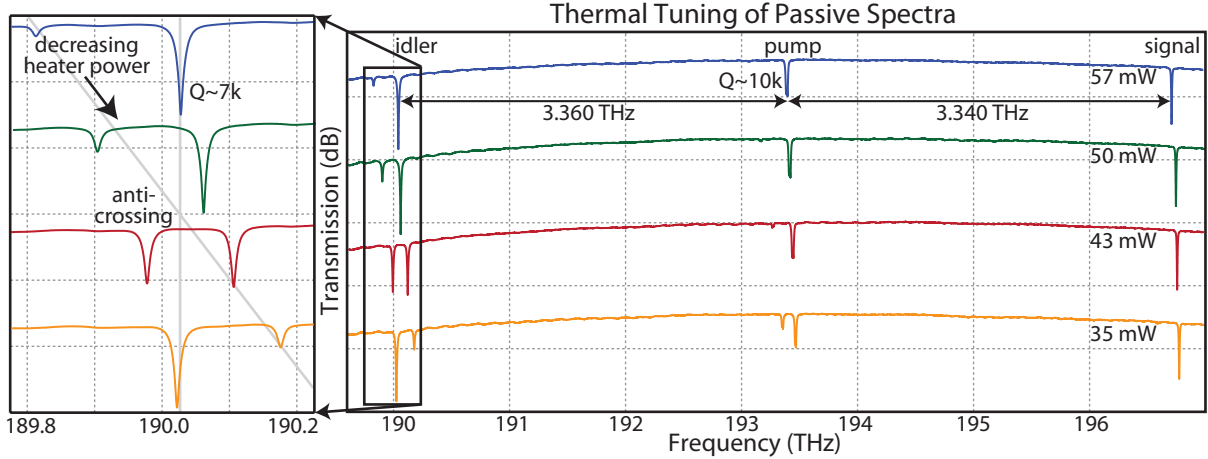


Figure 3.13: Example transmission spectra of the coupled cavities for heater powers of 35 mW, 43 mW, 50 mW, and 57 mW. At a heater power of 57 mW a small transmission dip due to the auxiliary ring is evident at a frequency less than the idler resonance frequency. As the heater power is reduced to 43 mW strong mode coupling at the idler resonance is displayed [48].

ing to a generated idler power of -52.8 dBm in the waveguide, was found at a heater power of 42.1 mW. The output to the optical spectrum analyzer (OSA) for this particular result is shown in Fig. 3.15. The device exhibits dispersion compensation leading to 8 dB of enhancement of the FWM efficiency from the uncoupled case as shown in Fig. 3.16. Due to the aforementioned thermal crosstalk of the heater, the wavelengths of the pump, signal, and idler varied by ~ 1 nm across the tuning range, centered around 1550 nm, 1524 nm, and 1578 nm respectively. This corresponds to FWM across an FSR of 3.334 THz (~ 27 nm) which is, to the best of our knowledge, the largest FSR in a silicon resonator demonstrated to support FWM. The efficiency dependence predicted from the measured idler linewidth and passively measured detuning ($\Delta\nu_{\text{FSR}}$) shown by the blue line in Fig. 3.16 according to Eq. 3.84, normalized to the -37.9 dB peak efficiency.

We note that the maximum FWM efficiency was found to be at a heater power different than one would predict from the passive spectra (42.1 mW vs 44.3 mW). We attribute this to the aforementioned nonlinear shift $\Delta\nu^{NL}$ at the higher pump powers used during FWM. It is well known that XPM is a factor of 2 larger than SPM due to wavelength degeneracy [4]. This effectively shifts the signal and idler modes further down in frequency than the pump mode causing additional FSR

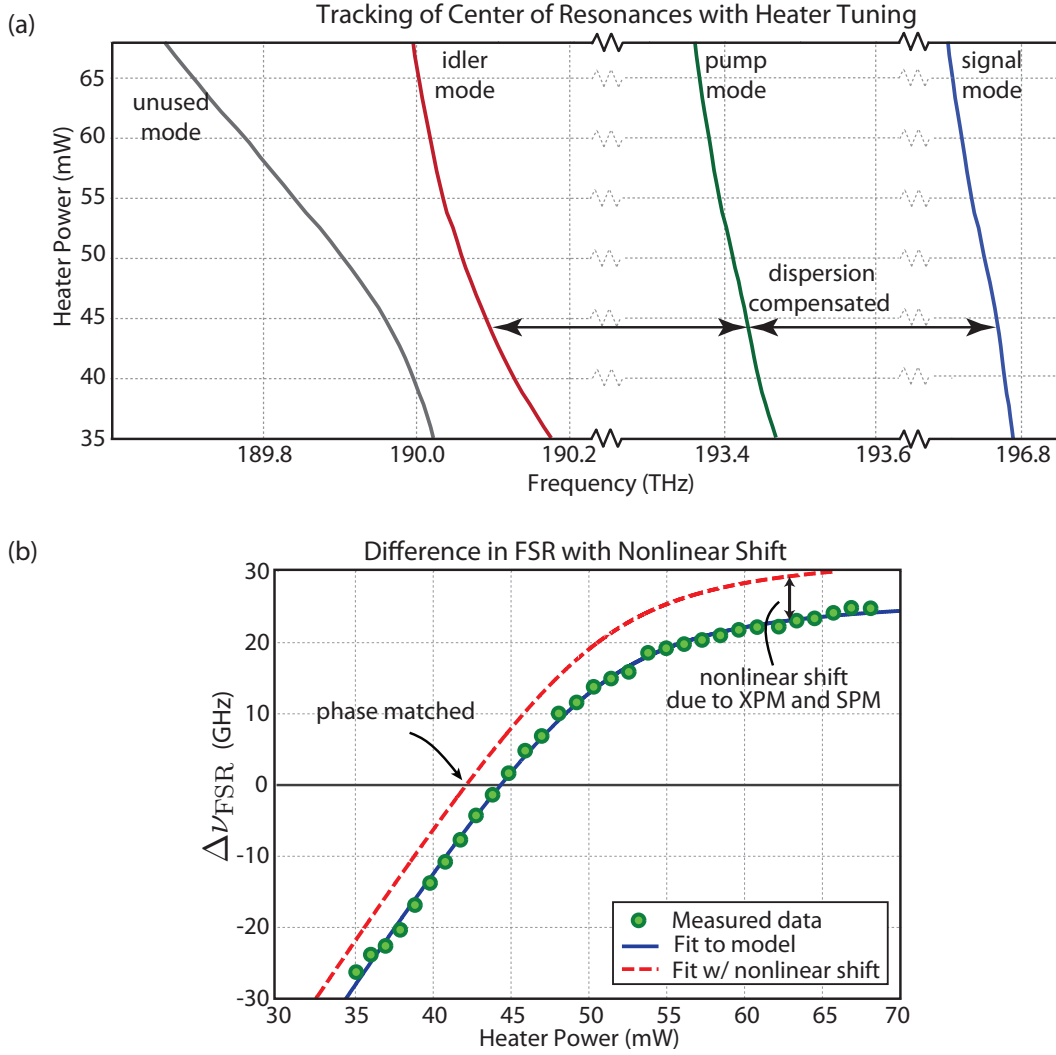


Figure 3.14: (a) Plot of the center frequency for each of the four relevant resonances over the range of heater powers applied. At 44.3 mW, the signal and idler resonances are equally spaced from the pump resonance, thereby demonstrating dispersion compensation. (b) Measured difference in adjacent free spectral range with heater power. The blue line is a fit to the data using temporal coupled mode theory and the dashed red line is the same line shifted up by 6 GHz to represent the combined effect of self- and cross-phase modulation [48].

mismatch to that caused by dispersion. The red dashed line in Fig. 3.14(b) shows the estimated $\Delta\nu$ with the additional $\Delta\nu^{NL} \approx 6$ GHz shift resulting in a much better fit to the measured data as shown in Fig. 3.16.

We note, specific to our resonator configuration, that the assumption that the FWM coefficient β_{fwm} in the coupled mode equations is independent of $\Delta\nu$ is not rigorously valid, since

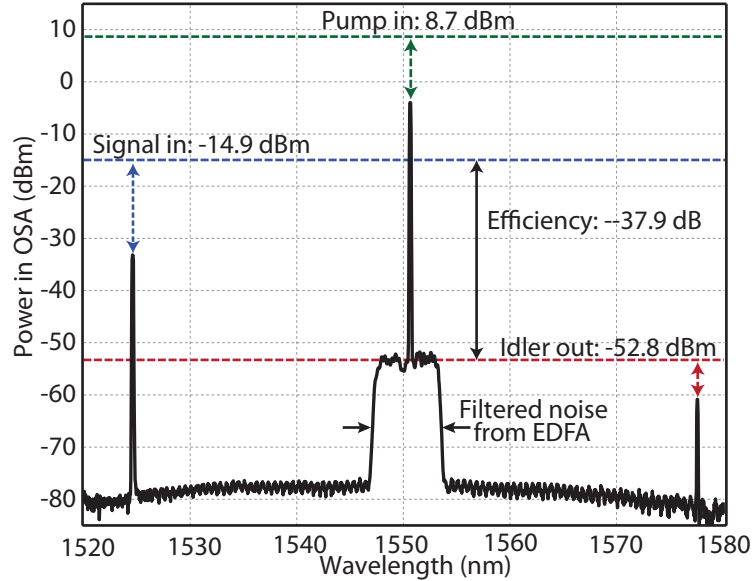


Figure 3.15: OSA output spectrum of highest efficiency (-37.9 dB) seeded four-wave mixing measurement. Dashed lines represent the corresponding powers of each mode in the waveguide. The actual values of the spectrum peaks for the pump and signal modes are reduced by the resonance as well as loss due to outcoupling through a grating coupler. Alternatively, the idler mode experiences little loss from the resonance since it is generated within the ring and only experiences loss on transmission through the grating coupler [48].

the idler mode becomes distributed across both cavities as the dispersion compensating frequency splitting occurs and the mode is more or less hybridized as a result [Fig. 3.11(d)]. However, we argue that the FWM coefficient can, at most, be reduced to $1/\sqrt{2}$ that of the uncoupled state (assuming maximally split idler supermodes are needed to compensate the dispersion). This is a much slower dependence than the Lorentzian rolloff in the stimulated efficiency relation (equation in previous section) and therefore can be ignored for understanding the underlying physics of the system. However, the reduced mode overlap does imply that this form of dispersion compensation can reduce the total efficiency to 1/2 that of a single dispersionless resonator of the same size as the primary cavity (while noting that a dispersionless design of the same mode volume and Q may not be possible). This may be a necessary trade-off and small price to pay to gain a small mode volume and large FSR, enabling broadly separated signal and idler and potentially higher overall conversion.

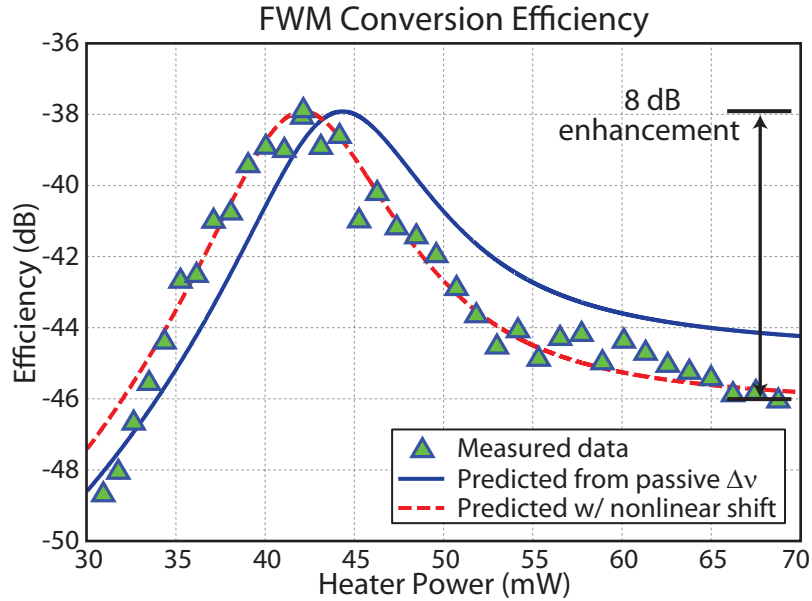


Figure 3.16: Measured converted efficiency versus heater power demonstrating tunable dispersion compensation. The blue line represents the expected efficiency from a model ignoring the effects of phase modulation while the red dashed line takes these effects into account and exhibits a stronger fit [48].

3.8 Conclusions

In this chapter we have described the origin of the four-wave mixing process through the nonlinear polarizability which is proportional to the cube of the applied electric field. We have analyzed the properties of four-wave mixing in a waveguide and described the important effect of phase matching and dispersion. In a ring resonator, we found that dispersion also results in a phase mismatch, but more importantly creates an asymmetry between adjacent free spectral range, thereby greatly reducing the stimulated four-wave mixing efficiency. While this condition is more restrictive than phase matching, it allows for the implementation of a novel design process which we described in Section 3.6.

In Section 3.7 we proposed and demonstrated a tunable mode coupling approach to dispersion compensation and phase matching in resonant four-wave mixing systems. We demonstrated resonant four-wave mixing across the largest FSR to our knowledge in silicon using a proposed

dual-cavity device designed to compensate dispersion through structural degrees of freedom. Having a large frequency separation between the pump and signal/idler modes can be advantageous for photon pair sources where significant pump rejection is required to remove the input light from the generated photons. We note also that the dispersion control demonstrated has multiple additional advantages. For instance, in applications such as heralded photon sources where additional signal-idler modes are undesirable, our configuration can be used to avoid generating extra comb lines. Compensating only one resonance will result in all other FSRs not being energy matched and therefore prevent additional signal-idler modes. On the contrary, this device can benefit the generation of a comb in an already dispersionless cavity by compensating the deleterious effect of differential SPM and XPM on the pump mode in an otherwise equispaced comb. This would address an important problem in comb design. In fact, since the original publication of this work [48] where the concept was first demonstrated, it has been subsequently used utilized by others to control the dynamics of the frequency comb generation process, including repetition rate selection and mode locking [164].

Chapter 4

Quantum regime: Photon pair generation and CMOS integration

4.1 Introduction and background

In the previous chapter, the classical description of four-wave mixing (FWM) provided significant insight into the design considerations needed for efficient operation. However, our ultimate goal is to produce and measure quantum correlated photons generated from this process and therefore we need to establish a mathematical description of the spontaneous FWM process in absence of an injected signal. In this chapter we will see how vacuum fluctuations “seed” the FWM interaction in a resonator.

In addition, we present the implementation a photon pair source on a chip fabricated in an advanced CMOS microelectronics process. By demonstrating that a commercial fabrication process which currently mass produces billions of interconnected electrical components can support the construction of a quantum correlated photon pair source, we provide a significant step towards future large-scale quantum photonic technologies. In four-wave mixing, two pump photons are, to a good approximation, instantaneously annihilated while a signal and idler pair are created, making the generated photons strongly correlated in time and energy. This correlation in time is the principle which allows for the construction of a heralded single photon source, where measuring one of the photons of the pair can inform the experimenter that another photon has been “prepared” (or heralded) for an experiment.

4.2 Theory

As we reviewed in Section 2.6.3, in order to treat the four-wave mixing process at the quantum level we must work with creation and annihilation operators in the place of the previous modal amplitudes. Since the pump will, for all intents and purposes in this thesis, be a classical coherent state we can keep its description identical to before, where the modal amplitude $a_p(t)$ is a classical complex number. The pump mode is normalized such that $|a_p(t)|^2$ is the classical energy (in Joules) of the pump light distributed throughout the resonator. Since the pump is kept classical, the formulation can be referred to as a “semi-classical” formulation. On the other hand, since the signal and idler modes have vacuum input into the resonator, their mode dynamics must be treated quantum mechanically. The amplitudes of the signal and idler modes are operators $\hat{a}_s(t)$ and $\hat{a}_i(t)$ normalized such that $\hat{a}_s^\dagger(t)\hat{a}_s(t) = \hat{N}_s(t)$ and $\hat{a}_i^\dagger(t)\hat{a}_i(t) = \hat{N}_i(t)$, where $\hat{N}_s(t)$ and $\hat{N}_i(t)$ are the photon number operators of the signal and idler cavity modes, respectively. To find the expected value of photons in the corresponding resonator modes at a given time t , one simply calculates

$$\text{expected signal photons in resonator} = \langle \hat{N}_s(t) \rangle = \langle a_s^\dagger(t) a_s(t) \rangle \quad (4.1)$$

$$\text{expected idler photons in resonator} = \langle \hat{N}_i(t) \rangle = \langle a_i^\dagger(t) a_i(t) \rangle. \quad (4.2)$$

We can mathematically describe the process of spontaneous four-wave mixing in a resonator with coupled differential equations very similar to the classical coupled mode equations of Eqs. 3.68, 3.69, and 3.70. The corresponding quantum formulation for the dynamics of the signal and idler modes are

$$\frac{d}{dt} \hat{a}_s(t) = (-i\omega_{s,o} - r_{s,o} - r_{s,e}) \hat{a}_s(t) + i\omega\beta_{\text{fwm}} a_p^2(t) \hat{a}_i^\dagger(t) + i\sqrt{2r_{s,o}} \hat{n}_{s,\text{in}}(t) + i\sqrt{2r_{s,e}} \hat{s}_{s,\text{in}}(t) \quad (4.3)$$

$$\frac{d}{dt} \hat{a}_i(t) = (-i\omega_{i,o} - r_{i,o} - r_{i,e}) \hat{a}_i(t) + i\omega\beta_{\text{fwm}} a_p^2(t) \hat{a}_s^\dagger(t) + i\sqrt{2r_{i,o}} \hat{n}_{i,\text{in}}(t) + i\sqrt{2r_{i,e}} \hat{s}_{i,\text{in}}(t), \quad (4.4)$$

where $\hat{n}_{s,\text{in}}(t)$ and $\hat{n}_{i,\text{in}}(t)$ are the quantum Langevin source terms due to loss for the signal and idler modes, respectively and $\hat{s}_{s,\text{in}}(t)$ and $\hat{s}_{i,\text{in}}(t)$ are the Langevin source terms due to the waveguide input coupling for the signal and idler modes, respectively. The resonance frequencies ($\omega_{s,o}$ and $\omega_{i,o}$) and decay rates due to intrinsic loss ($r_{s,o}$ and $r_{i,o}$) and external coupling ($r_{s,e}$ and $r_{i,e}$), and the

four-wave mixing coefficient β_{fwm} are identical to those used in the classical coupled mode equations of Eq. 3.69 and Eq. 3.70.

Note that noise from the vacuum states of the environment can couple into the resonator through the input waveguide channel as well as through loss channels such as roughness scattering or bending loss. The mode operators obey the commutation relations:

$$[\hat{a}_{\mathbf{k}}(t), \hat{a}_{\mathbf{k}'}^\dagger(t')] = \delta_{\mathbf{k},\mathbf{k}'}\delta(t-t') \quad (4.5)$$

$$[\hat{s}_{\mathbf{k},\text{in}}(t), \hat{s}_{\mathbf{k}',\text{in}}^\dagger(t')] = \delta_{\mathbf{k},\mathbf{k}'}\delta(t-t') \quad (4.6)$$

$$[\hat{n}_{\mathbf{k},\text{in}}(t), \hat{n}_{\mathbf{k}',\text{in}}^\dagger(t')] = \delta_{\mathbf{k},\mathbf{k}'}\delta(t-t'). \quad (4.7)$$

The quantum Langevin equations of Eq. 4.3 and Eq. 4.4 can be found from a phenomenological Hamiltonian

$$\hat{H} = \hat{H}_{\text{linear}} + \hat{H}_{\text{FWM}} \quad (4.8)$$

where

$$\begin{aligned} \hat{H}_{\text{linear}} = \sum_{\mathbf{k}=\text{p},\text{s},\text{i}} \left\{ \right. & \hbar\omega_{\mathbf{k}}\hat{a}_{\mathbf{k}}^\dagger(t)\hat{a}_{\mathbf{k}}(t) + \hbar \int \omega \hat{s}_{\mathbf{k}}^\dagger(\omega)\hat{s}_{\mathbf{k}}(\omega)d\omega \\ & + i \frac{\hbar}{\sqrt{2\pi}} \int [\kappa_{\mathbf{k},\text{e}}\hat{s}_{\mathbf{k}}(\omega)\hat{a}_{\mathbf{k}}^\dagger(t) - \kappa_{\mathbf{k},\text{e}}^*\hat{a}_{\mathbf{k}}(t)\hat{s}_{\mathbf{k}}^\dagger(\omega)]d\omega \\ & \left. + i \frac{\hbar}{\sqrt{2\pi}} \int [\kappa_{\mathbf{k},\text{o}}\hat{n}_{\mathbf{k}}(\omega)\hat{a}_{\mathbf{k}}^\dagger(t) - \kappa_{\mathbf{k},\text{o}}^*\hat{a}_{\mathbf{k}}(t)\hat{n}_{\mathbf{k}}^\dagger(\omega)]d\omega \right\} \quad (4.9) \end{aligned}$$

and

$$\hat{H}_{\text{FWM}} = -\hbar\chi[\hat{a}_{\text{p}}^2(t)\hat{a}_{\text{s}}^\dagger(t)\hat{a}_{\text{i}}^\dagger(t) + \hat{a}_{\text{p}}^{\dagger 2}(t)\hat{a}_{\text{s}}(t)\hat{a}_{\text{i}}(t)] \quad (4.10)$$

with the input and output operators defined in the way described in Chapter 2 and χ defined as

$$\chi \equiv \omega\beta_{\text{fwm}}, \quad (4.11)$$

where $\omega \equiv \omega_{\text{p}} \approx \omega_{\text{s}} \approx \omega_{\text{i}}$.

The pump mode can be described classically and once again we will work in the undepleted pump approximation

$$\frac{d}{dt}a_{\text{p}}(t) = (-i\omega_{\text{p},\text{o}} - r_{\text{p},\text{o}} - r_{\text{p},\text{e}})a_{\text{p}}(t) + i\sqrt{2r_{\text{p},\text{e}}s_{\text{p},\text{in}}}(t). \quad (4.12)$$

Despite later assigning vacuum input for the signal and idler mode, we need to include corresponding quantum Langevin noise sources $\hat{n}_{k,\text{in}}(t)$ and $\hat{s}_{k,\text{in}}(t)$ due to the intrinsic loss and the external coupling to the waveguide bus, respectively. The output operators in the waveguide, $\hat{s}_{s,\text{out}}(t)$ and $\hat{s}_{i,\text{out}}(t)$, are related to the Langevin sources and the cavity modes by

$$\hat{s}_{s,\text{out}}(t) = \hat{s}_{s,\text{in}}(t) + i\sqrt{2r_{s,e}}\hat{a}_s(t) \quad (4.13)$$

$$\hat{s}_{i,\text{out}}(t) = \hat{s}_{i,\text{in}}(t) + i\sqrt{2r_{i,e}}\hat{a}_i(t). \quad (4.14)$$

4.2.1 Generated photon flux with CW pump

Solving equations (4.3)-(4.4) can be achieved by a transformation to the frequency domain by a Fourier transform $\hat{f}(\omega) = \frac{1}{\sqrt{2\pi}} \int \hat{f}(t)e^{i\omega t} dt$ with corresponding inverse Fourier transform $\hat{f}(t) = \frac{1}{\sqrt{2\pi}} \int \hat{f}(\omega)e^{-i\omega t} d\omega$. After Hermitian conjugation of the signal equation, the coupled mode equations for the signal and idler lead to the steady state solutions

$$\hat{a}_s^\dagger = \frac{(-i\sqrt{2r_{s,o}}\hat{n}_{s,\text{in}}^\dagger - i\sqrt{2r_{s,e}}\hat{s}_{s,\text{in}}^\dagger - i\chi a_p^* \hat{a}_i)}{i(\omega_s - \omega_{s,o}) + r_{s,o} + r_{s,e}} \quad (4.15)$$

$$\hat{a}_i = \frac{(i\sqrt{2r_{i,o}}\hat{n}_{i,\text{in}} + i\sqrt{2r_{i,e}}\hat{s}_{i,\text{in}} - i\chi a_p^2 \hat{a}_s^\dagger)}{-i(\omega_i - \omega_{i,o}) + r_{i,o} + r_{i,e}}, \quad (4.16)$$

where for clarity we have dropped the notation of frequency dependence of all variables with the understanding that all operators and amplitudes henceforth are in the frequency domain (i.e. $\hat{a}_i(\omega_i) \rightarrow \hat{a}_i$, etc.) unless explicitly noted. Defining $\Omega_{k,o} \equiv \omega_k - \omega_{k,o}$ and $r_{k,\text{tot}} \equiv r_{k,o} + r_{k,e}$ we find the idler mode annihilation operator

$$\hat{a}_i = C_{\text{thresh}}^{-1} \left[\frac{-\chi a_p^2 (\sqrt{2r_{s,o}}\hat{n}_{s,\text{in}}^\dagger + \sqrt{2r_{s,e}}\hat{s}_{s,\text{in}}^\dagger)}{(-i\Omega_{i,o} + r_{i,\text{tot}})(i\Omega_{s,o} + r_{s,\text{tot}})} + \frac{i\sqrt{2r_{i,e}}\hat{s}_{i,\text{in}} + i\sqrt{2r_{i,o}}\hat{n}_{i,\text{in}}}{-i\Omega_{i,o} + r_{i,\text{tot}}} \right], \quad (4.17)$$

where

$$C_{\text{thresh}} \equiv 1 - \frac{\chi^2 |a_p|^4}{(-i\Omega_{i,o} + r_{i,\text{tot}})(i\Omega_{s,o} + r_{s,\text{tot}})}. \quad (4.18)$$

It can be seen that as pump power is increased, $C_{\text{thresh}} \rightarrow 0$ and \hat{a}_i approaches infinity which is unphysical. This is due to the assumption of an undepleted pump. $C_{\text{thresh}} = 0$ can simply be interpreted as the same threshold condition for parametric oscillation we found in Eq 3.82. In the

spontaneous regime which we are considering C_{thresh} is essentially unity. With $C_{\text{thresh}} = 1$ we find an expression for the idler output operator of

$$\begin{aligned} \hat{s}_{i,\text{out}} = & \left(1 - \frac{2r_{i,e}}{-i\Omega_{i,o} + r_{i,\text{tot}}}\right)\hat{s}_{i,\text{in}} - \frac{\sqrt{2r_{i,e}}\sqrt{2r_{i,o}}}{-i\Omega_{i,o} + r_{i,\text{tot}}}\hat{n}_{i,\text{in}} \\ & + \frac{-i\sqrt{2r_{i,e}}\chi a_p^2(\sqrt{2r_{s,o}}\hat{n}_{s,\text{in}}^\dagger + \sqrt{2r_{s,e}}\hat{s}_{s,\text{in}}^\dagger)}{(-i\Omega_{i,o} + r_{i,\text{tot}})(i\Omega_{s,o} + r_{s,\text{tot}})}. \end{aligned} \quad (4.19)$$

We now consider the idler photon spectral photon flux operator $\hat{s}_{i,\text{out}}^\dagger \hat{s}_{i,\text{out}}$. Therefore we can now find the average idler photon flux $I_i = \langle \hat{s}_{i,\text{out}}^\dagger(t) \hat{s}_{i,\text{out}}(t) \rangle$ (i.e. idler photons in the output waveguide per second) as

$$I_i = \frac{1}{2\pi} \iint \langle \hat{s}_{i,\text{out}}^\dagger(\omega_i) \hat{s}_{i,\text{out}}(\omega'_i) \rangle e^{i(\omega_i - \omega'_i)t} d\omega_i d\omega'_i. \quad (4.20)$$

All cross terms are zero since $\langle n|n' \rangle = 0$ for $n \neq n'$. We also know from our initial conditions that

$$\langle \hat{s}_{i,\text{in}}^\dagger(\omega_i) \hat{s}_{i,\text{in}}(\omega'_i) \rangle = \langle \hat{n}_{i,\text{in}}^\dagger(\omega_i) \hat{n}_{i,\text{in}}(\omega'_i) \rangle = 0, \quad (4.21)$$

since the inputs at the idler frequency are vacuum and any thermal excitation of the noise fields would be far below optical frequencies at room temperature [60]. Energy conservation requires $\Omega_{s,o} = \Delta\omega_{\text{FSR}} - \Omega_{i,o}$ where $\Delta\omega_{\text{FSR}} = 2\omega_{p,o} - \omega_{s,o} - \omega_{i,o}$ is the radial frequency offset of the adjacent FSRs due to dispersion and where we have assumed that the pump is on resonance (i.e., $\omega_p = \omega_{p,o}$). With the use of the commutation relations we find the spectral flux density (defined to be the number of photons per second per unit frequency) of the generated idler photons in the output waveguide

$$S_{i,\text{out}}(\Omega_{i,o}) = \langle \hat{s}_{i,\text{out}}^\dagger(\omega_i) \hat{s}_{i,\text{out}}(\omega_i) \rangle = \frac{4r_{i,e}r_{s,\text{tot}}\chi^2|a_p|^4}{(\Omega_{i,o}^2 + r_{i,\text{tot}}^2)[(\Omega_{i,o} - \Delta\omega_{\text{FSR}})^2 + r_{s,\text{tot}}^2]} \quad (4.22)$$

with a total idler photon flux of $I_{i,\text{out}} = \frac{1}{2\pi} \int_{-\infty}^{\infty} S_{i,\text{out}}(\Omega_{i,o}) d\Omega_{i,o}$. From Eq. 4.22 we see that the spectrum of photons leaving is actually a Lorentzian squared and that they, in fact, become more narrow band in frequency with larger dispersion.

Integrating Eq (4.22) over all frequencies $\Omega_{i,o}$ gives the idler photon flux in the output of the waveguide as

$$I_{i,\text{out}} = \omega^2 \beta_{\text{fwm}}^2 P_p^2 \frac{2r_{i,e}}{r_{i,\text{tot}}} \left(\frac{2r_{p,e}}{r_{p,\text{tot}}} \right)^2 \frac{r_{s,\text{tot}} + r_{i,\text{tot}}}{\Delta\omega_{\text{FSR}}^2 + (r_{s,\text{tot}} + r_{i,\text{tot}})^2}, \quad (4.23)$$

where we assume the pump is on resonance. The equation for I_i is the expectation value for the number of idler photons per second in the output waveguide but not yet a full measure of the number of photon pairs in the output since not all of the corresponding signal photons necessarily make it to the output waveguide. Since the decay rates determine the proportion of photons that were generated in the cavity which make it to the intended output waveguide, we can use these to formulate an escape efficiency for each mode. Therefore the escape efficiency of the signal photons $\eta_{\text{esc},s} = r_{s,e}/r_{s,\text{tot}}$ is the probability that a signal photon in the resonator couples to the output waveguide. At critical coupling $r_{s,\text{tot}} = 2r_{s,e}$ and the escape efficiency is 50%. Since we expect $I_{i,\text{out}}$ idler photons per second in the output waveguide, we expect the rate of idler photons which **also** have a corresponding signal photon (which we will call I_{coinc} , since it refers to the flux of coincident photons in the output waveguide) to be related to the escape efficiency of the signal photons by

$$I_{\text{coinc}} = \eta_{\text{esc},s} I_i \quad (4.24)$$

and similarly

$$I_{\text{coinc}} = \eta_{\text{esc},i} I_s. \quad (4.25)$$

For the total expected photon flux of coincident (photons that are still travelling in pairs in the waveguide), we find

$$I_{\text{coinc}} = \omega^2 \beta_{\text{fwm}}^2 P_p^2 \frac{2r_{i,e}r_{s,e}}{r_{i,\text{tot}}r_{s,\text{tot}}} \left(\frac{2r_{p,e}}{r_{p,\text{tot}}} \right)^2 \frac{r_{s,\text{tot}} + r_{i,\text{tot}}}{2\pi \Delta\nu_{\text{FSR}}^2 + (r_{s,\text{tot}} + r_{i,\text{tot}})^2}. \quad (4.26)$$

In deriving Eq. 4.26, we first solved for the photon flux in the waveguide of the idler photons and multiplied by the escape efficiency of the signal photons. This was an arbitrary decision, and performing the same derivation in terms of the signal flux multiplied by the idler photons' escape efficiency should provide an identical result. As a sanity check, we can confirm that Eq. 4.26 is invariant under the exchange of subscripts denoting the signal and idler resonances (i.e. substituting $r_{i,e} \leftrightarrow r_{s,e}$ and $r_{i,\text{out}} \leftrightarrow r_{s,\text{out}}$). We note that Eq. 4.26 for the coincidence rate was first formally derived by Vernon *et al.* [155] soon after Helt *et al.* [63] derived the rate in the special case that the resonator is lossless.

Eq. 4.26 also demonstrates that the efficiency of the four-wave mixing process (this time described by the pair generation rate) has a Lorentzian dependence upon the “FSR mismatch” $\Delta\nu_{\text{FSR}}$ caused by dispersion. In the spontaneous four-wave mixing case, however, the Lorentzian linewidth is the sum of the total decay rates of the signal and idler, rather than just the idler decay rate as we found in Eq. 3.84. This difference arises due to the fact that spontaneous four-wave mixing process is seeded by vacuum fluctuations with spectral content spanning across the entire signal resonance linewidth, whereas in the classical case we assumed that the signal was a monochromatic seed set to the center of the resonance.

4.3 Implementation in advanced CMOS

Recently, monolithic integration of classical photonics in commercial CMOS processes has been pursued in the context of enabling energy efficient optical interconnects between processors and memory [9] resulting in the demonstration of a chip-to-chip optical link [139] and the first single chip microprocessor to communicate directly using light [141]. The IBM 12SOI 45 nm CMOS process [81], has proven to be a particularly well-suited platform for integration of photonic devices alongside millions of transistors [110] and has enabled the control of photonic components by on-chip digital electronics for an optical transmitter and receiver [49]. High-performance classical photonic components such as 5 fJ/bit modulators [130], record tuning-efficiency filters [158], and highly efficient fiber-to-chip grating couplers [157, 104] have also been demonstrated in this CMOS process. Furthermore, microelectronic circuits in the 45 nm SOI CMOS process used here have been shown to operate at cryogenic temperatures down to 4 K [152], potentially enabling additional integration with cryogenically cooled quantum systems at liquid Helium temperatures.

While there has been much interest in implementing photon pair sources and systems into “CMOS-compatible” platforms to benefit from some of the proven fabrication techniques of the microelectronics industry, many of these demonstrations have relied on processes which are not compatible with fabrication in CMOS foundries such as electron-beam lithography and custom silicon device layer thicknesses, which are typical in silicon photonics research and low-volume

fabrication but are incompatible with advanced (sub-100 nm) CMOS transistors. This departure from standard CMOS processes has prevented monolithic integration of electronics and quantum photonics on a single chip. While utilization of CMOS materials and fabrication processes offer certain processing benefits, until now, monolithic integration of quantum photonic sources within a microelectronics platform had not been investigated. Owing to the potential speed, energy, and temperature requirement for electronic control circuits in quantum photonic integrated systems, we investigate the demonstration of a CMOS monolithic photon pair source.

4.3.1 Device design

As a photon pair source we use a microring-resonator [Fig. 4.2] fabricated in the crystalline silicon (c-Si) CMOS layer typically used for the body of a MOSFET transistor [Fig. 4.1(a)]. The fabrication is performed within a CMOS foundry without any processing changes while maintaining compliance with the existing CMOS design rules. Upon delivery from the foundry, the silicon handle wafer is removed as a post-processing step, via a XeF_2 etch as described in [110], to provide confinement for the optical mode since the buried oxide layer (<200 nm) is not sufficiently thick to prevent optical leakage into the silicon substrate. This single post-processing step has been shown

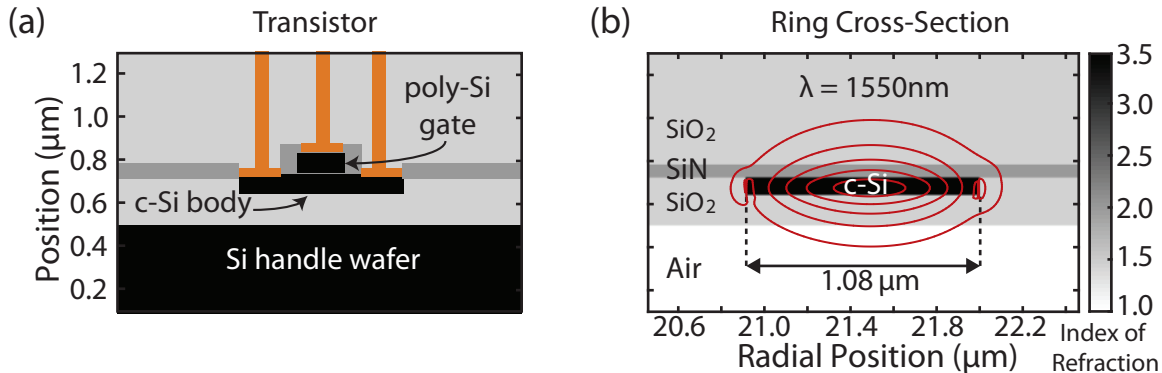


Figure 4.1: (a) Schematic of a typical transistor composed of a crystalline silicon (c-Si) body and a polysilicon gate. (b) Cross-section illustration of the microring-resonator pair source showing how the sub-100 nm c-Si transistor body layer can be used to confine light after removal of the Si handle wafer. The fundamental resonator mode contours are superimposed in red to illustrate how the majority of the modal field extends into the cladding.

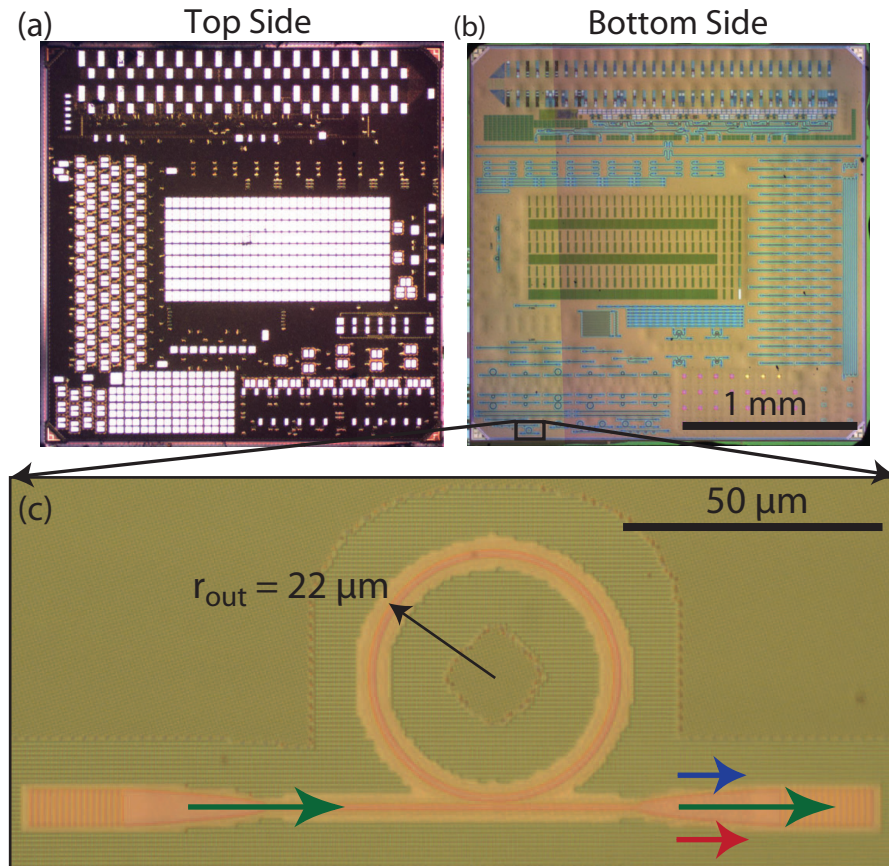


Figure 4.2: (a) Optical micrograph of the top-side of the CMOS chip showing the various backend metals. (b) The corresponding optical micrograph of the bottom of the CMOS chip, with silicon device layer visible, and zoom-in (c) of the ring-resonator photon pair source and grating couplers [46].

to preserve integrated transistor performance characteristics to within 5% [110]. We note that the sub-100 nm thick¹ crystalline silicon guiding layer is too thin to fully confine light vertically, and results in a significant portion of the optical mode extending into the SiN and SiO₂ claddings as shown in Fig. 4.1(b). This not only confines a smaller fraction of the modal power within the silicon core, the dominant Kerr medium, but also prevents the design of a resonator with zero group velocity dispersion, as we show.

When a degenerate pump beam is tuned on resonance, adjacent resonances are intrinsically momentum matched but dispersion results in a difference between adjacent free-spectral ranges

¹ Exact layer dimensions are available in the IBM 12SOI Process Design Kit under nondisclosure agreement

(FSRs) introducing an energy mismatch, which we referred to as $\Delta\nu_{\text{FSR}}$ in Eq. 3.84 and Eq. 4.26. This effect of dispersion becomes negligible if the “FSR mismatch” is significantly smaller than the linewidths of the resonances involved. A plot of the simulated “FSR mismatch,” $\Delta\nu_{\text{FSR}}$, for various ring widths and radii is shown in Fig. 4.3 for a pump wavelength near 1550 nm for various ring widths and radii. A ring width of $1.08 \mu\text{m}$ and outer radius of $22 \mu\text{m}$ with a predicted difference in FSR of 1.4 GHz is chosen in order to obtain a small mode volume while also supporting a suitably small $\Delta\nu_{\text{FSR}}$. A transmission spectrum [Fig. 4.4(a)] of the CMOS foundry-fabricated device shows a difference in FSRs of 1.8 GHz centered around a pump resonance near 1558 nm. The 0.4 GHz difference between measured and simulated values is likely due to uncertainty in refractive indices and fabricated dimensions. Fitting the passive resonance gives a total quality factor, Q_{tot} , of 31,000, with an intrinsic quality factor of $Q_{\text{o}} = 114,000$ due to intrinsic losses such as linear absorption and roughness loss and an external quality factor of $Q_{\text{ext}} = 43,000$ due to coupling to the waveguide bus. The total Q corresponds to a linewidth of 6.2 GHz, which is significantly greater than the measured 1.8 GHz difference in FSRs. Using Eq. 4.27 and 4.29 we can quantify the effect of dispersion for stimulated and spontaneous FWM, respectively. By comparing the results of these equations for

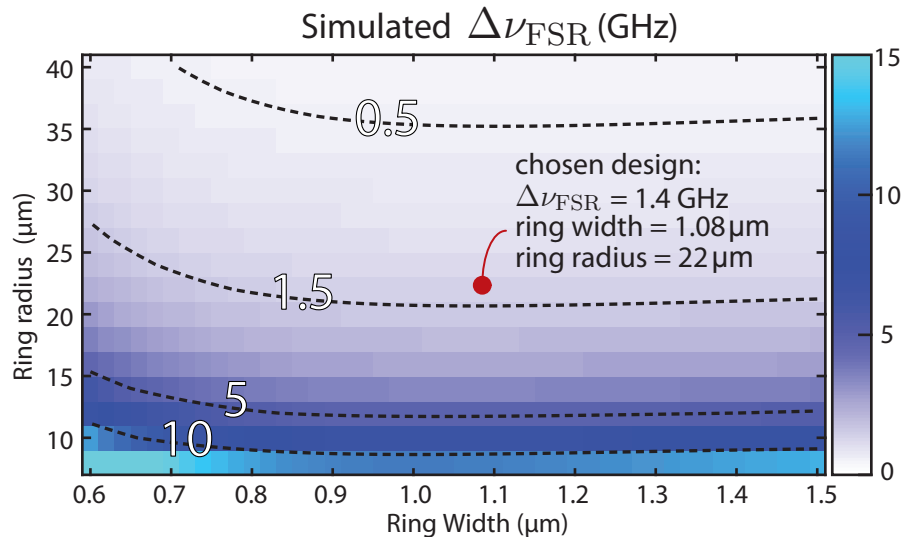


Figure 4.3: Simulated difference in FSR $\Delta\nu_{\text{FSR}}$ at 1550 nm due to dispersion with chosen design predicted to be a negligible 1.4 GHz [46].

a 1.8 GHz “FSR mismatch” compared to a 0 GHz “FSR mismatch” we find that the predicted efficiency of stimulated FWM decreases by $\sim 14.6\%$ and photon pair generation by only $\sim 7.5\%$.

The resonator is over-coupled to provide higher tolerance to dispersion while also providing a higher escape efficiency for generated photon pairs. We note that the absence of a single ring geometry with $\Delta\nu_{\text{FSR}} = 0$ does not fundamentally limit the achievable four-wave mixing efficiency in this platform since additional dispersion engineering methods involving coupling multiple resonators can completely compensate for dispersion, though at the expense of increased complexity. However, such complex schemes are especially suitable for electronic-photonic integrated circuits enabled by this platform, which can provide feedback control for complex photonic devices [140]. Therefore, it is the intrinsic optical quality factor determined by losses and lithographic line-edge roughness induced light scattering that is the fundamental limitation for four-wave mixing efficiency in this process.

4.3.2 Stimulated four-wave mixing characterization

In order to characterize the photon pair source, we first measure stimulated four-wave mixing (FWM) where a seed laser is used in addition to the pump to stimulate the four-wave mixing process. The efficiency of classical FWM is commonly defined as the ratio of idler power in the output bus to seed power in the input bus. Measuring FWM with pump powers ranging from -21 dBm to -2 dBm results in efficiencies of -70 dB to -42 dB, respectively, as shown in Fig. 4.5. The efficiencies with pump power below -10 dBm follow an expected quadratic dependence on pump power. At higher pump powers, parasitic nonlinearities such as two-photon absorption (TPA), free-carrier absorption (FCA), and self- and cross-phase modulation, in addition to thermal heating of the resonator due to linear absorption, result in a deviation from the quadratic trend. Assuming that the pump and seed lasers are both placed on resonance, from Eq. 4.27 we find in the case that the intrinsic and external decay rates of the three resonances are approximately equal (i.e., $r_o \equiv r_{p,o} \approx r_{s,o} \approx r_{i,o}$

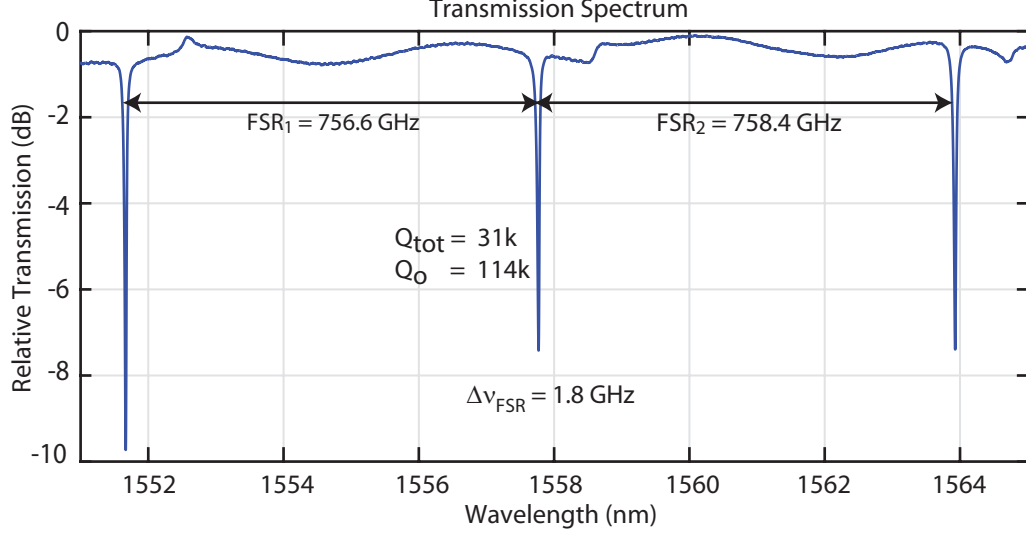


Figure 4.4: Passive wavelength sweep of the three interacting resonances showing a difference in FSR of 1.8 GHz and intrinsic quality factor of 114,000 [46].

and $r_e \equiv r_{p,e} \approx r_{s,e} \approx r_{i,e}$)

$$\eta_{\text{stim}} = P_p^2 \omega^2 \beta_{\text{fwm}}^2 \left(\frac{2r_e}{r_{\text{tot}}^2} \right)^3 \frac{2r_e}{(2\pi \Delta\nu_{\text{FSR}})^2 + r_{\text{tot}}^2}. \quad (4.27)$$

Here, $\Delta\nu_{\text{FSR}}$ is the difference in adjacent FSRs due to dispersion, P_p is the pump power in the waveguide at optical angular frequency ω , and β_{fwm} is a parameter containing the nonlinearity of silicon and is inversely proportional to the mode volume. The decay rates r_{tot} (total energy amplitude decay rate due to all mechanisms) and r_{ext} (decay rate due to coupling to waveguide only) are related to the measured quality factors $Q_{\text{tot}} = \omega/2r_{\text{tot}}$ and $Q_{\text{ext}} = \omega/2r_{\text{ext}}$. Fitting the measured efficiencies in the region of pump powers before parasitic nonlinearities are present (below -10 dBm) to Eq. 4.27 we find $\beta_{\text{fwm}} = 5.32 \times 10^6 \text{ J}^{-1}$. The β_{fwm} parameter is related to the Kerr nonlinearity, denoted n_2 , of the silicon core by

$$\beta_{\text{fwm}} = \frac{n_2 c}{n_{\text{Si}}^2 V_{\text{eff}}}, \quad (4.28)$$

where c is the speed of light, n_{Si} is the refractive index of silicon, and $V_{\text{eff}} = 18.5 \mu\text{m}^3$ is an effective mode volume [168] calculated using a numerical modesolver [116]. Here, the fitted β_{fwm}

corresponds to $n_2 = 3.96 \times 10^{-14} \text{ cm}^2/\text{W}$, well within the uncertainties of previously measured values for crystalline silicon [28, 16].

4.3.3 Photon pair generation measurements

Spontaneous four-wave mixing is tested by performing coincidence measurements between generated photon pairs. A schematic of the experimental setup is illustrated in Fig. 4.6. A continuous-wave (CW) telecom pump laser is passed through a series of two C-band (1530-1565 nm) separators and two ~ 1 nm wide telecom bandpass filters (each with over 60 dB out-of-band rejection) to remove laser spontaneous emission noise at the signal and idler wavelengths. The pump is subsequently coupled to the input waveguide via a grating coupler and tuned to the pump resonance near 1558 nm. The generated photon pairs are coupled from the output grating coupler and then individually filtered by cascaded telecom filters with an estimated 180 dB total isolation from the pump. The signal and idler photons are sent to 81% and 87% efficient WSi superconducting

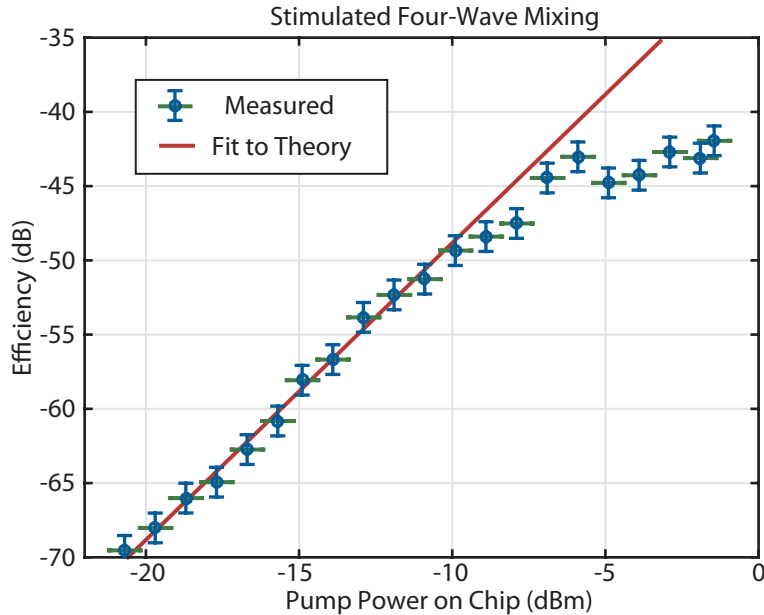


Figure 4.5: Measured stimulated four-wave mixing efficiency with fit to Eq. (4.27). Horizontal (vertical) error bars correspond to uncertainty in input (output) coupling. Deviation from theory at higher pump powers are result of parasitic nonlinear and thermal effects [46].

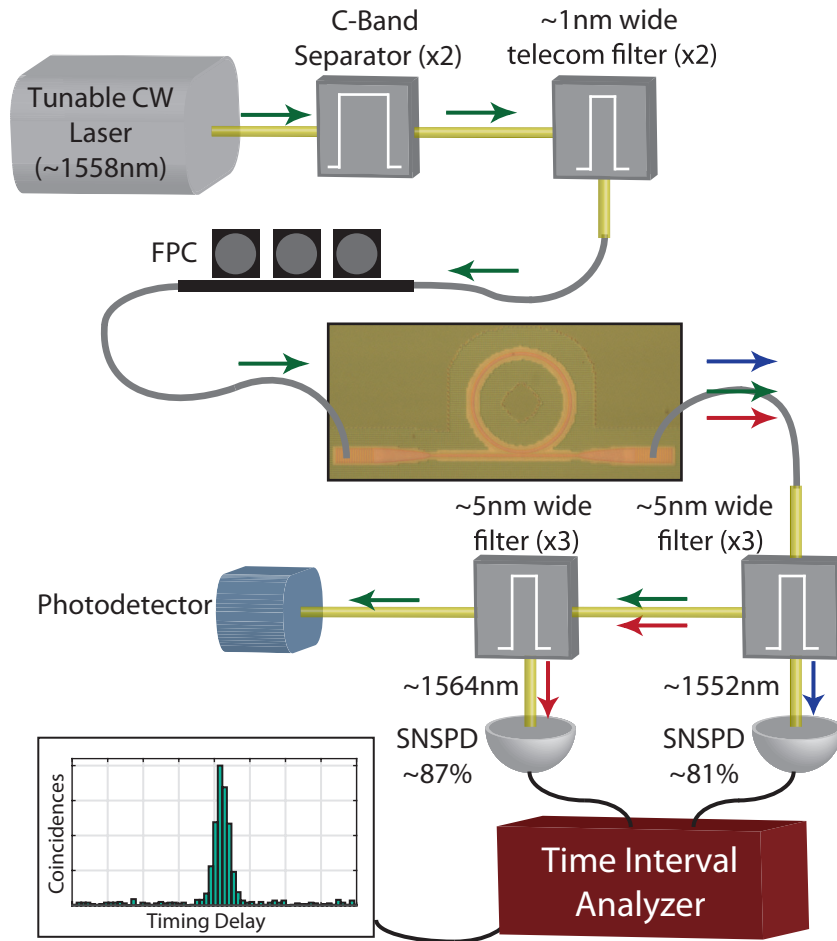


Figure 4.6: Simplified schematic of the pair generation measurement. The pump light is passed through two C-band (1530-1565 nm) separators and two telecom filters to eliminate noise from the laser. A fiber polarization controller (FPC) is used to optimize coupling efficiency. The signal and idler photons are then filtered individually and sent to high efficiency superconducting nanowire single photon detectors (SNSPDs). A time interval analyzer is then used to count coincidences. The pump power is monitored by a classical photodetector to ensure the pump light is on resonance [46].

nanowire single photon detectors (SNSPDs) [94], respectively. While microring-resonator sources of photon pairs generally generate a comb of signal-idler pairs [123] since FSRs multiple mode orders away from the pump resonance are often also phase-matched, we use ~ 5 nm bandwidth telecom filters at the signal (~ 1552 nm) and idler (~ 1564 nm) wavelengths to ensure measurement of pairs only at the FSRs immediately adjacent to the pump. A time interval analyzer (TIA) records counts verses relative time delay between the two detectors. As shown in Fig. 4.6, the TIA allows for the

construction of a histogram plot of coincidences (i.e, the number of times a photon is detected in both detectors for a certain timing delay bin). At a particular range of timing delay bins, we find a peak corresponding to highly temporally correlated photons, which we can reasonably infer are generated from the four-wave mixing process. The timing delay is not necessarily at zero, since the signal and idler photons have different optical path lengths as they pass through their respective filtering stages.

From here, we can use each coincidence plot to find a coincidence rate for each measurement time period, which we will call integration time. The coincidence rate is simply the sum of all the coincidences in the histogram plot within the coincidence peak (with background subtracted), divided by the integration time. Coincidence rate versus estimated pump power in the waveguide is measured as shown in Fig. 4.7(a). Measurements at each pump power are performed with a sufficiently long collection time to accumulate the same number (approximately 200 counts) of coincidences in the zero-delay time bin. The collection times ranged from 2 seconds at the highest pump power to 1 hour at the lowest pump power. The pair rate on chip shown in Fig. 4.7 (b) is estimated by subtracting out the losses (in dB) of each mode from the measured coincidence rate [8]. Since both the signal and idler modes experience approximately 15 dB of loss due to the combination of both the detection efficiency and loss from the output waveguide to the detectors, the measured coincidence rate (which relies on the joint probability of both photons of a pair being detected) will be ~ 30 dB lower than the pair rate on chip. Measurements of grating coupler loss are performed immediately after each coincidence measurement in order to account for potential drift in the coupling to the waveguide. The uncertainty of individual grating coupler loss and fiber alignment is visible in the error bars in Fig. 4.7. The grating coupler efficiency uncertainty arises from the fact that only the combination of both input and output gratings, which we assume to be identical, can be directly measured and that the coupling efficiency slightly drifts over the time of the measurement. The later contribution is assumed to be dominate and was monitored over the course of the measurements.

Pair generation rates were measured over three orders of magnitude with on-chip rates rang-

ing from 165 to 332×10^3 pairs per second. The rate of photon pairs in the output waveguide can be described by Eq. 4.7, which in the case that the signal, idler, and pump resonances have approximately equal decay rates becomes

$$I_{\text{coinc}} = \eta_{\text{esc}} P_{\text{p}}^2 \omega^2 \beta_{\text{fwm}}^2 \left(\frac{2r_e}{r_{\text{tot}}^2} \right)^2 \frac{4r_e}{(2\pi\Delta\nu_{\text{FSR}})^2 + (2r_{\text{tot}})^2}. \quad (4.29)$$

The escape efficiency η_{esc} for photons generated in the ring defined as $r_{\text{ext}}/r_{\text{tot}}$. The escape efficiency

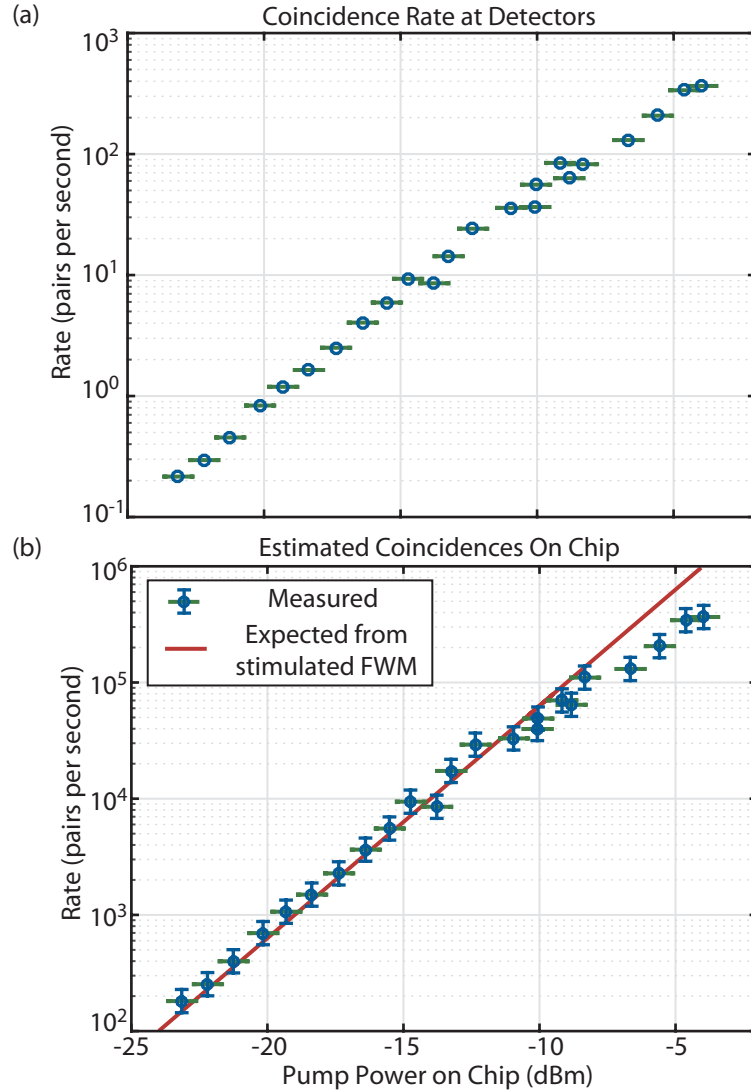


Figure 4.7: Coincidence rate of photon pairs at the detectors with the estimated rate on-chip (b) after subtracting out losses to the detectors. The solid line is the rate expected based on the stimulated four-wave mixing measurements [46].

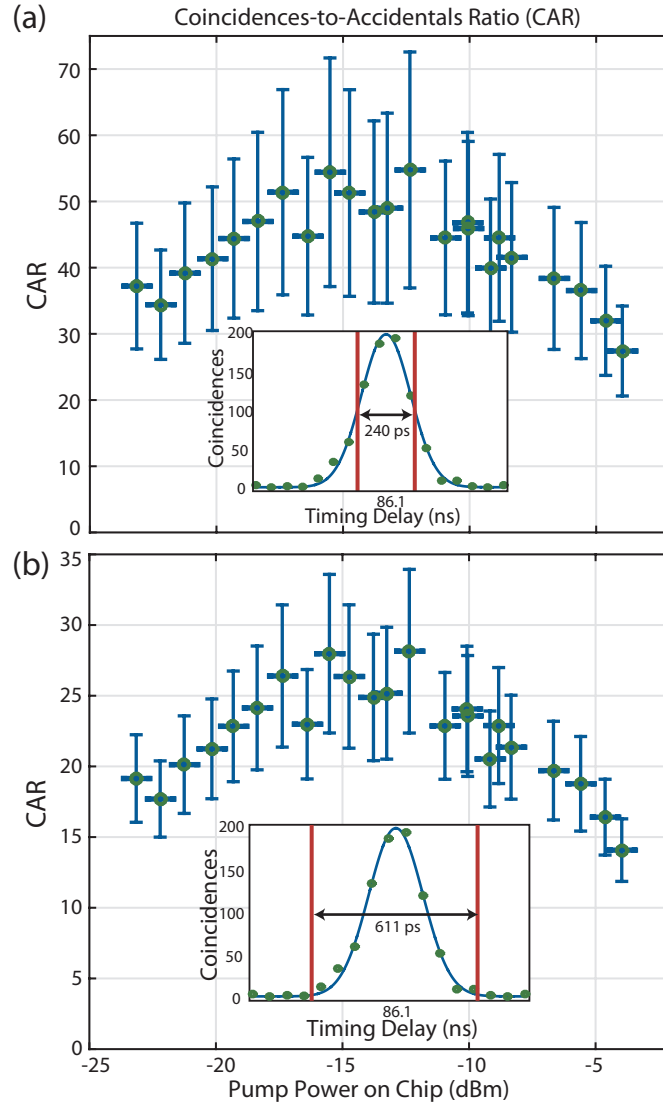


Figure 4.8: Coincidences-to-accidentals ratio (CAR) for various pump powers where the coincidence peaks were fit to a Gaussian function (insets) and delay windows selected at the (a) full-width-half-maximum and (b) ± 3 standard deviations [46].

accounts for the photon pairs generated within the cavity where one of the photons is lost due to loss mechanisms such as sidewall roughness scattering and absorption. Use of the fitted β_{fwm} from the classical FWM measurements to predict pair generation rate provides excellent agreement with the measured data, as seen in Fig. 4.7(b). Similar to the case of classical measurements, at higher pump powers the pair rate experiences a deviation from theory due to parasitic nonlinear [35, 68, 63]

and thermal effects.

4.3.4 Noise characterization

Coincidence measurements also provide a coincidences-to-accidentals ratio (CAR), often used as a figure of merit characterizing the quality (signal to noise ratio) of a photon pair source. The coincidence peak has a finite width resulting from the convolution of the timing jitters of the two detectors (measured at ~ 105 ps and ~ 130 ps for the signal and idler, respectively) and the temporal width of the photon pairs determined by the linewidth of the resonator. Here, we perform a Gaussian fit to the coincidence peak and use the full-width-half-maximum (FWHM) as the coincidence window as shown in the inset of Fig. 4.8(a). The coincidence window is the range of timing delay bins for which we define the photons to be coincident. The FWHM window size was specifically chosen for comparison to previously demonstrated photon pair sources. The measured CARs are shown versus pump power in Fig. 4.8(a). CARs were consistently measured greater than 40 with a maximum CAR of 55 at a pump power of -12.4 dBm. The choice of FWHM as the coincidence window is somewhat arbitrary [35, 31], though useful for comparison to other demonstrations in the literature. A larger delay window results in a larger pair rate but lower CAR, while a smaller delay window results in a higher CAR at the sacrifice of pair rate. Since the measured coincidence rates in Fig. 4.7 include all true coincidences, we provide the corresponding CARs in Fig. 4.8(b) where the timing window is chosen to cover ± 3 standard deviations (~ 611 ps) of the fitted Gaussian. We note, the larger window results in about 50% lower CARs compared to using the FWHM.

The SNSPDs display negligible intrinsic dark count rates (< 1 count per second [94]) with device background count rates (measured with the pump laser off) for the signal and idler detectors of 400 and 980 counts per second, respectively, resulting from “parasitic” room-temperature thermal radiation that manages to reach the detectors. The pump power dependence of the CAR displayed in Fig. 4.8 can be explained by categorizing the CAR into three regimes: (1) In the very low pump power regime, the CAR is dominated by noise sources that do not vary with laser power (i.e., device

background count rates) and increased pump power will yield more coincidences with negligible increase in accidentals. (2) In the optimal pump power regime for peak CAR, higher pump power results in increased coincidences but also increased accidentals from system background counts due to noise sources depending linearly on pump power such as leakage of pump light through the filters and spontaneous Raman emission generated in the devices cladding. (3) In the higher pump power regime, multi-pair emission along with nonlinear loss due to two-photon absorption and free-carrier absorption limit the CAR.

4.4 Conclusions

Despite a device geometry limited by implementation in a 45 nm-node CMOS microelectronics process, the pair source presented here demonstrated high generation rates up to 332×10^3 pairs per second and CARs exceeding 50. These pair rates and CARs are on the same order as many custom fabricated Si sources [23, 8, 27, 77, 57]. The relationship between stimulated and spontaneous four-wave mixing performance in the same device has been a subject of recent investigation [62, 7] as it is useful to determine the effectiveness of predicting pair generation rates from classical FWM measurements. In fact, classical measurements have recently been demonstrated for fast and efficient characterization of entangled-photon sources [125]. In the limit of no dispersion, Equations 4.27 and 4.29 give a simple formula relating the pair generation rate to seeded four-wave mixing efficiency of

$$I_{\text{coinc}} = \frac{\eta_{\text{esc}}}{2} \left(\frac{2r_{\text{ext}}}{r_{\text{tot}}^2} \right)^{-1} \eta_{\text{stim}}. \quad (4.30)$$

Until recently [155], a complete description of SFWM in lossy microcavities had not been available, leading to a significant discrepancy in measured pair rates and theoretical predictions [23]. Here we accurately predict the SFWM-based coincidence rates from classical FWM measurements of the CMOS-integrated microresonator. To our knowledge, this is the first demonstration of using classical FWM measurements of a microresonator to accurately predict the non-classical correlations revealed by coincidence counting of photon pairs generated by SFWM. In addition, these results

confirm the findings of [7] where classical FWM measurements were first used to predict the optical powers generated by parametric fluorescence from a microring resonator.

In addition to pair rates generated on chip in the range of thousands of pairs per second, a low pump power of $4.8 \mu\text{W}$ was also used to generate photons at 165 pairs per second on-chip, which is, *to the best of our knowledge, the lowest pump power used to produce photon pairs in silicon*. This was primarily enabled by the first use of highly efficient SNSPDs for coincidence measurements of pairs generated in a Si microring source, despite the significant loss from the output grating coupler to the detectors. These losses can be greatly reduced in future implementations by integration with on-chip filters and highly efficient grating couplers which have already been demonstrated in this process [157], potentially enabling heralded single photon sources with high heralding efficiency, necessary to compete with parametric down-conversion-based sources, which have demonstrated source-to-fiber coupling of 97% [30].

Chapter 5

Source purity: characterization, pump filtering, and parasitic noise

Generation rate is an important metric for a photon pair source. In Chapter 3, we found that resonantly enhancing the pump, signal, and idler fields greatly increases the four-wave mixing efficiency and in the previous chapter, we showed that photon pairs could be generated with microWatts of pump power. However, in addition to efficiency and generation rate, the source purity and the amount of excess “noise” photons must be taken into consideration when building a photon pair source. While we characterized the coincidences-to-accidentals ratio of the source in Chapter 4, the details of this figure of merit beyond retrieving it from a coincidence measurement were left to be described in this chapter. Furthermore, we develop and demonstrate a configuration for implementing on-chip pump rejection, which at this time can be considered the primary obstacle to large-scale implementations of photon pair sources on a single chip.

5.1 Coincidences-to-accidentals ratio

The coincidences-to-accidentals ratio (CAR) is a measure of how many of the coincidence events in the chosen set of timing delay bins (our “coincidence window”) are from photon pairs generated in the ring and how many are “accidental,” meaning that they are a result of the statistical probability that two uncorrelated photons arrive in the same time bin within the “coincidence window.” Note that one photon of a pair being lost does not contribute to the “accidentals” since it does not register a coincidence event. CAR is important to many quantum optical measurements, since it often sets the signal-to-noise ratio possible when making a measurement of a non-classical

effect. For example, if one were to attempt to use a ring resonator photon pair source to generate a two photon path-entangled N00N state (introduced in Chapter 1 Fig. 1.2), the CAR would limit the bi-photon interference visibility. While all coincidences would be recorded, the contribution from “accidentals” would not interfere since they are not quantum mechanically correlated, while the “true coincidences” would produce an interference pattern.

“Accidentals” result from the statistical chance that photons which are not quantum mechanically correlated, arrive at the corresponding detectors within the “coincidence window,” τ_{win} . Fig. 5.1 illustrates how a coincidence plot is processed from an example of two detector recordings (clicks in each time bin of length τ_{bin} denoted by a 1). With such a short collection time, we are unlikely to find accidental coincidences far from zero delay due to the finite measurement time. In

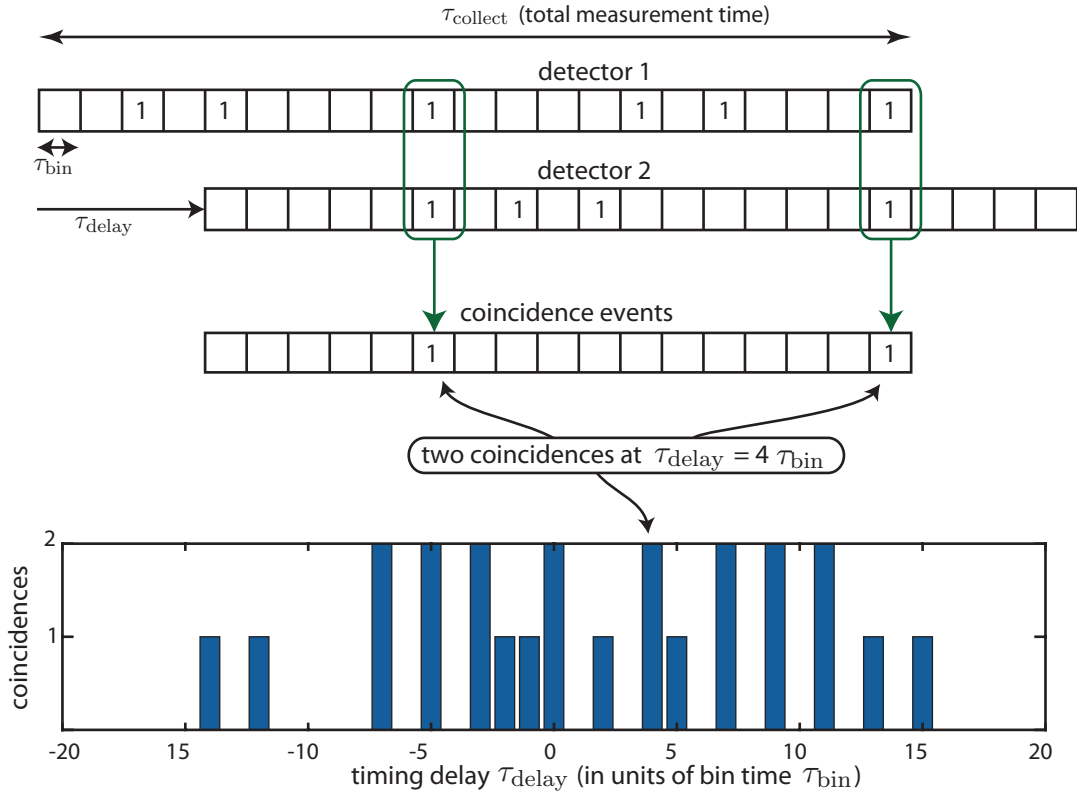


Figure 5.1: Simplified illustration of coincidence counting and the method coincidence histograms are generated from two arrays of detection events versus time at two detectors. The two arrays are cross-correlated to make a coincidence plot. The number 1 is used as notation for a detection in a given time bin.

practice, the measurement time τ_{collect} is much larger than a timing bin length and can be well approximated as infinite. For example the measurement times in the previous chapter were on the scale of minutes while the bin time was 64 ps, a difference of 12 orders of magnitude. In this approximation, the coincidences versus timing delay for uncorrelated (i.e., classical) light is statistically flat.

Assuming uncorrelated Poissonian distributed light we can predict the number of accidental photons in a give timing window τ_{win} . The total number of photons detected in detector 1 and detector 2 is their corresponding detection rates multiplied by the total collection time such that

$$n_{\text{counts},1} = d_1 \tau_{\text{collect}}. \quad (5.1)$$

Dividing the total counts in each detector by the number of timing windows it takes to span the full collection time (i.e., $\tau_{\text{collect}}/\tau_{\text{win}}$) we find the average number of photons in a given timing window for each detector ($\bar{n}_{1,\text{win}}$ and $\bar{n}_{2,\text{win}}$, respectively) to be

$$\bar{n}_{1,\text{win}} = d_1 \tau_{\text{win}} \quad (5.2)$$

$$\bar{n}_{2,\text{win}} = d_2 \tau_{\text{win}}. \quad (5.3)$$

The probability, $P(n)$ of finding n photons in a length of time that contains on average of \bar{n} photons is given by the Poisson distribution

$$P(n) = \frac{\bar{n}^n}{n!} e^{-\bar{n}}. \quad (5.4)$$

Since detection rates are limited to $\sim 10^7$ for the SNSPD's used here [94], and the timing window is less than 1 ns for resonance Q's less than 100,000, we can safely make the assumption that average number of photons in each timing window $\bar{n}_{1,\text{win}}$ and $\bar{n}_{2,\text{win}}$ are less than 0.01 photons. This allows us to make the approximation that the probability [$P_{1,\text{win}}(1)$ and $P_{2,\text{win}}(1)$] for finding one photon in a timing window for detectors 1 and 2 are

$$P_{1,\text{win}}(1) = \bar{n}_{1,\text{win}} \quad (5.5)$$

and

$$P_{2,\text{win}}(1) = \bar{n}_{2,\text{win}}, \quad (5.6)$$

respectively. The product of $P_{1,\text{win}}(1)$ and $P_{2,\text{win}}(1)$ then gives us the probability that there is a coincidence between uncorrelated photon streams, within a span of time τ_{win} . As we found, Poissonian statistics tells us that this probability is also the average number of events in this time span, allowing us to find that the average number of coincidences that we would expect after a time τ_{win} is given by $d_1 d_2 \tau_{\text{win}}^2$. Therefore, the total number of expected coincidences due to uncorrelated light, $N_{\text{uncorrelated}}$, within a range of timing delays defined by τ_{win} , in a given collection time τ_{collect} , is

$$N_{\text{uncorrelated}} = \tau_{\text{collect}} \tau_{\text{win}} d_1 d_2. \quad (5.7)$$

When measuring the coincidences from a photon pair experiment, the detection rates include all detection events, even false ones such as dark counts. The detection rates on each detector can be decomposed into the rate of photons generated as part of a pair $I_{\text{src,pairs}}$, noise photons $I_{\text{src,noise}}$ from the source, background counts I_{bckgrnd} from blackbody radiation and other external noise sources, and dark counts d_{dark} . Since the photons originating from the source have a non-unity transmission efficiency we include the efficiencies (η_1 and η_2) from the source to detector 1 and 2, respectively, to give

$$d_1 = \eta_1 (I_{\text{src,pairs}} + I_{\text{src,noise}}) + I_{\text{bckgrnd},1} + d_{\text{dark},1} \quad (5.8)$$

$$d_2 = \eta_2 (I_{\text{src,pairs}} + I_{\text{src,noise}}) + I_{\text{bckgrnd},2} + d_{\text{dark},2}. \quad (5.9)$$

Using Eq. 5.7, we can estimate the total number of coincidences (in a coincidence window τ_{win}) which would result from uncorrelated light in a photon pair measurement to be

$$N_{\text{uncorrelated}} = \tau_{\text{collect}} \tau_{\text{win}} (d_1 d_2 - \eta_1 \eta_2 I_{\text{src,pairs}}^2), \quad (5.10)$$

where we have subtracted out the expected number of coincidence events

$$N_{\text{fwm,chance}} = \tau_{\text{collect}} \tau_{\text{win}} \eta_1 \eta_2 I_{\text{src,pairs}}^2, \quad (5.11)$$

that we would expect from random chance (Poisson statistics) if the four-wave mixing source did not emit in pairs, but instead in two uncorrelated trains of photon. These are removed since we know that spontaneous four-wave mixing photons are in fact correlated and therefore one might suspect the inclusion of $N_{\text{fwm, chance}}$ in the number of uncorrelated photons would be incorrect. It is interesting to consider the factor $N_{\text{fwm, chance}}$ in terms of a coincidence plot, illustrated in Fig. 5.2(a). Outside the coincidence window, this factor represents uncorrelated photons originating from different photon pairs (i.e., the idler from one pair overlapping in time with a signal from a different pair) and therefore contributes to the background.

Inspecting Fig. 5.2(a), may give the impression that CAR is not simply the signal to background ratio of the coincidence plot as we calculated in the previous chapter. However, we have not yet included the parasitic effect of multi-pair production in spontaneous parametric sources. Multi-pair photons result from the fact that a spontaneous parametric source does not always emit exactly only one pair of photons at a given time. A small proportion of the time a parametric source will emit multiple pairs (four or six or eight photons etc.) with the likelihood of occurrence decreasing with number of pairs. We would like for the events for which this occurs to be characterized as “accidentals” as multi-pairs are often undesirably limit the signal-to-noise of an quantum optical experiment. For example, when using a photon pair source to herald single photons, multi-pair events would result in heralding two or more photons instead of one. Conveniently, light generated in each mode of a spontaneous parametric source can be approximated as a thermal distribution [146]. When following thermal statistics [37], the probability of generating a four-photon photon event is approximately the square of that for a pair (two-photon) event, allowing us to find the expected number of multi-pair events

$$N_{\text{multi-pair}} = \tau_{\text{collect}} \tau_{\text{win}} \eta_1 \eta_2 I_{\text{src, pairs}}^2. \quad (5.12)$$

Coincidentally this is *exactly* the same value we found for $N_{\text{fwm, chance}}$. The expected number of

“accidentals” then becomes

$$\begin{aligned}
 N_{\text{acc}} &= N_{\text{uncorrelated}} + N_{\text{multi-pair}} \\
 &= \tau_{\text{collect}} \tau_{\text{win}} d_1 d_2.
 \end{aligned}
 \tag{5.13}$$

The number of truly coincident photons N_{coinc} is the number of pairs that are generated

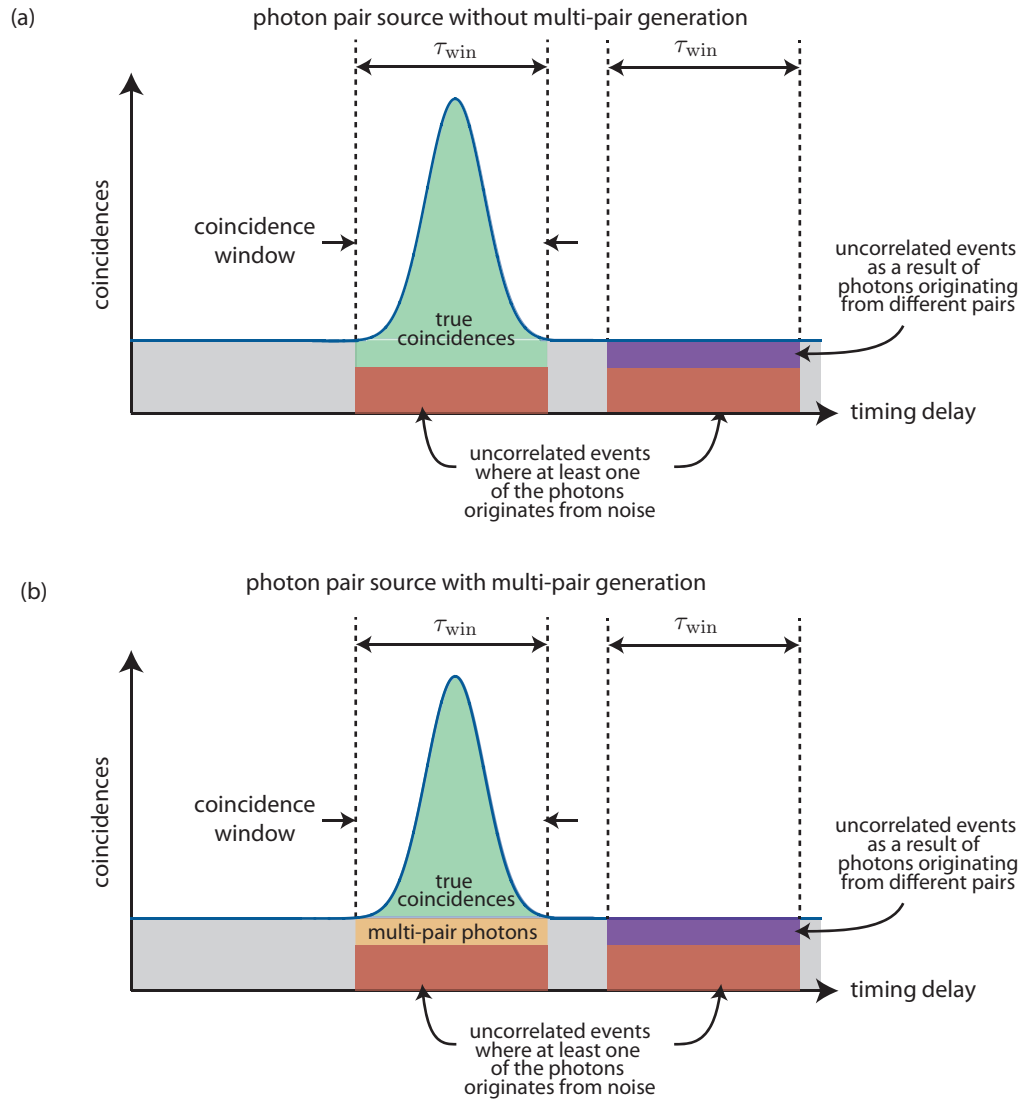


Figure 5.2: Illustration of possible coincidence peaks for (a) a hypothetical source which does not exhibit multi-pair generation and (b) a source which does. Multi-pair photons contribute equally to accidentals as uncorrelated events resulting from photons from different pairs contribute to the out of coincidence measurement background. This mathematical coincidence allows for indirect measurement of the number of accidentals by averaging the number of photons outside the coincidence window.

where both photons of the pair are detected. Since both photons have a probability of being lost on their way to their respective detectors, this is proportional to both efficiencies η_1 and η_2 such that the total number of coincidences is

$$N_{\text{coinc}} = \tau_{\text{collect}} \eta_1 \eta_2 I_{\text{src,pairs}} \quad (5.14)$$

and the CAR can be found by

$$CAR = \frac{N_{\text{coinc}}}{N_{\text{acc}}}. \quad (5.15)$$

Considering an ideal spontaneous parametric source (and system where there are no background counts, dark counts, or excess noise photons) we find the optimal CAR

$$CAR_{\text{multi-pair}} = \frac{1}{\tau_{\text{win}} I_{\text{src,pairs}}}. \quad (5.16)$$

This demonstrates the effect of multi-pair events on the CAR, intrinsic to a spontaneous parametric source. If more than one photon pair are generated within the time window these act as excess photons and can result in an accidental coincidence even if all the photons were generated through the spontaneous parametric process. It is important to note that this equation implicitly assumes that the photon pairs being generated are done so with an approximately thermal probability distribution with respect to the other pairs being generated. In other words, this formula (and the experimental practice of averaging the coincidences per bin far outside the timing window) would not accurately describe an ideal periodic photon pair source which emitted exactly one photon pair at a designated temporal period. Eq. 5.16 also shows that in the absence of background counts and dark counts, losses have no effect over the CAR, as it contributes equally to reducing true coincidences and accidental coincidences.

5.2 Pump filtering

Eq. 5.16 describes the CAR for an ideal spontaneous parametric photon pair source with accidentals only caused by multi-pair events. We can now start to introduce other noise sources to

quantify the degree to which they contribute to the CAR. In the measurements in Chapter 4, we used high extinction telecom fiber filters to filter the photon pairs away from the pump which we cascaded until the CAR was no longer affected. We ended up cascading three such filters resulting in > 180 dB extinction (> 60 dB each). It is difficult to determine exactly how much extinction we truly utilized since the practice of measuring over ~ 80 dB extinction is quite difficult at optical frequencies, as we will see in this section.

We may now ask ourselves the question: “how much pump filtering is needed?” Of course, this will depend on the application and the sensitivity required. It will also depend on the other sources of noise along with background rates and dark count rates, for if the impurity of the detected photons is dominated by these contributions then filtering out the pump more strongly will not improve the systems performance. For now, we will assume that accidentals only originate from multi-pair events (intrinsic to spontaneous parametric sources) and pump photons leaking through the filters. Given a pump rejection of R_{dB} (in dB) we can find the number of pump photons detected to be

$$\text{pump photons detected} = 10^{R_{\text{dB}}/10} I_{\text{pump}}, \quad (5.17)$$

where I_{pump} is the on-chip pump power in units of photons per second (i.e., $\frac{P_{\text{pump}}}{\hbar\omega_p}$) Solving Eqs. 5.8, 5.9, 5.17, and 5.15 gives an upper limit on CAR of

$$\text{CAR}_{\text{pump+multipair}} = \frac{I_{\text{src,pairs}}}{\tau_{\text{win}}(I_{\text{src,pairs}} + 10^{R_{\text{dB}}/10} I_{\text{pump}})^2}. \quad (5.18)$$

We can invert this relation to see the minimum we will need to filter the pump to be able to observe a given CAR.

$$R_{\text{dB}} = 10 \log_{10} \left[\frac{1}{I_{\text{pump}}} \left(\sqrt{\frac{I_{\text{src,pairs}}}{\tau_{\text{win}} \text{CAR}}} - I_{\text{src,pairs}} \right) \right] \quad (5.19)$$

As an example, we consider the CMOS ring source analyzed in the previous chapter. We can calculate R_{dB} for the generation rate of this source and find the minimum pump rejection needed for a CAR of 100 over a pump power range from $1 \mu\text{W}$ to 1mW . Fig. 5.3(a) shows that between 89 dB and 93 dB is sufficient to provide a CAR of 100 for our previous source. At first glance this

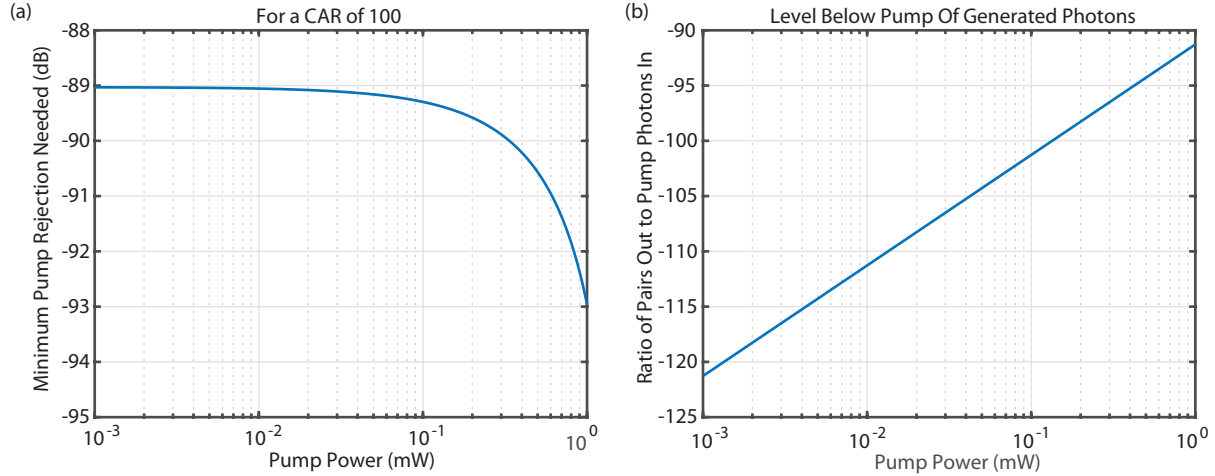


Figure 5.3: (a) The amount of pump rejection required found using Eq. 5.19 for the source demonstrated in Chapter 5 to allow for a multi-photon limited CAR of 100. (b) The corresponding ratio of output photon pairs to input pump photons for a range of pump powers.

might be much less than one might think as there are anywhere between 120 dB and 90 dB more pump photons on-chip than generated photon pairs over the same pump power range as shown in Fig. 5.3(b). So even though there can be more than a thousand more pump photons after filtering than generated photon pairs, we can still detect the photon pairs with over 99% of the coincidences being true coincidences. This somewhat counterintuitive result relies on the fact that the photon pairs are strongly correlated in time while the pump photons are not. While there can be many more pump photons incident on the detectors than photon pairs, they are much less likely to arrive at the same time since they are uncorrelated.

Since the four-wave mixing process is much more efficient at higher pump powers (proportional to the square of the pump power), the ratio of generated photon pairs to pump photons is greatly increased at higher pump powers, as shown in Fig. 5.3(b). However, we found in Fig. 5.3(a) that at higher pump powers we will require stronger pump filtering to maintain the same CAR. We can intuitively understand this through a comparison of the dependence of accidentals from multi-pair events and leaking pump photons. Since the leaked pump photons require two photons to make it through the filtering process, their accidental contribution scales as the pump squared.

However, the accidentals originating from multi-pair events scale as the fourth power of the pump power as shown in Fig. 5.4 and found from Eq. 5.12 and Eq. 4.26. So even though the ratio of photon pairs to pump photons decreases as higher pump powers, the contribution from multi-pair events increases much faster, thereby resulting in the need to reject more pump photons to maintain a constant CAR.

5.2.1 Unintentional light scattering and other modes

While there have been many successful demonstrations of photon pair sources in silicon, including the demonstration in a zero-change CMOS process we presented in the previous chapter, attempts to implement pump filtering on-chip have presented a significant challenge. To date, there have only been two demonstrations with sufficient pump filtering to measure photon pair generation via coincidence counting. Both examples required an additional chip for the pump filtering resulting

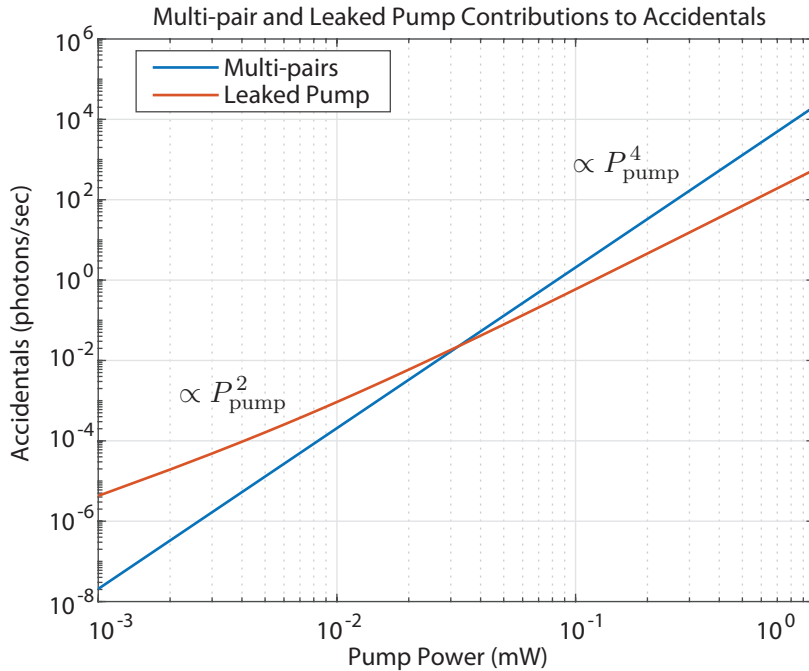


Figure 5.4: Comparison of accidental contributions from multi-pairs and leaked pump assuming 110dB pump rejection. The increased slope of the multi-pairs line shows that at higher pump powers more pump rejection is required to maintain a constant CAR.

in significant insertion loss. When photon pair generation and pump rejection occurs on two fiber coupled chips, the generated photon pairs are subject to two additional grating couplers (input and output of the second chip) compared to if the pump filtering had been completely integrated on a single-chip.

It turns out that the challenge of monolithically integrating a source and pump rejection circuit on the same chip is that stray light scattering around a chip outside of waveguides from the input grating to the output grating is larger than the roughly 90 dB extinction we found was required in the previous section. This is due to the fact that most silicon photonic chips primarily consist of only materials which are transparent to telecom wavelength light (Si and SiO₂). Since greater than 90 dB rejection is needed, only one photon out of every billion pump photons being scattered throughout a chip to the output fiber is enough to significantly contribute noise. To quantify this, we characterized an example standard silicon-on-insulator (SOI) chip. We positioned

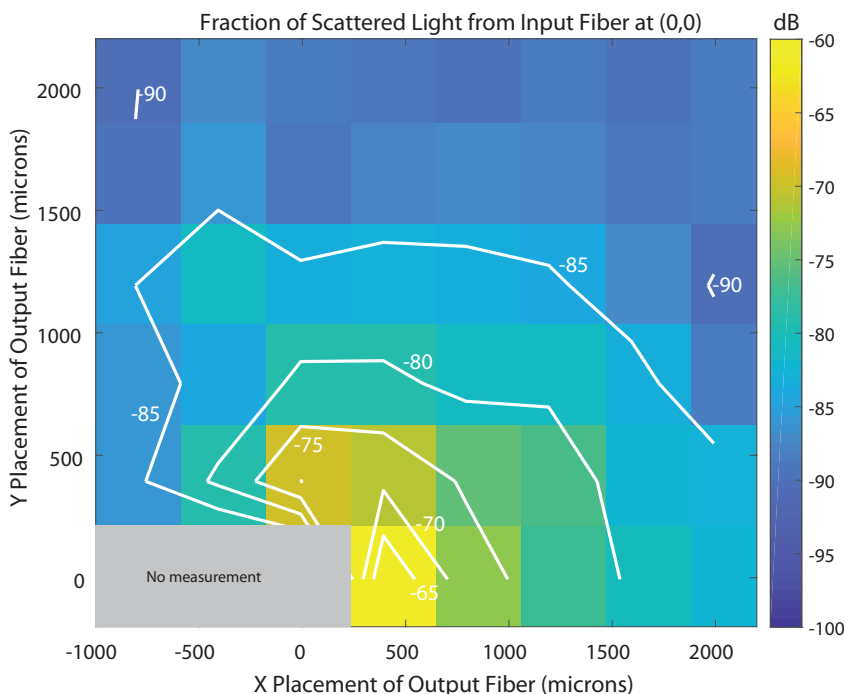


Figure 5.5: Measurement of scattered light on a standard SOI photonic chip demonstrating that even 2 mm away, there is still significant background light that will limit the extinction of an on-chip filter.

an input fiber (in a near surface normal configuration) near the center of the standard SOI photonic chip (not coupling to a photonic device) and scanned the output fiber (also near surface normal) around the chip to monitor the level of scattered light. We find that even after 2 mm of transverse translation on the chip surface there is still significant background light as shown in Fig. 5.5.

In addition to light scattering outside of the waveguides on a chip, there are unintentional ways that light can pass through a filter while still guided. For instance, one can simply cascade

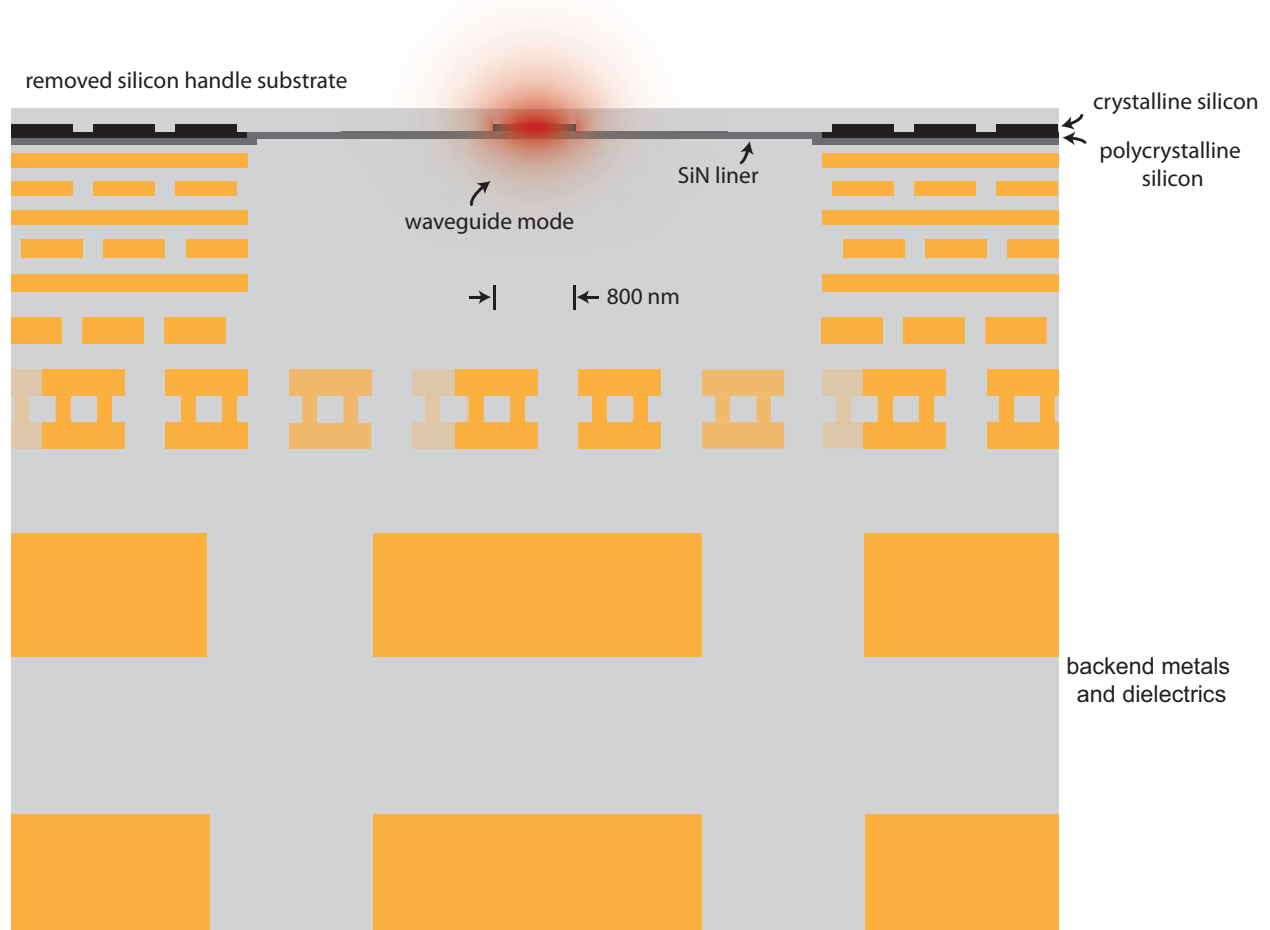


Figure 5.6: Illustration of the CMOS process layer stack-up after the substrate has been removed and the chip as been placed upside down such that the silicon device layer is at the top. We hypothesize that the presence of metal fill patterns will aid in the attenuation of scattered light.

10 ring filters which filter 10 dB each and still not achieve 100 dB filtering of the light within the waveguide. This is because the waveguide cross-section in 220 nm thick oxidized-cladded silicon is not actually single-mode as we found in Chapter 2, it supports at least one mode of both TE and TM polarizations. This results in the ability for light to couple from the intended mode to the other polarization. However, the filter passbands for TE and TM modes are at different wavelengths and the opposite polarization light is not sufficiently rejected. For this reason it is important to either use waveguides that are truly single mode (including single polarization) or to add a mechanism to additionally filter the alternate polarization.

The CMOS process in which we demonstrated a photon pair source in the previous chapter supports the use of dense metal “fill patterns” which are used to ensure uniform density for planarization steps and incidentally, have the potential to block much of the stray light. In addition, as part of the chip packaging in this process, we remove the transparent silicon handle substrates. This aids in removing reflections from the wafer-air interface. Finally, there are no TM modes present at the wavelengths of interest due to the asymmetry provided by the SiN liner layer and upper air cladding, in addition to the thin sub-100 nm silicon. A diagram of how the waveguides are encompassed by metal fill is shown in the process cross section in Fig. 5.6. We conjecture that this metal fill contributes to attenuating non-guided stray light within the chip.

5.2.2 FSR-doubled ring-based filters

For on-chip pump filtering, we proposed and demonstrated using cascaded second-order filters constructed from ring resonators with twice the free-spectral range of the source ring. In this way, the signal and idler resonances of the source can align with the pass-bands of the filter, while the pump is in the region with the highest rejection as illustrated in the schematic in Fig. 5.7. A bandpass configuration was chosen due to two main advantages. (1) a bandpass filter removes light at all frequencies except for the passband. This allows the filter to remove other broadband noise sources in addition to the pump, including broadband Raman generation from the waveguides. However, as we will see, resonant Raman generation from every other resonance of the source will

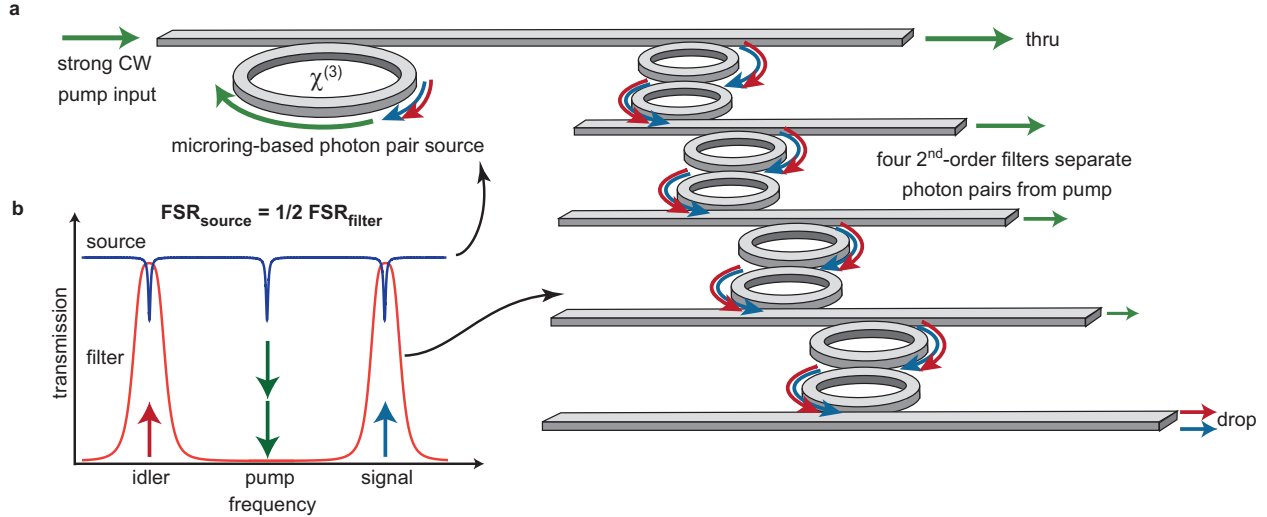


Figure 5.7: Proposed filtering scheme for removing the generated photon pairs from the collinear pump. A serial cascade of four second-order ring resonator filters, each of twice the free-spectral range (FSR), of the source will be used to remove the signal and idler photons simultaneously [44].

still play a factor. (2) A ring based bandstop filter is very difficult to fabricate with high rejection as the precise critical coupling condition is subject to fabrication uncertainties. This results from the sensitivity the on-resonance rejection has to slight differences between the external and intrinsic coupling. On the other hand, the out-of-band rejection of a bandpass filter is much less sensitive to this condition.

5.2.3 Experimental demonstration of on-chip pump rejection

We experimentally implemented the FSR-doubled ring-based filters in the same 12SOI CMOS process as we had investigated in Chapter 4. For reasons not fundamental to the CMOS process, on this experimental chip, we did not have access to the electronics on-chip to implement any tunable resonator devices. For this reason, we were not able to put a single source ring and tune its resonance in alignment with the filters. Instead, for this demonstration, we placed 13 serially cascaded source rings on the input waveguide with slightly different radii, corresponding to slightly shifted resonant frequencies with respect to each other. This distribution of many sources across a full spectral range ensures that at least one of the sources will align with the filters while not contributing any

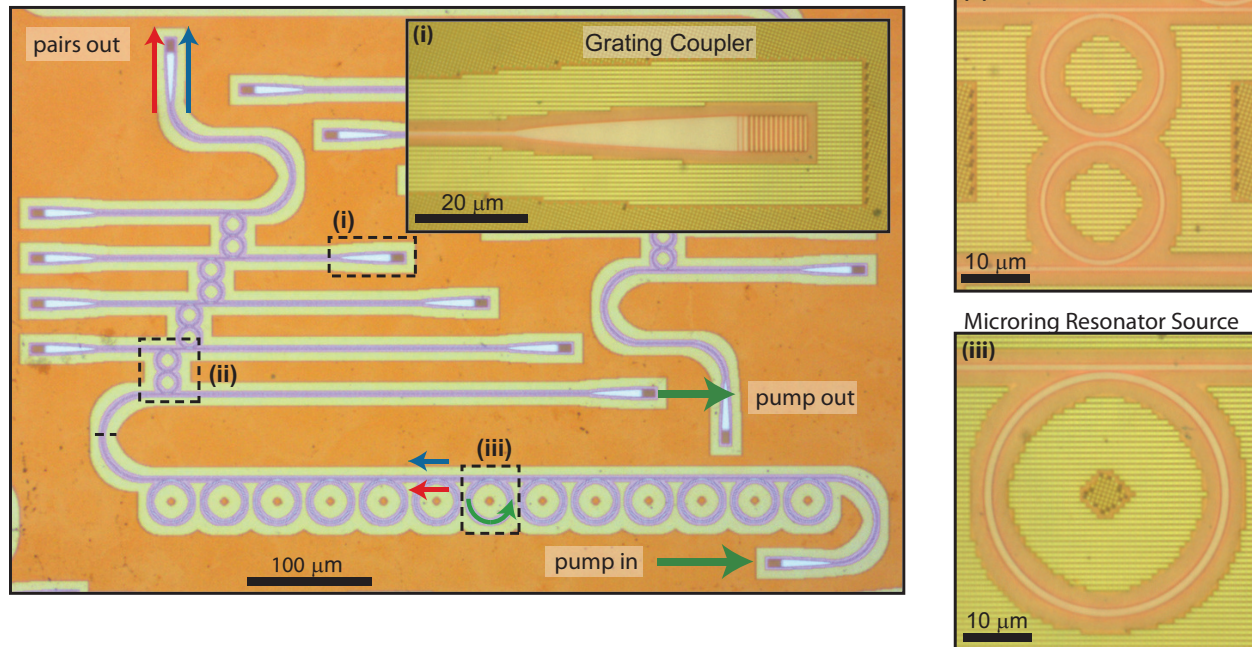


Figure 5.8: Micrograph of the fabricated source and filtering circuit. Thirteen sources of slightly varied radii were used to ensure that at least one would exhibit signal and idler resonances which overlap with the filter passband. Zoomed in micrographs of a (i) grating coupler, (ii) filter, and (iii) microresonator source show the presence of the processes fill pattern in the silicon layers. A similar fill pattern (not visible) is present below in the metallic absorbing layers [44].

additional losses to the generated photons since they will be away from the resonance of the unused sources. The fabricated system is shown in Fig. 5.8.

We were fairly conservative in the previous chapter by using a $22\ \mu\text{m}$ outer radius source ring. Here, we use a slightly reduced radius of $17.8\ \mu\text{m}$, thereby increasing the free spectral range and improving the extinction capabilities of the pump rejection filter. In Fig. 5.9(a) we plot the response of thru port showing the distinct resonances of the 13 sources and the drop port of the filters in red showing greater than 75 dB extinction. Fig. 5.9(c) shows a portion of the transmission response from Fig. 5.9(a) (in blue and red) in addition to high dynamic range transmission measurement of the filter response displaying greater than 95 dB extinction, where special care was taken to remove amplified spontaneous emission (ASE) from the probe laser. The different colors in Fig. 5.9(c) represent different transmission measurements taken using telecom filters to remove the amplified

spontaneous emission from the tunable laser used for testing. Without the addition of these telecom filters, the laser emits ASE at the bassband wavelengths (even when nominally set to the pump wavelength) which would pass through the filter providing a fictitious noise floor to the filter rejection. We believe the noise shown at the ~ -105 dB to -110 dB in Fig. 5.9 is from light scattering through and around the density fill on the CMOS chip. However, even with this scattered light present, the observed > 95 dB rejection is more than enough pump filtering to permit measurement of coincidences-to-accidentals ratios (CARs) greater than 100 as we found in Fig. 5.3.

Fig. 5.9(b) shows the spontaneous emission spectrum from the device under test when an ASE filtered pump is placed at the resonance near 1560 nm. This measurement was taken by sweeping the passband of a tunable Fabry-Perot filter at the output of the chip and before the

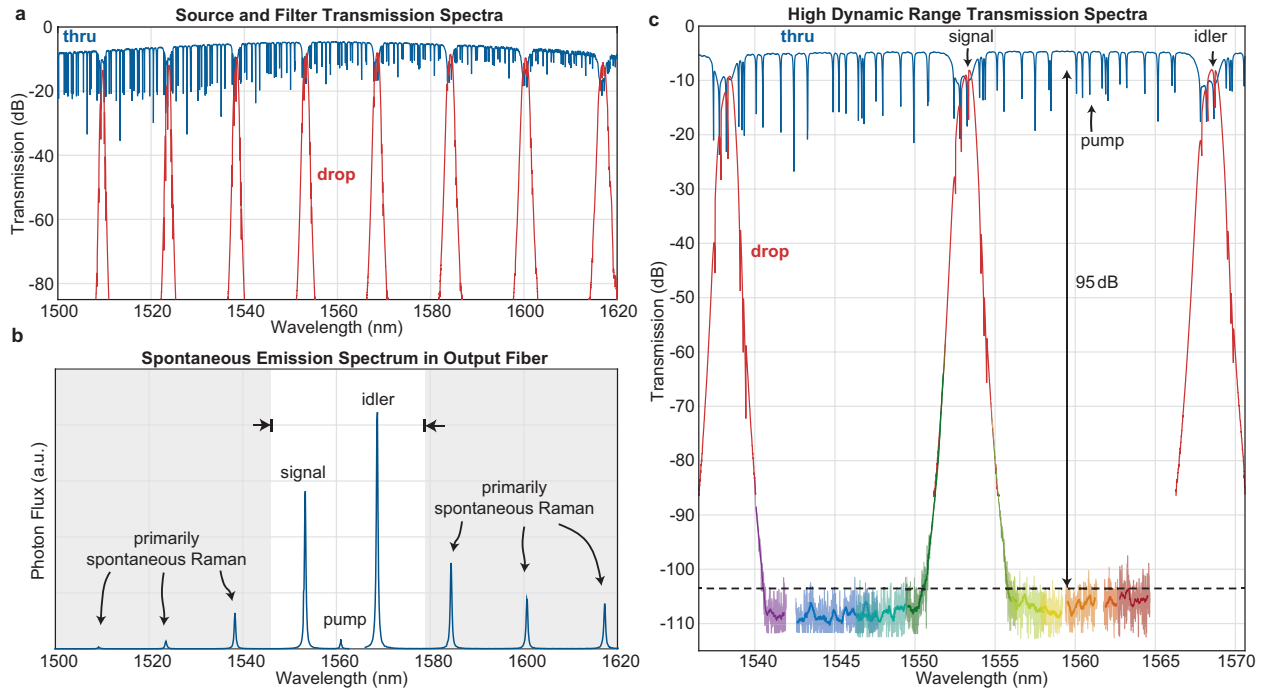


Figure 5.9: (a) Broadband transmission spectrum of the source thru port (blue) exhibiting resonances and the transmission spectrum of the filters (red). (b) The spectrum of photon counts received at the detector from the output of the chip when the pump is placed on resonance. (c) High dynamic range transmission spectra of the filter demonstrating over 95 dB pump rejection. Various colors below -70 dB represent measurements through different telecom filters which eliminate excess spontaneous emission from the swept laser source, thereby increasing the measurements dynamic range [44].

superconducting nanowire detectors, thereby serving as an in-house single photon spectrometer. The pump is rejected to a level approximately an order of magnitude lower than the signal and idler output levels. In addition, we observe at resonances more than two free spectral ranges away that there is still light being generated. This light is not correlated in time since the four-wave mixing process is not phase matched at these widely separated resonance. The source of these excess photons is likely spontaneous Raman scattered light from the cladding materials around the waveguide, as crystalline silicon has negligible Raman gain at these detunings. In future implementations, this excess noise can be easily filtered by an addition on-chip wideband filter passing the signal, idler, and pump wavelengths while rejecting all others.

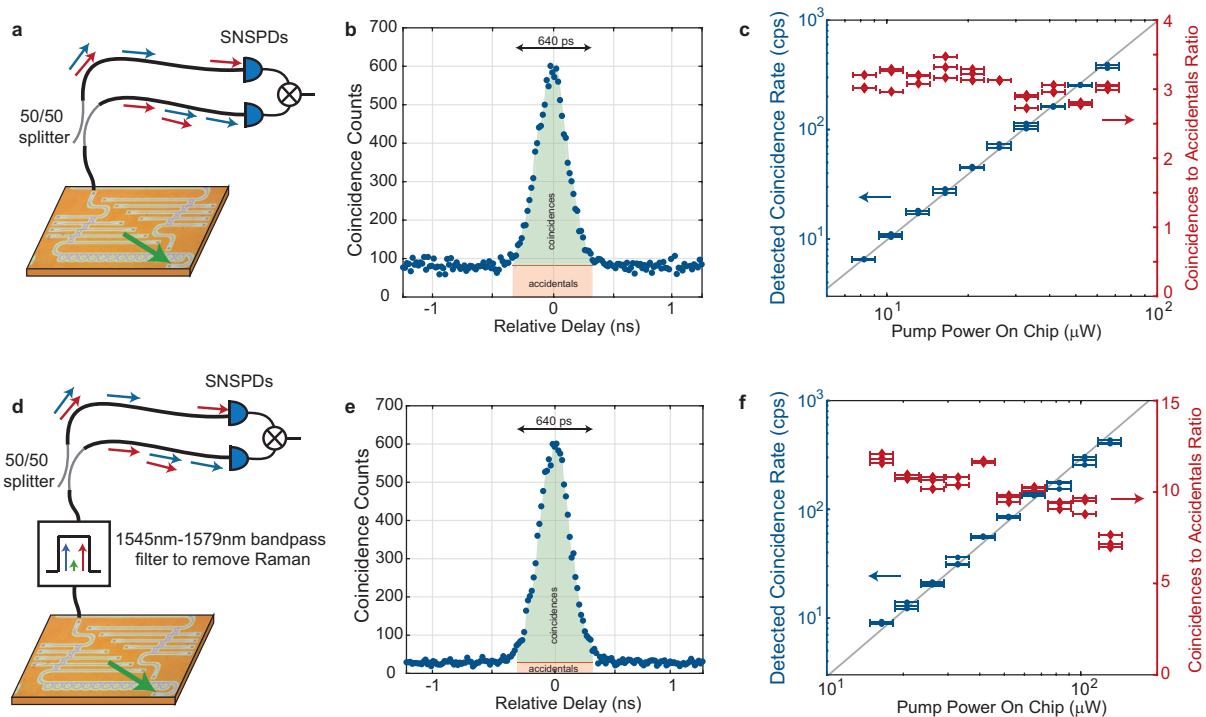


Figure 5.10: (a) Schematic of experimental setup for demonstrating all on-chip pump filtering with a 50%-50% fiber directional coupler probabilistically separating signal and idler photons. (b) Example coincidence histogram with coincidence window of 640 ps for the setup in (a). (c) Detected coincidence rates and CARs for various on-chip pump powers for the setup in (a). (d) Schematic of experimental setup where an off-chip filter was used to remove excess noise photons not contributed by the pump with (e) example coincidence histogram and (f) corresponding measured coincidence rates and CARs [44].

To characterize the noise from the remaining pump along with the generated noise at other resonances, we perform coincidence measurements where the signal and idler photons are separated using a fiber 50%-50% splitter as shown in Fig. 5.10(a). Since there is a 50% probability that a signal and idler pair will exit the same port of the beam splitter, this separation technique is not deterministic, but benefits from being broadband. An example coincidence peak is shown in Fig. 5.10(b) displaying at the center of the peak approximate 5 times the number of coincidences as accidentals. Since, all filtering was performed on a single chip and the pair is only subject to the loss from a single output coupler (~ 2 dB), we were able to measure coincidence rates of near 400 coincidences per second as shown in Fig. 5.10(c) with CARs around 3. This is nearly a three orders of magnitude improvement in rate over previous demonstrations with on-chip pump filtering which relied on multiple cascaded chips [57, 114].

To characterize the effect of the spontaneous Raman generated noise on the CAR, we also performed coincidence measurements with a wide-band off-chip fiber filter with a transmission spanning from 1545 nm to 1579 nm to remove the Raman noise but importantly still pass any pump light that may have leaked through as shown in Fig. 5.10(d). This ensures that we are still demonstrating pump rejection entirely on chip. Comparing the resultant coincidence plot in Fig. 5.10(e) to Fig. 5.10(b) we find a significant improvement in noise from the chip, with CARs exceeding 10 as shown in Fig. 5.10(f). This illustrates that the CAR was being limited by the Raman noise and not the pump leaking through the device. This confirms the effectiveness of our implemented on-chip pump rejection.

In addition to CAR, another way to characterize the noise performance of a source is to measure the degree of entanglement. Using a continuous wave pump guarantees that the photon pairs being generated are entangled in energy and time. We built a folded Franson interferometer [149] from fiber optic components as illustrated schematically in Fig. 5.11(a). The interferometer is in a Michelson configuration where one arm is shorter than the other by a length greater than the coherence length of the generated photons. This guarantees that there is no classical interference exhibited by the measured entangled photons. The bi-photon state however will have an

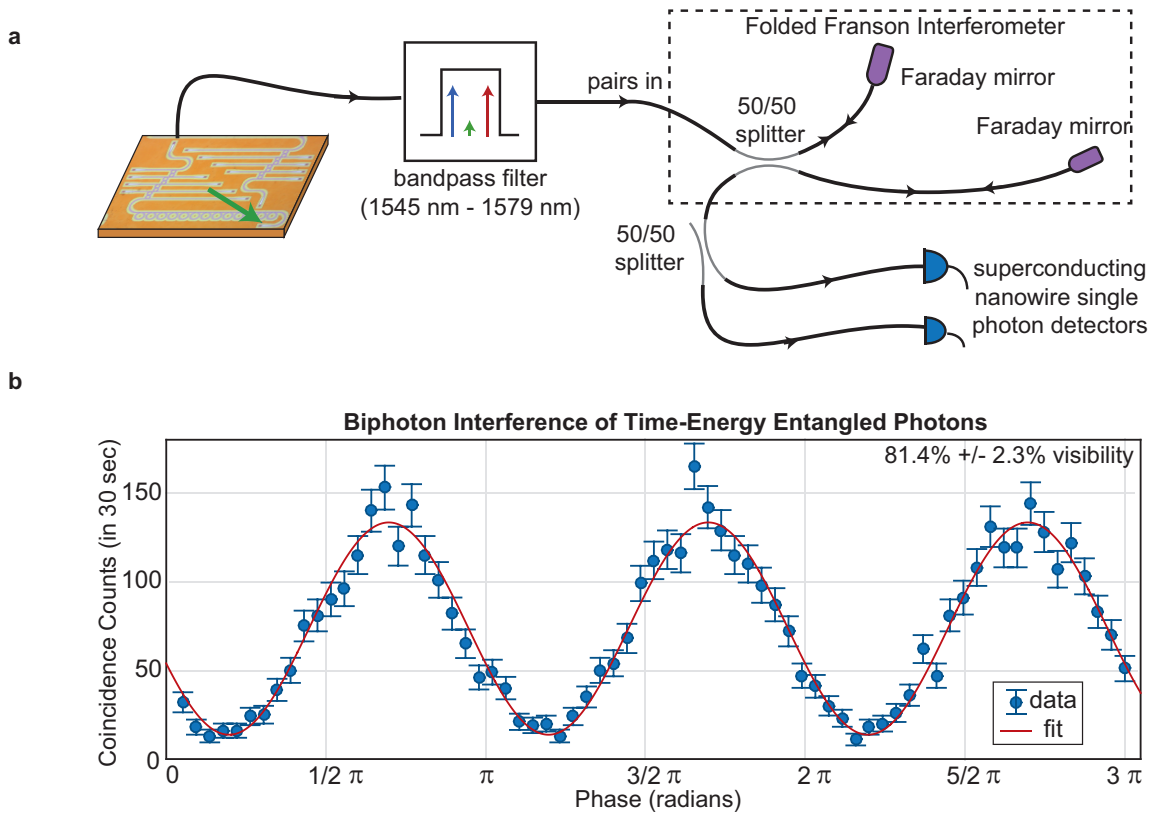


Figure 5.11: (a) Schematic illustration of the setup of a folded Franson interferometer [149] which was used to measure time-energy entangled photons. (b) The corresponding coincidences demonstrating bi-photon interference and non-classical visibility of $81.4\% \pm 2.3\%$ [44].

effective coherence length determined by the pump coherence and therefore will exhibit quantum interference. By measuring the photons which arrive at a time delay which guarantees that they took the same path within the interferometer (either the short or the long path taken together are indistinguishable from each other in the quantum mechanical sense), the bi-photon state are able to interfere. By measuring the number of coincidences in this delay window at a range of phases in the interferometer we find a strong interference pattern at half the period that the classical interference in the interferometer would be as shown. This data is shown in Fig. 5.11(b) demonstrating an interference and fitted visibility $[(\text{peak}-\text{trough})/(\text{peak}+\text{trough})]$ of $81.4\% \pm 2.3\%$. A visibility of $\sqrt{2}/2 \approx 70.1\%$ is sufficient to violate a Bell inequality [149], demonstrating that the pump filtering implemented on-chip is sufficient for many quantum information applications such

as entanglement-based quantum key distribution.

5.3 Conclusions

In this chapter, we explored the coincidences-to-accidentals (CAR) figure of merit in detail. We justified the procedure for determining the CAR used in Chapter 5 and investigated two primary contributors to noise in leaked pump light and multi-pair events. We theoretically showed that multi-pair events are intrinsic to spontaneous parametric sources and set the upper limit for CAR for a given device. We then investigated the amount of pump rejection needed so that the CAR would still be dominated by multi-pair events and found that, somewhat surprisingly, the pump photon flux at the detectors did not need to be less than the photon pair detection rate since the pump photons are uncorrelated in time.

We implemented a four-stage pump filtering device in a commercial CMOS process and demonstrated over 95 dB pump rejection. **Generation rates two orders of magnitude higher than the state-of-the-art were demonstrated**, as all pump filtering was performed on a single chip. In addition, we further characterized the noise quality of the source by measuring time-energy entanglement and demonstrated that the pump filtering was sufficient to show non-classical visibility in two-photon interference. These results demonstrate the feasibility of implementing many photon pair sources on a single electronic-photonic chip and could provide an important step to next generation quantum photonic technologies.

Chapter 6

Resonance linewidth engineering for enhancing quantum and classical sources

Integrated photonics platforms provide access to various degrees of freedom for device design that are otherwise inaccessible by free space optics. In Chapter 3, we demonstrated four-wave mixing across a free-spectral range (FSR) of over 3 THz using two coupled micron-scale ring resonators. This experiment was primarily enabled by the ability to fabricate ultra-small resonators as the FSR is inversely proportional to resonator size. In this chapter we introduce linewidth engineering (i.e., frequency dependent port coupling to a resonator) as another degree of freedom which is readily available in an integrated platform for both quantum and classical photonic sources. We will first establish the concept and demonstrate ways in which its use can improve the performance of spontaneous four-wave mixing sources. We will then introduce imaginary coupling as a mechanism for linewidth engineering and propose how its use in a laser cavity can lead to wide-band single mode tuning of an integrated laser.

6.1 Increasing the generation efficiency of a resonant photon pair source

In Chapter 4, we formulated the spontaneous four-wave mixing generation of rate (in the case of a CW pump on resonance) in Eq. 4.26 to allow for the case of unequal pump, signal, and idler external couplings ($r_{p,e}$, $r_{s,e}$, and $r_{i,e}$, respectively) as well as unequal pump, signal, and idler intrinsic decay rates ($r_{p,o}$, $r_{s,o}$, and $r_{i,o}$, respectively). In demonstrating a resonant photon pair source in Chapter 4 and 5, we used a single ring resonator which had approximately equal couplings and decay rates (and therefore Q's) for each of the three modes.

We now investigate whether there is an optimal choice for the resonator-bus couplings to optimize photon generation rate. The intrinsic loss is often independent of frequency over the range of three resonant modes, such that we can define $r_o \equiv r_{p,o} = r_{s,o} = r_{i,o}$. We can also treat the signal and idler modes symmetrically, so that they have the same external couplings, but different from the pump external couplings (i.e., $r_{s,e} = r_{i,e}$). Eq. 4.26 then allows us to find the pair generation rate for symmetric couplings $I_{\text{src,pairs,sym}}$ to be

$$I_{\text{src,pairs,sym}} = 4P_p^2 \omega^2 \beta_{\text{fwm}}^2 \frac{r_{s,e}^2}{(r_{s,e} + r_o)^3} \frac{r_{p,e}^2}{(r_{p,e} + r_o)^4}, \quad (6.1)$$

where we have assumed the resonator has been dispersion engineered such that $\Delta\nu_{\text{FSR}} = 0$. A first derivative test of Eq. 6.1 with respect to pump external coupling $r_{p,e}$ allows us to find that the optimal pump coupling corresponds to the critical coupling condition (i.e., $r_{p,e} = r_o$). This should be expected since critical coupling maximizes the pump power in the resonator as we found in Section 2.5. On the other hand, a first derivative test with respect to the signal/idler external coupling (which we assumed were equal and denoted as $r_{s,e}$) optimizes generation rate at

$$r_{s,e,\text{opt}} = 2r_o. \quad (6.2)$$

Therefore, if our only goal was to optimize generation rate we should design the resonator such that the signal and idler modes have twice the external coupling of the critically coupled pump. To quantify how large of an enhancement of generation rate this is over equal couplings we can assume equal couplings on all three resonance (i.e., $r_{p,e} = r_{s,e} = r_{i,e}$) and perform a first derivative test once again. In the case of equal coupling we find the optimal external coupling for the three resonances to be

$$r_{\text{e,equal,opt}} = \frac{4}{3}r_o. \quad (6.3)$$

Calculating the ratio of the efficiency in the case of optimal symmetric couplings to optimal equal couplings allows us to find that the ability to control the resonance linewidth provide only an 18.5% improvement in total generation rate as shown in Fig. 6.1.

However, in our current analysis we have only been considering total generation efficiency. We can now consider applications where a certain escape efficiency ($\eta_{\text{esc}} = \frac{r_{s,e}}{r_{s,e}+r_{s,o}}$), a device parameter we introduced in Section 4.2.1, is desirable. For example, to perform a detection-loophole-free test of quantum nonlocality the total system efficiency (the efficiency from photon pair generation to detection) must be greater than $2/3$ [132]. In the case of critical coupling of all resonances, the system efficiency is intrinsically limited to 50%, since the corresponding escape efficiency is 50%. We can reformulate Eq. 6.1 in terms of escape efficiency, where in the symmetric coupling case ($r_{s,e} = r_{i,e}$) and the pump is set to critical coupling that

$$\text{symmetric signal and idler coupling: } I_{\text{src,pairs,sym}} \frac{r_o^3}{(P_p \omega \beta_{\text{fwm}})^2} = \frac{1}{4} \eta_{\text{esc}}^2 (1 - \eta_{\text{esc}}). \quad (6.4)$$

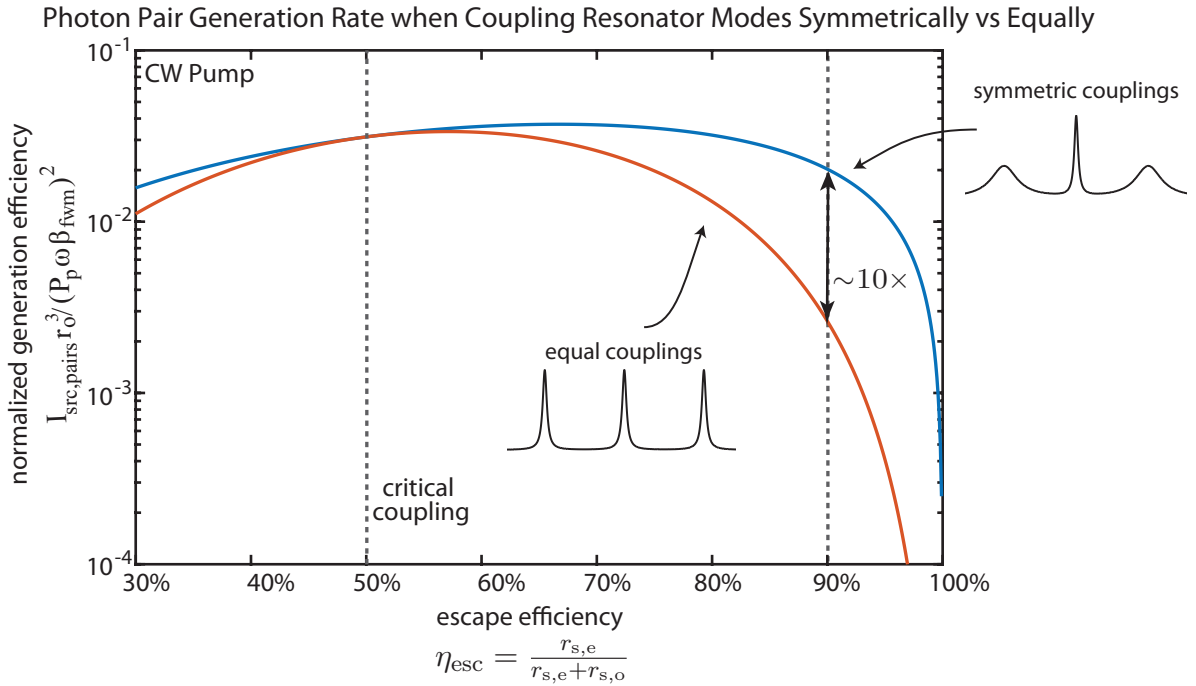


Figure 6.1: Plot of normalized generation efficiencies given by Eq. 6.4 for symmetrically coupled resonators where the signal and idler are coupled equally while the pump is fixed at critical couplings and Eq. 6.5 where all three resonances are equally coupled. At large escape efficiencies the symmetric coupling configuration is much more efficient, including greater than 10 times more efficient at escape efficiencies over 90% [43].

In the equal coupling case we find

$$\text{equal pump, signal, and idler coupling: } I_{\text{src,pairs,equal}} \frac{r_o^3}{(P_p \omega \beta_{\text{fwm}})^2} = 4\eta_{\text{esc}}^4 (1 - \eta_{\text{esc}})^3. \quad (6.5)$$

We note that this trade-off for the case of equal couplings was originally shown by Vernon *et al.* [154]. Plotting Eq. 6.4 and 6.5 in Fig. 6.1, we see that as higher escape efficiencies are required, the symmetric coupling configuration greatly outperforms the equal couplings condition. In the case that a 90% escape efficiency is desired, one would be able to obtain approximately $\sim 10\times$ higher generation rate by chosen properly tailored symmetric couplings over equal couplings.

Heralding single photons from a photon pair source is one particular application where a very high escape efficiency is desirable. However, the above solution introduces a problem if the application requires the measuring quantum interference between two heralded single photons. When an ideal CW pump is used, there is a perfect energy correlation between the signal and idler photons, restricted by energy conservation. Therefore the detection of one photon in a heralding experiment “collapses” the heralded photon to a specific frequency within the resonance linewidth. When heralding a second photon the frequency that the heralded photon collapses to has a finite probability of being elsewhere within the resonance. Since the two heralded photons will have definite and different frequencies they will not interfere in a Hong-Ou-Mandel type measurement [67]. The frequency correlations of a photon pair source are often visually depicted by plotting their “joint spectral intensity” (JSI). An example of a highly correlated JSI is shown in Fig. 6.2(a) and is said to be a “mixed state” since the JSI is not able to be described by a product of a function solely dependent on signal frequency and a function solely dependent on idler frequency as the ideal joint spectral distribution in Fig. 6.2(b) is.

6.2 Engineering signal and idler spectral correlations

The joint spectral intensity can be engineered through the use of parameterizable signal, idler, and pump external couplings in addition to tailoring the width of a pump pulse, where we now work in the regime that the pump is not CW. A pulsed pump is required such that the pump is not

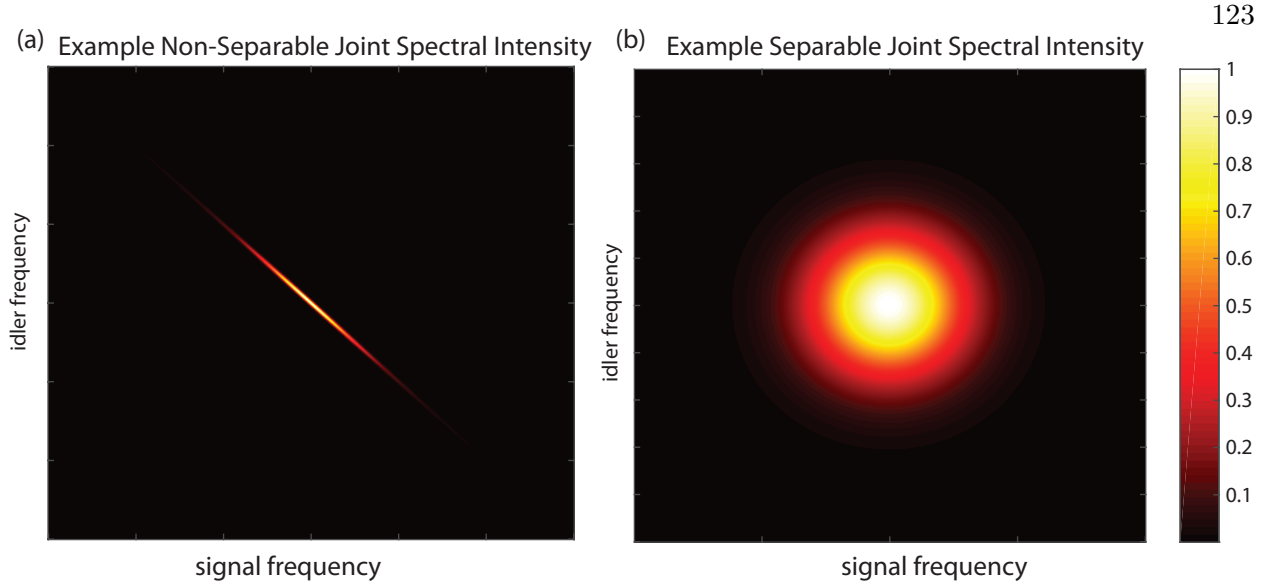


Figure 6.2: (a) Joint spectral intensity of a photon pair generated in a highly mixed bi-photon state. (b) Example normalized joint spectral intensity of an ideal separable bi-photon state.

single frequency and therefore can allow a heralded photon to not collapse to a specific frequency.

The formula for the joint spectral intensity¹ can be found by solving Eqs. 4.3, 4.4, and 4.12 with a pulsed pump to be

$$\Phi_{\text{JSI}} = \frac{4\omega^2 \beta_{\text{fwm}}^2 r_{s,e} r_{i,e}}{[(\omega_i - \omega_{i,o})^2 + r_{i,\text{tot}}^2][(\omega_s - \omega_{s,o})^2 + r_{s,\text{tot}}^2]} |F_{\text{p}}(\omega_s, \omega_i)|^2 \quad (6.6)$$

where

$$|F_{\text{p}}(\omega_s, \omega_i)|^2 = \frac{1}{2\pi} \int \int a_{\text{p}}(\omega_{\text{p1}}) a_{\text{p}}(\omega_{\text{p2}}) \delta(\omega_{\text{p1}} + \omega_{\text{p2}} - \omega_s - \omega_i) d\omega_{\text{p1}} d\omega_{\text{p2}}, \quad (6.7)$$

where ω_{p1} and ω_{p2} takes into consideration that during pulsed pump operation the two pump photons could be slightly different frequencies. In Fig. 6.3 we plot four example joint spectral intensities where we show the difference between Fig. 6.3(a) equal coupled CW pumped and Fig. 6.3(b) symmetric coupled with pump pulsed wider than the resonance linewidth. In Fig. 6.3(c) and Fig. 6.3(d) we plot the JSI for the pulsed pump case where the signal, idler and pump resonance all have different couplings. This configuration allows a source to exhibit a much larger spectral breadth in one mode than the other. This can be useful in applications where it might be favorable for a heralding

¹ See [155] and [153] for detailed derivations

tailoring bi-photon probability distributions

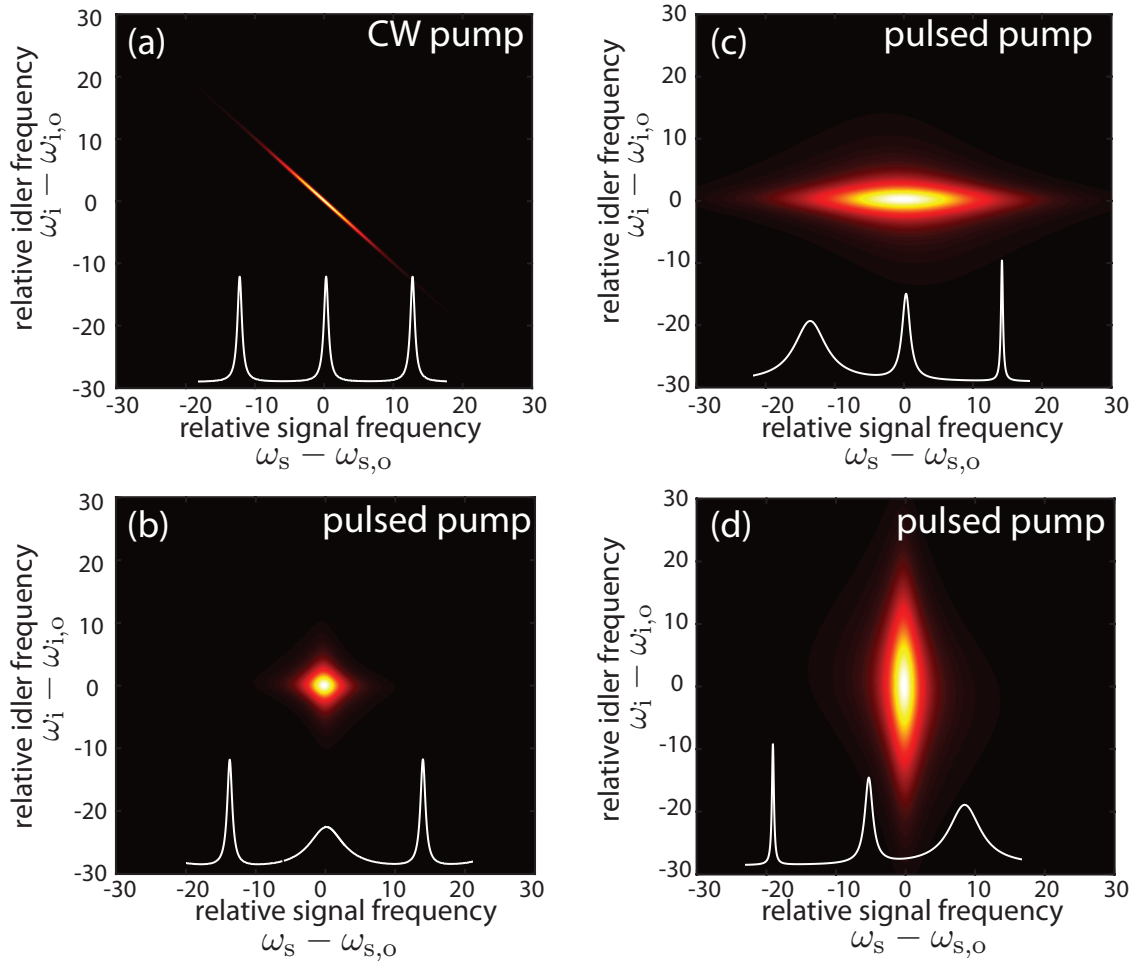


Figure 6.3: Joint spectral intensities for a resonator with (a) equal couplings ($r_{s,e} = 6r_o$, $r_{p,e} = 6r_o$, and $r_{i,e} = 6r_o$) and a CW pump, (b) symmetric couplings ($r_{s,e} = r_o$, $r_{p,e} = 10r_o$, and $r_{i,e} = r_o$) and a broad pulsed pump (pulse bandwidth of $15r_o$), (c) unequal couplings ($r_{s,e} = 20r_o$, $r_{p,e} = 10r_o$, and $r_{i,e} = r_o$) with a pulsed pump (pulse bandwidth of $40r_o$), and (d) unequal couplings ($r_{s,e} = r_o$, $r_{p,e} = 10r_o$, and $r_{i,e} = 20r_o$) with a pulsed pump (pulse bandwidth of $40r_o$) [43].

photon to be significantly more broadband than the corresponding signal photon or vice versa. It was later shown [153] that the symmetric coupling configuration can arbitrarily approach a truly separable bi-photon state as the coupling of the signal and idler resonance become arbitrarily more strongly coupled than the pump resonance.

A frequency dependent coupler can be implemented using many of the degrees of freedom available in an integrated platform. A fairly simple method consists of coupling a bus waveguide to a

coupling (higher external Q) than would otherwise be provided by the output coupler to either one of the two cavities in isolation. A coupling of modes in time model describes all the relevant physics:

$$\frac{d}{dt}\vec{a} = -i\bar{\omega} \cdot \vec{a} + i\bar{\mu} \cdot \vec{a} + i\bar{M}_i s_{\text{in}} \quad (6.8)$$

$$s_{\text{out}} = i\bar{M}_o \cdot \vec{a} + s_{\text{in}} \quad (6.9)$$

where

$$\vec{a} = \begin{pmatrix} a_1 \\ a_2 \end{pmatrix} \quad (6.10)$$

$$\bar{\omega} = \begin{pmatrix} \omega_o + \delta\omega_o - ir_o & 0 \\ 0 & \omega_o - \delta\omega_o - ir_o \end{pmatrix} \quad (6.11)$$

$$\bar{\mu} = i \begin{pmatrix} r_e & r_e \\ r_e & r_e \end{pmatrix}. \quad (6.12)$$

$$\bar{M}_i = \sqrt{2r_e} \begin{pmatrix} 1 \\ 1 \end{pmatrix} \quad (6.13)$$

$$\bar{M}_o = \bar{M}_i^T \quad (6.14)$$

Here a_1 and a_2 are the energy amplitudes of the resonant modes in the two cavities; $\omega_o \pm \delta\omega_o$ are the individual, uncoupled resonance frequencies of the two cavities whose detuning $2\delta\omega_o$ can be controlled; and r_e and r_o are the decay rates due to external coupling and intrinsic loss (radiation loss, roughness loss, absorption), respectively. We have assumed (without loss of generality) that the decay rates are the same in each cavity and that there is negligible direct (real) coupling between the cavities. Solving the system (6.8) in the steady state for zero input ($s_{\text{in}} = 0$) gives the eigenfrequencies (resonances) of the system

$$\omega_{\pm} = \omega_o - i(r_o + r_e \pm \sqrt{r_e^2 - \delta\omega_o^2}) \quad (6.15)$$

with corresponding eigenvectors (supermodes)

$$\begin{pmatrix} a_1 \\ a_2 \end{pmatrix}_{\pm} = \frac{1}{C} \begin{pmatrix} 1 \\ \pm \sqrt{1 - \left(\frac{\delta\omega_o}{r_e}\right)^2} - i\frac{\delta\omega_o}{r_e} \end{pmatrix} \quad (6.16)$$

where C is a normalization constant.

We next explore the salient features of this system. In the range of detunings smaller than the external coupling (i.e. $\delta\omega_o < r_e$), it is evident that both supermodes have equal **real** resonant frequencies at the arithmetic mean of the individual resonator cavities' uncoupled resonant frequencies. Therefore, the imaginary coupling term results in an ‘‘attraction’’ of resonant frequencies, illustrated in Fig. 6.4, in contrast to the usual energy level repulsion that is prototypical of a real (reactive) coupling term [58]. Instead of splitting along the real frequency axis the eigenfrequencies split along the imaginary axis. Physically this means there is no energy exchange coupling between the individual cavities while the corresponding quality factors, $Q = \frac{Re\{\omega\}}{2Im\{\omega\}}$ [151], for the two supermodes split due to interaction at the point of coupling to the shared radiation channel. Q-splitting has been demonstrated via far-field interference in radiation loss [151, 13] and in a single-mode external coupling bus radiation channel [26, 163]. It has also been demonstrated in Bragg matching of momentum detuned modes to achieve scatterer-avoiding cavity supermodes [89, 131]. Imaginary k-splitting, a waveguide equivalent to Q-splitting, has also been demonstrated for ultra-low-loss waveguide crossings [90]. The supermodes in the case of zero detuning are illustrated in Fig. 6.4 and consist of a high-loss ‘bright state’, $\vec{a}_{BS} = \frac{1}{\sqrt{2}}(1, 1)^T$ at frequency ω_{BS} , with large external coupling and an antisymmetric, low-loss ‘dark state’, $\vec{a}_{DS} = \frac{1}{\sqrt{2}}(1, -1)^T$ at frequency ω_{DS} , with zero external coupling. The corresponding resonant frequencies are split along the imaginary axis, $\omega_{BS} - \omega_{DS} = -i2r_e$.

We propose two ring resonators as a laser cavity structure with different FSRs coupled to a waveguide as shown in Fig. 6.5(a). In the case of a laser we can substitute $r_o - r_g$ for r_o in the equations above to explicitly include the gain rate r_g . Therefore, for a small-signal gain, described by gain rate r_{ssg} , larger than the intrinsic loss rate r_o , but smaller than the loaded passive decay rate $r_o + r_e$, **only** the dark state will be above lasing threshold. For small signal gain above

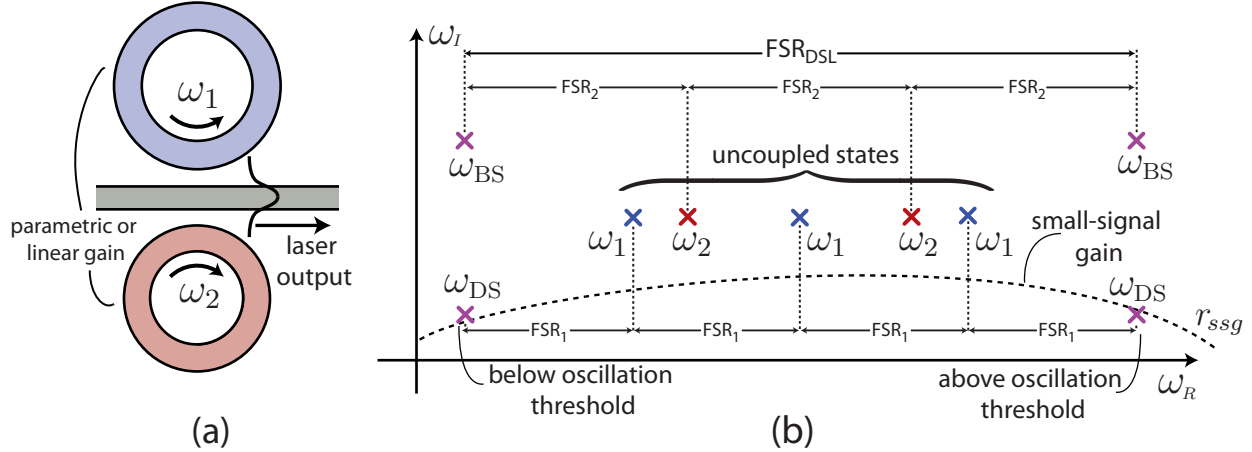


Figure 6.5: (a) Proposed laser resonator geometry enabling farfield interference at the output coupler resulting in eigenfrequency imaginary splitting at matched resonances to create (b) a broad Vernier-like FSR for ultrawide tuning [45].

$r_e + r_o$, resonances at other FSRs may see net gain and begin to lase, in our current discussion an undesirable feature. If the two cavities have different FSRs then the Q-splitting will only occur where the resonant frequencies match, resulting in an effective FSR between dark states determined by the least common multiple of the FSRs of the individual cavities as illustrated in Fig. 6.5(b). This allows for a Vernier-like selection (and tuning) effect over an ultra-wide wavelength range.

The dark state is named as such because there is exactly no coupling of cavity light energy into the output waveguide. As with any laser, for dark state lasing to be useful there must be a finite external output coupling. This is achieved via a slight detuning of the resonators. The dependence of laser output on detuning is illustrated in Fig. 6.7(b). Since the supermodes are, in general, two-dimensional complex eigenvectors normalized to unit energy they can be visualized similarly to polarization (spin) on a Poincaré (Bloch) sphere. Fig. 6.6 illustrates the evolution of the supermodes with increased detuning. The dependence of the total external coupling of the dark state supermode on detuning is described by

$$r_{DS,e} = r_e - \sqrt{r_e^2 - \delta\omega_0^2} \quad (6.17)$$

Physically, this finite external coupling results from the no longer perfect destructive interference

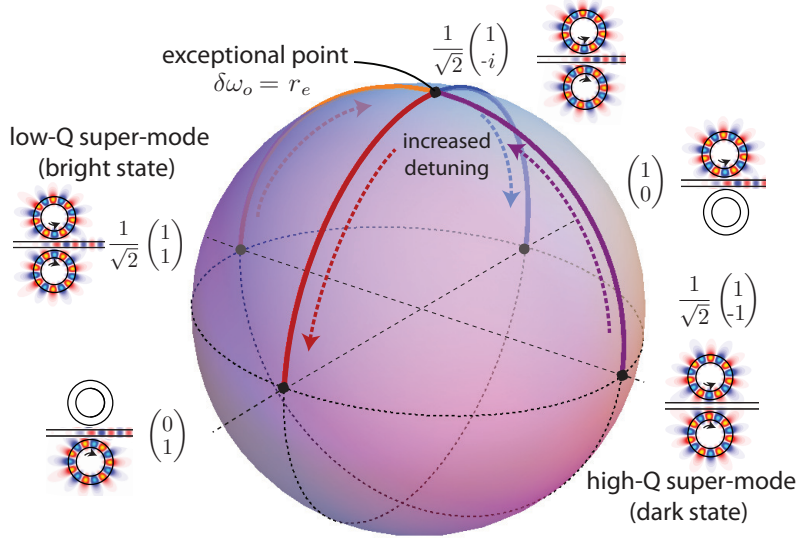


Figure 6.6: Visualization of supermodes with detuning on a Poincaré (Bloch) sphere. For detuning less than the single ring external coupling ($\delta\omega_o < r_e$) the energy is equally distributed across both rings. At greater detuning the supermodes approach the modes of the individual uncoupled rings.

in the waveguide due to the phase difference between the cavities deviating from π with detuning [Fig. 6.7(a)]. This results in a lasing threshold condition on the dark state of $r_{\text{ssg}} > r_o + r_{\text{DS,e}}$. Too high an external coupling will result in the laser dropping below threshold as shown in Fig. 6.7(b) at large cavity-cavity detuning $\delta\omega_o$.

To investigate design of the cavity for optimal lasing characteristics we introduce a saturable gain into the model as we introduced in Section 2.6.2. Assuming equal gain properties in each ring, when the dark state is over threshold the gain rate is

$$r_g = \frac{r_{\text{ssg}}}{1 + \frac{|a_{\text{DS}}|^2}{|a_{\text{sat}}|^2}}. \quad (6.18)$$

The steady state output power relative to the saturation energy, $\frac{P_{\text{out}}}{|a_{\text{sat}}|^2}$, is maximized at a particular, optimal choice external coupling,

$$r_{\text{DS,e(max)}} = \sqrt{r_{\text{ssg}} r_o} - r_o. \quad (6.19)$$

We can consider the saturation of the whole 2-cavity resonator rather than that of each ring individually because in the range of detuning $\delta\omega_o$ where Q-splitting occurs the energy in each ring

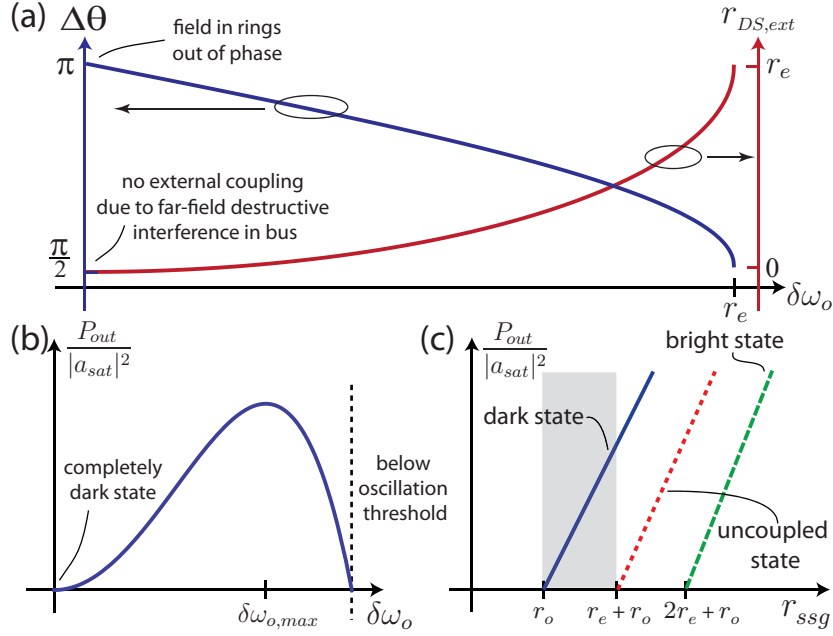


Figure 6.7: (a)Phase difference between mode-fields of each ring and resulting external coupling of dark state with detuning. (b)Dependence of tuning on output power for fixed r_e (c)Threshold/slope efficiency curves as a function of small-signal gain (pumping), with the operating region of dark-state-only lasing shaded.

is equal (6.16). Here the size difference of the rings is assumed to be negligible with respect to its saturation properties. From this model, the threshold and slope efficiencies are described by

$$\frac{P_{out}}{|a_{sat}|^2} = \begin{cases} 0 & , r_{ssg} < r_{DS,e} + r_o \\ \frac{2r_{DS,e}}{r_o + r_{DS,e}}(r_{ssg} - r_{DS,e} - r_o), & r_{ssg} \geq r_{DS,e} + r_o \end{cases} \quad (6.20)$$

This expression is general to any laser cavity. To find similar parameters for the uncoupled states and bright state $r_{DS,e}$ is simply replaced with their respective output couplings. The laser mode outputs as a function of small signal gain are illustrated in Fig. 6.7(c). Note that a high output coupling increases the threshold requirement of a lasing mode but also results in a higher slope efficiency with respect to the small signal gain r_{ssg} .

Vernier-like tuning has been used in lasers featuring sampled grating distributed Bragg reflectors with different periods [69]. We note that this is a fundamentally different mechanism than that presented in this paper, not based on imaginary coupling due to far-field interference. Here,

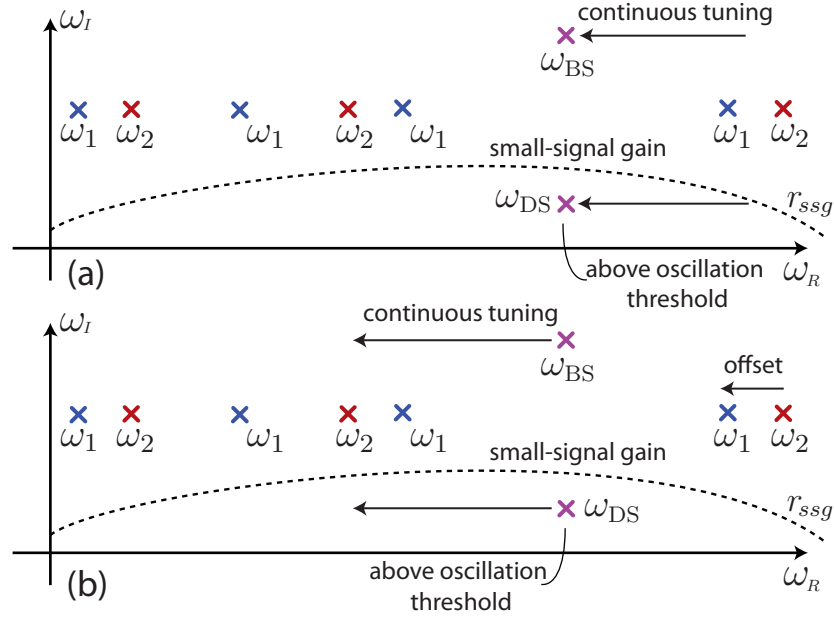


Figure 6.8: An illustration of quasi-continuous tuning of the dark state laser. First (a) both rings are tuned an FSR of the smaller ring (larger FSR). Then the laser can be turned off and reset to the start position Fig 1 (d). (b) An offset can then be introduced to shift the Q-splitting to the previous location where both rings can then be continuously tuned across another FSR. The process can then be repeated across the gain bandwidth.

we will briefly outline possible tuning strategies for dark state lasers. Tuning only one of the two rings is the simplest method but results in discontinuous tuning. In this method the resonance frequency of a single ring is shifted, for example using the thermo-optic effect, resulting in the two cavities' resonances aligning at a different FSR and therefore shifting at which wavelength the laser is operating. This will result in successful tuning of the laser across a gain bandwidth, albeit in discrete steps of the FSR of the larger ring. In principle, it is also possible to tune the laser almost continuously over many FSRs if one is able to carefully tune both rings. This can be achieved even if the tuning range of each resonator is limited to less than two FSRs (as it is often difficult to thermally tune across several FSRs). This quasi-continuous tuning strategy is illustrated in Fig. 6.8. Both rings can be tuned an FSR of the smaller cavity (larger FSR) where the laser can be briefly shut off and tuned back to the start position in Fig. 6.5(b). Then one can introduce an offset by detuning the rings until the Q-splitting occurs at the wavelength the laser was operating

previously, but at the next longitudinal-order mode pair. This process can continue allowing a quasi-continuous tuning across the dark state FSR.

An interesting property of the dark state laser cavity is the manifestation of an exceptional point at $\delta\omega_o = r_e$. The exceptional point is characterized by the coalescing of both eigenvalues and eigenvectors of the system as shown in Fig. 6.4 and Fig. 6.6 respectively, along with a vanishing norm [61]. This results from a square root branch point in Eq. 6.15 and physically occurs at the transition from resonant frequency attraction to Q-splitting.

The proposed resonator may enable a new approach to the design of widely tunable laser sources, and in principle extends to table top resonators with a shared output coupler. It is compatible with any system where microcavity lasers have been demonstrated in a disk or ring configuration, such as those based on III-V disks [88]. The design need not use different size resonators if the Vernier property is not of importance.

6.4 Conclusions

In this Chapter we explored the application of linewidth engineering as a degree of freedom in on-chip optical sources, including photon pair sources as well as classical laser sources. The benefits towards generation rate of a spontaneous four-wave mixing source were explored, and we found that in the case of high extraction efficiency, this approach can provide significant enhancement over a resonator with equal couplings. We then investigated the frequency correlations between the photons in generated photon pairs and showed that tuning the frequency dependence of the external coupling and the pump bandwidth we could control the joint spectral intensity. We then proposed a dark state laser geometry which can provide wide-band tuning of a single mode output using imaginary coupling.

Chapter 7

Conclusions

7.1 Summary of major achievements

In this thesis we explored the theoretical development and experimental investigation of small footprint and low-power nonlinear sources of quantum light. These sources are fabricated using standard microelectronics processing techniques, enabling ultra-large scale quantum photonic systems which can support the rapid growth of quantum information technologies such as quantum computing and secure communications. We introduced the tool box of components available within the silicon photonic platform, including waveguides, directional couplers, and ring resonators. We then introduced the coupling of modes in time formalism which most of the resonant analysis of sources is described by in this thesis.

A discrete resonance dispersion engineering technique for designing efficient four-wave mixing resonators was presented. We demonstrated four-wave mixing in dual coupled cavity configuration where dispersion can be actively tuned to phasematch the nonlinear process. We also theoretically explored the production of photon pairs through the spontaneous four-wave mixing process using a quantized coupling of modes in time model. We then experimentally demonstrated the first photon pair source fabricated within a commercial CMOS process on the same wafer as billions of electronic transistors. In addition, classical four-wave mixing experiments were used to accurately predict the efficiency of the spontaneous four-wave mixing process.

Noise properties present in on-chip silicon photon pair sources were studied and we specifically discussed the contribution of excess pump photons accompanying the photon pairs to the single pho-

ton detectors. We demonstrated the first single chip system of photon pair source with monolithic pump rejection and measure a pump extinction of over 95 dB. In addition to a coincidences-to-accidentals ratio (CAR), we also measured the time-energy entanglement of the generated photons to demonstrate sufficient pump filtering for multiple applications.

Independently tunable external coupling was explored as a degree of freedom in quantum and classical light sources. We found that this degree of freedom, readily available in integrated photonic platforms provides significant improvements in the state-of-the-art for photon pair sources, by allowing higher generation rates and control over bi-photon frequency correlations. Using imaginary coupling, we also showed that linewidth engineering could be used to construct a laser geometry which would support single mode lasing and wide-band tuning.

7.2 Remaining challenges and future work

While the work in this thesis presents significant advancements in the field of integrated quantum photonics, there are many additional challenges confronting its development into a mature technology. Excess losses are the primary obstacle to useful quantum information technologies based on integrated photonics. While losses to and from a photonic chip can be mitigated by engineering robust high-efficiency grating couplers, the repeatability, scalability, and stability of the coupling will require advancements in packaging techniques such as fiber attachment. Not only should the packaging techniques be robust, but they should also be low cost, in both time and money, such that many input and output ports can be connected between photonic chips. This challenge may be circumvented by implementing all photonic components on a single integrated chip. Stray light scattered throughout a chip will require sufficient engineering to successfully integrated sources and detectors on a single die, but the work presented in Chapter 5 provides a promising foundation which future implementations can be built from.

Once a platform where high purity photon pair sources and efficient single photon detectors are implemented on the same chip is developed, a transition in the utility of integrated quantum photonics will be evident. Not only will the technology provide the promise of scalability, but also

measurements superior to bulk optical experiments will begin to be demonstrated. The ability for an entire system to span mere square millimeters of physical area on a chip means that they can be mounted completely at the sub-Kelvin cryogenic temperatures, thereby allowing for systems where the photons not only never have to physically leave a photonic chip, but are also shielded from the additional noise of a room temperature environment. The primary environmental noise for superconducting detectors is blackbody radiation originating from room temperature components. If all components are implemented at cryogenic temperatures this background can be reduced by many orders of magnitude, providing unprecedented performance advantages to quantum photonic experiments. A particularly important first application of a single-chip platform supporting both sources and detectors is the demonstration of non-classical interference between two heralded single photon sources with visibilities which cannot be rivaled by bulk optical experiments. By utilizing counter propagating travelling modes of a ring resonator source, a single optical cavity can actually provide two independent sources of photon pairs as shown in Fig. 7.1. The photon pairs from both directions can then be filtered from their pump beams and then demultiplexed to four

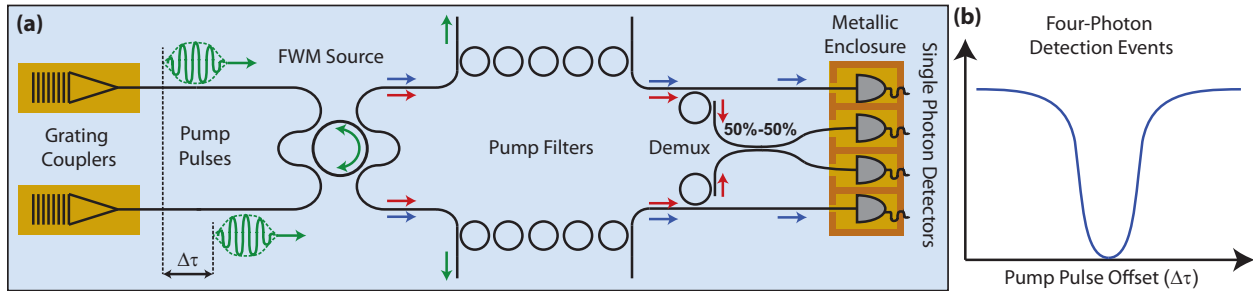


Figure 7.1: (a) Schematic of the proposed fully integrated Hong-Ou-Mandel (HOM) interference experiment for the characterization of heralded single photon sources. Two heralded single photon sources based on Four-Wave Mixing (FWM) consist of counter-propagating pump pulses in the same resonator to generate photon pairs. Each pair of photons then pass through separate high-extinction filters to isolate them from the pump and are then de-multiplexed. The blue arrows represent the trigger photons and the red arrows the heralded single photons. Metallic enclosures isolate the superconducting detectors from stray light, providing access only through the single optical mode of the waveguide. (b) For zero pump pulse offset all four-photon detection events are suppressed due to HOM interference.

individual waveguide paths. From here the heralding photons for each source can be coupled to an upper waveguide layer to be detected while the heralded photons can be interfered on a 50%-50% directional coupler before similarly being sent to their corresponding detectors. With conventional Hong-Ou-Mandel (HOM) interference the optical path length of the heralded photons would be varied to produce a HOM dip. An equivalent procedure on-chip would require significant advancements to the ability of actively reconfiguring silicon photon circuits at temperatures near absolute zero. Instead a similar HOM dip can be observed by varying the time delay between the arrival time of the two pump pulses coupled from off-chip via fiber grating couplers, as shown in Fig. 7.1. This would allow for the configurability needed to vary the degree of interference to be implemented outside the cryostat without introducing any additional background noise to the system. This would provide a feasible first step to demonstrating the inherent advantages of a completely on-chip quantum photonic circuit.

The experiment illustrated in Fig. 7.1 shares a similar characteristic to the on-chip pump filtering presented in Chapter 5, in that it is feasible to demonstrate without reconfigurable photonic circuits, which are challenging to implement at cryogenic temperatures. However, for large scale systems, reconfigurability is a requirement and much research needs to be pursued on engineering methods for supporting fast and energy efficient tunable components. The lack of high-speed and low-power phase shifters that operate at sub-4K temperatures is arguably the primary obstacle to large scale quantum photonic systems at this time. However, there are many promising results in the literature that can potentially lead to a solution to this problem [41, 150].

Quantum photonic integration in the 12SOI CMOS platform also calls for additional research. Specifically, the contribution due to spontaneous Raman generation which we found in Chapters 4 and 5 to be the primary noise source requires further study. Noise characterization experiments at different temperatures and phase matching conditions should be conducted to acquire additional understanding of the source of the noise and therefore provide the knowledge required to eliminate the parasitic effect. While it is likely that the effect will become negligible at cryogenic temperatures (since the phonons involved the process will be removed), additional study is still required.

In summary, the experimental and theoretical advancements presented within this thesis demonstrate the potential of future integrated quantum photonic systems which may enable a new era of measurement technology, communication security, and information processing.

Bibliography

- [1] S. Aaronson and A. Arkhipov. The computational complexity of linear optics. In Proceedings of the 43rd annual ACM symposium on Theory of computing - STOC '11, number 333. ACM, 2011.
- [2] Scott Aaronson. Quantum computing since Democritus. Cambridge University Press, 2013.
- [3] P. P. Absil, J. V. Hryniewicz, B. E. Little, P. S. Cho, R. A. Wilson, L. G. Joneckis, and P.-T. Ho. Wavelength conversion in GaAs micro-ring resonators. Optics Letters, 25:554–556, 2000.
- [4] Govind Agrawal. Nonlinear Fiber Optics. Academic Press, 2012.
- [5] A. Aspect, P. Grangier, and G. Roger. Experimental tests of realistic local theories via Bell's theorem. Physical Review Letters, 47:460–463, 1981.
- [6] Amir H. Atabaki. Reconfigurable silicon photonic devices for optical signal processing. PhD thesis, Georgia Institute of Technology, 2011.
- [7] S. Azzini, D. Grassani, M. Galli, L. C. Andreani, M. Sorel, M. J. Strain, L. G. Helt, J. E. Sipe, M. Liscidini, and D. Bajoni. From classical four-wave mixing to parametric fluorescence in silicon microring resonators. Optics Letters, 37:3807–3809, 2012.
- [8] S. Azzini, D. Grassani, M. J. Strain, M. Sorel, L. G. Helt, J. E. Sipe, M. Liscidini, M. Galli, and D. Bajoni. Ultra-low power generation of twin photons in a compact silicon ring resonator. Optics Express, 20:2310023107, 2012.
- [9] C. Batten, A. Joshi, J. Orcutt, A. Khilo, B. Moss, C. Holzwarth, M. A. Popović, H. Li, H. Smith, J. Hoyt, F. Kärtner, R. Ram, V. Stojanović, and K. Asanovic. Building manycore processor-to-dram networks with monolithic silicon photonics. in 16th IEEE Symposium on High Performance Interconnects (IEEE, 2008), pages 21–30, 2008.
- [10] J.S. Bell. On the Einstein Podolsky Rosen paradox. Physics, 1:195–200, 1964.
- [11] C. H. Bennett, F. Bessette, G. Brassard, L. Salvail, and J. Smolin. Experimental quantum cryptography. Journal of Cryptology, 5:3–28, 1992.
- [12] C. H. Bennett and G. Brassard. Quantum cryptography: Public key distribution and coin tossing. In Proceedings of IEEE International Conference on Computers, Systems and Signal Processing, number 175. IEEE, 1984.

- [13] M. Benyoucef, J.-B. Shim, J. Wiersig, and O. G. Schmidt. Quality-factor enhancement of supermodes in coupled microdisks. Optics Letters, 36:1317, 2011.
- [14] A. N. Boto, P. Kok, D. S. Abrams, S. L. Braunstein, C. P. Williams, and J. P. Dowling. Quantum interferometric optical lithography: exploiting entanglement to beat the diffraction limit. Physical Review Letters, 85:2733, 2000.
- [15] Robert W. Boyd. Nonlinear Optics. Academic Press, 2008.
- [16] A. D. Bristow, N. Rotenberg, and H. M. van Driel. Two-photon absorption and Kerr coefficients of silicon for 850-2200 nm. Applied Physics Letters, 90:191104, 2007.
- [17] R. Hanbury Brown and R. Q. Twiss. A test of a new type of stellar interferometer on Sirius. Nature, 178:1046–1048, 1956.
- [18] R. Hanbury Brown and R. Q. Twiss. Interferometry of the intensity fluctuations in light. I. Basic theory: the correlation between photons in coherent beams of radiation. Proceedings of the Royal Society A., 242:300–324, 1957.
- [19] D. C. Burnham and D. L. Weinberg. Observation of simultaneity in parametric production of optical photon pairs, 1970.
- [20] C. M. Caves. Quantum-mechanical noise in an interferometer. Physical Review D., 23:1693–1708, 1981.
- [21] J. Chen, A. J. Pearlman, A. Ling, J. Fan, and A. Migdall. A versatile waveguide source of photon pairs for chip-scale quantum information processing. Optics Express, 17:6727–6740, 2009.
- [22] W. C. Chew and M. A. Nasir. A variational analysis of anisotropic inhomogeneous dielectric waveguides. IEEE Transactions on Microwave Theory and Techniques, 37:661–668, 1989.
- [23] S. Clemmen, K. P. Huy, W. Bogaerts, R. G. Baets, P. Emplit, and S. Massar. Continuous wave photon pair generation in silicon-on-insulator waveguides and ring resonators. Optics Express, 17:1655816570, 2009.
- [24] Claude Cohen-Tannoudji, Jacques Dupont-Roc, and Gilbert Grynberg. Photons and Atoms: Introduction to Quantum Electrodynamics. Wiley, 1989.
- [25] M. J. Collins, C. Xiong, I. H. Rey, T. D. Vo, J. He, S. Shahnia, C. Reardon, M. J. Steel, T. F. Krauss, A. S. Clark, , and B. J. Eggleton. Integrated spatial multiplexing of heralded single-photon sources. Nature Communications, 4:2582, 2013.
- [26] M. S. Dahlem, C. W. Holzwarth, H. I. Smith, E. P. Ippen, and M. A. Popović. Dynamical slow light cell based on controlled far-field interference of microring resonators. In Integrated Photonics Research, number IMC4. Optical Society of America, 2010.
- [27] M. Davanco, J. R. Ong, A. B. Shehata, A. Tosi, I. Agha, S. Assefa, F. Xia, W. M. J. Green, S. Mookherjea, and K. Srinivasan. Telecommunications-band heralded single photons from a silicon nanophotonic chip. Applied Physics Letters, 100:261104, 2012.
- [28] M. Dinu, F. Quochi, and H. Garcia. Third-order nonlinearities in silicon at telecom wavelengths. Applied Physics Letters, 82:2954–2956, 2003.

- [29] P. A. M. Dirac. The quantum theory of the emission and absorption of radiation. Proceedings of the Royal Society of London. Series A., Containing Papers of a Mathematical and Physical Character, 114:243265, 1917.
- [30] P. Ben Dixon, D. Rosenberg, V. Stelmakh, M. E. Grein, R. S. Bennink, E. A. Dauler, A. J. Kerman, R. J. Molnar, and F. N. C. Wong. Heralding efficiency and correlated-mode coupling of near-ir fiber-coupled photon pairs. Physical Review A, 90:043804, 2014.
- [31] S. Dyer, B. Baek, and S. W. Nam. High-brightness, low-noise, all-fiber photon pair source. Optics Express, 17:10290–10297, 2009.
- [32] A. Einstein. Über einen die erzeugung und verwandlung des lichtes betreffenden heuristischen gesichtspunkt [On a heuristic viewpoint concerning the production and transformation of light]. Annalen der Physik, 17:132–148, 1905.
- [33] A. Einstein. Zum gegenwertigen stand des strahlungsproblems [On the current state of the radiation problem]. Physikalische Zeitschrift, 10:185–193, 1909.
- [34] A. Einstein. Zur quantentheorie der strahlung [On the quantum mechanics of radiation]. Physikalische Zeitschrift, 18:121–128, 1917.
- [35] E. Engin, D. Bonneau, C. M. Natarajan, A. S. Clark, M. G. Tanner, R. H. Hadfield, S. N. Dorenbox, V. Zwiller, K. Ohira, N. Suzuki, H. Yoshida, N. Iizuka, M. Ezaki, J. L. O'Brien, and M. G. Thompson. Photon pair generation in silicon micro-ring resonator with reverse bias enhancement. Optics Express, 21:2782627834, 2013.
- [36] U. Fano. Quantum theory of interference effects in the mixing of light from phase independent sources. American Journal of Physics, 29:539, 1961.
- [37] Mark Fox. Quantum optics: an introduction. Oxford University Press, 2006.
- [38] S. J. Freedman and J. F. Clauser. Experimental test of local hidden-variable theories. Physical Review Letters, 28:938, 1972.
- [39] B. J. Frey, D. B. Leviton, and T. J. Madison. Temperature-dependent refractive index of silicon and germanium. In Optomechanical technologies for Astronomy, number 62732J in Proceedings of SPIE 6273. SPIE, 2006.
- [40] C. W. Gardiner and M. J. Collett. Input and output in damped quantum systems: Quantum stochastic differential equations and the master equation. Physical Review A, 31:3761–3774, 1985.
- [41] M. Gehl, C. Long, D. Trotter, A. Starbuck, A. Pomerene, J. B. Wright, S. Melgaard, J. Sirola, A. L. Lentine, and C. DeRose. Operation of high-speed silicon photonic micro-disk modulators at cryogenic temperatures. Optica, 4:374–382, 2017.
- [42] C. M. Gentry, G. Triginer Garces, X. Zeng, and M. A. Popović. Passive linewidth narrowing through nondegenerate optical parametric oscillation with asymmetric port couplings. In 2016 Conference on Lasers and Electro-Optics (CLEO), number FF2M.6. OSA, 2016.
- [43] C. M. Gentry, G. Triginer Garces, X. Zeng, and M. A. Popović. Tailoring of individual photon lifetimes as a degree of freedom in resonant quantum photonic sources. In 2016 Conference on Lasers and Electro-Optics (CLEO), number JTU5A.17. OSA, 2016.

- [44] C. M. Gentry, O. S. Magaña-Loaiza, M. T. Wade, F. Pavanello, T. Gerrits, S. Lin, J. M. Shainline, S. D. Dyer, S. Woo Nam, R. P. Mirin, and M. A. Popović. Monolithic source of entangled photons with integrated pump rejection. In 2018 Conference on Lasers and Electro-Optics (CLEO), number JTh4C.3. OSA, 2018.
- [45] C. M. Gentry and M. A. Popović. Dark state lasers. Optics Letters, 39:4136–4139, 2014.
- [46] C. M. Gentry, J. M. Shainline, M. T. Wade, M. J. Stevens, S. D. Dyer, X. Zeng, F. Pavanello, T. Gerrits, S. Woo Nam, R. P. Mirin, and M. A. Popović. Quantum-correlated photon pairs generated in a commercial 45 nm complementary metal-oxide semiconductor microelectronic chip. Optica, 2:1065–1071, 2015.
- [47] C. M. Gentry, X. Zeng, and M. A. Popović. A discrete resonance, all-order dispersion engineering method for microcavity design for four-wave mixing. In Frontiers in Optics, number FTu5D.3. Optical Society of America, 2014.
- [48] C. M. Gentry, X. Zeng, and M. A. Popović. Tunable coupled-mode dispersion compensation and its application to on-chip resonant four-wave mixing. Optics Letters, 39:5689–5692, 2014.
- [49] M. Georgas, B. R. Moss, C. Sun, J. Shainline, J. S. Orcutt, M. Wade, Y. H. Chen, K. Nam-mari, J. C. Leu, A. Srinivasan, R. J. Ram, M. A. Popović, and V. M. Stojanović. A monolithically-integrated optical transmitter and receiver in a zero-change 45 nm SOI process. In VLSI Circuits Symposium, number 247. IEEE, 2014.
- [50] M. Gimeno-Segovia, P. Shadbolt, D. E. Browne, and T. Rudolph. From three-photon Greenberger-Horne-Zeilinger states to ballistic universal quantum computation. Physical Review Letters, 115:020502, 2015.
- [51] M. Giustina, M. A.M. Versteegh, S. Wengerowsky, J. Handsteiner, A. Hochrainer, K. Phe-lan, F. Steinlechner, J. Kofler and J.-A. Larsson, C. Abelln, W. Amaya, V. Pruneri, M. W. Mitchell, J. Beyer, T. Gerrits, A. E. Lita, L. K. Shalm, S. W. Nam, T. Scheidl, R. Ursin, B. Wittmann, and A. Zeilinger. Significant-loophole-free test of Bell’s theorem with entangled photons. Physical Review Letters, 115:250401, 2015.
- [52] R. J. Glauber. Coherent and incoherent states of the radiation field. Physical Review, 131:27766–2788, 1963.
- [53] D. Grassani, S. Azzini, M. Liscidini, M. Galli, M. J. Strain, M. Sorel, J. E. Sipe, and D. Bajoni. Micrometer-scale integrated silicon source of time-energy entangled photons. Optica, 2:88–94, 2015.
- [54] M. A. Green and M. J. Keevers. Optical properties of intrinsic silicon at 300 K. Progress in Photovoltaics, 3:189–192, 1995.
- [55] X. Guo, C. l. Zou, C. Schuck, H. Jung, R. Cheng, and H. X. Tang. Parametric down-conversion photon-pair source on a nanophotonic chip. Light: Science and Applications, 6:e16249, 2017.
- [56] K.-I. Harada, H. Takesue, H. Fukuda, T. Tsuchizawa, T. Watanabe, K. Yamada, Y. Tokura, and S.-I. Itabasha. Generation of high-purity entangled photon pairs using silicon wire waveguide. Optics Express, 16:2036820373, 2008.

- [57] N. C. Harris, D. Grassani, A. Simbula, M. Pant, M. Galli, T. Baehr-Jones, M. Hochberg, D. Englund, D. Bajoni, and C. Galland. Integrated source of spectrally filtered correlated photons for large-scale quantum photonic systems. Physical Review X, 4:041047, 2014.
- [58] H. A. Haus and W. Huang. Coupled-mode theory. Proceedings of the IEEE, 79:1505–1518, 1991.
- [59] Hermann A. Haus. Waves and Fields in Optoelectronics. Prentice Hall, 1983.
- [60] Hermann A. Haus. Electromagnetic Noise and Quantum Optical Measurements. Springer, 2000.
- [61] W. D. Heiss. Exceptional points of non-hermitian operators. Journal of Physics A, 37:2455, 2004.
- [62] L. G. Helt, M. Liscidini, and J. E. Sipe. How does it scale? comparing quantum and classical nonlinear optical processes in integrated devices. Journal of the Optical Society of America B, 29:2199–2212, 2012.
- [63] L. G. Helt, M. J. Steel, and J. E. Sipe. Parasitic nonlinearities in photon pair generation via integrated spontaneous four-wave mixing: critical problem or distraction? Applied Physics Letters, 102:201106, 2013.
- [64] B. Hensen, H. Bernien, A.E. Dréau, A. Reiserer, N. Kalb, M.S. Blok, J. Ruitenbergh, R.F.L. Vermeulen, R.N. Schouten, C. Abelln, W. Amaya, V. Pruneri, M.W. Mitchell, M. Markham, D.J. Twitchen, D. Elkouss, S. Wehner, T.H. Taminiiau, and R. Hanson. Loophole-free bell inequality violation using electron spins separated by 1.3 kilometres. Nature, 526:682–686, 2015.
- [65] S. Heron, R. W. P. McWirtter, and E. H. Rhoderick. Measurements of lifetimes of excited states of atoms by the method of delayed coincidences. Nature, 174:564, 1954.
- [66] C. M. Herzinger, B. Johs, W. A. McGahan, J. A. Woollam, and W. Paulson. Ellipsometric determination of optical constants for silicon and thermally grown silicon dioxide via a multi-sample, multi-wavelength, multi-angle investigation. Journal of Applied Physics, 83:3323–3336, 1998.
- [67] C. K. Hong, Z. Y. Ou, and L. Mandel. Measurement of subpicosecond time intervals between two photons by interference. Physical Review Letters, 59:2044–2046, 1987.
- [68] C. A. Husko, A. S. Clark, M. J. Collins, A. D. Rossi, S. Combrié, G. Lehoucq, I. H. Rey, T. F. Krauss, C. Xiong, and B. J. Eggleton. Multi-photon absorption limits to heralded single photon sources. Scientific Reports, 3:3087, 2013.
- [69] V. Jayaraman, Z.-M. Chuang, and L. A. Coldren. Theory, design, and performance of extended tuning range semiconductor lasers with sampled gratings. IEEE Journal of Quantum Electronics, 29:1824–1834, 1993.
- [70] W. C. Jiang, J. Zhang, N. G. Usechak, and Q. Lin. Dispersion engineering of high-Q silicon microresonators via thermal oxidation. Applied Physics Letters, 105:031112, 2014.

- [71] S. G. Johnson, P. Bienstman, M. A. Skorobogatiy, M. Ibanescu, E. Lidorikis, and J. D. Joannopoulos. Adiabatic theorem and continuous coupled-mode theory for efficient taper transitions in photonic crystals. Physical Review E, 66:066608, 2002.
- [72] R. A. Kaplan. Optical waveguides of macroscopic dimension in single mode operation. Proceedings of the IEEE, 51:1144–1145, 1963.
- [73] A. E. Karbowiak. New type of waveguide for light and infrared waves. Electronic Letters, 1:47–48, 1965.
- [74] S. Khan, M. A. Baghban, and S. Fathpour. Electronically tunable silicon photonic delay lines. Optics Express, 19:11780–11785, 2011.
- [75] J. S. Kilby. Miniaturized electronic circuits. United States Patent Office, US Patent 3,138,743, filed February 6, 1959, issued June 23, 1964.
- [76] E. Knill, R. Laflamme, and G. J. Milburn. A scheme for efficient quantum computation with linear optics. Nature, 409:46–52, 2001.
- [77] R. Kumar, J. R. Ong, J. Recchio, K. Srinivasan, and S. Mookherjea. Spectrally multiplexed and tunable-wavelength photon pairs at 1.55 μm from a silicon coupled-resonator optical waveguide. Optics Letters, 38:2969–2971, 2013.
- [78] P. G. Kwiat, K. Mattle, H. Weinfurter, A. Zeilinger, A. V. Sergienko, and Y. Shih. New high-intensity source of polarization-entangled photon pairs. Physical Review Letters, 75:4337, 1995.
- [79] B. G. Lee, A. Biberman, J. Chan, and K. Bergman. High-performance modulators and switches for silicon photonic networks-on-chip. IEEE Journal of Select Topics on Quantum Electronics, 16:6–22, 2010.
- [80] H. Lee, T. Chen, J. Li, O. Painter, and K. J. Vahala. Ultra-low-loss optical delay line on a silicon chip. Nature Communications, 3:867, 2012.
- [81] S. Lee, B. Jagannathan, S. Narasimha, A. Chou, N. Zamdmer, J. Johnson, R. Williams, L. Wagner, J. Kim, J. O. Plouchart, and J. Pekarik. Record RF performance of 45-nm SOI CMOS technology. In Electron Devices Meeting, pages 255–258. IEEE International, 2007.
- [82] Z. Li, S. Gao, Q. Liu, and S. He. Modified model for four-wave mixing-based wavelength conversion in silicon micro-ring resonators. Optics Communications, 284:2215–2221, 2011.
- [83] Q. Lin and G. P. Agrawal. Silicon waveguides for creating quantum-correlated photon pairs. Optics Letters, 31:3140–3142, 2006.
- [84] Q. Lin, O. J. Painter, and G. P. Agrawal. Nonlinear optical phenomena in silicon waveguides: Modeling and applications. Optics Express, 15:16604–16644, 2007.
- [85] A. E. Lita, A. J. Miller, and S. W. Nam. Counting near-infrared single-photons with 95% efficiency. Optics Express, 16:3032–3040, 2008.
- [86] B. E. Little, S. T. Chu, H. A. Haus, J. Foresi, and J. P. Laine. Microring resonator channel dropping filters. Journal of Lightwave Technology, 15:998–1005, 1997.

- [87] A. Liu, R. Jones, L. Liao, D. Samara-Rubio, D. Rubin, O. Cohen, R. Nicolaescu, and M. Paniccia. A high-speed silicon optical modulator based on a metal-oxide-semiconductor capacitor. Nature, 427:615–618, 2004.
- [88] L. Liu, R. Kumar, K. Huybrechts, T. Spuesens, G. Roelkens, E.-J. Geluk, T. De Vries, P. Regreny, D. Van Thourhout, R. Baets, and G. Morthier. An ultra-small, low-power, all-optical flip-flop memory on a silicon chip. Nature Photonics, 4:182, 2010.
- [89] Y. Liu and M. A. Popović. High-Q contacted ring microcavities with scatterer-avoiding “wiggler” bloch wave supermode fields. Applied Physics Letters, 104:201102, 2014.
- [90] Y. Liu, J. M. Shainline, X. Zeng, and M. A. Popović. Ultra-low-loss cmos-compatible waveguide crossing arrays based on multimode bloch waves and imaginary coupling. Optics Letters, 39:335–338, 2014.
- [91] X. Lu, S. Rogers, W. C. Jiang, and Q. Lin. Selective engineering of cavity resonance for frequency matching in optical parametric processes. Applied Physics Letters, 105:151104, 2014.
- [92] T. H. Maiman. Stimulated optical radiation in ruby. Nature, 187:493–494, 1960.
- [93] Dietrich Marcuse. Theory of Dielectric Optical Waveguides. Elsevier, 1991.
- [94] F. Marsili, V. B. Verma, J. A. Stern, S. Harrington, A. E. Lita, T. Gerrits, I. Vayshenker, B. Baek, M. D. Shaw, R. P. Mirin, and S. W. Nam. Detecting single infrared photons with 93% system efficiency. Nature Photonics, 7:210–214, 2013.
- [95] N. Matsuda, H. L. Jeannic, H. Fukuda, T. Tsuchizawa, W. J. Munro, K. Shimizu, K. Yamada, Y. Tokura, and H. Takesue. A monolithically integrated polarization entangled photon pair source on a silicon chip. Scientific Reports, 2:817, 2012.
- [96] N. Matsuda, H. Takesue, K. Shimizu, Y. Tokura, E. Kuramochi, and M. Notomi. Slow light enhanced correlated photon pair generation in photonic-crystal coupled-resonator optical waveguides. Optics Express, 21:85968604, 2013.
- [97] A. Melloni, A. Canciamilla, C. Ferrari, F. Morichetti, L. O’Faolain, T. F. Krauss, R. De La Rue, A. Samarelli, and M. Sorel. Tunable delay lines in silicon photonics: coupled resonators and photonic crystals, a comparison. IEEE Photonics Journal, 2:181–194, 2010.
- [98] A. L. Migdall, D. Branning, and S. Castelletto. Tailoring single-photon and multiphoton probabilities of a single-photon on-demand source. Physical Review A, 66:053805, 2002.
- [99] Alan Migdall, Sergey V. Polyakov, Jingyun Fan, and Joshua C. Bienfang. Single-Photon Generation and Detection: PHysics and Applications. Academic Press, 2013.
- [100] S. E. Miller. Integrated optics: An introduction. The Bell System Technical Journal, 48:2059–2069, 1969.
- [101] S. E. Miller. Citation classic - integrated optics: An introduction. Current Contents/Physical Chemical and Earth Sciences, 5:141, 1979.
- [102] R. A. Millikan. A direct determination of “h”. Physical Review, 4:73–75, 1914.

- [103] F. Najafi, J. Mower, N. C. Harris, F. Bellei, A. Dane, C. Lee, X. Hu, P. Kharel, F. Marsili, S. Assefa, K. K. Berggren, and D. Englund. On-chip detection of non-classical light by scalable integration of single-photon detectors. Nature Communications, 6:5873, 2015.
- [104] J. Notaros, F. Pavanello, M. T. Wade, C. M. Gentry, A. Atabaki, L. Alloatti, R. J. Ram, and M. A. Popović. 75% efficient wide bandwidth grating couplers in a 45 nm microelectronics cmos process. In Optical Interconnects Conference, pages 46–47. IEEE, 2015.
- [105] R. N. Noyce. Semiconductor device-and-lead structure. United States Patent Office, US Patent 2,981,877, filed July 30, 1959, issued April 25, 1961.
- [106] J. L. O’Brien. Optical quantum computing. Science, 318:1500–1503, 2007.
- [107] J. L. O’Brien, A. Furusawa, and J. Vuckovic. Photonic quantum technologies. Nature Photonics, 3:687–695, 2009.
- [108] J. L. O’Brien, G. J. Pryde, A. G. White, T. C. Ralph, and D. Branning. Demonstration of an all-optical quantum controlled-not gate. Nature, 426:264, 2003.
- [109] J. R. Ong, R. Kumar, and S. Mookherjea. Ultra-high-contrast and tunable-bandwidth filter using cascaded high-order silicon microring filters. IEEE Photonics Technology Letters, 25:15431546, 2013.
- [110] J. S. Orcutt, B. Moss, C. Sun, J. Leu, M. Georgas, J. M. Shainline, E. Zraggen, H. Li, J. Sun, M. Weaver, S. Urošević, M. A. Popović, R. Ram, and V. M. Stojanović. Open foundry platform for high-performance electronic-photonic integration. Optics express, 20:12222–12232, 2012.
- [111] Edward Palik. Handbook of Optical Constants. Elsevier, 1998.
- [112] M. Pant, H. Krovi, D. Englund, and S. Guha. Rate-distance tradeoff and resource costs for all-optical quantum repeaters. Physical Review A, 95:012304, 2017.
- [113] W. H. P. Pernice, C. Schuck, O. Minaeva, M. Li, G. N. Goltsman, A. V. Sergienko, and H. X. Tang. High-speed and high-efficiency travelling wave single-photon detectors embedded in nanophotonic circuits. Nature Communications, 3:1325, 2012.
- [114] M. Piekarek, D. Bonneau, S. Miki, T. Yamashita, M. Fujiwara, M. Sasaki, H. Terai, M. G. Tanner, C. M. Natarajan, R. H. Hadfield, J. L. O’Brien, and M. G. Thompson. High-extinction ratio integrated photonic filters for silicon quantum photonics. Optics Letters, 42:815–818, 2017.
- [115] M. Planck. Über das gesetz der energieverteilung im normalspektrum [On the law of distribution of energy in the normal spectrum]. Annalen der Physik, 4:553–563, 1901.
- [116] M. A. Popović. Complex-frequency leaky mode computations using PML boundary layers for dielectric resonant structures. In Integrated Photonics Research, number ITuD4. Optical Society of America, 2003.
- [117] M. A. Popović, T. Barwicz, M. S. Dahlem, F. Gan, C. W. Holzwarth, P. T. Rakich, H. I. Smith, E. P. Ippen, and F. X. Kärtner. Tunable, fourth-order silicon microring-resonator add-drop filters. In European Conference on Optical Communication, number 1.2.3. ECOC, 2007.

- [118] Miloš A. Popović. Theory and Design of High-Index-Contrast Microphotonic Circuits. PhD thesis, Massachusetts Institute of Technology, 2008.
- [119] W. Primak. Refractive index of silicon. Applied Optics, 10:759–763, 1971.
- [120] S. Ramelow, A. Farsi, S. Clemmen, J. S. Levy, A. R. Johnson, Y. Okawachi, M. R. E. Lamont, M. Lipson, and A. L. Gaeta. Strong polarization mode coupling in microresonators. Optics Letters, 39:5134–5137, 2014.
- [121] D. M. Ramirez, A. W. Rodriguez, H. Hasahemi, J. D. Joannopoulos, M. Soljačić, and S. G. Johnson. Degenerate four-wave mixing in triply resonant Kerr cavities. Physical Review A, 83:033834, 2011.
- [122] R. Raussendorf, J. Harrington, and K. Goyal. Topological fault-tolerance in cluster state quantum computation. New Journal of Physics, 9:199, 2007.
- [123] C. Reimer, L. Caspani, M. Clerici, M. Ferrera, M. Kues, M. Peccianti, A. Pasquazi, L. Razzari, B. E. Little, S. T. Chu, D. J. Moss, and R. Morandotti. Integrated frequency comb source of heralded single photons. Optics Express, 22:6535–6546, 2014.
- [124] S. Rogers, D. Mulkey, X. Lu, W. C. Jiang, and Q. Lin. High visibility time-energy entangled photons from a silicon nanophotonic chip. ACS Photonics, 3:1754–1761, 2016.
- [125] L. A. Rozema, C. Wang, D. H. Mahler, A. Hayat, A. M. Steinberg, and J. E. Sipe. Characterizing an entangled-photon source with classical detectors and measurements. Optica, 2:430–433, 2015.
- [126] T. Rudolph. Why I am optimistic about the silicon-photonics route to quantum computing. APL Photonics, 2:030901, 2017.
- [127] C. D. Salzberg and J. J. Villa. Infrared refractive indexes of silicon, germanium, and modified selenium glass. Journal of Optical Society of America, 47:244–246, 1957.
- [128] E. R. Schineller. Summary of the development of optical waveguides and components. Wheeler Laboratories, Report 1471, 1967.
- [129] J. M. Shainline, S. M. Buckley, N. Nader, C. M. Gentry, K. C. Cossel, J. W. Cleary, M. A. Popović, N. R. Newbury, S. W. Nam, and R. P. Mirin. Room-temperature-deposited dielectrics and superconductors for integrated photonics. Optics Express, 25:10322–10334, 2017.
- [130] J. M. Shainline, J. S. Orcutt, M. T. Wade, K. Nammari, B. Moss, M. Georgas, C. Sun, R. J. Ram, V. M. Stojanović, and M. A. Popović. Depletion-mode carrier-plasma optical modulator in zero-change advanced cmos. Optics Letters, 38:2657–2659, 2013.
- [131] J. M. Shainline, J. S. Orcutt, M. T. Wade, K. Nammari, O. Tehar-Zahav, Z. Sternberg, R. Meade, R. J. Ram, V. M. Stojanović, and M. A. Popović. Depletion-mode polysilicon optical modulators in a bulk complementary metal-oxide semiconductor process. Optics Letters, 38:2729–2731, 2013.
- [132] L. K. Shalm, E. Meyer-Scott, B. G. Christensen, P. Bierhorst, M. A. Wayne, M. J. Stevens, T. Gerrits, S. Glancy, D. R. Hamel, M. S. Allman, K. J. Coakley, S. D. Dyer, C. Hodge, A. E. Lita, V. B. Verma, C. Lambrocco, E. Tortorici, A. L. Migdall, Y. Zhang, D. R. Kumor, W. H.

- Farr, F. Marsili, M. D. Shaw, J. A. Stern, C. Abelln, W. Amaya, V. Pruneri, T. Jennewein, M. W. Mitchell, P. G. Kwiat, J. C. Bienfang, R. P. Mirin, E. Knill, and S. W. Nam. Strong loophole-free test of local realism. Physical Review Letters, 115:2504024, 2015.
- [133] Ramamurthi Shankar. Principles of Quantum Mechanics. Springer Sciences and Business Media, 2012.
- [134] J. E. Sharping, K. F. Lee, M. A. Foster, A. C. Turner, B. S. Schmidt, M. Lipson, A. L. Gaeta, and P. Kumar. Generation of correlated photons in nanoscale silicon waveguides. Optics Express, 14:12388–12393, 2006.
- [135] J. W. Silverstone, D. Bonneau, K. Ohira, N. Suzuki, H. Yoshida, N. I. Izuka, M. Ezaki, R. Hadfield, G. D. Marshall, V. Z. Willer, J. G. Rarity, J. L. O'Brien, and M. G. Thompson. On-chip quantum interference between silicon photon-pair sources. Nature Photonics, 8:104–108, 2014.
- [136] J. W. Silverstone, R. Santagati, D. Bonneau, M. J. Strain, M. Sorel, J. L. O'Brien, and M. G. Thompson. Qubit entanglement between ring-resonator photon-pair sources on a silicon chip. Nature Communications, 6:7948, 2015.
- [137] E. C. G. Sudarshan. Equivalence of semiclassical and quantum mechanical descriptions of statistical light beams. Physical Review Letters, 10:277–279, 1963.
- [138] W. Suh, Z. Wang, and S. Fan. Temporal coupled-mode theory and the presence of non-orthogonal modes in lossless multimode cavities. IEEE Journal of Quantum Electronics, 40:1511–1518, 2004.
- [139] C. Sun, M. Georgas, J. Orcutt, B. Moss, Y.-H. Chen, J. Shainline, M. Wade, K. Mehta, K. Nammari, E. Timurdogan, D. Miller, O. Tehar-Zahav, Z. Sternberg, J. Leu, J. Chong, R. Bafrafi, G. Sandhu, M. Watts, R. Meade, M. A. Popović, R. Ram, and V. Stojanović. A monolithically integrated chip-to-chip optical link in bulk CMOS. IEEE Journal of Solid State Circuits, 50:828–844, 2015.
- [140] C. Sun, M. Wade, M. Georgas, S. Lin, L. Alloatti, B. Moss, R. Kumar, A. Atabaki, F. Pavanello, R. Ram, and M. A. Popović. A 45 nm SOI monolithic photonics chip-to-chip link with bit-statistics-based resonant microring thermal tuning. In Symposium on VLSI Circuits, pages C122–C123. IEEE, 2015.
- [141] C. Sun, M. T. Wade, Y. Lee, J. S. Orcutt, L. Alloatti, M. S. Georgas, A. S. Waterman, J. M. Shainline, R. R. Avizienis, S. Lin, B. R. Moss, R. Kumar, F. Pavanello, A. H. Atabaki, H. M. Cook, A. J. Ou, J. C. Leu, Y.-H. Chen, K. Asanović, R. J. Ram, M. A. Popović, and V. M. Stojanović. Single-chip microprocessor that communicates directly using light. Nature, 528:534–538, 2015.
- [142] J. Suo, S. Dong, W. Zhang, Y. Huang, and J. Peng. Generation of hyper-entanglement on polarization and energy-time based on a silicon micro-ring cavity. Optics Express, 23:39853995, 2015.
- [143] H. Takesue, N. Matsuda, E. Kuramochi, and M. Notomi. Entangled photons from on-chip slow light. Scientific Reports, 4:3913, 2014.

- [144] H. Takesue, Y. Tokura, H. Fukuda, T. Tsuchizawa, T. Watanabe, K. Yamada, and S.-I. Itabashi. Entanglement generation using silicon wire waveguide. Applied Physics Letters, 91:201108, 2007.
- [145] S. Tanzilli, H. de Riedmatten, W. Tittel, H. Zbinden, P. Baldi, M. de Micheli, D. B. Ostrowski, and N. Gisin. Highly efficient photon-pair source using periodically poled lithium niobate waveguide. Electronics Letters, 37:26–28, 2001.
- [146] P. R. Tapster and J. G. Rarity. Photon statistics of pulsed parametric light. Journal of Modern Optics, 45:595–604, 1998.
- [147] B. Tatian. Fitting refractive-index data with the sellmeier dispersion formula. Applied Optics, 23:4477–4485, 1984.
- [148] G. I. Taylor. Interference fringes with feeble light. Proceedings of the Cambridge Philosophical Society, 15:114–115, 1909.
- [149] R. T. Thew, S. Tanzill, W. Tittel, H. Zbinden, and N. Gisin. Experimental investigation of the robustness of partially entangled qubits over 11 km. Physical Review A, 66:062304, 2012.
- [150] E. Timurdogan, C. V. Poulton, M. J. Byrd, and M. R. Watts. Electric-field induced second-order nonlinear optical effects in silicon waveguides. Nature Photonics, 11:200–206, 2017.
- [151] K. Vahala. Optical Microcavities. World Scientific, 2004.
- [152] I. V. Vernik, T. A. Ohki, M. B. Ketchen, and M. Bhushan. Performance characterization of PD-SOI ring oscillators at cryogenic temperatures. In IEEE International SOI Conference, pages 1–2. IEEE, 2010.
- [153] Z. Vernon, , M. Menotti, C. C. Tison, J. A. Steidle, M. L. Fanto, P. M. THomas, S. F. Preble, A. M. Smith, P. M. Alsing, M. Liscidini, and J. E. Sipe. Truly unentangled photon pairs without spectral filtering. Optics Letters, 42:3638–3641, 2017.
- [154] Z. Vernon, M. Liscidini, and J. E. Sipe. No free lunch: the trade-off between heralding rate and efficiency in microresonator-based heralded single photon sources. Optics Letters, 41:788–791, 2016.
- [155] Z. Vernon and J. E. Sipe. Spontaneous four-wave mixing in lossy microring resonators. Physical Review A, 91:053802, 2015.
- [156] Y. Vlasov, W. M. J. Green, and F. Xia. High-throughput silicon nanophotonic wavelength-insensitive switch for on-chip optical networks. Nature Photonics, 2:242–246, 2008.
- [157] M. T. Wade, F. Pavanello, R. Kumar, C. M. Gentry, A. Atabaki, R. J. Ram, V. M. Stojanović, and M. A. Popović. 75% efficient wide bandwidth grating couplers in a 45 nm microelectronics CMOS process. In Optical Interconnects Conference, pages 46–47. IEEE, 2015.
- [158] M. T. Wade, J. M. Shainline, J. S. Orcutt, C. Sun, R. Kumar, B. Moss, M. Georgas, C. Sun, R. J. Ram, V. M. Stojanović, and M. A. Popović. Energy-efficient active photonics in a zero-change, state-of-the-art CMOS process. In Optical Fiber Communication Conference, number Tu2E.7. Optical Society of America, 2014.

- [159] R. Wakabayashi, M. Fujiwara, K.-I. Yoshino, Y. Nambu, M. Sasaki, and T. Aoki. Time-bin entangled photon pair generation from a micro-ring resonator. Optics Express, 23:1103–1113, 2015.
- [160] M. R. Watts, T. Barwicz, M. Popovic, L. Socci, P. T. Rakich, E. P. Ippen, H. I. Smith, and F. Kartner. Design, fabrication, and characterization of a free spectral range doubled ring-resonator filter. In Conference on Lasers and Electro-Optics: CLEO 2005, number CMP3. Optical Society of America, 2005.
- [161] F. Xia, M. Rooks, L. Sekaric, and Y. Vlasov. Ultra-compact high order ring resonator filters using submicron silicon photonic wires for on-chip optical interconnects. Optics Express, 15:1193411941, 2007.
- [162] C. Xiong, C. Monat, A. S. Clark, C. Grillet, G. D. Marshall, M. J. Steel, J. Li, L. O'Faolain, T. F. Krauss, J. G. Rarity, and B. J. Eggleton. Slow-light enhanced correlated photon pair generation in a silicon photonic crystal waveguide. Optics Letters, 36:34133415, 2011.
- [163] Q. Xu, S. Sandhu, M. L. Povinelli, J. Shakya, S. Fan, and M. Lipson. Experimental realization of an on-chip all-optical analogue to electromagnetically induced transparency. Physical Review Letters, 96:123901, 2006.
- [164] X. Xue, Y. Xuan, P.-H. Wang, Y. Liu, D. E. Leaird, M. Qi, and A. M. Weiner. Normal-dispersion microcombs enabled by controllable mode interactions. Laser and Photonics Reviews, 9:L23–L28, 2015.
- [165] S.-J. Yang, X.-J. Wang, X.-H. Bao, and J.-W. Pan. An efficient quantum light-matter interface with sub-second lifetime. Nature Photonics, 10:381, 2016.
- [166] Anthony Zee. Quantum field theory in a nutshell. Princeton University Press, 2010.
- [167] X. Zeng, C. M. Gentry, and M. A. Popović. Four-wave mixing in silicon coupled-cavity resonators with port-selective, orthogonal supermode excitation. Optics Letters, 40:210–2123, 2015.
- [168] X. Zeng and M. A. Popović. Design of triply-resonant microphotonic parametric oscillators based on kerr nonlinearity. Optics Express, 22:15837–15867, 2014.